University of Strathclyde Glasgow

Department of Chemical & Process Engineering

Nitrogen-Enriched Carbon Materials for High-Power Electrochemical Capacitors

Anthony Rennie

Degree of Doctor of Philosophy

2011

Copyright Statement

Signed:

Date:

Acknowledgements

I would like to express my gratitude to my supervisor, Prof. Peter Hall, for the opportunity to undertake this project and for his guidance, patience and support throughout. Thanks are extended to my colleagues in the energy storage research group, and I am exceptionally grateful to Dr. Fiona Sillars for her feedback, positivity and helpful discussions during this endeavour.

It is my pleasure to thank all of the people who have contributed in any way to this work, including the technical and secretarial staff in the Dept. of Chemical & Process Engineering. Special thanks go to Jim Murphy for ensuring that the lab runs smoothly, and to Matthew Kidd for knowing what to do when computers misbehave. I am sincerely thankful for the support of Karen Morrison and Alexis McDonald - without their help this project would not have been completed. In addition, I would like to thank my fellow students and wish them all the best for the future.

I would like to acknowledge Prof. Patrick Grant, Dr. Alison Crossley and Dr. Hugh Bishop at the Dept. of Materials, University of Oxford for allowing me to use their XPS equipment which was essential for the completion of this work. Also, I am especially grateful for the assistance of Denise Gilmour in the Dept. of Pure & Applied Chemistry who performed the elemental analyses. Furthermore, I am extremely grateful for being given beam time at ISIS, and the assistance of Dr. Sarah Rogers, instrument scientist for LOQ, is very much appreciated.

I have been extremely fortunate to receive a fantastic amount of support and encouragement from my family, for which I am immensely grateful. Finally, I would like to express my unreserved thanks to Dr. Cheryl McGeachan for always being there for me.

Contents

Abstract

Electrochemical capacitors (ECs) are devices that have the potential to be very useful in the supply of electrical energy. The behaviour of nitrogen-enriched carbon materials in ECs has been investigated using materials produced through the co-carbonisation of resorcinol-formaldehyde xerogels with *m*-phenylene diamine (*m*PDA). Materials were found to display specific surface areas between 615 m^2g^{-1} and 27 m^2g^{-1} depending on the amount of catalyst used during xerogel synthesis and the fraction of *m*PDA added before carbonisation. Using materials that possessed a similar pore size distribution, up to 5.6 wt.% nitrogen was incorporated into the carbon structure. Nitrogen content was also controlled by treating the materials at 1000°C in the presence of hydrogen, which was shown to selectively remove nitrogen groups, especially pyridinic nitrogen. Physical characterisation was performed using thermal gravimetric analysis (TGA), nitrogen adsorption/desorption (at 77K), elemental analysis, X-ray photoelectron spectroscopy (XPS), small-angle neutron scattering (SANS) and contrast-matched SANS (CM-SANS). CM-SANS was proposed as a unique tool that can be used to investigate the degree of electrochemically inactive porosity in carbon electrode materials. Electrochemical testing was undertaken in symmetrical two-electrode cells using potassium hydroxide solution (28.5 wt.%) as the electrolyte. Electrochemical impedance spectroscopy (EIS), Galvanostatic charge/discharge at rates between roughly 0.1 Ag^{-1} and 12 Ag^{-1}, and cyclic Voltammetry between potentials of 0 V and 1 V (*vs* OCP) were carried out in order to characterise the materials. Surface nitrogen groups on carbon electrode materials were found to have a beneficial effect on the surface area normalised capacitance of materials; specifically a linear relationship between surface area normalised capacitance and pyridinic nitrogen content was shown for materials of comparable specific surface area (465 - 580 m^2g^{-1}) that contained between 1.0 wt.% and 2.2 wt.% nitrogen. It was proposed that electrode reactions are not responsible for this effect, but that it may arise from a greater amount of charge being displaced at pyridinic nitrogen sites.

1 Introduction

1.1 Energy Storage

With overwhelming evidence demonstrating that climate change is anthropogenic, there is an urgent need to reduce the effects that our growing global population has on our environment [**1**]. There has been a well documented rise in atmospheric carbon dioxide levels due to fossil fuel combustion which currently accounts for at least 80% of global energy output [**2**]. Also, the demand for energy has been forecasted to grow by 50% over the next twenty years with a concurrent increase in emissions [**3**] and, as a consequence, global energy costs are increasing. New markets are emerging that exploit alternative, renewable, and more efficient energy sources.

In many applications the demand for energy changes significantly with time and, as energy becomes more costly, energy storage becomes increasingly important to maximise the overall efficiency of supply systems. It has been argued that for the supply of energy with reduced carbon emissions a large scale renewable energy program is required [**4**]. Renewable energy is projected to provide for an ever increasing proportion of global energy demand [**3**] and due to the inherently intermittent nature of renewable energy sources, this in turn requires the development of alternative energy management techniques, one of which is improved energy storage technologies [**4**, **5**].

Renewable energy sources, such as wind, wave and solar energy, produce highly variable quantities of power and cannot be controlled to meet demand. The fluctuations in the power output of these conversion technologies require energy storage mechanisms that operate over varying time scales in order to maximise the overall efficiency of such systems. Over relatively short time scales (less than 1 s in duration), high power devices may be required in a frequency response capacity, whereas larger time scales (*e.g.* diurnal, seasonal) necessitate the storage of vast quantities of energy. As there is no single technology that has the capability to cater

for all energy storage needs, a variety of devices have been developed to suit certain situations.

There are many viable methods for energy storage that have received much attention of late including flywheels, compressed air energy storage (CAES) and superconducting magnetic energy storage (SMES), in addition to the established technique of pumped hydro storage.

1.2 Electric transport

On the smaller scale, a significant reduction in carbon dioxide emissions can be made by exploring alternatives to petrol and diesel powered vehicles. For example, in the UK road transportation currently accounts for approximately 25% of all carbon dioxide emissions [**6**]. There has been a recent growth in the production of electric and hybrid electric vehicles with a number of manufacturers releasing vehicles powered purely by energy stored in batteries. Several models of electric vehicle are commercially available, and the technology is currently the focus of government incentives in many countries.

The most promising alternative vehicles use either hydrogen or electrons as an energy carrier. These vehicles are frequently marketed as producing 'zero-emissions', however this does not take the emissions produced in the manufacture of the energy carrier into account. Nevertheless, it has been estimated that with the current energy mix in the UK the total CO_2 emissions associated with the life cycle of an electric vehicle would be 40% lower than that of an equivalent vehicle powered by an internal combustion engine [**7**].

Some drawbacks associated with electric vehicles include their limited range, slow charging time and the relatively high initial and repair costs. (A range of roughly 100 miles is available at the moment, with a full charge taking 8 hours in a domestic charging scenario.) Typically, vehicles using alternative energy carriers are compared to currently available technology (*i.e.* internal combustion engines) which

does not take into account that changes in behaviour may be required to accommodate new technologies. For example, the fuel tank of a conventional vehicle may provide a range of 400 miles, while the average daily round trip for a large proportion of vehicles is substantially less than 40 miles [**8**]. This would necessitate more frequent 'refuelling' than current vehicles, but shows that it may not be necessary for alternative vehicles to match the performance of current vehicles in every aspect. However, comparisons with currently available technology are useful as they provide well-defined challenges for the design of alternatively powered vehicles.

1.2.1 Hydrogen

Hydrogen is seen as an ideal energy carrier based on the large value of specific energy it possesses. It is usually envisaged that hydrogen would be supplied to a fuel cell where it would be converted to electrical energy (although direct combustion is also being explored [**9**]). In a similar manner, electrons can be delivered through the conversion of chemicals in electrochemical cells (*i.e.* batteries). In both of these scenarios, the electrical energy produced is converted to mechanical work in the same manner but there is a marked difference in the overall efficiency of the process.

Under the assumption that electrical energy is produced from a renewable source, no direct CO_2 emissions are associated with either process. An electric vehicle charged from the grid will be subject to losses due to transmission efficiency (*ca.* 10%) and the efficiency of a battery cycle (*ca.* 15%). Using the same electrical energy to produce hydrogen *via* electrolysis is estimated to be 45 – 75% efficient with similar values of efficiency being achieved for the conversion of hydrogen to electrical energy. Even using the most generous estimates of efficiency for the hydrogen cycle, and a conservative estimate of battery efficiency, the battery powered vehicle is at least 20% more energy efficient. This also ignores several additional factors required for the adoption of hydrogen vehicles, including the vast infrastructure necessary for dispensing hydrogen and the technology for storage.

Current prototype vehicles using fuel cells usually store hydrogen at high pressure (up to 700 bar), which has an efficiency of roughly 90% and depending on the method of production, (either centralised, with a transportation efficiency of 80%, or microgenerated, and subject to a transmission efficiency) further losses reduce the efficiency of the hydrogen cycle even further.

The above comparison of efficiencies between hydrogen and electric energy storage for vehicle propulsion is grossly oversimplified, but highlights the fact that current battery technology is more energy efficient than the equivalent hydrogen cycle, and the infrastructure required for recharging, (*i.e.* the grid) is essentially in place.

Another major challenge in the production of hydrogen powered vehicles is a safe and efficient method for hydrogen storage. As mentioned previously, the most common method of storage in fuel cell powered vehicles that has been used is compressed gas cylinders. The compression of the gas has an associated energy loss as well as a much lower energy density in comparison with hydrocarbon fuels. An alternative storage mechanism is where hydrogen is stored in the liquid state through cryogenic cooling. The current emphasis on hydrogen storage has been in solid state systems where hydrogen is adsorbed on high surface area materials or stored in the form of metal/chemical hydrides. There are still several challenges in the field of hydrogen storage, with a major hurdle being the development of a system capable of storing a sufficient amount of hydrogen at a reasonable temperature and pressures less than 100 bar while demonstrating that hydrogen can be quickly liberated.

1.3 Electrochemical Energy Storage

Established technologies in the field of electrical energy storage are electrochemical cells (batteries) and capacitors. In electrochemical cells, electrical energy is released as a result of chemical reactions between materials in the cell, whereas no reactions occur in capacitors and energy is stored purely through the physical separation of charges. As a result, capacitors can provide energy at rates far greater than that supplied by batteries, but only over very short time scales.

Types of energy storage technology can be characterised by the power and energy available to a load, which is usually illustrated by a plot of specific power against specific energy (or power density against energy density). Graphs of this form are generally referred to as a Ragone plot [**10**, **11**] and an example indicating the regions associated with different electrical energy storage devices is given in Figure 1.1 [**12**]. These plots are useful as they indicate the limits of different technologies and provide a simple method of matching the time scale of the application to the appropriate technology.

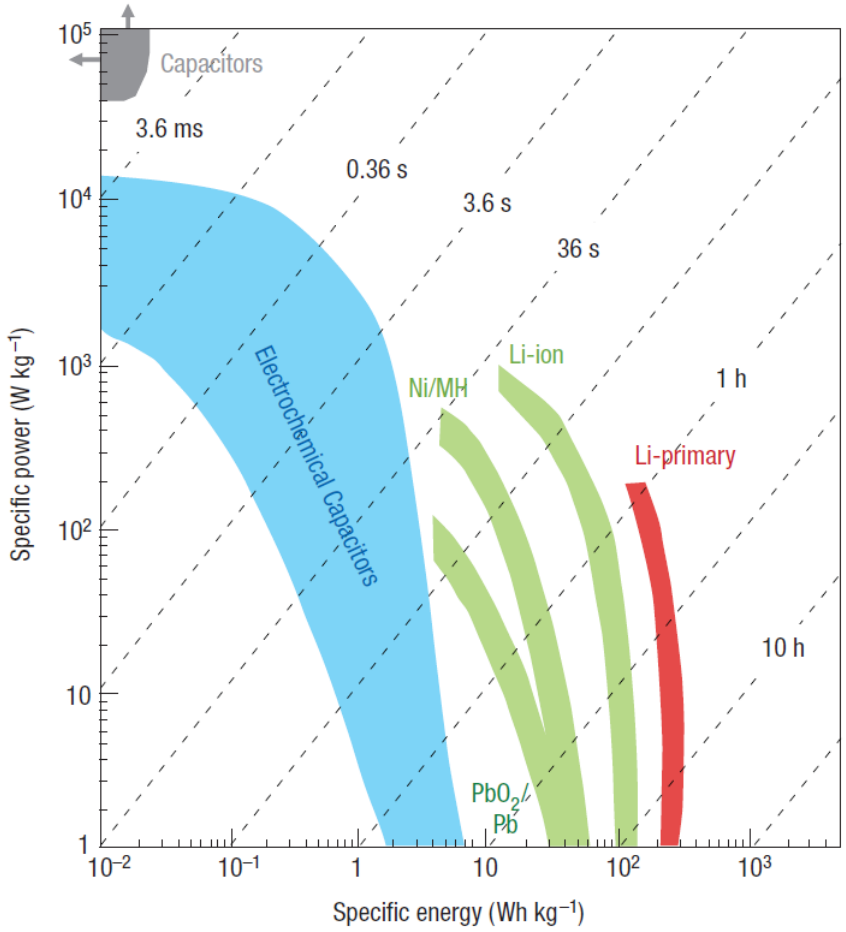

Figure 1.1: Specific power against specific energy (Ragone plot) for various electrical energy storage devices [12]

Electrochemical capacitors (ECs) are a relatively undeveloped energy storage technology that spans the gap in terms of energy and power density between batteries and capacitors. As indicated in Figure 1.1 these devices possess an energy density an order of magnitude greater than that of capacitors and a power density significantly

greater than current battery technology. For this reason, ECs are frequently referred to as ‘supercapacitors’ or ‘ultracapacitors’ as they store a huge amount of energy in contrast to traditional capacitor devices, and therefore have been the focus of an increasing volume of research and review articles [**10**, **12-32**]. For example, an AA cell sized capacitor stores less than 0.05 mA h of charge whereas an identically sized EC stores 50 mA h of charge. Batteries of this size can currently store up to 3000 mA h depending on the reaction chemistry employed [**33**].

ECs are not a replacement for batteries in the majority of applications but should be seen as a complementary technology that can be immensely useful in an energy supply system. From the Ragone plot (Figure 1.1) it can be seen that ECs match applications that require energy storage on the order of seconds and can fulfil demands that cannot be met by capacitors or batteries alone.

1.3.1 Small Scale Applications for ECs

ECs initially found commercial success in the provision of short term backup power in electronic circuits and perform similar functions in many modern devices. Small ECs can store enough energy to retain data when there are interruptions to the primary energy source (*e.g*. bridge power when changing battery). Under certain circumstances, where only a low energy density is required, ECs can replace batteries in gadgets such as toys, remote transmitters and local-area pagers [**34**].

In the case of automatic meter readers (‘smart meters’) ECs have been adopted as the power source as they were found to increase the useful life of the device by up to 300% when compared to the lead-acid batteries that were used previously [**35**]. By replacing the power source with six ECs, the smart meters are better equipped to handle the pulses of power requested by the wireless connection and can operate efficiently over a wide temperature range (-40 to 80 °C). ECs also allow for the design of smaller and lighter devices.

The fast charge/discharge time of ECs has been exploited in cordless tools such as screwdrivers and pipe cutters. Primarily aimed at the ‘home improvement’ market,

EC powered screwdrivers have a major advantage over battery powered devices as they can fully recharge after months of being inactive in approximately 90 s [**36**], whereas batteries frequently require many hours of charging before becoming useful. Pipe cutting tools using ECs allow for the efficient use of standard alkaline batteries, by charging at a low rate (which extends battery life) and delivering charge in the pulse of power required for the task, which could not be provided by batteries alone [**37**].

Wireless connectivity is now ubiquitous and demands increasing amounts of power. Modem cards, mobile phones and GPS devices all operate using pulses of power which frequently results in a battery that is many times larger than strictly necessary to provide average power [**38**]. Sensor nodes that require no external power source and need very little maintenance have been produced using ECs to store the low, steady rate of energy harvested from radio waves [**39**] or vibrations [**40**] and to release energy in the high power pulses required for wireless communication.

Hybrid power supply systems incorporating ECs can also be used to reduce the total mass and volume of devices as well as increasing the efficiency and operating life of the system. For example, in digital cameras the addition of an EC to provide additional power during energy intensive operations (*e.g.* flash, auto-focus *etc.*) increases the operating life by up to 200% [**41**]. The robust design of ECs also allows them to operate reliably under extreme conditions and they have been employed in portable electronics to eliminate the effects of battery 'chatter' when the unit is dropped.

Current mobile phones, especially 'smart phones', include many features that have been previously mentioned (GPS, wireless, video camera, audio, *etc.*) and represent a technology that demonstrates the immense value of ECs in power supply systems.

1.3.2 Transport applications for ECs

The majority of the applications where ECs have been of benefit mentioned above are on the small scale. Larger devices suitable for use in transport systems have been developed with the aim of exploiting some of the benefits of EC technology.

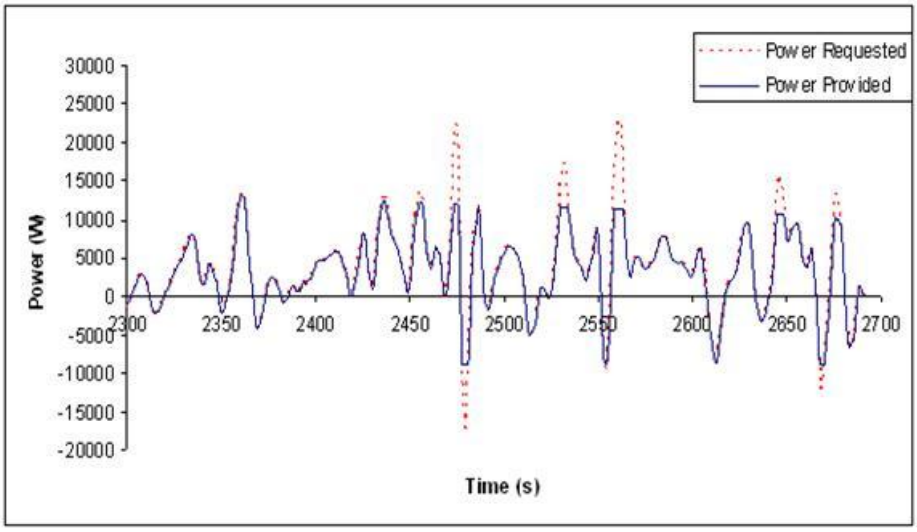

Figure 1.2: Typical urban drive cycle data [42, 43]

Figure 1.2 represents a typical urban journey in an electric vehicle where frequent changes in speed are necessary. For positive values of power, the solid blue line represents the power supplied by the battery pack, and the dotted red line represents the power requested by the driver. Negative values of power correspond to charging of the battery pack through regenerative braking. The average power output has a value of roughly 5 kW, and the power output from the battery was limited to a value of 12 kW to prolong the lifetime of the battery pack. It is clear that the power requested is intermittent and varies greatly, with values of power well in excess of the battery limit being requested frequently. Peak power is requested when moving from a standstill, overtaking or hill climbing, and these situations occur repeatedly when driving in a city setting.

Batteries (and fuel cells) are most efficient when supplying a consistent load, therefore systems designed to cope with peak power demands are larger than necessary and suffer from a reduced efficiency and life cycle. Incorporating a

different energy storage technology to cater for high power pulses, such as ECs, has the potential to increase the overall energy efficiency and to produce smaller, lighter systems. In addition, ECs can help to maximise the amount of energy recuperated through the regenerative braking process. By operating the electric motor as a generator during braking, the momentum of the vehicle is converted back into electrical energy which can be used to charge the battery. However, the power produced is generally too large for all of the energy to be used in charging the battery, as indicated by the discrepancy between the dotted red line and the solid blue line in Figure 1.2. From Figure 1.1, processes suited to ECs operate in the region of 1 - 10 s which corresponds to the time scale of regenerative braking systems, and therefore ECs can be employed to absorb the power developed during braking and subsequently charge the batteries at a lower rate.

To date, the application of ECs in passenger vehicles has been mainly at the prototype stage [**44**, **45**], but their use is likely to become more prevalent as electric vehicle technology matures, especially if improvements in the energy and power densities of EC devices are made.

Diesel buses incorporating ECs to recover braking energy have been successfully trialled [**46**, **47**], and light rail vehicles using ECs, developed to reduce the need for caternary lines, have been found to provide energy savings of 30% [**48**].

As a primary source of energy in large vehicles ECs only store enough energy to travel a few miles on a single charge. However ECs can be used without batteries in certain applications that follow a consistent route with regular stops. For example, buses supplied with energy solely from ECs have become a viable alternative to conventionally powered vehicles [**49**, **50**]. Along bus routes, the quick charging time of ECs is exploited, as bus stops can also act as charging stations that provide enough charge in 30 s for the bus to travel a few miles to the next stop/charging station. In addition ECs are not affected by the heat management problems associated with battery systems and by employing regenerative braking, these vehicles have been estimated to be 40% more energy efficient than a similar bus using overhead lines [**49**].

1.4 Outline

For the aforementioned reasons, it is attractive to incorporate ECs into the energy supply system of vehicles; however, the cost to performance ratio of currently available technology hinders their widespread adoption. Broadly, this work aims to investigate a method by which the performance of EC electrode materials is increased, while being mindful of the cost, as any gains should be of practical benefit. In the course of this work it became evident that complicated relationships exist between the physical characteristics of the electrode materials and their performance in ECs, and that investigating some of these factors could be constructive for the understanding and development of EC technology.

Chapter 2 provides background information relevant to ECs including different modes of operation, materials involved, and some issues that influence their performance. At the end of chapter 2, the use of nitrogen-enriched carbon materials in EC electrodes is discussed in depth and the main aim of this study is identified. Details of the different physical, chemical and electrochemical methods used in the characterisation of the materials produced and studied in this work are given in chapter 3. Experimental details are given in chapter 4 and the results are given and discussed in chapter 5. Chapter 6 summarises the findings of this work and proposes some opportunities for further study. Appendices and references are given thereafter.

2 Background

2.1 Capacitance

The storage of electrical energy can be achieved through direct or indirect means. Indirect energy storage is used in electrochemical cells, where electrical energy is stored as the potential for reactions between chemicals to occur. Capacitors are direct electrical energy storage devices that store energy purely through the physical separation of electrostatic charges.

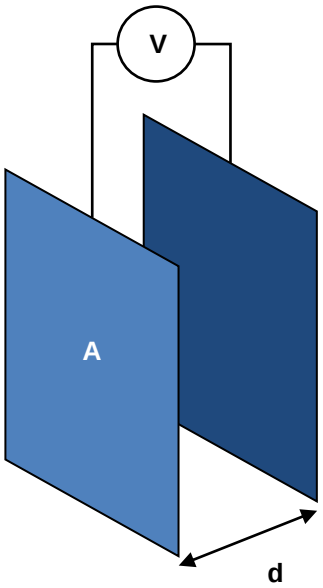

Figure 2.1: Parallel plate capacitor schematic. Two conductive plates of area *A* are separated by a distance *d* and have an applied potential of *V* between them. Each plate has equal but opposite charge, ±*Q*.

The simplest capacitor arrangement is found in a parallel-plate capacitor, illustrated in Figure 2.1, where two electrically conductive materials are separated by an insulator. When a potential difference is applied between the plates, electrons accumulate on one plate and are removed from the other. The deficiency of electrons on one plate when coupled with the excess of electrons on the opposing plate results in an electric field whose strength varies inversely with the separation distance. When the potential is removed, the plates remain charged and the stored energy can be discharged through an external load. As no chemical or phase changes occur during charge/discharge, capacitors have an almost infinite cyclability [**10**].

However, if the strength of the electric field increases beyond the dielectric strength of the insulator, the material degrades rapidly and a short circuit occurs. The potential at which this is observed limits the energy density of the capacitor and is known as the breakdown voltage.

Capacitance is the ability of a body to hold electrical charge and is a measure of the amount of charge stored at a given potential. This is described by Eq. 2.1 where *C* represents capacitance (measured in Farads), *Q* represents charge (Coulombs) and *V* represents the potential (Volts) at which the charge is stored.

$$C = \frac{Q}{V} \qquad \textbf{Eq. 2.1}$$

The capacitance of a parallel plate capacitor, as illustrated in Figure 2.1, where two plates of surface area *A* (m^2), separated by a distance *d* (m) is given by Eq. 2.2, where ε_0 is the permittivity of free space (8.854×10^{-12} F m^{-1}) and ε_r is the relative dielectric constant of the interface.

$$C = \varepsilon_0 \varepsilon_r \frac{A}{d} \qquad \textbf{Eq. 2.2}$$

2.1.1 Energy

The energy stored, *E*, in an ideal capacitor can be calculated by considering the work done during charging, *i.e.* moving an element of charge from one plate to the other against the electric field [**10**]. This is represented by Eq. 2.3.

$$E = \int_{q=0}^{Q} V dq = \int_{q=0}^{Q} \frac{q}{C} dq = \frac{1}{2}\frac{Q^2}{C} = \frac{1}{2} C V^2 \qquad \textbf{Eq. 2.3}$$

The amount of energy stored per unit mass of the device is referred to as the *specific energy* or *gravimetric energy density* and the amount of energy stored per unit volume is known as the *energy density* or *volumetric energy density*.

2.1.2 Power

The maximum power that can be delivered, P_{max}, is inversely proportional to the resistance of the device, R, as illustrated by Eq. 2.4. The derivation of Eq. 2.4 is given in Appendix A [**10**].

$$P_{max} = \frac{1}{4}\frac{(\Delta V)^2}{R} \qquad \textbf{Eq. 2.4}$$

2.2 Capacitors

The history of capacitors dates back to 1745 with the discovery of the 'Leyden jar', illustrated in Figure 2.2. The original device consisted of a foil coated glass phial containing an acidic solution in which a metal electrode was immersed. Initially the electrolyte solution was thought to be essential, however a further modification where foil was coated on both sides of the jar showed that energy could be stored by the separation of two metallic electrodes by an insulating material. This is analogous to the parallel plate capacitor illustrated in Figure 2.1, where glass is the dielectric material between the two plates.

Figure 2.2: A Leyden Jar

Capacitors can be classified based on the medium between the conductive plates as vacuum, dielectric or electrolytic capacitors. Each of these systems is associated with different values of ε_r and d in Eq. 2.2. A vacuum by definition has a relative dielectric constant of 1, and is used in low capacitance, high voltage devices.

Materials used in dielectric capacitors, (*e.g.* mica, mylar, PTFE), have ε_r values in the range 1 - 10. Ceramic materials are widely used in the production of small capacitors and can have a dielectric constant as high as 15,000. Dielectric and ceramic capacitors usually have an energy density less than 0.01Wh l^{-1}.

Electrolytic capacitors use thin films of metal oxides, usually aluminium or tantalum oxide, connected to another plate by an electrolyte. The main advantage of electrolytic over dielectric capacitors is that oxide films can be reliably manufactured in very thin layers resulting in a substantially smaller effective plate separation (*d* in Figure 2.1 and Eq. 2.1). Electrolytic capacitors are normally used in applications requiring a capacitance greater than 1 μF, however these devices are polarised and are unreliable when dealing with a fluctuating signal. The energy density of electrolytic capacitors is roughly 0.2 Wh l^{-1}.

2.3 Batteries

Electrochemical cells (batteries) differ from capacitors as they store electrical energy indirectly as a reaction potential and require a change in the oxidation state of cell materials during charge/discharge. In contrast with capacitors, battery technology has developed rapidly in the past 200 years with many different reactions being exploited to produce a variety of cells that in turn have enabled massive advances in technology.

Rechargeable (or secondary) batteries store a considerably larger amount of energy between charges than capacitors; approximate energy densities of some different cell technologies are given in Table 2.1.

Rechargeable Battery Technology	Energy Density [Wh l^{-1}]
Lead-Acid	75
Nickel-Cadmium	150
Alkaline	250
Nickel-Metal Hydride	300
Lithium-ion	350

Table 2.1: Energy densities of rechargeable battery systems [33]

Repeated chemical and phase changes in the cell normally limit operating life to less than one thousand cycles. The cycle life of batteries has been found to vary with the conditions under which the cell is charged and discharged, and battery operating life is drastically reduced by operation at relatively high rates or repeated deep discharges [**33**].

The discharge profiles of capacitors and batteries also differ markedly, and are illustrated in Figure 2.3. Under Galvanostatic discharge (where a constant current is drawn from the cell) the potential between the electrodes in a capacitor decays linearly with time, whereas in a battery the potential remains roughly constant before decaying sharply. (In Figure 2.3 the time scale of discharge between the capacitor and battery are not comparable; for a full discharge at the same rate a battery will have a discharge time at least three orders of magnitude greater than a capacitor of similar mass.)

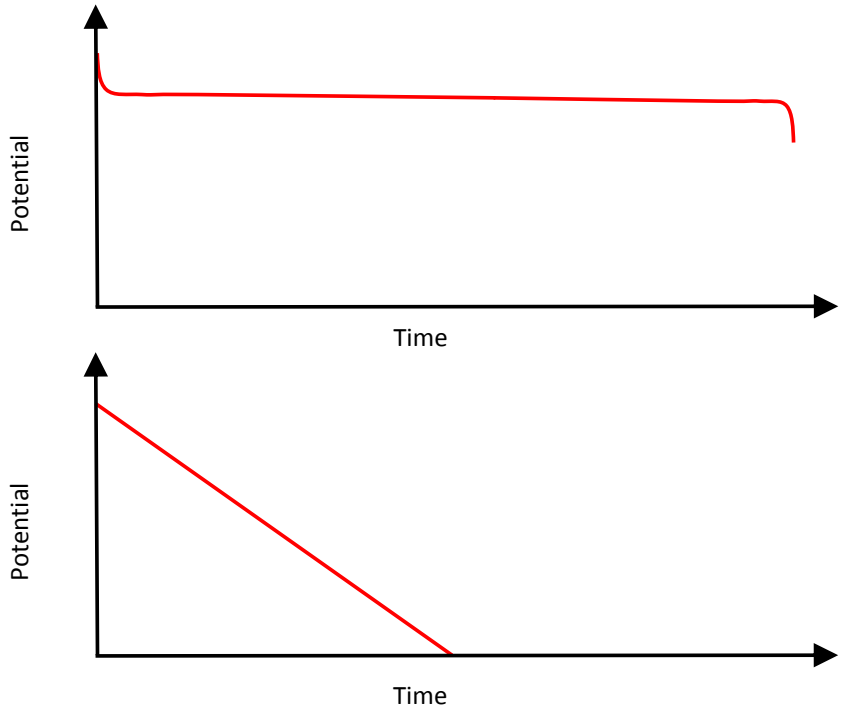

Figure 2.3: Discharge behaviour for batteries (top) and capacitors (bottom)

2.4 Electrochemical Capacitors

Electrochemical capacitors (ECs) are devices that can store electrical charge but differ from batteries as they can absorb and release charge much more quickly. ECs differ from conventional capacitors as they can store a much greater amount of energy per unit volume. The first commercial EC can be traced back to a patent by Becker in 1957 [**51**] which displayed a significantly higher energy density than electrolytic capacitors and consisted of porous carbon electrodes immersed in an aqueous electrolyte. A diagram of the original EC design is given in Figure 2.4 [**51**].

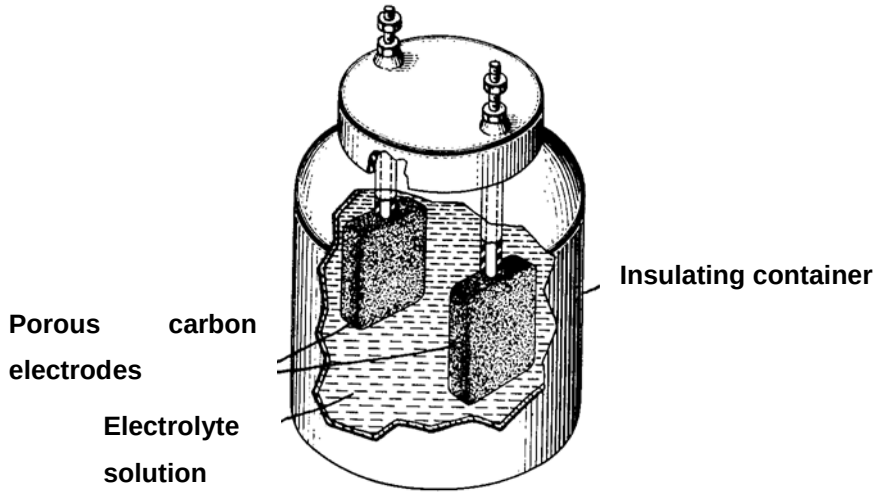

Figure 2.4: Diagram from the original EC patent [51]

The patent acknowledged the uncertainty over the charge storage mechanism involved but did indicate that the capacitance increased with the surface area of the electrodes. From Eq. 2.2 it can be seen that the amount of energy stored in a capacitor can be increased by expanding the surface area of the electrodes or by reducing the distance between the electrodes. By employing porous carbon as an electrode material the apparent surface area of the electrode is increased by many orders of magnitude and the double-layer mechanism reduces the effective separation between the charges to the size of ions in the electrolyte. Double-layer capacitance arises at the interface between electrodes and an electrolyte solution and can be thought of as the specific adsorption of ions at a polarised surface. This is illustrated in Figure 2.5 where capacitance arises through the double layer mechanism between a negatively charged electrode and electrolyte cations.

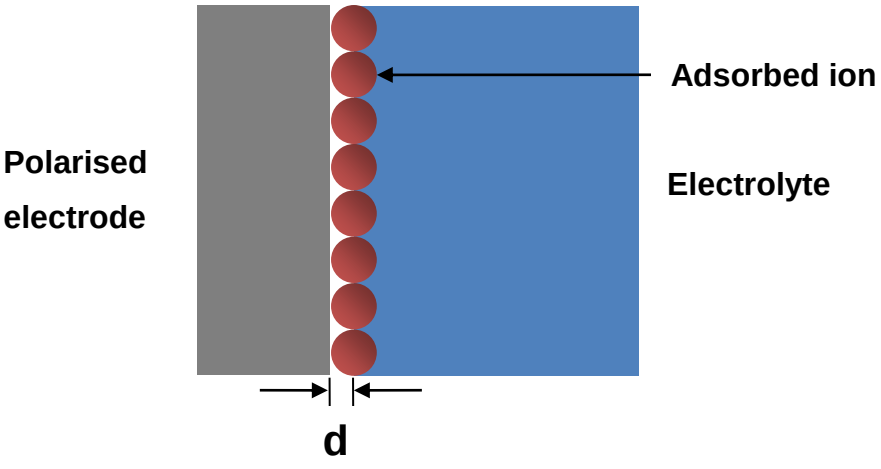

Figure 2.5: Double-layer capacitance at a charged electrode surface

2.4.1 Electrochemical Double-Layer Capacitors (EDLCs) [10]

2.4.1.1 Helmholtz model of the double-layer

The first mathematical model to describe the structure of an electrochemical double-layer was the parallel plate model, adapted from the von Helmholtz model of charge distribution on colloidal surfaces. The 'double-layer' consists of two surfaces of opposite charge that face each other and are separated by a small distance, analogous to the parallel plate capacitor discussed earlier. This is illustrated in Figure 2.6, where it can be seen that the excess of charge on the electrode is balanced with a compact layer of ions that are considered to be adsorbed on the electrode surface. In Eq. 2.2 the value of *d*, the distance between the plates, is reduced to roughly one ionic radius (a separation typically on the order of Ångstroms) which is significantly smaller than any separation that can be reliably manufactured using conventional capacitor technology.

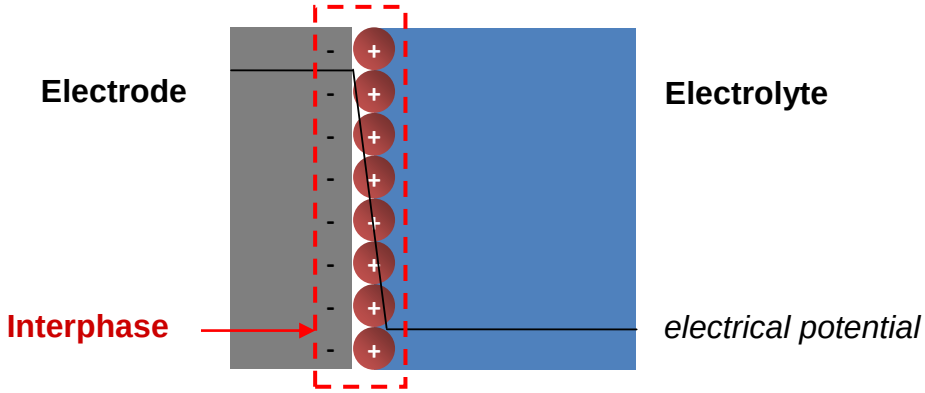

Figure 2.6: Helmholtz model of the double-layer

When discussing electrode processes the electrode-electrolyte interface is more accurately described as an 'interphase', as the properties of both the electrolyte and electrode in this region differ from the respective bulk properties. Double-layer models normally assume that this region is ideally polarisable; specifically, that a potential difference between the electrode surface and electrolyte can be created, without charge transfer occurring between electrode and electrolyte.

2.4.1.2 Gouy-Chapman model

An alternative model, known as the Gouy-Chapman model, considers ions as point charges and the double-layer to be diffuse, as indicated in Figure 2.7. In this model the variation in electrode surface charge density is balanced by the concentration of electronic charge in the adjacent electrolyte, *i.e.* the net charge over the interphase is zero. This model acknowledges the thermal fluctuations that occur in the double-layer and introduced the idea that the double-layer is not a rigid arrangement of ions but a region in electrostatic equilibrium. However, by treating the ions only as point charges, this model vastly overestimates the capacitance associated with the double layer.

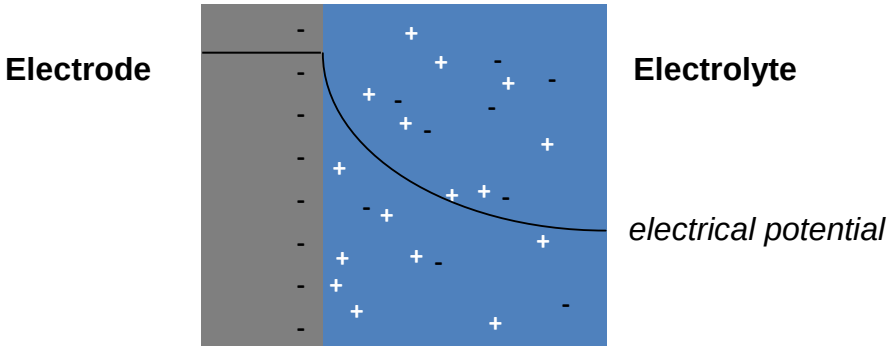

Figure 2.7: Gouy-Chapman model

2.4.1.3 Stern model

The Stern model combines both of the previously described double-layer models and considers the layer in contact with the electrode surface to consist of specifically adsorbed ions, while the concentration of the diffuse layer approaches the bulk concentration. In this model, shown in Figure 2.8, the electrode charge density is partially opposed by a compact layer of ions of finite size and the remainder is balanced with the net charge in the diffuse layer.

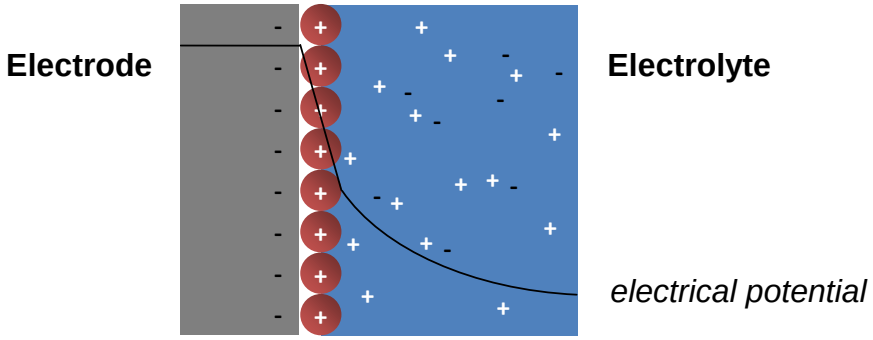

Figure 2.8: Stern model

From this model, the capacitance of the double layer, C_{dl}, is seen as the series addition of the capacitive contribution of the Helmholtz layer, C_H, and that of the diffuse layer C_{diff}. This relationship is shown in Eq. 2.5.

$$\frac{1}{C_{dl}} = \frac{1}{C_H} + \frac{1}{C_{diff}} \qquad \textbf{Eq. 2.5}$$

An accurate determination of the thickness of the Helmholtz layer is required to apply the Stern model. This is loosely defined as the distance of closest approach for electrolyte ions and is not only dependent on the ion size, but also on their degree of solvation.

2.4.1.4 Grahame model of the Helmholtz layer

A more rigorous definition of Helmoltz layer thickness was proposed based on investigations into the behaviour of aqueous solutions at a mercury interface [**52**]. In this model the Helmholtz layer is divided into 'Inner' and 'Outer' Helmholtz planes to account for differences between anions and cations and how they interact with positively and negatively charged electrodes. This is illustrated in Figure 2.9.

Generally the distance of closest approach for anions is smaller than that of cations. Even though cations typically have a smaller ionic radius, they are usually strongly solvated and the distance of closest approach must include a contribution from the solvation sphere surrounding the ion. Anions on the other hand are frequently

adsorbed in the unsolvated state, and the distance of closest approach is equal to the ionic radius. The smaller of these distances is termed the Inner Helmholtz Plane (IHP), and the larger termed the Outer Helmholtz Plane (OHP).

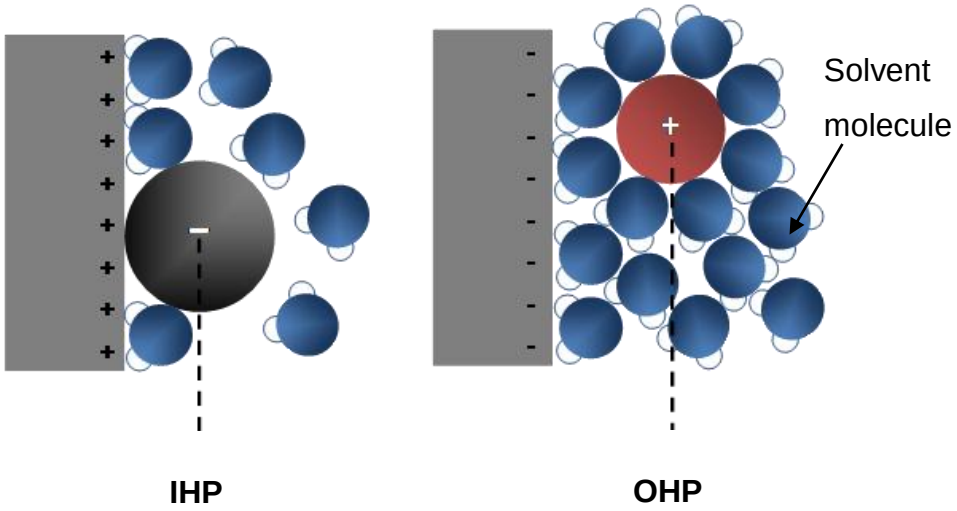

Figure 2.9: Grahame model for ion adsorption in the Helmholtz layer

This model accounts for the fact that differences in the behaviour of ions at a polarized electrode can result in the capacitance determined at a positively charged electrode being twice that obtained on a negatively charged electrode [**52**] and has been found to be accurate for a large amount of electrode-electrolyte systems.

Further models have continually refined the double-layer theory to take into account the orientation of adsorbed dipoles and variations in electron density with potential, but still remain two-dimensional treatments. In practical devices using porous electrodes, these planar models are insufficient but nevertheless indicate that the effective separation between the plates in Figure 2.1 and Eq. 2.2 is reduced to a very small value when the electrochemical double-layer mechanism is responsible for charge storage.

2.4.2 Pseudocapacitance [10]

While the EDLC mechanism stores charge in a manner similar to dielectric capacitors, an alternative charge storage mechanism more akin to that seen in

batteries can result in capacitor-like behaviour. This mechanism is termed 'pseudocapacitance' to differentiate it from the classical electrostatic capacitance mechanism and involves the passage of charge across the double-layer usually altering the oxidation state of the electrode material.

Pseudocapacitance occurs when there is a change in the extent of charge acceptance with changes in potential, and a derivative (d*q*/d*V*) arises that is equivalent to a useful capacitance (*cf.* Eq. 2.1). Pseudocapacitance can occur when certain interactions become thermodynamically favourable over distinct regions of potential.

The pseudocapacitive behaviour of metal oxides was discovered in 1971 [**53**] when the cyclic Voltammetry and Galvanostatic charge/discharge behaviour of a ruthenium dioxide (RuO_2) electrode was found to be similar to that of an 'electric condenser'. In the case of RuO_2, pseudocapacitance occurs due to redox reactions between electrolytic protons and the hydrated oxide lattice as indicated by Eq. 2.6 [**10**].

$$RuO_x(H_2O) \leftrightharpoons RuO_{(x+\delta)}H_2O_{(y-\delta)} + 2\delta H^+ + 2\delta e^- \qquad \textbf{Eq. 2.6}$$

Electroconductive polymers (ECPs) also have the ability to store charge through a pseudocapacitive mechanism as they possess π-orbital conjugation [**14**]. This enables the materials to conduct electrons and to participate in redox reactions with electrolyte species. Also, the intercalation of mobile ions such as protons, Li^+ and K^+ into transition metal oxide electrodes (*e.g.* vanadium pentoxide [**54**], manganese dioxide [**27**] *etc.*) can generate a pseudocapacitive response.

2.4.2.1 Asymmetric ECs

Pseudocapacitor materials are usually only suitable for operation as one electrode in a cell, requiring the use of a different counter electrode material. In ECs that operate solely through the EDLC mechanism, each electrode can be thought of as an ideal capacitor connected in series where the capacitance of the cell, C_T is related to the capacitance of each electrode, C_+/C_-, through the relationship seen in Eq. 2.7.

$$\frac{1}{C_T} = \frac{1}{C_+} + \frac{1}{C_-} \qquad \textbf{Eq. 2.7}$$

For electrodes of the same mass and same specific capacitance, the cell capacitance is equal to roughly half the capacitance associated with one electrode. However when using a pseudocapacitive material, the EC is of asymmetric design and the capacitance associated with one electrode can be much larger than the other in a similar mass or volume. From Eq. 2.7 it can be seen that if the capacitance of one electrode is increased by a factor of three, the capacitance of the cell is increased by 50%. Therefore if the capacitance of one electrode is increased sufficiently, the total cell capacitance can approach twice the value of that attained in a symmetrical cell that employs only the lower capacitance material [**55**].

2.5 Charge storage

Electrical energy storage technologies can be considered as being part of a continuum on the basis of the degree of charge transfer that occurs during charge and discharge [**31**]. At one end of the scale are dielectric capacitors where energy is stored directly in the electric field generated by the separation of charges. In an EDLC, charge transfer is achieved by the delocalisation of electrons at the surface of the electrode. Under the assumption that 30 μF cm^{-2} is realisable at a carbon electrode [**56**], an equivalent charge transfer coefficient for the EDLC mechanism is roughly 0.18 e^- per surface carbon atom [**10**]. In a pseudocapacitor, charge is transferred across the double layer and is described as Faradaic charge transfer. In this case as much as 3 e^- per surface atom can be transferred. Batteries exhibit a huge quantity of Faradaic charge transfer in comparison with pseudocapacitors, as the charge transferred can propagate into the bulk of the electrode material and is not restricted by the available surface area. In the case of some battery chemistries as much as 3 e^- per atom/molecule of bulk phase can be transferred.

Based on these charge storage mechanisms, and their charge/discharge characteristics (summarised in Figure 2.3), EDLCs and pseudocapacitors can be seen

as transitional states between conventional capacitor technology and intercalation batteries [**57**]. This emphasises the fact that ECs should not be seen as a replacement for batteries but are a complementary technology that can assist in the design of new energy storage systems.

2.6 EC Electrolytes

The type of electrolyte employed in an EC cell has a marked effect on the amount of energy stored, and how quickly this energy can be released. The potentials at which the electrolyte decomposes determine the operating voltage of an EC, which in turn defines the amount of energy stored as this varies with the square of the operating voltage (Eq. 2.3).

The conductivity of the electrolyte solution contributes significantly to the resistance associated with an EC and is affected by many related physical properties such as solubility, viscosity and the relative mobility of ions to name but a few [**10**]. The resistance in turn determines the power output capabilities of the EC system (Eq. 2.4).

2.6.1 Aqueous-based electrolytes

For ECs using aqueous solutions as electrolytes, the maximum operating voltage is theoretically limited by the electrolysis of water to 1.229 V (at 25°C), but are usually operated over a narrower range of 1 V. In some ECs, the potentials at which hydrogen and oxygen evolution occur can shift depending on the electrode materials employed, and a wider operating window can be used. Aqueous electrolytes tend to produce faster rates of charge/discharge than other electrolyte solutions due to the relatively high conductivity and low viscosity of concentrated aqueous solutions.

In EDLCs that use carbon electrodes the most commonly encountered aqueous electrolytes are sulphuric acid and potassium hydroxide solutions [**10**]. The variation

in electrical conductivity of some aqueous solutions with solute concentration is shown in Figure 2.10. In the case of sulphuric acid, a maximum conductivity of roughly 750 mS cm^{-1} is observed at a concentration of 33 wt.%, which is the grade used in lead-acid batteries [**33**]. However, in ECs it is more common to see 1 M solutions of H_2SO_4 used as an electrolyte due to chemical incompatibility with test cell components. The use of acid electrolytes usually necessitates some cell components to be manufactured from gold or platinum to overcome corrosion problems, although a conductive rubber has been used in a commercially available EDLC that makes use of sulphuric acid solution [**58**].

Potassium hydroxide solutions are less corrosive than strongly acidic solutions and show a similar relationship between concentration and conductivity to that seen for H_2SO_4. The conductivity of a 6 M KOH (~ 30 wt.%) solution approaches 600 mS cm^{-1} at room temperature. Similar concentrations of KOH are widely used in the battery industry [**33**], and the use of KOH rather than concentrated acid allows for a wider range of materials to be used in cell construction.

Milder aqueous solutions have been explored for use in ECs including potassium chloride [**59-64**], ammonium sulphate [**65-68**] and alkali sulphates [**69-73**], however these are mainly used in systems where the double-layer mechanism is secondary to the charge stored through pseudocapacitance. Significantly greater values of conductivity are seen in aqueous solutions when compared with organic solutions as greater ion concentrations are achievable when using water as a solvent, and proton conduction can take place through the Grotthuss mechanism in aqueous solutions.

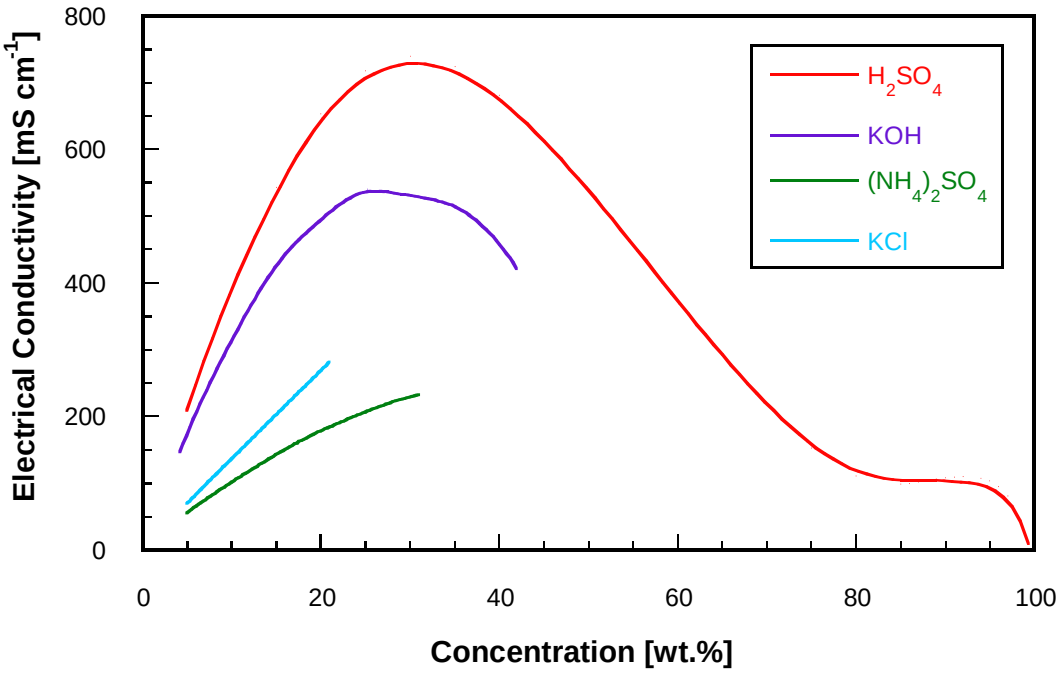

Figure 2.10: Electrical Conductivity against concentration for aqueous solutions used in ECs (at 15°C) [74]

The main advantage to using aqueous solutions as EC electrolytes is the relatively high conductivity but further advantages include their low cost and relative ease of manufacture. Relatively concentrated electrolytes are required to minimise the ESR and maximise power output, however, strong acids and bases determine materials selection for cell manufacture which can be costly, as well as posing a hazard in the event of cell rupture. The use of concentrated electrolytes also increases the rate of self-discharge displayed by the capacitor [**10**].

2.6.2 Organic-based electrolytes

The majority of ECs commercially available at present use organic based electrolytes which are electrochemically stable over a wider operating range than aqueous solutions. As a result the amount of energy stored in an EC using organic based electrolytes can be an order of magnitude greater than that of a device using an aqueous solution. The most widely used electrolyte consists of a solution of tetraethylammonium tetrafluoroborate ($(C_2H_5)_4N\ BF_4$ or "TEA BF_4") in propylene

carbonate which can theoretically operate over a range of 4 V, however the useful operating potential is usually limited to *ca.* 2.7 V. (Although the total electrochemical window of propylene carbonate is 4V, only the cathodic or anodic window can be utilised when a practical device is polarised as the electrolyte will decompose at greater potentials.)

As the amount of energy that can be stored is vastly increased through the use of organic based electrolytes, a great deal of research into various organic solvent/solute systems has been conducted. Unfortunately the conductivity of organic based electrolytes is significantly reduced in comparison with the values that can be achieved using aqueous solutions. For example, a 1.0 M solution of $(C_2H_5)_4N\,BF_4$ in propylene carbonate has an electrical conductivity in the region of 13 mS cm^{-1} [**10**].

This reduced electrolyte conductivity results in a significantly higher resistance in comparison with cells using a concentrated aqueous solution; the increase in resistance can be by as much as a factor of 100. This has a detrimental effect on the power capability of ECs that use organic based electrolytes, which is governed by Eq. 2.4. (However, the increased operating voltage compensates in part for the reduction in power density [**17**]).

The most commonly employed organic solvent is propylene carbonate although acetonitrile was often preferred for use in EDLCs. Acetonitrile results in cell resistances that are roughly a factor of three lower than those produced using propylene carbonate [**10**], however a relatively high toxicity and flammability has led to concern over the use of acetonitrile as a cell component, and carbonates have been employed as a safer alternative.

It has been calculated that ECs using an aqueous solution with an operating voltage of 1 V can theoretically achieve a power density almost an order of magnitude greater than a cell employing an organic based electrolyte that operates at 2.3 V. This is illustrated by the curves in Figure 2.11 that show how the energy density and power density vary with the electrode thickness for an EC using an aqueous electrolyte (800 mS cm^{-1}) and for a cell employing an organic based electrolyte (16 mS cm^{-1}).

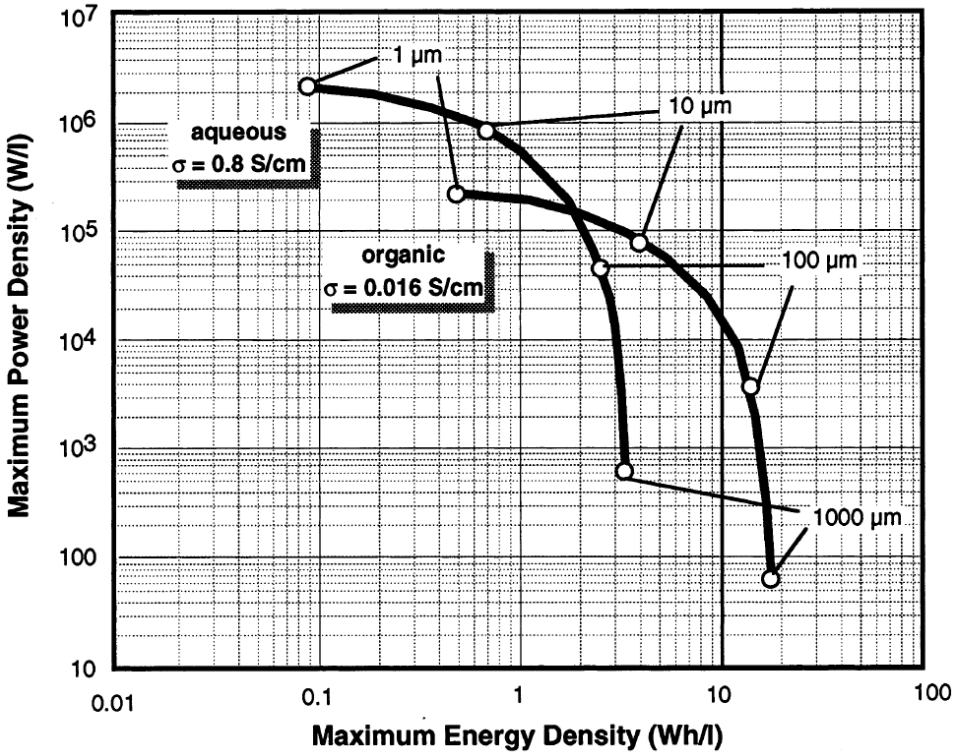

Figure 2.11: Maximum achievable power and energy densities for ideal aqueous electrolyte and organic based EDLCs [17]. (Electrode thickness is indicated on the curves, other parameters are assumed to be constant)

Organic based electrolytes are relatively expensive in comparison with aqueous solutions and require both the salt and solvent to be free from moisture and oxygen. This is necessary as operation over the wider potential range leads to the decomposition of any water contained in the solution, and causes gases to be evolved in the cell. As well as increasing the rate of self-discharge and resistance of the cell, the generation of gases can also cause the electrodes to disintegrate and can lead to hazardous operating conditions. A major disadvantage of cells using organic based electrolytes is that they introduce the possibility of the release of flammable compounds in the event of cell rupture.

The use of organic based electrolytes also requires more complicated (and more costly) processing methods, but there are fewer restrictions with regard to materials selection for cell components.

2.6.3 Ionic liquid electrolytes

Ionic liquids (ILs) are salts with relatively low melting points and for this reason they are sometimes referred to as 'molten salts' or 'room temperature ILs'. ILs usually consist of highly asymmetric combinations of anion and cation and some typical examples of cations are given in Figure 2.12, where R_1 to R_6 represent locations of alkyl groups or hydrogen atoms. Other examples include ammonium and phosphonium based ions [**75**-**81**].

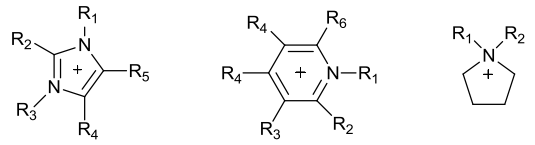

Figure 2.12: Structures of cations found in ILs. (a) imidazolium, (b) pyridinium and (c) pyrrolidinium

Typical examples of anions include simple halides (*e.g.* Cl^-, I^-, Br^-), larger more complex ions (*e.g.* $BF_4^-$and PF_6^-) and even larger ions, such as those shown in Figure 2.13.

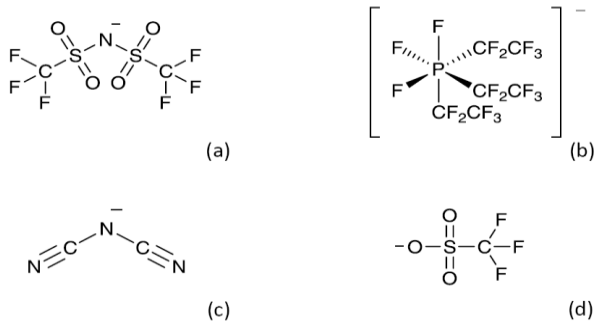

Figure 2.13: Structures of anions found in ILs. (a) bis(trifluoromethylsulfonyl) imide, (b) tris(pentafluoroethyl) trifluorophosphate (c) dicyanamide and (d) trifluoromethylmethane sulfonate.

Currently one of the most popular ILs for use as an electrolyte is 1-ethyl-3-methylimidazolium bis(trifluoromethylsulfonyl)imide and many new ILs are being developed and synthesised. The main advantage of IL electrolytes is their stability over a wide range of potential. Anodic voltages of up to 4.2 V have been reported [**82**, **83**], which equates to a significant increase in the quantity of energy that can be

stored in comparison with organic based electrolytes. Other advantages of ILs include low volatility and some ILs are non-flammable which addresses some of the safety issues associated with organic based electrolytes.

There are however, some disadvantages as ILs have relatively high viscosities [**84-89**] and the conductivity is of a similar magnitude to that seen in organic based electrolytes [**81**, **89-96**]. Also, low temperature operation may be problematic as many ILs have melting temperatures just above 273K [**86**]. As with organic based electrolytes, ILs are relatively expensive and require purification to ensure that no water is present in the system.

A promising area of interest in the application of ILs as EC electrolytes is in the use of protic ionic liquids (PILs) which usually consist of a Brønsted acid-base mixture, such as α-picoline with trifluoroacetic acid. It has been reported that the conductivity of these proton transfer salts can be an order of magnitude higher than that for the ILs described previously [**97**]. It was then identified that these salts could be applied to pseudocapacitive systems [**98**], coupling the benefits of a wider potential range with the high specific capacitance available using RuO_2. The use of carbon electrodes containing surface functionalities, as a lower cost alternative to RuO_2, with PIL electrolytes has also been investigated [**99**]. Although the operating potentials associated with PILs are not as wide as other ILs, the development of these electrolytes has allowed the operating voltage of pseudocapacitor devices to be doubled.

Different electrolytes are suited to different charge storage mechanisms and electrode materials, which emphasises the fact that compromises between the cost and performance of ECs have to be made during design. Therefore, no single system is appropriate for all applications.

2.7 Electrode Materials

2.7.1 Metal Oxides

Pseudocapacitance is observed when fast, potential-dependent reactions result in Faradaic charge transfer between the electrode and electrolyte. These reactions become favourable over discrete ranges of potential and result in capacitor-like charge/discharge characteristics. Faradaic charge transfer reactions are mainly of the redox type where changes in the oxidation state of the materials occur (which is similar to battery systems [**57**]). However, these reactions do not propagate into the bulk material and occur only at the electrode/electrolyte interface.

Many metal oxides exhibit pseudocapacitive behaviour over small ranges of potential, with Ruthenium Dioxide (RuO_2) exhibiting the highest reported specific capacitance (*ca.* 850 F g^{-1}) [**100**]. RuO_2 can participate in redox reactions with a very high degree of reversibility and consequently charge/discharge lifetimes in excess of 10^6 cycles are possible [**10**, **30**].

Carbon based ECs are an established technology and have been commercially available for many years, whereas metal oxide based devices have been restricted to niche applications where cost is not the determining factor. These are mainly military applications where the reduction in device volume afforded by the high capacitance density is a highly valuable feature [**10**, **18**].

Despite RuO_2 electrodes exhibiting the highest reported specific capacitances, the current material cost is too high for commercial development. Nevertheless, fundamental studies on this material have greatly added to the understanding of pseudocapacitive materials and indicate that metal oxides could result in a step change for electrochemical capacitor technology.

From the extensive research available, it can be concluded that the unique properties of RuO_2 that results in useful pseudocapacitance, are that the material exhibits a metallic electronic conductivity [**101**-**103**], and that several redox processes occur

during charge/discharge which results in a capacitance value that is fairly constant with changes in cell potential [**16**].

The morphology and hydration state of RuO_2 have been found to be of great importance in determining the level of protonic conductivity exhibited by the material. It has been found that the amorphous, hydrated form of RuO_2 produced using a sol-gel process, resulted in a specific capacitance of 720 F g^{-1} [**104**, **105**]. Further systematic studies [**100**] revealed that the electronic conductivity of RuO_2 nanocrystals is balanced with the protonic conductivity of the surrounding structural water when one mole of RuO_2 is hydrated by 0.58 moles of water ($RuO_2 \cdot 0.58\ H_2O$) corresponding to a maximum capacitance of 850 F g^{-1}.

Although the commercialisation of metal oxide ECs has been limited to date, a great deal of research is being conducted in this area. One research direction that has received much attention is to maximise the electrochemical utilisation of RuO_2 and hence reduce the cost of RuO_2 based devices. The high rates typically associated with ECs result in only a small amount of the RuO_2 particles being active during charge/discharge. Recent studies have focussed on increasing the electrochemical utilisation of RuO_2 by dispersing small active particles or forming thin films on conductive substrates.

Electrolytic production methods yield hydrous forms of RuO_2 [**106**] which enables increased electrochemical utilisation of the metal oxide by forming thin layers (*ca.* 3 nm thick) on substrates with a developed surface area. Electrodes based on high surface area conductive substrates, such as CNT film [**106**] or activated carbon [**107**] result in more efficient use of RuO_2.

Significantly cheaper alternatives to RuO_2 are currently being researched with a variety of directions being pursued [**29**, **32**]. Pseudocapacitive behaviour is displayed to some extent by many transition metal oxides, however, the research carried out on RuO_2 suggests that for a metal oxide to be of use in a practical device the combination of several complementary characteristics are required. These include the chemical and structural reversibility of the reactions occurring during

charge/discharge, a high electrical conductivity, and for both electron and proton hopping to occur in the oxide lattice [**10**].

Although Iridium dioxide has a desirable 'metallic' electronic conductivity [**103**], it is more expensive than RuO_2 and, in a trait shared with other metal oxides, it exhibits a variable pseudocapacitance over a narrower operating voltage than RuO_2 [**16**]. Well known battery materials such as nickel oxides [**108-110**] and cobalt oxides [**111-113**] have received interest as EC electrode materials however they suffer from a significantly narrower operating voltage in comparison with RuO_2 as well as capacitance values that vary markedly with cell potential. The typical operating voltage for these materials is *ca.* 0.5 V which results in comparatively reduced energy and power densities. Wider operating windows have been reported for oxides of vanadium [**54**, **60**, **64**, **66**, **114-120**] and iron [**72**, **121-124**] although the materials have been found to degrade during cycling.

The most promising alternative to RuO_2 for use in ECs are manganese oxides as they can be manufactured in a wide variety of forms that exhibit different electrochemical properties. These materials are of great use in battery technology, with manganese (IV) oxide (usually γ-MnO_2) being found in primary alkaline cells [**33**, **125**], and the $LiMnO_2$ spinel being an attractive intercalation material for rechargeable Li-ion batteries [**126**].

Hydrous, amorphous manganese dioxide (MnO_2) was identified as "an excellent electrode for a faradaic electrochemical capacitor" [**59**] when pseudocapacitive behaviour was observed during cycling in a mild aqueous electrolyte. A specific capacitance in the region of 200 Fg^{-1} was reported for this material, and subsequently many different forms of MnO_2 have been investigated with respect to their performance as EC electrode materials [**27**, **59**, **63**, **67-71**, **73**, **127-132**].

As MnO_2 is electrochemically active in neutral aqueous electrolytes, it is thought that asymmetric ECs using MnO_2 could offer similar performance to currently available devices while eliminating the need for potentially hazardous flammable solvents.

Since the electrical conductivity of these alternative metal oxides is typically many orders of magnitude lower than that of RuO_2, minimising the "diffusion length" for ionic species is essential. Materials with increased surface area have been developed with this aim, and electrodes employing conductive substrates covered with a thin layer of pseudocapacitive metal oxide show particular promise [**120**, **123**, **133**].

2.7.2 Lithium Intercalation Capacitors

Asymmetric cells, where a porous carbon electrode is paired with a doped lithium intercalation compound, are devices that combine the charge storage mechanism of an EDLC with that seen in Li-ion batteries. Referred to as lithium intercalation capacitors (LICs), these devices produce a higher specific energy than other ECs and deliver a higher specific peak power than Li-ion batteries. LICs exploit the reduction in open circuit voltage caused by lithium doping to produce devices with higher output voltages in comparison with symmetric ECs.

This technology was first realised using nanostructured $Li_4Ti_5O_{12}$ combined with activated carbon in an organic electrolyte to construct a device that produced a specific energy equal to five times that of EDLCs available at the time [**134**]. Subsequent to this study, advances in this system and different materials combinations in LICs were explored [**135-142**]. Devices using $Li_4Ti_5O_{12}$ have been shown to exhibit long cycle lives, as this compound does not exhibit a great degree of expansion or contraction during Li^+ intercalation [**134-136**], a problem observed with other hybrid devices. Graphite has also been investigated as an intercalation host in LICs with increased specific energy due to a larger operating voltage [**137**, **138**]. However LICs, especially those using a graphite electrode, have the disadvantage that excessive discharge rates can result in solid lithium forming on the electrode surface which significantly reduces cycle life and is potentially hazardous. In some Li-ion batteries, the repeated solution and precipitation of lithium during charge and discharge causes the uneven deposition of metallic lithium in the form of *dendrites*. Excessive dendrite formation can produce a short circuit leading to overheating and possible ignition of the flammable electrolyte. Also, the

intercalation electrode can limit the power of these devices as the solid state diffusion of lithium ions is a slow process in comparison with the EDLC mechanism [**136-138**].

To be competitive with established devices, LICs need to exhibit a specific power and cycle life comparable with that of non-aqueous EDLCs [**24**, **143**] as the increased energy density can be met with available battery technology.

2.7.3 Electroconductive Polymers

Electroconductive polymers (ECPs) that have been considered as electrode materials for ECs include polythiophenes, polypyrrole and polyaniline [**14**, **26**, **144**].

A drawback associated with these materials is the high ESR from the random deposition method utilised in manufacturing. To reduce the influence of the resistance arising from ECPs they are usually found in composite electrodes with fillers that exhibit high electrical conductivity and a high specific surface area (*i.e.* carbon materials). The use of activated carbon and carbon nanotubes as a substrate allows for an enlarged active surface area of conductive polymer, which increases the specific capacitance of composites to values exceeding those seen in EDLCs.

The long-term stability of ECPs has been identified as a problem due to the repeated swelling and shrinking that occurs during charge/discharge [**17**, **30**] however this has been mitigated slightly by the deposition of a thin layer of ECP onto a conductive substrate [**145**, **146**].

2.7.4 Carbon

When considering the double-layer mechanism it is clear that the surface area of electrode materials influences the capacitance of devices, with Eq. 2.2 indicating that capacitance is proportional to the surface area of the electrode. This has led to a great deal of interest in the use of porous carbon materials as EC electrodes.

Carbon materials are available in many different physical forms, many of which have been used in the fabrication of EC electrodes [**12, 17**, **19**, **22**, **25**, **30**, **31, 147**]. From the available literature, it can be seen that the properties of carbon materials that render them useful in ECs are that they are electrically conductive, chemically inert and can be produced with relatively high specific surface areas. These useful physical properties arise from the extraordinary bonding mechanisms available to carbon atoms.

Carbon atoms have four valence electrons which allows for several different allotropic forms of carbon to exist through hybridisation of the *2s* and *2p* electron shells. The majority of carbon forms exhibit some degree of π-bonding which permits electron conduction through delocalised electron clouds. Diamond is a highly ordered form of carbon formed exclusively *via* sp^3 hybridisation (where π-bonding is not possible) and consequently has an extremely low electrical conductivity. Graphite on the other hand is highly conductive along the basal plane as a result of an extensive sp^2 hybridised network. The difference between these two bonding mechanisms is also manifested in other distinct physical properties; for example, diamond and graphite define opposite ends of the Mohs scale of mineral hardness.

2.7.4.1 Graphene

Graphite is a layered structure of parallel graphene sheets, which are planes of sp^2 hybridised hexagonally arranged carbon rings. The remaining valence electrons form π-bonds with adjacent carbon atoms which are stabilised by resonance structures and form a layer of delocalised electrons above and below the graphene plane. The plane in which the carbon atoms are bound to one another is termed the basal plane (or *ab* plane), and perpendicular to this plane is the *c*-axis as shown in Figure 2.14. In graphite, layers of graphene sheets are separated by a distance of 3.354 Å [**148**] and are loosely held together through van der Waals' interactions. The weak forces of attraction between layers results in graphene sheets being easily cleaved from bulk graphite, and the ability of these layers to slide over each other

allows graphite to be used as a lubricant. Stacking of graphene sheets can show a high degree of three-dimensional crystallographic order; however defects in the crystal lattice, such as dislocations or interstitial atoms, are frequently found. As a consequence of the anisotropic structure of graphite, electrons are easily conducted along the basal plane but not along the *c*-axis.

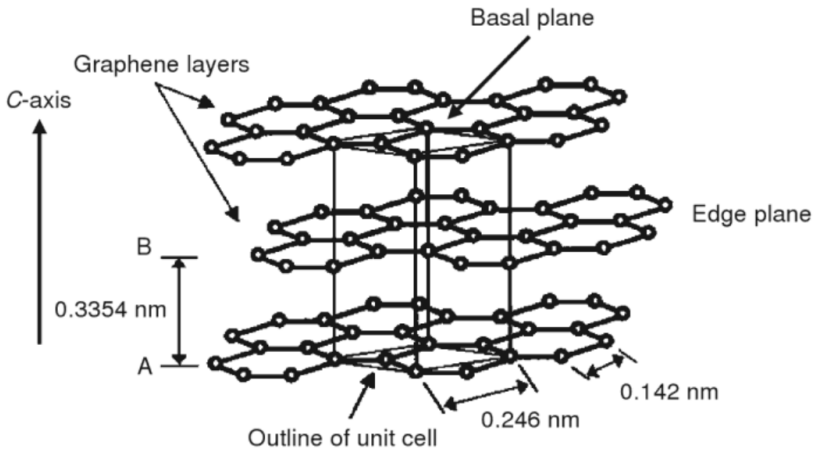

Figure 2.14: Structure of graphite [148]

Amorphous carbons show no long range order but are considered to consist of graphene-like microstructures showing little order parallel to these layers. The absolute density of amorphous carbon forms can be as low as 1.8 g cm^{-3} [**149**], whereas pure graphite is notably denser at 2.267 g cm^{-3}. A wide variety of carbon materials can be prepared that have an absolute density and structural order between those seen in graphite and amorphous carbon [**22**]. These carbon materials include graphene, nanotubes, glass-like carbon, carbon fibres, carbon blacks, activated carbons, templated carbons and carbide-derived carbons and are produced using various techniques.

Graphite is unsuitable for direct use as the primary component in EC electrodes as it has a dense, non-porous form although it is possible to increase the specific surface area slightly by forming different morphologies such as graphite whiskers.

Graphite has been studied with respect to the double-layer capacitance that can be generated at the crystal surface and it was found that the basal plane of graphite is associated with double-layer capacitance values in the region of 10 μF cm^{-2}, whereas

the edge plane can generate values as high as 70 μF cm^{-2} [**150**]. Single layers of graphene can however be isolated from pyrolytic graphite by mechanical exfoliation [**151**, **152**] which has inspired a rapidly increasing amount of research. Alternative processes focussed on the scale up of graphene production have been reported and include the annealing of silicon carbide wafers, epitaxial growth, precipitation from a molten transition metal [**153**] and solvothermal synthesis [**154**]. Graphene oxide can also be reduced to yield graphene films but can results in a large amount of functional groups remaining after treatment [**155**].

Graphene has a theoretical specific surface area of 2630 m^2g^{-1} and an electrical conductivity that approaches that of graphite, [**155**] which are desirable properties for EC electrode materials. The suitability of graphene as an electrode material has been investigated by several groups with specific capacitances in the region of 135 F g^{-1} being measured in aqueous media, and 94 F g^{-1} using 1 M TEA BF_4 in PC [**155**]. Graphene materials currently display relatively low specific surface areas in comparison with the theoretical maximum, especially when included in composite electrodes using polymer binder. Current research is directed toward increasing the amount of graphene exposed to electrolyte [**156**], and particularly by increasing the surface area arising from edge planes [**157**].

2.7.4.2 Nanotubes

An alternative stable arrangement of sp^2 hybridised carbon atoms was discovered in 1985 [**158**] with the synthesis of buckminsterfullerene. Through the vaporisation of graphite using laser pulses, reordering of the carbon atoms was observed to produce stable C_{60} molecules. The same production method led to the synthesis of another allotrope, namely carbon nanotubes (CNTs) and a great deal of research concerning CNTs followed a report in 1991 [**159**], although their existence was previously reported [**160**]. CNTs have a cylindrical nanostructure and can be produced with extremely large length-to-diameter ratios. CNTs can be capped by a fullerene-type structure and when the body of the cylinder is formed by one graphene layer, tubes are termed single-walled nanotubes (SWNTs), and multi-walled nanotubes

(MWNTs) are formed when multiple concentric layers of graphene sheets are present in the structure. The arrangement of the graphene layers in the formation of CNTs results in remarkable physical properties being observed, and a wide variety of CNT structures are possible. In particular, the conduction of electrons is affected by the chirality and curvature of CNTs, with some arrangements resulting in semiconductor behaviour [**161**].

As with graphene, nanotubes can exhibit an electrical conductivity similar to that of graphite but their morphology usually restricts the specific surface area of CNTs to less than 400 m^2g^{-1} [**19**, **22**]. However, CNTs can be used to produce large, electrically conductive porous networks which have been seen as an ideal material for use in EC electrodes. The specific capacitance of CNT electrodes has been found to vary according to their morphology and frequently, a significant amount of purification is required to remove catalyst particles and amorphous carbon residues from CNTs. Electrodes mainly comprised of pure CNTs seldom produce specific capacitance values greater than 100 F g^{-1} [**22**], however this can be increased by activation or by the addition of surface functional groups [**19**].

As CNTs possess a highly accessible porosity but exhibit a relatively low specific surface area, research utilising CNTs is focussed on the preparation of composite structures incorporating metal oxides or electrically conducting polymers.

CNTs have been found to be a useful conductivity enhancer in place of the carbon blacks that are commonly employed in the production of EC electrodes. The high aspect ratio and electrical conductivity of CNTs allows for lower relative concentrations to be used and, can offer an increase in the specific power of the device. It was reported that the equivalent series resistance of an activated carbon electrode was reduced from 45 Ω to 2.5 Ω by substituting acetylene black particles for an equal mass of 100 μm long MWNTs [**162**].

2.7.4.3 Carbide-derived carbons

Carbide-derived carbons are manufactured by the selective removal of atoms from metal carbides through chlorination. By controlling the raw material and synthesis conditions, carbon materials with a very narrow pore size distribution and highly controlled pore structure are produced [**163**, **164**]. These structural features have been especially useful in the elucidation of the charge storage mechanism in materials containing very fine pores [**165-168**]. Electrodes produced using a carbon with a BET surface area of 1590 m^2g^{-1} derived from TiC, have been reported to exhibit a specific capacitance of 120 F g^{-1} in an organic based electrolyte [**164**].

Graphene, carbon nanotubes and carbide-derived carbons are produced by relatively unconventional and costly methods whereas the majority of carbon materials are produced using thermal treatments known as carbonisation and activation.

2.7.4.4 Carbonisation

The carbon content of organic materials is increased through thermal treatment under an inert atmosphere. By heating carbonaceous materials to temperatures in the range of 700 - 1000°C [**148**], volatile compounds are generated and removed from the structure, disproportionately stripping the original material of atoms other than carbon. Residues are mainly composed of carbon planes showing two-dimensional order (but no crystallographic order perpendicular to the hexagonal ring planes) and are referred to as being *non-graphitic*.

Treatment at significantly higher temperatures (> 2500K [**148**]) can cause the solid-state transformation of a non-graphitic carbon to produce aligned graphene sheets *i.e.* graphite. Carbon materials that can be converted to graphite in this manner are classified as *graphitisable*, and usually undergo transformation into a fluid phase during the carbonisation process. Coal tar pitch, for example, forms a fluid mesophase during carbonisation which allows for the partial alignment of large aromatic structures. Figure 2.15 illustrates possible structural transformations of a graphitisable carbon with increasing temperature [**148**]. When a fluid phase is not

observed during carbonisation, the residual materials are usually referred to as *chars* and are encountered in the production of activated carbons.

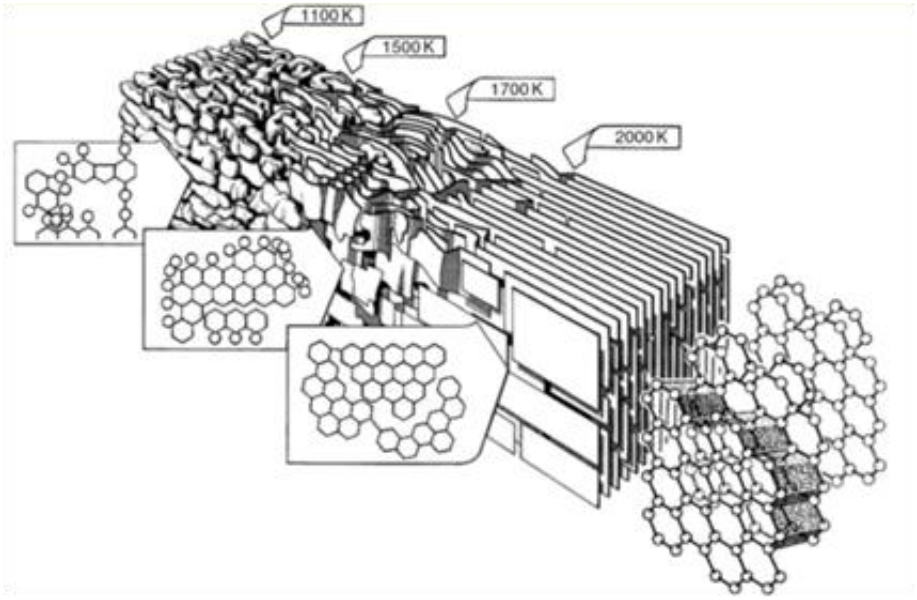

Figure 2.15: Transformation of a graphitisable carbon [148]

2.7.4.5 Porosity

In the discussion of carbon materials it is clear that the specific surface area of materials can be increased by incorporating voids into the solid phase. These voids are known as pores and they influence the physical characteristics of materials in different ways. Solid materials can be defined as being porous or non-porous based on the presence of voids within individual particles, although any solid that contains cavities, channels or interstices can be regarded as porous [**169**]. Irregularities in the surface of solid particles are termed *surface roughness* as indicated in Figure 2.16 and a distinction between surface roughness and porosity is generally drawn at the point where surface irregularities are deeper than they are wide.

Figure 2.16 represents a cross-section of a roughly spherical porous particle, and shows that pores can be loosely classified as being either closed or open with respect to their availability to an external fluid. Closed pores are completely surrounded by solid and cannot be accessed by an external fluid. Pores of this type influence the

physical properties of the particles such as the bulk density, mechanical strength, electrical conductivity *etc.* on the macroscopic scale, but are inactive with respect to the flow of fluids and adsorption processes.

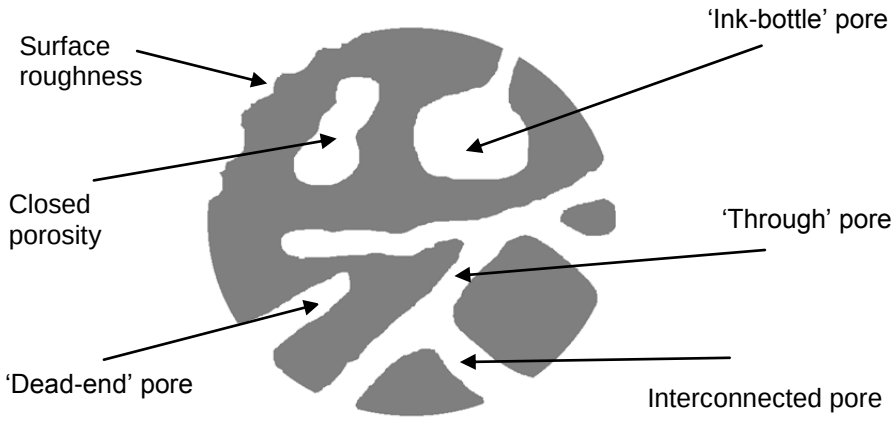

Figure 2.16: Diagram of a porous particle

The other pores shown in Figure 2.16 are termed open porosity *i.e.* they are accessible to an external fluid. When the pores are open only at one end, such as the '*dead-end*' and '*ink-bottle*' pore, they can be described as blind or saccate, whereas *interconnected* and '*through*' pores can be considered to be open at both ends.

Pores may also be classified based on their shape, with cylindrical/spherical or slit-shapes being employed in the majority of models relevant to porous materials. In the case of cylindrical pores the term 'pore width' or 'pore size' usually refers to the diameter of the pore whereas the same terms refer to the separation between the pore walls for slit-shaped pores.

Pores are usually classified according to size, with the term *micropore* referring to pore widths less than 2 nm, *mesopore* indicating a pore width between 2 and 50 nm and *macropore* denoting pores greater than 50nm in width [**170**]. Alternative definitions are encountered but are not widely used; for example, the term *ultramicropore* has been adopted to classify pores that are less than 0.7 nm wide, with *supermicropore* referring to pores between 0.7 nm and 2.0 nm wide.

Extremely high specific surface areas are usually associated with materials containing a substantial quantity of very fine micropores, as the ratio of surface area-to-volume varies inversely with pore width for an ideal pore.

2.7.4.6 Activation

Carbonisation produces materials that usually have a low level of porosity and consist of graphitic crystallites separated by regions filled with disorganised tarry carbon residues. Activation processes preferentially remove these disordered regions from chars to leave rigid, complex materials with increased porosity. The amount of each structure present in the final carbon material is dependent on the precursor and carbonisation conditions. The heating rates, temperatures and processing times all influence the final structure of the carbon.

Physical activation is used to describe the process of controlled carbon gasification at an elevated temperature (700 - 1100°C) in an oxidising atmosphere. Air, steam, carbon dioxide, and mixtures of these gases provide suitable atmospheres for the reaction of carbon, although using CO_2 activation allows for more control over the process.

Atmospheric oxygen reacts with carbon at elevated temperatures to produce carbon dioxide or carbon monoxide through strongly exothermic reactions. As a consequence, these reactions can be self-propagating and are difficult to control. Activation in air is seldom used as the exothermic nature of the reactions can result in appreciable combustion of the carbon structure and undesired pore structures. [**171**, **172**].

When steam activation is used, the main reaction is the oxidation of carbon to produce carbon monoxide and hydrogen through an endothermic reaction. However, the exothermic reaction of the produced carbon monoxide with steam introduces a degree of instability into the activation process, but not to the same extent as air activation. Due to secondary reactions, steam activation has been shown to produce carbons with a broader pore size distribution in comparison with chemical or CO_2

activated carbons [**173**] and in general produces materials with a larger amount of residual oxygen functional groups.

The reaction between carbon and carbon dioxide is endothermic and is known as the Boudouard reaction [**174**] and is shown in Eq. 2.8.

$$C + CO_2 \rightleftharpoons 2CO \qquad \textbf{Eq. 2.8}$$

Conversion to carbon monoxide in Eq. 2.8 is favoured at temperatures greater than 700°C, and can be easily controlled by adjusting the reaction temperature. Activation with CO_2 has been shown to produce activated carbons with a large micropore volume, narrow pore size distribution and little surface functionality [**172**].

Chemical activation differs from physical activation as it is usually carried out simultaneously alongside carbonisation, and at lower temperatures in the region of 400 - 900°C [**172**]. An activating agent such as phosphoric acid, zinc chloride or potassium hydroxide is impregnated into the precursor and has a dehydrating effect during carbonisation [**172**]. In chemical activation processes the energy saved by operating at lower temperatures is at the cost of additional processing being required to add and recover the activating agent. Chemical activation has been found to yield predominantly microporous activated carbons with specific surface areas as high as 3000 m^2g^{-1} [**172**].

2.7.4.7 Templated Carbons

Templated carbons are produced by constraining the carbonisation of organic material within a porous inorganic matrix. This is usually achieved by impregnating a silica based template with the liquid form of a carbonaceous precursor such as sucrose [**175**] before carbonisation, however the decomposition of hydrocarbon gases (e.g. propylene [**176**]) into the pores of a template has also been successful. Templates are usually dissolved using hydrofluoric acid to yield carbon materials with well-defined structural characteristics. By using templates such as ordered

silica, a regularly connected pore structure of controllable pore size is present in the carbon structure.

Templated carbons have been explored as electrode materials for ECs with an extensive study reporting specific capacitance values in the region of 220 Fg^{-1} when aqueous electrolytes were used [**177**]. Also, templated carbons have been found to maintain their specific capacitance with increasing rate of discharge in comparison with commercial devices whose performance is substantially decreased at higher rates of discharge [**178**].

2.7.4.8 Glass-like Carbon

Glass-like, 'glassy', or 'vitreous', carbons are usually formed through the slow, controlled carbonisation of phenolic resins which are then treated at temperatures up to 3000°C. The carbon atoms in glassy carbon have been shown to be bound through sp^2 hybridisation but there is little long range order between the graphene-like planes. Consequently, glass-like carbons exhibit high electrical conductivity [**56**]. Glass-like carbon can be thought to consist of entangled graphitic ribbons that define cavities within the structure which can account for 30% of the bulk volume of the material [**22**]. This closed porosity can be opened up by activation to increase specific surface area and create a porous network. The development of an EC using activated glass-like carbon electrodes shows that free standing electrodes requiring no external current collector, binder or conductivity enhancing additive can be produced [**179**, **180**] which may be useful in the development of high-power ECs.

2.7.4.9 Carbon Blacks

Carbon blacks are a group of carbon materials that are characterised by having spheroidal particles of colloidal dimensions and are produced in the gas phase by the thermal decomposition of hydrocarbons. Porosity can be developed by activation with CO_2 to produce specific surface areas greater than 1600 m^2g^{-1} and values of

specific capacitance in excess of 200 Fg^{-1} [**181**, **182**]. However relatively large binder concentrations are required to produce mechanically stable electrodes using carbon blacks, which has a detrimental effect on the resistance and power capabilities of carbon black based electrodes.

Carbon blacks are almost always added in relatively low concentrations (*ca.* 10 wt.%) to electrode mixtures when a polymer binder is used to form composite electrodes, in an effort to enhance the overall electrode conductivity of the electrode.

2.7.4.10 Activated carbons

Activated carbons are usually produced by the carbonisation of an organic precursor to produce a char whose specific surface area is enhanced by controlled oxidation. Activated carbons displaying specific surface areas in excess of 1000 m^2g^{-1} are commonplace and values as high as 3000 m^2g^{-1} are possible [**172**]. By varying the temperature, duration and reagent concentrations used in activation processes, the degree of material removed (*burn-off*) can be controlled to produce materials with a range of surface areas. The widespread use of activated carbons in adsorption and catalytic processes has occurred because they are easy to manufacture, display relatively large specific surface areas, have a well-developed pore structure and can be easily modified to include surface functionality. By far the majority of commercially available ECs use activated carbons as the main component in their electrodes.

Activated carbon can be produced from many materials with the main requirements being that the precursor is predominantly composed of carbon and contains a low amount of matter that cannot be removed through gasification. Many natural feedstocks are available for activated carbon production as well as several by-products from industrial processes. Coconut shells, coals and woods are used to produce the vast majority of activated carbons [**172**].

2.7.4.10.1 Synthetic Carbon Precursors

Synthetic carbon precursors are generally more expensive and involve additional processing in the production of activated carbons, but offer several advantages over natural/by-product derived materials. The pore characteristics are controllable to a greater extent using polymers or resins as a feedstock as carbonisation can produce a carbon pseudomorph of the precursor. Pore size distributions are in general more well-defined when using synthetic precursors (*i.e.* narrower) and are more reproducible. There is also a significant degree of variability in the quality of natural feedstocks, and by using synthetic precursors mineral contaminants can be minimised to produce highly inert materials. Also, by employing synthetic precursors specific macro-scale forms of carbon materials can be produced in the shape of monoliths or fibres.

Through a combination of reactions and sol-gel processing used in the manufacture of ceramics, organic compounds with controllable pore characteristics suitable for carbonisation can be produced. Organic gels produced using resorcinol and formaldehyde are the most widely studied and the sol-gel chemistry of many compounds that undergo similar reaction mechanisms have been explored; a few are listed below:

Catcechol-formaldehyde [**183**], Phloroglucinol-formaldehyde [**183**, **184**], Melamine-formaldehyde [**185**, **186**], Phenolic (novolak)- furfural [**187**], Polyurethane [**188**], Cresol-formaldehyde [**189**], Phenolic (resole) [**190**], Phenol-formaldehyde [**191**], PVC [**192**], Polyurea [**193**]

2.7.4.10.2 Resorcinol Formaldehyde Gels

Resorcinol Formaldehyde (RF) gels were selected as the carbon precursor in this work as they are widely used in the production of carbons for research into ECs [**194-196**], and have controllable pore characteristics.

Resorcinol undergoes an addition reaction with formaldehyde under alkaline conditions which, through further condensation reactions, forms a cross-linked network. Under certain conditions the cross-linked network can extend throughout a liquid phase to produce an organic gel, in a similar manner to the sol-gel manufacture of ceramics. Removal of the liquid phase yields a porous solid with useful characteristics such as a high pore volume (0.25 - 1.25 $cm^3 g^{-1}$), low bulk density (0.06 - 0.103 g cm^{-3}) and large specific surface area (400 - 1000 $m^2 g^{-1}$) [**197**]. Subsequent carbonisation (and activation) yields a pseudomorph of the dried RF gel with a large amount of open, connected porosity and a relatively high surface area.

Reaction mechanism

The reaction of resorcinol (1,3-dihydroxy benzene, R) with formaldehyde (F) is initiated by the formation of a resorcinol anion resulting from hydrogen abstraction. Resorcinol anions are more reactive than uncharged resorcinol towards formaldehyde, and react to produce hydroxymethyl derivatives. Condensation polymerisation between these hydroxymethyl compounds is catalysed by H^+ ions, which remove the hydroxyl group leaving a benzyl-type cation that undergoes an electrophilic reaction with the benzene ring of another molecule [**198**]. These cations are connected by either methylene ($-CH_2-$) or methylene ether ($-CH_2-O-CH_2-$) bridges [**183**] which occur mainly in the 4- and 6- ring positions. The 2- position of the resorcinol ring has the highest electron density but is surrounded by two hydroxyl groups which inhibit access. Successive condensation reactions create clusters which subsequently cross-link and agglomerate to produce a three-dimensional network structure. Cluster size and the resultant pore network are dependent on several controllable parameters, which allows for the design of organic gels with desired physical properties. Factors that have been found to influence the pore structure of RF gels include the ratio of reagents, degree of dilution, type and amount of catalyst used, reaction temperature and the method by which the gel is dried.

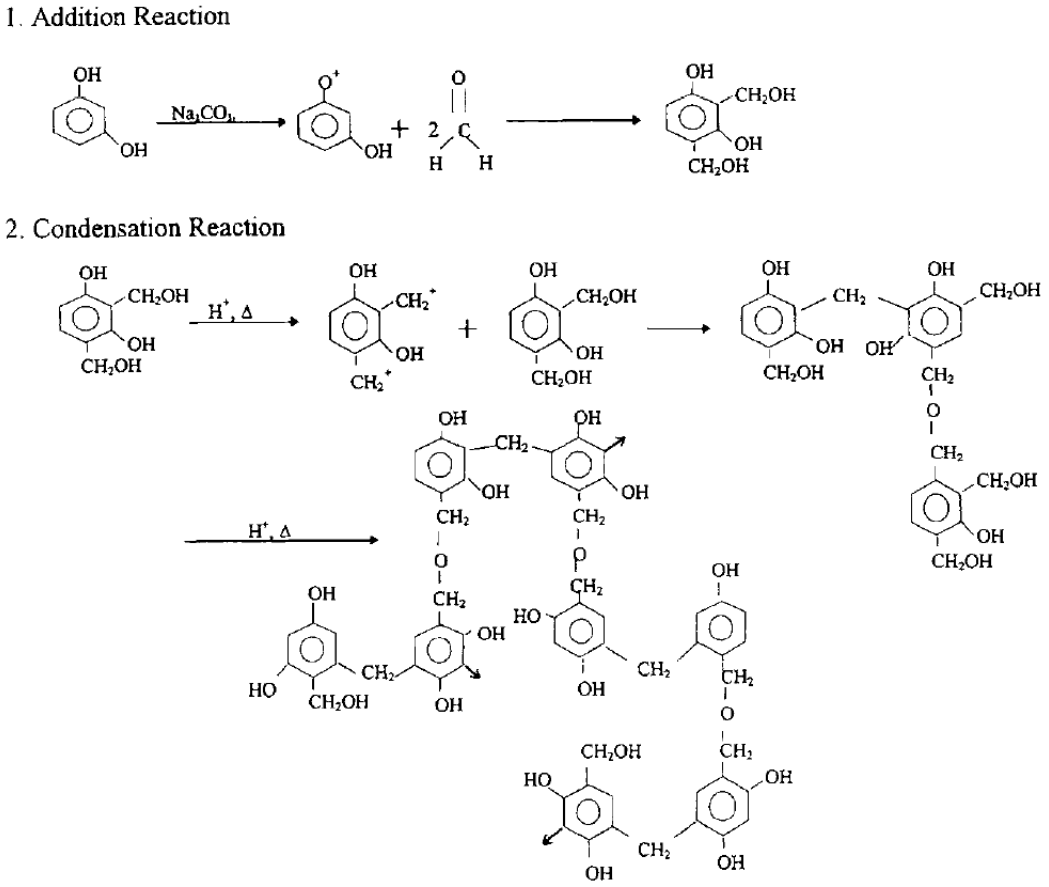

Figure 2.17: Reaction mechanism of the sol-gel polymerization of resorcinol with formaldehyde [198]

Factors affecting structure

RF Ratio

The molar ratio of resorcinol to formaldehyde (R/F) is usually maintained at a constant value of 0.5 which corresponds to the stoichiometric ratio for the initial addition reaction in Figure 2.17 *i.e.* all formaldehyde is consumed when the gel is fully crosslinked. In an investigation of the effect of R/F on the porous structure of aerogels [**199**], it was found that a gel did not form at a molar ratio of 1, and at values less than 0.34, excess formaldehyde causes the mesopore structure to collapse. At molar ratios greater than around 0.7, it appears that there is insufficient formaldehyde present to allow the formation of a solid network. The BET surface area of the

resultant gels was found to be independent of R/F for gels produced with an R/F ratio between 0.4 and 0.7.

Dilution

In the majority of cases RF gels are synthesised in aqueous solution and are sometimes referred to as aquagels or hydrogels. The degree of dilution has been found to affect the structure and density of the gel and has been the subject of several investigations. R/W ratios commonly used are between 0.05 and 0.5, and give a rough indication of the bulk density of the dried gel (under the assumption that no shrinkage during drying occurs). Generally, a reduction in the concentration of reactants increases the void fraction of the dried gel. In the region 0.05 - 0.25 g cm^{-3} the BET surface area of RF aerogels was not found to vary greatly, however the mesopore volume varied from 0.5 to 3.0 cm^3 g^{-1} [**199**]. At very low concentrations of reactants a gel may not form, and the final product will be a suspension of polymer in solvent [**200**].

RC Ratio/pH

The most influential factor on the pore structure of RF gels has been found to be the ratio of resorcinol to catalyst, which is an indirect measurement of the initial pH of the reactant solution. From the reaction mechanism in Figure 2.17 it is seen that the addition reaction is base catalysed whereas the subsequent polymerisation reaction is acid catalysed, therefore there is a small range of initial pH in which gels are produced ($5.5 < pH < 7.5$). The pH of the reaction mixture decreases as the condensation reaction proceeds. As the first step of the reaction mechanism is the abstraction of hydrogen from a resorcinol molecule, higher concentrations of catalyst enhance the reaction rate, producing many tightly cross-linked clusters. In general, an increased level of catalyst results in materials with larger BET surface areas and narrower pore size distributions.

Catalyst type

The nature of the compound that catalyses the initial addition reaction has been found to alter the reaction mechanism and consequently affects the final pore

structure of the gel. Sodium carbonate (Na_2CO_3) is the most commonly used 'catalyst' for the initiation of the addition reaction in Figure 2.17, however many other basic compounds have been explored [**183**, **201**, **202**].

The use of amines to basify the reagent mixture has been explored in an attempt to incorporate nitrogen into the structure of a carbon material [**203**]. However the relatively low concentration of amines required to adjust the pH of the solution results in very low nitrogen concentrations (*ca.* 0.4 wt.%).

Reaction temperature/time

At room temperature the gelation process proceeds very slowly, therefore after initial mixing of the reagents an elevated temperature is required to promote the cross linking reaction. Temperatures in the region of 85°C are usually used and produce stable gels in approximately 3 days. The reaction has also been carried out at 25°C using a relatively high reactant concentration and was found to gel within 7 days. [**201**] The time required for gelation at a constant temperature is dependent on the R/W and R/C ratios used during synthesis.

Alternative reaction schedules have been used and typically increase the temperature of the reaction mixture in stages *e.g.* 24 hours at 25°C, 24 hours at 50°C followed by 72h at 90°C [**194**, **199**]. In a comparison of reaction schedules, it was found that using a constant temperature of 90°C for 72h produced RF xerogels with a well-defined, unimodal pore size distribution that varied predictably with RC ratio, shown in Figure 2.18 (a) whereas xerogels produced using a reaction schedule similar to that described above, possessed broad, irregular pore size distributions as shown in Figure 2.18 (b) [**195**].

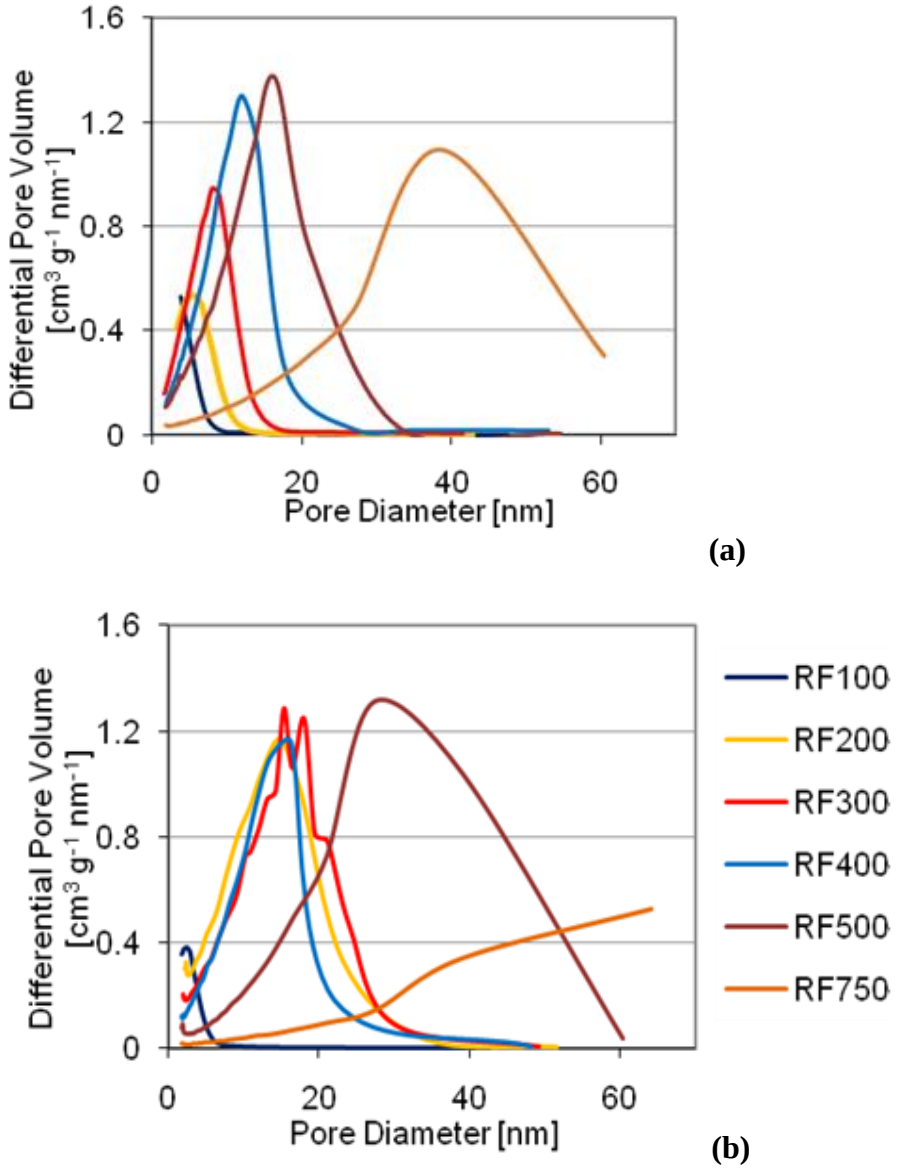

Figure 2.18: Pore size distribution of RF xerogels produced using different R/C ratios using (a) a constant temperature and (b) a phased temperature schedule [195]

Drying Method

The method of solvent removal from the gel has been found to have a pronounced effect on the materials produced as the forces generated during drying can cause the pore structure to rupture or collapse. Figure 2.19 shows a generalised phase diagram for solvents used in organic gel manufacture, and the arrows indicate different drying methods; the orange arrow represents conventional evaporative drying (and vacuum

assisted drying), the blue arrow represents freeze drying, and the red arrow signifies supercritical drying.

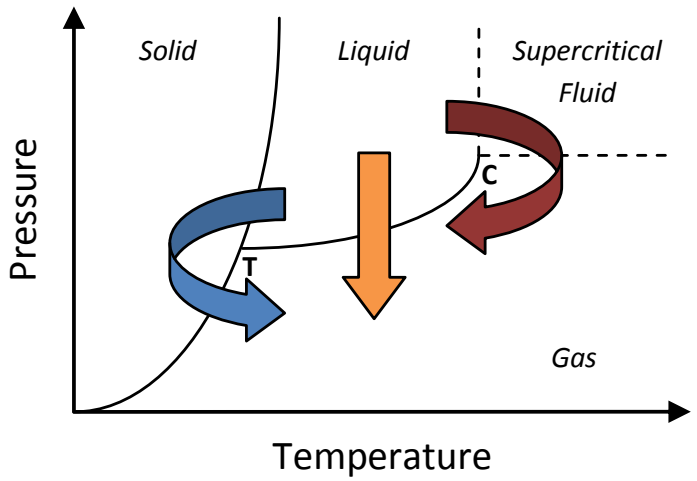

Figure 2.19: Phase changes during solvent removal in RF gels. The orange arrow represents evaporative drying, the blue arrow represents freeze drying, and the red arrow signifies supercritical drying.

Aerogels

Supercritical drying of organic gels is used to retain the morphology of the gel phase and produces materials known as aerogels. Aerogels usually have the lowest values of bulk density and exhibit the highest surface areas.

In the production of aerogels, the water in the sol-gel mixture is replaced with a fluid that has a greater miscibility with liquid CO_2. Solvent exchange is usually carried out over a few days under constant agitation, and may be performed at an elevated temperature to enhance diffusion. The solvent may also be replaced periodically to ensure that all traces of water have been removed from the gel structure. To exchange the solvent with CO_2, a high pressure chamber with temperature control is required and liquid CO_2 is fed to the chamber with regular purges to remove any remaining solvent. The temperature and pressure in the vessel is raised above the critical point (the critical point for CO_2 is 75.8 bar at 31°C) and the CO_2 vented to produce a dry aerogel.

Xerogels

Xerogels are produced when the solvent is removed subcritically, *i.e.* using convective and/or vacuum drying. Solvent exchange is usually carried out before drying to replace the water used in gel synthesis with a liquid that has a lower value of surface tension. For example the surface tension of water at 20°C is 72.75×10^{-3} Nm^{-1} whereas acetone has a surface tension of 23.7×10^{-3} Nm^{-1} at the same temperature [**200**]. This is done to reduce the capillary forces that arise at the liquid-vapour interface as these forces have been found to be responsible for the shrinkage, and in some cases the complete collapse, of the pore network. The drying rate has been reported to influence the final texture of the material [**204**]. Microwave assisted drying has been found to produce xerogels with similar textural characteristics to those dried under vacuum, but in a much shorter time [**205**].

Cryogels

Freeze drying (lyophilisation) can also be used to dry gels and avoids the capillary forces associated with liquid-vapour interfaces. When freeze drying has been carried out, gels are usually referred to as cryogels. In freeze drying, the temperature of the sample is reduced to freeze the solvent, the surrounding pressure is then reduced and the temperature gradually increased to allow the sublimation of the solvent.

In the case of freeze drying the water contained in the gel matrix is usually exchanged with *t*-butanol [**206**] as the change in volume of water on freezing can rupture the pore network. Also ice crystal growth during the freezing process has been found to create large fissures in the dried gel [**200**].

RF gel derived activated carbons in EC electrodes

Carbon materials derived from RF gels have been studied by many groups with respect to their performance in EC electrodes. Initially, carbonised RF aerogels were considered as an ideal electrode material as monolithic forms can be produced which display a significantly reduced resistance in comparison with electrodes formed using a powdered carbon and polymer binder. In addition, the unique nanostructure

that can be controlled in an organic aerogel was expected to perform well as electrodes in EDLCs [**194**]. It was reported that for a fixed R/C ratio, the specific capacitance was found to decrease with increasing material density. Also, in general, gels produced with a larger amounts of catalyst (*i.e.* R/C=50) produced the highest values of specific capacitance at a constant reactant concentration. A subsequent study used similar RF aerogels to investigate the effects of the temperature used during carbonisation on the capacitance density of EC electrodes [**207**]. Maximum capacitance density was observed at carbonisation temperatures of 800 and 900°C using a gel produced at an R/C ratio of 200. Activation of the carbon aerogels at 1050°C in CO_2 was also studied using a gel produced at R/C=200, and it was found that the capacitance density of was increased by almost 50% after 1 hour, with a substantially smaller increase being observed thereafter. Depending on the degree of activation of RF gel derived carbons, specific capacitance values as high as 220 Fg^{-1} can be attained [**208**].

However, the main benefit of using RF gels as a carbon precursor in the study of EC electrodes is that the pore structure can be easily controlled by changing the R/C ratio during synthesis, as seen in Figure 2.18(a), and this has recently been exploited to investigate the influence of pore size on the electrochemical behaviour of ionic liquid electrolytes in ECs [**196**].

2.7.4.11 Porosity in EDLC electrodes

An important area of research concerning carbon electrodes in ECs, particularly with the use of ionic liquid electrolytes [**195**, **196**], is the influence of electrode porosity on capacitor performance. As double-layer capacitance is theoretically proportional to the surface area of the electrode (Eq. 2.2), activated carbons are commonly used for EDLC production. In practice, a direct relationship between specific surface area and specific capacitance is seldom observed but linearity is frequently assumed in the analysis of the electrochemical behaviour of electrode materials. Specific capacitance values are usually 'normalised' before analysis to provide a relative measure of the charge storage capacity per unit surface area. This assumes that the

relationship in Eq. 2.2 is satisfied under all conditions and that materials with the same specific surface area exhibit the same specific capacitance, (*i.e.* (*C*/*S*) is a constant for a material). However, the values of (*C*/*S*) for graphite has been found to depend on crystallographic orientation, and porous carbon materials can be expected to produce values that lie between the two extremes seen in graphite. Experiments carried out on the interface between an electrolyte and cleaved graphite crystal oriented on the basal plane produced values in the region of 3 - 12 μF cm^{-2} whereas polished edge plane crystals produced values between 50 - 70 μF cm^{-2} due to the anisotropic electrical conductivity seen in graphite [**10**, **150**].

Also, Eq. 2.2 (and the Grahame model in Figure 2.9) is strictly applicable only to planar electrodes whereas activated carbons are three-dimensional structures. Normalisation on the basis of surface area introduces a possible source of errors into the data as many different methods can be used to define 'area'. Typically the BET surface area obtained from nitrogen adsorption data at 77K is used as a standard definition despite the well known limitations of this method, although different characterisations have been used [**209**, **210**]. Furthermore, the exact surface area that takes part in charge storage is subject to a certain degree of uncertainty which complicates the interpretation of experimental data. For example, pores may be inaccessible to the electrolyte solution or even too small to permit ion insertion.

Several comprehensive studies have used activated carbons investigate the relationship between porosity and electrochemical performance in EC electrodes. Over 30 activated carbons with BET surface areas between 500 and 2500 m^2g^{-1} were tested using KOH electrolyte [**211**, **212**]. The single electrode specific capacitance was observed to vary over the range 94 - 413 F g^{-1}, but the relationship between surface area and specific capacitance was not directly proportional. Two reasons were offered to explain this behaviour. Firstly, all surface area accessed by nitrogen at 77K may not be accessible to the electrolyte and secondly, that the local electroadsorption properties are dependent on the size of the pore in which they occur. Under the assumption that the entire measured surface area was accessible to electrolyte during electrochemical tests and based on the fact that a nitrogen molecule is of similar size to a hydrated K^+ or OH^- ion [**19**], the latter explanation

was explored. It was proposed that the specific capacitance of an activated carbon could be written as the sum of the capacitances arising from micropore surfaces and from the remaining surface area, where different values of (*C*/*S*) apply to each region. This model provided a better fit to the experimental data and suggested that the double layer capacitance per unit of micropore surface area is of a similar value to that measured on the basal plane of graphite.

The results of this study also show that the testing conditions influence the findings greatly and require consideration before any conclusions can be drawn. Typically, the highest values of specific capacitance are observed at the lowest rates of charge and discharge, as there is a greater amount of time for ions to migrate to, and be optimally packed on the electrode surface. As the specific current increased the measured specific capacitance decreases, and this effect was more pronounced in activated carbons whose surface area originates mainly from micropores. In other words, the study concluded that larger amounts of charge could be accepted or released at high rates when activated carbons with a greater proportion of larger pores were used. This is seen in Figure 2.20 [**212**] where a predominantly microporous activated carbon (M-20) yields high amounts of charge stored at low rates and performance deteriorates rapidly with increasing current density, whereas a carbon with a larger average pore size (M-30) stores a greater amount of charge at current densities greater than 700 mA g^{-1}.

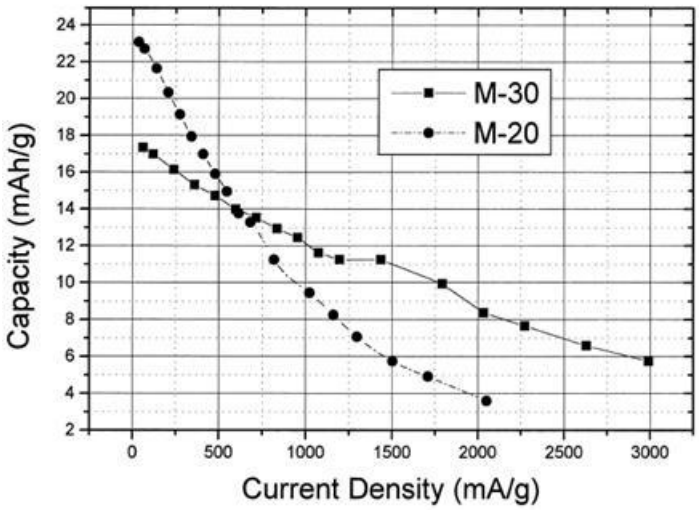

Figure 2.20: Charge stored against discharge current density for a microporous activated carbon (M-20) and mesoporous activated carbon (M-30) [212]

Activated carbons derived from bituminous coal were used to investigate the effects of changing 'nano-textural characteristics' on capacitive behaviour in aqueous and organic media [**213**]. Activated carbons were produced with BET surface areas between 800 and 3030 m^2g^{-1} and resulted in specific capacitances between 124 and 286 F g^{-1}. It was concluded that mean pore size was more important than specific surface area for enhanced specific capacitance, and the optimum pore sizes for aqueous and organic electrolytes were 0.7 and 0.8 nm respectively.

The narrow pore size distributions that are achievable using carbide-derived carbons were utilised in the determination of the mechanism by which micropores become accessible to ions [**165-168**]. An apparently anomalous increase in specific capacitance was found when the electrochemical behaviour of a carbon with a modal pore width of 1 nm using an organic electrolyte was compared to that of a carbon with a modal pore width of 2 nm [**165**]. This was attributed to the desolvation of ions upon entering the micropores. To confirm this supposition, ionic liquid electrolyte was combined with microporous carbide-derived carbons and studied in an attempt to match pore size to ion size [**167**]. When the average pore size was matched to ion size, a maximum specific capacitance of 160 F g^{-1} was obtained which was 40 F g^{-1} higher than that measured using an equivalent mesoporous material. This indicates that ion adsorption is achieved in a more efficient manner when average pore size is matched to ion size. It was established that as the average

pore size increased above the optimum, specific capacitance decreased and below the optimum pore width, ions were sterically hindered from entering the pores. This was confirmed by a different study that used microporous activated carbon with four IL electrolytes of varying cation size (0.8 - 2 nm) [**214**]. It was observed that specific capacitance decreased with increasing ion size, confirming the importance of the relationship between pore size and ion size in the determination of capacitor performance.

Traditionally, the most widely accepted EDLC model is based on the formation of a double-layer between planar electrodes and an electrolyte [**215**]. However, this model is insufficient where three-dimensional networks of interconnected pores are involved in the charge storage mechanism. In light of findings concerning the effect of pore size on capacitance a heuristic model that incorporates the effect of pore curvature on capacitance was proposed and was found to apply to carbons with unimodal pore size distributions [**216**]. This model assumes that in the macroporous region, curvature has negligible effect on the specific capacitance and the planar electrode model remains valid, as illustrated in Figure 2.21(a). In the mesopore region a different model is appropriate, that of an electric double-cylinder as shown in Figure 2.21(b). For micropores, it was proposed that the ions are aligned along the pore axis when the electrode is charged, producing an electric wire-in-cylinder capacitor which is a reduction of the double-cylinder model, where the inner cylinder diameter is defined by the ion size. This is illustrated in Figure 2.21(c).

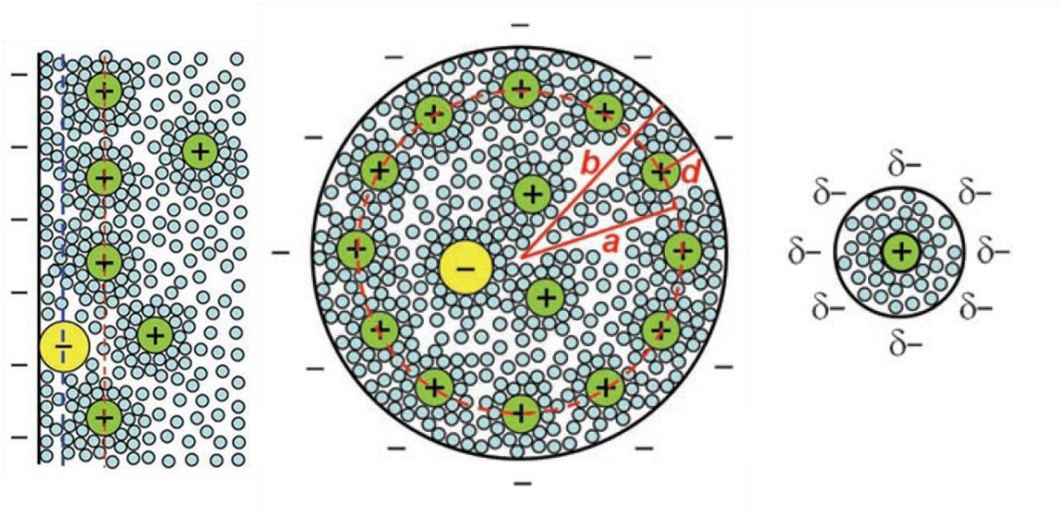

Figure 2.21: (a) an EDLC formed at the carbon/electrolyte interface (b) schematic of a negatively charged mesopore forming an electrical double-cylinder capacitor (EDCC) with radii *a* and *b* for the inner and outer cylinders respectively and (c) a negatively charged micropore of radius *b* with solvated cations of radius a_0 lining up to form an electric wire-in-cylinder capacitor (EWIC) [216]

In Figure 2.21 (a) the double-layer capacitance is found through the planar electrode relationship seen in Eq. 2.2.

$$C = \varepsilon_0 \varepsilon_r \frac{A}{d} \qquad \textbf{Eq. 2.2}$$

When the pore size is in the mesopore region, the capacitance is approximated by Eq. 2.9, where *a* and *b* represent the radii of the inner and outer cylinders respectively.

$$C = \frac{\varepsilon_0 \varepsilon_r \, A}{b \ln\left(b/a\right)} \qquad \textbf{Eq. 2.9}$$

For the smallest pores where solvated or unsolvated ions are positioned along the axis of the pore, Eq. 2.10 applies where a_0 represents the effective size of the counterions in the electrolyte.

$$C = \frac{\varepsilon_0 \varepsilon_r \, A}{b \ln\left(b/a_0\right)} \qquad \textbf{Eq. 2.10}$$

As indicated previously, porosity is not only an issue in defining capacitance but has ramifications for the power densities displayed by ECs. This is illustrated by the findings of a study that compared the values of specific capacitance obtained at high discharge rates with those measures at low rates for three templated carbons. Each of the template carbons exhibited a distinct pore regime; one carbon was exclusively microporous, another possessed mainly small mesopores (~3 nm) and the third primarily contained large mesopores (~16 nm) [**217**]. At low rates (*ca.* 1 mA cm^{-2}) all carbon samples had a specific capacitance of 200 F g^{-1}. However, as the rate increased, specific capacitance decreased in a different manner for each carbon. The microporous carbon showed a decrease in capacitance of 75%. For the carbon with small mesopores, the reduction in capacitance was lower but showed a continual decrease in capacitance with increasing current density. The carbon with larger mesopores reached a minimum value of 100 F g^{-1} at much lower current densities, and would continue to allow for higher discharge rates with no further deleterious effect on capacitance.

This discussion serves to highlight the complex relationship between the porosity of electrode materials and the energy/power densities of EC devices. It is evident that carbon materials with different pore characteristics respond to electrochemical tests in a different manner and in the investigation of electrode materials, this effect always requires consideration before any conclusions can be drawn.

In particular, normalisation of specific capacitances on the basis of surface area assumes that all surface area influences the capacitance in the same manner which has been shown not to be the case. Ideally, when comparing different electrode materials it is desirable for them to have the same surface area and pore size distribution, however this is very unlikely to occur in practice. Therefore, when experimental results require data normalisation, the uncertainty over the influence of different pore sizes can be reduced by ensuring that the materials possess as similar a surface area and pore characteristics as possible. Also, the microstructure of the carbon should be as similar as possible in order to negate the influence of different proportions of surface area arising from edge or basal plane regions.

In addition, if the surface area and pore size distribution of materials are similar, the addition of binder can be expected to influence each material in a similar manner and the amount of porosity that is not wetted by electrolyte can also be expected to similar for each sample. This reduces the degree of uncertainty regarding these factors in the analysis of electrochemical data.

2.7.4.12 Surface Functionality

Carbon has an amphoteric nature which results in a wide range of electrochemical behaviour from electron donor to acceptor state [**19**, **172**], and the presence of heteroatoms in graphene planes can affect the acid/base character of the surface by either donating electrons to or withdrawing electrons from the delocalised π-electrons associated with aromatic carbon [**218**-**220**].

2.7.4.12.1 Oxygen

After a high temperature process in the production of carbon materials there are residual surface bonds, unfilled valencies, which behave as reactive free radicals towards oxygen on exposure to the atmosphere. Many carbons contain regions that are graphitic on the microscopic scale, and the distinct properties of the planes present in graphite result in edge sites of the basal plane being substantially more reactive towards oxidation. As oxygen is bound primarily to the edges of graphitic planes the relative proportion is usually found to vary with the specific surface area of the material.

Some oxygen functionalities are electrochemically active, and when present on EC electrodes can contribute to the overall specific capacitance through pseudocapacitance. It has been estimated that in activated carbons pseudocapacitive reactions can account for 5 – 10% of the total capacitance [**10**]. The distinction between these charge storage mechanisms on plane surfaces is feasible using EIS, however in porous electrodes the electrochemical behaviour of the functional groups becomes intertwined with the effects of the pore network.

The reversible oxidation/ reduction of hydroquinone/ quinone groups at the edge of graphitic planes occurs in the presence of protons as illustrated in Figure 2.22.

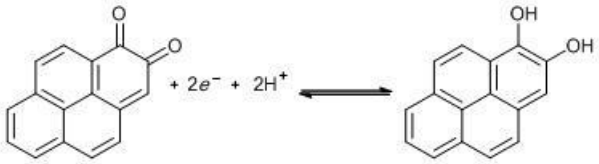

Figure 2.22: Redox reaction involving quinone/ hydroquinone groups

It can be seen that the pseudocapacitive contribution of this group has the potential to be quite significant as this mechanism permits the storage of one electron per oxygen group in comparison with the double layer mechanism that can store the equivalent of 0.18 electrons per carbon atom [**10**, **221**]. The presence of this pseudocapacitive reaction in acid electrolyte is characterised by a noticeable peak in cyclic Voltammograms centred at a potential of 0.55 V (*vs.* SHE), as shown in Figure 2.23, where the authors estimated that the contribution of quinone/ hydroquinone pseudocapacitance to the overall capacitance was estimated to be around 30% [**221**].

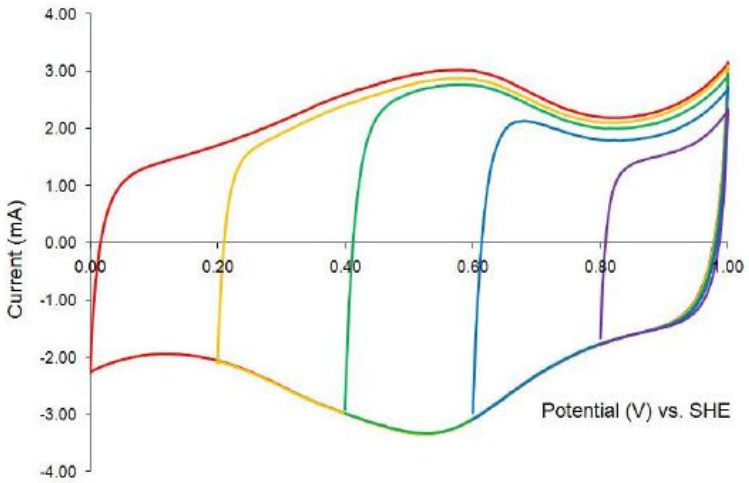

Figure 2.23: Cyclic Voltammogram of carbon cloth (Spectracorp 2225) in 1.0 M H_2SO_4 at 1 mVs^{-1} showing redox pseudocapacitance of quinone/ hydroquinone functional groups [221]

Other oxygen containing functional groups were found to participate in pseudocapacitive reactions, but to a much lesser extent than the quinone couple. For

example, the same study found that pyrone oxygen groups can be rendered electrochemically active in basic electrolyte after being subjected to electrochemical cycling in acidic electrolyte.

Carbon materials containing surface functional groups can also exhibit an acidic or basic character which influences the wettability of the electrode. An increased wettability is desirable for use in EC electrode carbons as this maximises the accessibility of electrode surface to electrolyte. The elemental composition of carbon blacks has been found to influence their wettability towards an external solvent. Carbon blacks with an oxygen content in the region of 1.0 – 15.0 wt.% were found to exhibit increased wettability (*i.e.* smaller contact angle with water) with increasing oxygen content [**222**]. It was also found that the residual hydrogen content has a negative effect on the wettability of the material. Another study found that electrochemical reduction of a carbon surface resulted in a decreased wettability [**56**].

However there is a major drawback associated with the inclusion of oxygen functional groups on EC electrodes, namely that a self-discharge mechanism is introduced to the system. Self-discharge is of practical importance in the design of ECs as it can have a detrimental effect on operating efficiency, energy and power density due to the additional hardware that may be required to provide a compensatory float current.

If impurities present in the EC materials undergo redox reactions in the operating potential range then the electrode becomes non-polarisable to a certain extent and is affected by an associated leakage current. In addition, oxygen can be reduced to produce H_2O_2 or HO_2^- which can then go on to act like a shuttle between the electrodes, where species react at one electrode, diffuse to the other electrode and are reduced or reoxidised, as indicated in Equation 2.11. This rapidly reduces the amount of charge stored in the cell [**10**].

$$O_2 + 2H^+ + 2e^- \rightleftharpoons H_2O_2 \qquad \textbf{Eq. 2.11}$$

Carbon materials that possess a higher concentration of acidic surface functional groups have been found to produce higher self-discharge rates [**223**]. Also, higher leakage currents have been observed in ECs using carbons with a larger oxygen content which suggests that oxygen functional groups catalyse surface redox and/or electrolyte decomposition reactions [**224**].

The presence of oxygen groups has also been found to correlate strongly with the degradation of capacitance and increased ESR seen after extended periods at the maximum operating voltage in propylene carbonate based electrolytes. Carbon materials with higher oxygen contents were found to evolve gas through the decomposition of electrolyte, possibly through overvoltage caused by an increased potential of zero charge [**22**, **225**].

2.7.4.12.2 Nitrogen

Nitrogen-enriched carbon materials have shown promise in several areas including CO_2 capture [**203**], hydrogen storage [**226**] and catalysis [**227**], and are usually produced by adding nitrogen to a carbon by treatment with ammonia or through the carbonisation of a nitrogenous precursor. In some cases nitrogen containing polymers are added to a carbon followed by subsequent heat treatment to introduce functional groups to the carbon surface.

With the beneficial effects of oxygen functional groups in carbon materials being known, the idea that similar effects (*e.g.* enhanced capacitance, increased wettability *etc.*) without the drawbacks can be induced by incorporating alternative heteroatoms is being widely explored. The most studied of these alternative heteroatoms is nitrogen, although others such as boron [**228**] have received some attention.

Different methods of producing nitrogen-enriched carbons for use in EC electrodes have been explored, with nitrogen being incorporated into carbon materials through thermal treatment with a mixture of ammonia and air [**229-234**] or through the controlled carbonisation of nitrogen containing organic compounds [**176, 209, 210, 235-249**].

The majority of investigations into the behaviour of nitrogen-enriched carbon materials as EC electrodes report a beneficial effect on capacitance resulting from the inclusion of nitrogen into the carbon structure. This is usually attributed to pseudocapacitance between nitrogen functional groups and electrolyte species [**147**], although this has not yet been confirmed [**245**]. As well as increasing the wettability of the surface of the carbon material, the addition of nitrogen is also thought to alter the electron donor characteristics of individual graphitic regions. The number and location of nitrogen heteroatoms in graphene planes has been shown to affect the energy levels of the highest occupied (E_{HOMO}) and lowest unoccupied (E_{LUMO}) molecular orbitals, and therefore on the band gap ($\Delta E = E_{HOMO} - E_{LUMO}$) and electron donor properties of the carbon [**218**-**220**].

A summary of several studies concerning nitrogen-enriched carbon materials and their application as EC electrodes, with a discussion of their results in light of recent findings, is given in the following section.

Ammoxidised Brown Coal [**229**]

Under the premise that pseudocapacitance arising from oxygen functionalities is limited to one electrode, and that oxygen groups are usually acidic in character, the addition of basic functional groups was investigated in an attempt to improve the performance of the whole EC cell. Nitrogen containing functional groups usually have an alkaline character and were added to demineralised brown coals through ammoxidation, which is a treatment at elevated temperature under the flow of an ammonia/air mix. The resulting nitrogen-enriched precursors were subsequently carbonised and activated, producing materials with BET surface areas in the range of 290 - 930 m^2g^{-1} and nitrogen contents between 0.0 wt.% and 13.2 wt.%

The specific capacitance of a sample containing 13.2 wt.% nitrogen and a surface area of 289 m^2g^{-1}, was 91 F g^{-1} in acidic electrolyte which is similar to the value obtained using a sample containing 0.0 wt.% nitrogen with a significantly larger surface area of 702 m^2g^{-1}. However, these samples are not directly comparable, as

the samples were obtained under significantly different synthesis conditions and have vastly different ash contents. The treatment temperature of carbon precursors can drastically alter the chemical structure of the carbon, especially with respect to the electrical conductivity of the resultant material.

Samples with a similar surface area (289 - 299 m^2g^{-1}) but different nitrogen content showed significantly different values of specific capacitance. These materials were produced under the same thermal conditions (700°C carbonisation) but different ammoxidation conditions, and indicated that an increase in nitrogen content resulted in a significant increase in specific capacitance. A sample possessing 9.2 wt.% nitrogen exhibited a specific capacitance of 29 F g^{-1}, whereas a sample containing 13.2 wt.% nitrogen displayed a specific capacitance of 91 F g^{-1} in acidic electrolyte. Nevertheless, these samples have significantly different compositions, especially a markedly different oxygen content.

The pseudocapacitive effect of oxygen functional groups is clearly seen on the cyclic Voltammograms presented for samples that had underwent steam activation when tested in acidic electrolyte. Notably, a sample produced using CO_2 as the activating agent did not show a similar pseudocapacitive peak, indicating that steam activation results in the formation of oxygen surface functional groups. However it is not clear to what extent the overall value of specific capacitance is enhanced by oxygen related pseudocapacitance.

The specific capacitance of a material containing 3.2 wt.% nitrogen was almost double that of a sample containing no nitrogen but also possessed a 15% larger micropore volume and 10% larger surface area. The authors acknowledged that the pore structure of the materials studied has an effect on the capacitive performance as the highest specific capacitance was attributed to "the evolution of a beneficial pore structure" in the sample *i.e.* interconnected pores with sufficient mesoporosity to facilitate electrolyte access.

This study concluded that nitrogen content affects the capacitive performance of carbon and activated carbon materials, however no clear trend between nitrogen content and capacitance was observed. From this study it can be seen that the

specific capacitance of nitrogen-enriched carbons is dependent on many factors and decoupling the effects of individual parameters is problematic, but suggests that the presence of nitrogen in carbon EC electrodes is advantageous.

Also, activated carbons produced from coal precursors typically have a broad pore size distribution and highly variable composition, including minerals ('ash') that may be electrochemically active. A more homogenous carbon precursor, such as carbides or polymers, would be more suitable for the investigation of the effects of functional groups. It is also evident that the use of steam as an activating agent, although practical, complicates the interpretation of electrochemical measurements by imparting oxygen functionalities on the carbon surface.

Ammoxidised Cellulose Fibres [**230**]

A further study treated cellulosic fibres using the same ammoxidation process and addressed some of the issues discussed above. However, the ammoxidation process, as well as steam activation, results in the inclusion of oxygen functional groups which are likely to have a much greater influence on the character of the surface than that of nitrogen groups. The main aim of this study was to investigate the effects of nitrogen addition at different stages of the carbon production process and considered the importance of the binding state of the nitrogen atoms in the carbon structure.

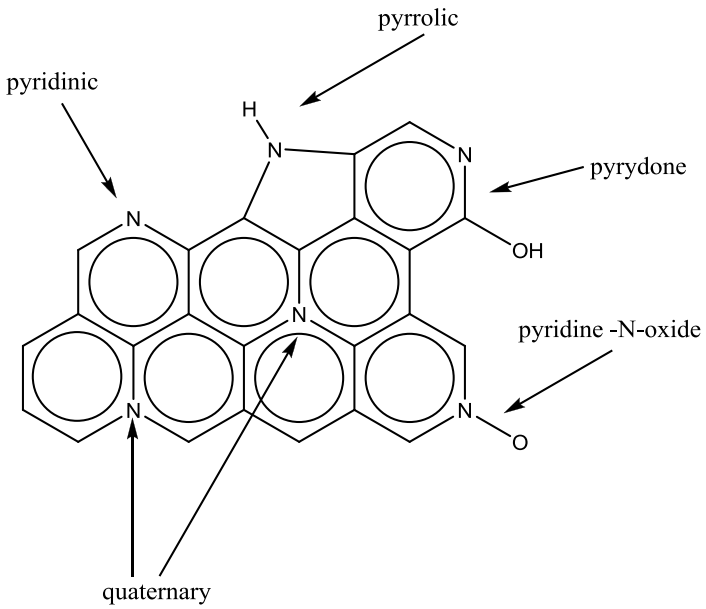

Figure 2.24: Distribution of nitrogen atoms in a graphene plane

Nitrogen added at relatively low temperatures (*ca.* 250°C) binds to the edges of graphene sheets, and at temperatures greater than 410°C can be incorporated into the graphene rings. Figure 2.24 shows that edge sites occupied by nitrogen can result in pyridinic, pyrrolic and N-oxide groups [**230**]. It was envisaged that nitrogen present on the edges of sheets would specifically interact with electrolyte ions and augment double layer capacitance with pseudocapacitive charge storage, whereas nitrogen incorporated into the graphene structure would influence the electron density, and therefore electrochemical behaviour, of the bulk material. When nitrogen is included in the graphene planes ('quaternary' in Figure 2.24), the location of atoms in relation to the graphene planes can result in electron donor behaviour which contributes to the amount of delocalised π-electrons.

XPS data showed that similar nitrogen groups were present in materials that underwent a high temperature step after ammoxidation. The spectra contained significant contributions from pyridine and pyridone/ pyrrole groups, which showed that the nitrogen atoms were incorporated into aromatic rings. In a sample that was ammoxidised after both carbonisation and activation of the fibres, the spectra is of a substantially different shape with no nitrogen present in aromatic groups and the

binding energies associated with imine, imide/ amide/ amine and ammonia groups were evident.

Nitrogen adsorption isotherms show that ammoxidised materials have a reduced porosity and smaller surface area than an untreated sample subjected to the same carbonisation and activation methods. This is caused by heteroatoms blocking and narrowing pores which also hinders the removal of the vapours that evolve on further heating. The reduced surface areas can be expected to reduce the contribution of the double layer effect to the specific capacitance of ammoxidised carbon materials.

The non-ammoxidised sample possessed the highest BET surface area (1020 m^2g^{-1}) but did not display the highest specific capacitance. A value of 144 F g^{-1} was obtained using EIS at 1 mHz in 4 M H_2SO_4, which equates to a surface area normalised specific capacitance of 14.4 µF cm^{-2}.

Rather than being evidence that ammoxidation has a beneficial effect on capacitance it is likely that this value is lower than expected due to incomplete electrochemical utilisation of the carbon surface, an effect which is more pronounced in carbons where a large proportion of surface area arises from micropores. The authors did not mention how carbon materials were prepared for electrochemical testing however it is highly likely that a polymer was used to produce a mechanically stable composite electrode and enhanced values of surface area normalised capacitance are an artefact of the electrode manufacture process. This could be attributed to some of the surface area not being accessible to the electrolyte, an effect which is more extensive when polymer binder is added to carbons that are predominantly microporous.[1]

It was reported that ammoxidation of the cellulose fibres prior to carbonisation and activation had little effect on specific capacitance. This was ascribed to an

[1]RF xerogel derived activated carbon with a surface area of 1120 m^2g^{-1} and micropore volume of 0.462 cm^3g^{-1} produced an electrode of surface area 470 m^2g^{-1} and micropore volume of 0.221 cm^3g^{-1} when mixed in an 80/10/10 weight ratio of sample/kynar/carbon black. Carbon materials of lower surface area (1090 and 840 m^2g^{-1}) and lower micropore volume (0.298 and 0.254 cm^3g^{-1}) produced electrodes with greater specific surface areas 630 and 520 m^2g^{-1} using the same process, indicating that a larger degree of micropores are occluded by polymer binder and that there is not a simple relationship between sample surface area and electrode surface area [**195**].

"inadequate" number of carbonyl or carboxyl groups to accompany the nitrogen groups imparted during ammoxidation. It should be noted however that this material had a substantially reduced surface area in comparison with the non-ammoxidised sample, and when specific capacitance values are normalised based on surface area, an increase of roughly 40% is observed.

By ammoxidation of the char and subsequent activation, an increase in specific capacitance is observed. (The surface area normalised capacitance is 28% greater than that of the non-ammoxidised sample.) The authors associated the increased capacitance with a "balanced" amount of electron donor/acceptor groups however in comparison with the other ammoxidised samples the most notable differences are the higher surface area and surface oxygen content. The surface area normalised capacitance is lower in comparison to the other ammoxidised samples which may again be due to incomplete wetting of the electrode surface as this material has a significant degree of surface area arising from microporosity.

In a sample that was ammoxidised after carbonisation and activation of the fibres, the specific capacitance was the lowest of all samples tested. This sample has the lowest surface area of 585 m^2g^{-1} and can be expected to produce the smallest specific capacitance from double layer capacitance. In addition, it was stated that this material would not store a great deal of energy through pseudocapacitance due to the smaller number and less favourable composition of oxygen groups. In cyclic Voltammograms no peaks associated with quinone redox reactions are observed with this sample, but are seen at roughly 0.2 V (*vs* Hg/Hg_2SO_4) in samples displaying a larger amount of carbonyl groups. When the surface area normalised specific capacitance is taken into consideration, this sample is comparable to the sample ammoxidised before carbonisation and activation (*i.e.* the sample with the highest value of surface area normalised capacitance). As was previously mentioned, the binding states of the nitrogen heteroatoms in this sample were substantially different to those seen in other ammoxidised samples, and nitrogen groups were concentrated mainly on the edge of graphene planes where interactions with electrolyte ions can contribute to the specific capacitance. No noticeable deviations from the rectangular cyclic Voltammograms produced by a purely double layer capacitive mechanism

were observed, the presence of which would signify the presence of a pseudocapacitive charge storage mechanism associated with non-aromatic nitrogen groups.

This study shows that nitrogen groups are frequently accompanied by oxygen functional groups on the surface of a material and it is difficult to quantify the effect that each heteroatom has on the electrochemical behaviour of such materials.

Ammoxidised Hard Coal [**231**]

Hard coals treated using ammoxidation were used to create carbon materials that were tested as both the positive and negative electrode in three electrode cells using 7 M KOH and 4 M H_2SO_4 electrolytes. In acid electrolyte, all electrode materials produced higher specific capacitances when operating as the positive electrode. The enhanced capacitance observed in alkaline electrolyte when working as the negative electrode was attributed to the small size of the K^+ ion.

Discerning between samples of different porosity and chemical composition is not possible by considering only the value of capacitance obtained at low frequency therefore this study used 'capacitance-frequency spectra' to explore the possibility that the dynamics of the charging process may be altered by the presence of nitrogen species.

Charge exchange dynamics of nitrogen containing materials as positive electrodes in acidic electrolyte were found to improve with increased nitrogen content, *i.e.* higher values of specific capacitance are obtained for any given frequency. As with the previous study, materials that had been ammoxidised after carbonisation and activation contain nitrogen groups of substantially different character in comparison to samples that are heat treated after ammoxidation, (imine, imide, amine, amide, lactam *etc.*). This may be reflected in the capacitance frequency spectra as this material performs in a similar manner to the unammoxidised sample in acidic electrolyte.

Substantial differences in the capacitance frequency spectra were seen between the samples that were ammoxidised prior to carbonisation and activation depending on the temperature of the ammoxidation step. When ammoxidation was carried out at 300°C, the resultant material contained 1.1 wt.% nitrogen whereas at 350°C, the material contains 1.4 wt.% nitrogen. The specific capacitance obtained under all conditions was larger for the material obtained at the higher ammoxidation temperature despite having a slightly smaller surface area, as well as substantially better performance at higher frequencies in acidic electrolyte.

Mica Template [**235**]

Another method of producing nitrogen containing carbon materials uses an expandable mica template to induce a structure on carbon precursors. By using quinoline or pyridine to swell the mica template, materials with different nitrogen contents were produced and were found to have an unusual structure. SEM images reveal that the carbons were disc shaped and consisted of a very thin film surrounded by a thicker rim. Despite having a relatively low specific surface area (87.5 m^2g^{-1}) the carbon derived by carbonisation of templated quinoline at 750°C produced an appreciable specific capacitance of over 100 Fg^{-1} in 1 M H_2SO_4. An even larger specific capacitance of 156 F g^{-1} was exhibited by pyridine derived carbon (83.0 m^2g^{-1}) synthesised at the same temperature. These equate to surprisingly large values of surface area normalised specific capacitance in the range of 115 - 188 µF cm^{-2}, which is over ten times the values usually seen when using porous carbons [**10**, **56**, **212**]. The difference in specific capacitance between these materials was attributed to the substantial difference in their nitrogen content. Elemental analysis shows that the quinoline derived carbon contained 10 wt.% nitrogen whereas the pyridine derived carbon included 18 wt.% nitrogen.

In an effort to explain these values of specific capacitance arising from apparently low surface area materials, the possibility of redox reactions between the electrolyte and nitrogen surface groups (*i.e.* pseudocapacitance) was considered but no characteristic peaks were evident on cyclic Voltammograms. The possibility of

several indistinct pseudocapacitive peaks combining to form a rectangular Voltammogram (in a manner similar to RuO_2 [**10**]) was proposed.

The notion that the surface area of the electrode may have increased due to swelling in the presence of electrolyte was also considered, however no evidence of this was observed. Additionally, the idea that electrode wettability is improved by the presence of nitrogen functional groups was offered as a reason for the enhanced capacitance of carbon materials enriched with nitrogen.

From this study it was suggested that the presence of nitrogen in a carbon material enhances specific capacitance per unit surface area, although the mechanism by which this occurs is unclear.

A similar synthesis procedure using melamine was used to study the electrochemical behaviour of nitrogen-enriched electrode materials in a range of electrolyte solutions [**209**, **238**]. Melamine was polymerised with formaldehyde in the presence of an expandable fluorine mica template to give a nitrogenous carbon precursor. By using different carbonisation procedures, materials with a nitrogen content in the region of 7 - 30 wt.% exhibiting specific surface areas between 17 m^2g^{-1} and 442 m^2g^{-1} were produced. As with the previous study using quinoline and pyridine, the melamine derived materials produce large values of specific capacitance per unit surface area, with a maximum of 366 μF cm^{-2} being reported.

The low yield of the carbonisation process was increased by roughly 10 wt.% at any given carbonisation temperature by prior oxidative stabilisation of the polymer at 250°C. Stabilisation was also found to yield materials containing a greater degree of nitrogen, and a larger fraction of pyridinic nitrogen species. Samples that were not stabilised before carbonisation generally have a larger degree of porosity and greater surface area than stabilised samples.

The sample displaying the highest surface area produced the highest value of specific capacitance, emphasising the fact that surface area is of critical importance in carbon electrodes for electrochemical capacitors.

Gravimetric capacitance values of stabilised samples are similar to, and in some cases larger than, those obtained with unstabilised samples despite the sizeable reduction in surface area caused by oxidative stabilisation. When the surface area normalised capacitance for these materials is considered, unstabilised samples display values between 78 - 366 µF cm^{-2} whereas the values obtained using stabilised samples are smaller and less variable (46 - 63 µF cm^{-2}). This appears to indicate that the presence of nitrogen increases the specific capacitance per unit surface area of electrode materials; however, this interpretation assumes that no electroactive oxygen moieties were present in the sample.

The precursor material can be expected to contain a significant amount of oxygen from the ether bridges created during polymerisation and unfilled valencies produced during carbonisation and acid washing, which can become oxygen groups on exposure to the atmosphere. It can also be expected that stabilised samples would contain more residual oxygen after carbonisation, however no quantification of oxygen content was reported and the presence of oxygen functional groups on the material does not seem to have been considered.

Cyclic Voltammograms were presented for samples carbonised at 750°C although only over a limited range of 0 - 0.5 V (*vs* Ag/AgCl) and at a very low sweep rate of 0.1 mV s^{-1}. These cyclic Voltammograms are reproduced in Figure 2.25 [**209**].

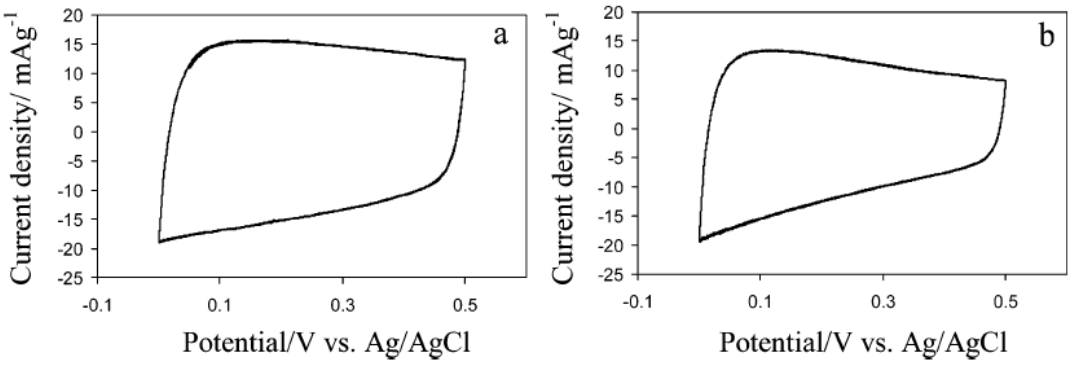

Figure 2.25: Cyclic Voltammograms of melamine-formaldehyde derived carbons produced at 750°C in 1 M H_2SO_4 at 0.1 mV s^{-1}. (a) Precursor was not oxidatively stabilised (b) Precursor underwent stabilisation prior to carbonisation.

For both samples, the Voltammogram deviates from the typical rectangular shape in two aspects: a broad peak on the upper portion and a significant slope on the lower portion. The peak has a maximum value at a potential of 0.1 - 0.2 V (*vs.* Ag/AgCl) for both stabilised and unstabilised samples, although the peak (and slope in the lower portion) is more pronounced in the stabilised sample, Figure 2.25(b). The unstabilised sample was reported to have a surface area of 442 m^2g^{-1} and N/C ratio of 0.20 (from XPS) and the stabilised sample had a surface area of 256 m^2g^{-1} and N/C ratio of 0.34.

The indistinct peak is possibly associated with the quinone/hydroquinone redox reaction, and is more pronounced in the stabilised sample (which could be expected to have a larger oxygen content). The slope that appears under negative polarisation could be attributed to electrode resistance/leakage current as the measurements were performed at a very low sweep rate. In a later publication [**238**] the resistance of each electrode was measured and the stabilised sample was found to have a resistance approximately 30% larger than the unstabilised sample, which corresponds with a steeper gradient on the cyclic Voltammogram.

The initial study concluded that enhanced values of capacitance in sulphuric acid electrolyte are associated with pseudocapacitance arising between nitrogen species (especially pyridinic nitrogen groups) and protons from the electrolyte. However, on closer inspection it appears that several unconventional experimental and analytical methods were used in these studies that may have affected the interpretation of the results. Surface areas were calculated from nitrogen adsorption data using the subtracting pore effect method (SPE) [**250**] which is based on a high-resolution α-plot method [**251**]. In the α-plot method, the experimental isotherm is compared with the isotherm obtained using a non-porous sample of the same chemical composition. The material used for comparison was a commercial carbon black (Mitsubishi #32) which has a significantly different chemical composition (*i.e.* no nitrogen content), as well as a significant surface area of 69-83 m^2g^{-1} [**252**, **253**]. The SPE method was proposed as method to allow for the over estimation of surface area by the BET model (due to micropore filling) and is applicable to materials with a surface area greater than 2000 m^2g^{-1}. The application of this method to the

materials under study is questionable as the results indicate that the surface areas are substantially lower than 2000 m^2g^{-1} and in some cases lower than that of the 'non-porous' sample used as a reference material.

In the subsequent report [**238**] the electrochemical behaviour of the same materials were evaluated in potassium hydroxide solution and an organic electrolyte ($TEABF_4$ in PC), as well as being physically characterised further. CO_2 adsorption at 298K was carried out to investigate the microporous nature of several samples. The higher analysis temperature used in CO_2 adsorption (in comparison with nitrogen adsorption) enhances adsorbate diffusivity, and it was expected that even the smallest pores would be accessible to the adsorbate. Higher values of micropore volume were recorded for all samples when using CO_2 rather than nitrogen as an adsorbate, which was attributed to the presence of ultramicropores (width less than 0.7 nm) in the sample. However it is possible that specific interactions between the adsorbate and functional groups complicate the interpretation of experimental isotherms.

The resistances of melamine derived carbons prepared using both stabilised and unstabilised samples at temperatures of 750°C, 850°C and 1000°C were evaluated. For materials produced at the same temperature, stabilised samples display higher values of resistance. Also, resistance decreases with increasing carbonisation temperature which could be attributed to several factors (i) decreasing porosity of the material (ii) possible increase in degree of graphitisation and (iii) decreasing heteroatom content.

In KOH electrolyte, samples that were not stabilised prior to carbonisation produced larger values of specific capacitance when compared with values obtained using H_2SO_4 electrolyte. The opposite is true for samples that were oxidatively stabilised, which indicates that the charge storage mechanism present is affected by the stabilisation process. As there is little difference in the binding state of nitrogen species due to stabilisation, it is unlikely that these groups are responsible for the difference in behaviour.

The large values of surface area normalised capacitance for these materials achieved in KOH, as with the values obtained in H_2SO_4, were given as proof that

pseudocapacitance contributes significantly to the overall specific capacitance. It was also proposed that the interactions between nitrogen functionalities and H_3O^+ ions are stronger than those with K^+ and that these interactions determine the overall capacitance.

From these results it was concluded that nitrogen-enriched carbons from melamine resins show good capacitive behaviour in KOH electrolyte despite the lack of protons that were previously considered to be responsible for enhanced capacitance.

Pitch/Polymer [**176**, **236**]

Coal tar pitch (CTP) blended in different fractions with nitrogenous polymers was used as an activated carbon precursor to investigate the role that nitrogen plays in the electrochemical behaviour of carbon EC electrodes. Polyacrylonitrile (PAN) and oxidised poly(4-vinylpyridine) cross-linked with divinylene benzene (PVPox) were co-pyrolysed with CTP to produce carbon materials with BET surface areas between 747 m^2g^{-1} and 1420 m^2g^{-1}, and nitrogen contents between 1.9 wt.% and 7.2 wt.%. The pH of the surface was found to increase in proportion with the nitrogen content of the material varying between pH = 7.4 at 1.9 wt.% nitrogen to pH = 9.3 at 7.2 wt.%.

Carbon materials were tested using cyclic Voltammetry, EIS and constant current charge/discharge with the same trends in capacitance values being observed using each method. Electrochemical behaviour was investigated in two different electrolytes, namely 1 M H_2SO_4 and 1 M TEA BF_4 in PC. With the exception of the material derived from PVPox, the specific capacitance of the materials increases with nitrogen content in acid electrolyte. (The PVPox derived material had a BET surface area at least 500 m^2g^{-1} greater than any other sample, and can be expected to display a substantial double layer capacitance.) These samples were said to have comparable microtextural properties as the proportion of micropore volume to total pore volume and BET surface areas were similar. However absolute values of the pore volumes were not reported and the structural properties of the material cannot be assumed to

be identical due to the vast differences in the chemical composition of the precursor blends. It is also worthwhile to note that the materials underwent steam activation which imparted varying degrees of oxygen functionality onto the carbon surface (up to 7.2 wt.%) and could therefore contribute to the overall specific capacitance through pseudocapacitance to an unknown degree for each sample. In fact the oxygen content rises in tandem with the nitrogen content, therefore any increase in capacitance observed could equally be attributed to the oxygen content.

It was proposed that the larger values of specific capacitance in 1 M H_2SO_4 was due to an enhanced wettability of the carbon surface as previously proposed [**176**, **231**, **236**] and that reactions between the electrolyte and nitrogen functionalities introduced a Faradaic component to the overall specific capacitance. Specifically, redox reactions involving pyridinic nitrogen were indicated as a possible source of pseudocapacitance. Further publications [**147**, **176**] discussing the same results introduced a few reaction mechanisms between protons and nitrogen functional groups bound to a graphene plane, especially that between a pyridinic nitrogen functionality and protons which could possibly account for the increased specific capacitance value of nitrogen enriched carbons.

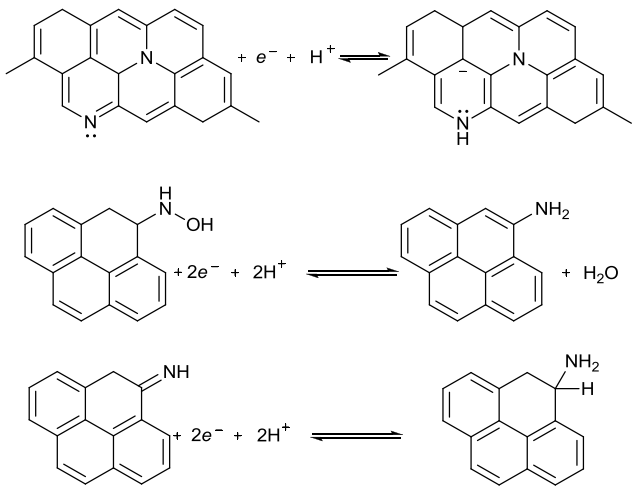

Figure 2.26: Redox reactions of nitrogen functional groups. (Aromatic rings indicate a larger 'graphene' network)

Cyclic Voltammograms recorded at different scan rates of the PAN derived material (nitrogen content 7.2 wt.%) in 1 M H_2SO_4 are presented in Figure 2.27 [**176**] and show a fairly rectangular form at a scan rate of 2 mV s^{-1}. This form becomes more skewed when the direction of the sweep rate was switched at increased sweep rates.

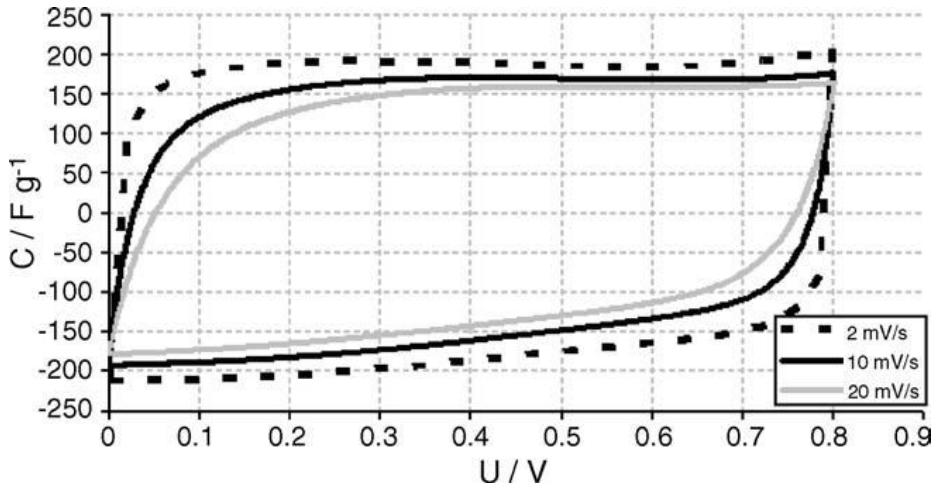

Figure 2.27: Capacitor performance of PAN derived carbon using cyclic Voltammetry at three different rates in 1M H_2SO_4 [176]

This limitation at higher load was cited as "proof that faradaic reactions connected with the nitrogen functionality" were involved. In light of the fact that there is a significant amount of oxygen on the sample surface (almost identical to the atomic concentration of nitrogen) it is possible that the effect seen on the CVs is due to an increase in the internal resistance and exacerbation of the non-ideal behaviour under polarisation of the interphase due to oxygen functionalities [**22**] which is supported by the same effect being observed in the aprotic organic medium. This effect was seen to increase with the oxygen content in the study of oxidised activated carbon fabrics [**224**].

Furthermore, no appreciable peaks that could be attributed to a reaction were evident on the CVs (except from a slight deviation at 0.1 - 0.2 V, seen in the same region for two electrode capacitors in other studies which could be attributed to the quinone/hydroquinone couple).

Electrospun PAN [**244**]

Porous nitrogen-enriched carbon materials were produced from an electrospun polyacrylonitrile (PAN) paper and tested as EC electrodes. Carbon materials produced in this manner require no binder or conductive additives to manufacture mechanically strong electrodes, which is beneficial in the production of devices with a high power density. By altering the activation temperature used in synthesis, carbon materials with nitrogen contents between 3.3 wt.% and 12.3 wt.% were produced. However, this also resulted in different textural properties being exhibited by each material which again complicates the interpretation of electrochemical results. Initial tests indicated that results from materials activated at 700°C and 800°C were highly influenced by the resistance of the materials which could be attributed to the larger values of nitrogen content, or differences in material structure. Therefore comparisons between two highly conductive materials were drawn over a series of electrochemical tests. An activation temperature of 900°C produced a material of specific surface area 365 m^2g^{-1} and a nitrogen content of 6.9 wt.% whereas a temperature of 1000°C produced material with a surface area of 705 m^2g^{-1}. (Surface areas were determined by the BET method using nitrogen adsorption data, and elemental analysis was conducted using XPS.) Moreover, these samples contained a similar amount of oxygen which allows for the assumption that any pseudocapacitive effects associated with oxygen functionalities would contribute to a similar extent in each sample.

Cyclic Voltammetry was carried out in 1 M H_2SO_4 and 6 M KOH and both samples performed similarly, producing larger values of specific capacitance in the alkaline electrolyte. Although the surface area of the sample activated at 900°C is roughly half that of the sample treated at 1000°C, similar values of specific capacitance were obtained in both electrolytes. It was assumed that if charge storage occurred only due to the double layer mechanism, a substantial difference in the values of specific capacitance would be observed and therefore the specific capacitance of the sample activated at 900°C included a significant pseudocapacitive component arising from the higher nitrogen content. The higher specific capacitance values obtained for both

samples in KOH seems to imply that nitrogen functionalities are more electrochemically active in basic electrolyte.

Nyquist plots for both samples in KOH and H_2SO_4 electrolyte were obtained and compared with an equivalent circuit consisting of an equivalent series resistance, double layer capacitance, Faradaic charge leakage and Warburg element (*i.e.* Randles' circuit [**10**, **254**]). In both electrolytes the Warburg element was found to influence the impedance over a wider frequency range for the sample activated at 900°C, with the largest effect being seen in KOH. This was correlated with the increased pseudocapacitive contribution to specific capacitance by nitrogen functional groups and it was asserted that the Warburg impedance region is associated with Faradaic reactions and 'kinetic leakage processes in the diffusion line'. On the other hand the behaviour of a porous electrode can be modelled by a transmission line and there is a significant difference in the pore characteristics of each sample. The sample activated at 1000°C has a micropore volume of 0.28 cm^3g^{-1} and a mesopore volume of 0.22 cm^3g^{-1} whereas the sample activated at 900°C has a significantly less porous structure exhibiting smaller volumes of 0.17 cm^3g^{-1} in the micropore region and 0.10 cm^3g^{-1} in the mesopore region.

It was also stated that the low frequency behaviour seen in the Nyquist plot was evidence that the entire surface area of the electrode was wetted by the electrolyte solution, however this is usually associated with the degree of electrode polarisability. It is possible that a substantial degree of microporosity is not fully wetted by electrolyte, an effect which would be more pronounced in the electrodes treated at 1000°C, which could account for the similarity in specific capacitance values between the two samples.

From the XPS quantification, larger amounts of pyrrolic, pyridonic and pyridinic groups present on the carbon surface were found to correspond to larger values of surface area normalised capacitance in agreement with the findings of previous studies.

The performance of the electrodes at high rates was investigated through Galvanostatic cycling between current densities of 50 mA g^{-1} and 50 A g^{-1}. Both

samples show typical behaviour with rate by exhibiting the highest values of specific capacitance under low charging current and fairly constant values are attained for charging currents greater than 1 A g^{-1}. As with the cyclic Voltammetry results, higher values of capacitance are achieved in basic electrolyte (*ca.* 175 F g^{-1}) in comparison with those using acid electrolyte (*ca.* 140 F g^{-1}). A Ragone plot showing the results of Galvanostatic cycling at different rates was presented that showed little loss in power density over the 1 – 10 s time scale. It is likely that this is due to the exceptional conductivity of the carbon fibre electrodes which is not inhibited by polymer binder and the intraparticle resistances associated with powder based electrodes. Extended Galvanostatic cycling over 5000 cycles at 1 A g^{-1} showed approximately 5% loss in the value of capacitance in KOH, whereas a loss of at least 10% was seen in acid electrolyte.

The materials were also tested using an organic electrolyte (1 M TEA BF_4 in acetonitrile) and a substantial difference their response to cyclic Voltammetry was observed. The specific capacitance of the sample activated at 900°C was negligible in comparison with the 100 F g^{-1} displayed by the more porous sample that was activated at 1000°C. In organic electrolyte it is assumed that double-layer charging is solely responsible for the specific capacitance as there are no free protons available to take part in pseudocapacitive reactions.

In short, this paper indicates particularly good cycling performance and enhanced specific capacitance of carbons enriched with pyrrolic, pyridonic and pyridinic nitrogen groups in KOH electrolyte.

Activated Carbon/(melamine or urea) [**210**]

Wood derived activated carbon was oxidised and treated with melamine or urea before further carbonisation to produce materials with varying amounts of surface functional groups. These materials contained nitrogen in the region of 0.2- 8.0 wt.%, had BET surface areas between 721 m^2g^{-1} and 2176 m^2g^{-1} and were used to study the effect of surface chemistry on the performance of carbons as EC electrodes.

‘As received’ carbon and oxidised carbon samples were tested as EC electrodes however the cyclic Voltammograms obtained show erratic capacitive behaviour. It is likely that the structure of the material changed significantly during thermal treatment at 950°C to produce a more conductive material. The use of wood derived activated carbon also introduces impurities into the material as the ash content could be as large as 2.0 wt.%, and a significant phosphorous content that could affect the electrochemical performance of the material was reported [**210**].

It was found that a larger amount of nitrogen was incorporated into the material when the precursor had previously underwent oxidation with nitric acid, and melamine was found to affect the residual nitrogen content to a greater extent than urea, but also had a greater effect on the pore characteristics of the material. Oxidised carbon was found to have a surface pH of 3.26 due to the increase in acidic surface groups and removal of basic groups. After treatment with melamine or urea, similar types of functional groups are formed although in different proportions. Melamine treatment resulted in a higher proportion of pyridinic groups than pyrrolic/ pyridinic groups when compared to treatment with urea.

To investigate the effect of surface chemistry and porosity, the results were analysed by considering the ‘nitrogen indices’ of the sample. Nitrogen indices were calculated by multiplying the proportion of each nitrogen-species by the total nitrogen content obtained from XPS deconvolution and dividing the result by a measure of surface area. This provides an indication of the surface density of specific functional groups and allows for the identification of the influence that each functional group has on the specific capacitance of the material.

Nitrogen indices were then plotted against the ‘volumetric capacitance’ which was determined by dividing the specific capacitance by the volume of the micropores. Volumetric capacitance is perhaps a more useful measure of the energy storage capability of porous electrode materials as this gives an indication of the efficiency of space utilisation, but by only considering the volume of micropores, a significant volume is ignored. A more appropriate volume to evaluate the capacitance with would be the total pore volume added to the volume occupied by the electrode matrix, *i.e.* the bulk volume of one electrode.

Also, by normalising the data on one axis with respect to micropore volume and by normalising the other axis with respect to BET surface area, the data is still affected by the pore characteristics of the material. For example there can be expected to be a good correlation between the BET surface area (a component of the N-indices) and the micropore volume (used in the calculation of 'volumetric capacitance').

From the plots of 'N-indices' *vs* 'Volumetric capacitance' it was stated that N-X and N-Q have the most pronounced effect on capacitance at high currents which was unexpected as the majority of reports attribute enhanced capacitive behaviour due to reactions involving pyridinic and pyrrolic species. The high positive charge on the nitrogen atom in these groups [**255**] was proposed as a possible reason for the changes in electrochemical behaviour, specifically by assisting in electron transfer through the electrode matrix. However it is noted that the sum of the N-Q and N-X type groups follows the same trend as the concentration of pyridinic groups which show a significantly better correlation with surface area normalised capacitance. It is therefore possible that the observed behaviour is not due to the N-Q and N-X groups but is rather a consequence of pyridinic nitrogen groups.

Through consideration of the electrochemical behaviour at different currents it was concluded that the capacitances consist of a contribution from the double-layer mechanism and a contribution from pseudocapacitance. It was argued that the formation of a double-layer is suppressed at high currents and that the contribution to capacitance through the double-layer mechanism reduced with increasing current. However it could be argued that the converse is true as the time required to form a double-layer can be expected to be shorter than the time required for charge to migrate towards and cross the interphase.

A similar technique using coconut shell derived activated carbon [**245**] was used to further investigate the importance of nitrogen functional groups in the electrochemical performance of EC electrodes, and also to consider the effects of oxygen functional groups imparted during synthesis. Materials with a nitrogen content up to 4.1 wt.% and surface areas in the region of 730 - 900 m^2g^{-1} were produced. As with the previous studies [**209**, **238**] a larger amount of nitrogen was

incorporated into oxidised precursor materials, and melamine was found to influence the residual nitrogen content to a greater extent than urea.

An interesting difference between the studies is seen in the electrochemical behaviour of the carbon samples that were oxidised but not subjected to any further heat treatment. In the case of the wood derived material a substantially reduced capacitance was observed in comparison with the other samples whereas the coconut shell derived carbon gave capacitance values significantly greater than the other samples. For wood derived carbons, the poor capacitance was attributed to a large electrical resistance arising from a relatively high oxygen content. On the other hand, the coconut shell derived carbon has a lower oxygen content and it was postulated that the structure of this material is more aromatic, and therefore more electrically conductive, when compared to the wood derived carbon. Therefore a large pseudocapacitive contribution to the specific capacitance was associated with the latter material and was confirmed by cyclic Voltammetry where a peak centred at 0.4 V (*vs* Ag/Ag^{+}) is clearly seen. (This is illustrated by the dashed line 'S-O' in Figure 2.28 [**245**].)

'N-indices' as well as oxygen indices were calculated in a similar manner to the previous study although a differential surface area, ΔS, was used. This was defined as the difference between the surface area obtained by the BET equation (presumably using a nitrogen adsorption isotherm) and the surface area from CO_2 adsorption measurements. The physical significance of this quantity was assumed to be equal to the surface area of pores larger than 10 Å where surface functional groups were assumed to be localised. N-and O- indices were then plotted against the specific capacitance divided by ΔS ($C_{\Delta s}$), which would imply that either all capacitance originates from pores larger than 10 Å, or that the contribution from these pores is a constant despite being present to varying extents in each sample.

By comparing how $C_{\Delta s}$ varied with different combinations of surface functionality 'indices' it was concluded that phenol and ether groups are not electrochemically active in acidic electrolyte. $C_{\Delta s}$ was found to increase linearly with the sum of the indices arising from pyrrolic, pyridinic, and quinonic groups. The indices of N-Q

and N-X and their effects on $C_{\Delta S}$ were found to be in agreement with the previous study, and it was suggested that the resistance of electrode carbons could be reduced by adding a controlled amount of these entities.

The cyclic Voltammograms obtained from nitrogen enriched carbons lacked the presence of any redox peaks that could be associated with pseudocapacitance as shown in Figure 2.28 [**245**].

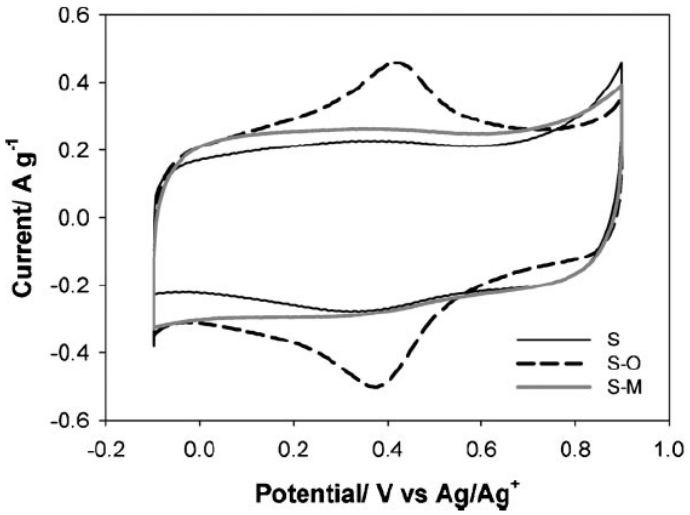

Figure 2.28: Cyclic Voltammograms of activated carbon (S, Calgon S208), oxidised carbon (S-O) and melamine treated carbon (S-M) in 1 M H_2SO_4 at 5 mVs^{-1} [245]

Summary

To summarise, various methods have been used to produce suitable nitrogen-enriched carbon materials for EC electrodes, but the interpretation of electrochemical data is influenced by differences in surface area and pore characteristics that inevitably accompany the addition of nitrogen groups. An increase in the surface area normalised capacitance with increasing nitrogen content is usually attributed to three factors; pseudocapacitance through redox reactions, enhanced electron conduction through the material and an increased electrochemical surface area. To date, there has not been an appropriate method to estimate the surface area that is in contact with electrolyte, and it is generally assumed that the surface area determined from nitrogen adsorption isotherms provides an accurate reflection of this parameter.

The contribution that the electron donor effect has on the specific capacitance of carbon materials is difficult to determine as it depends on the nitrogen content, the distribution of nitrogen atoms, and the size of the graphitic regions in which they are located [**218-220**, **234**].

Different reactions through which charge transfer with nitrogen functional groups can occur have been proposed, but it has been noted that these mechanisms have not been confirmed experimentally. The absence of any peaks during cyclic Voltammetry experiments indicates that any pseudocapacitive contribution is independent of the potential across the cell. However for this to be the case, the voltages over which several reactions occur would be required to overlap, and moreover, the pseudocapacitance from each reaction would have to superimpose perfectly to produce a consistent contribution towards the specific capacitance. This behaviour is exhibited somewhat by RuO_2, where it is thought that at least three reactions overlap within the operating range of the EC [**10**], and noticeable deviations from the ideal rectangular cyclic Voltammograms are still seen. It is more likely that a different mechanism, probably related to the double-layer mechanism, is responsible for the enhanced values of surface area normalised capacitance seen in nitrogen-enriched carbons.

It is noted that reports frequently use the term "pseudocapacitance" to account for any values of surface area normalised specific capacitance greater than that usually associated with double-layer charging (assumed to be 10 - 30 μF cm^{-2}) whereas it strictly refers to a change in the rate of charge acceptance with changes in potential [**10**]. There is clearly some uncertainty over the role of nitrogen atoms in nitrogen-enriched carbon electrodes and the materials and techniques currently used to investigate this topic may be inadequate.

The process of nitrogen enrichment usually has a detrimental effect on the evolution of porosity and specific surface area, and frequently a complicated relationship between the nitrogen content and pore characteristics exists. In order to decouple the effects that surface area, porosity and nitrogen content have on the specific capacitance of nitrogen-enriched carbon materials, a process that could produce materials with the same surface area, pore and structural characteristics, but a different chemical composition would be desirable. It is also evident that the influence of oxygen functional groups complicates the interpretation of electrochemical behaviour as the quinone/hydroquinone reaction can provide a large contribution to the overall specific capacitance. Therefore any materials used to investigate the electrochemical behaviour of nitrogen-enriched carbons would ideally exhibit no pseudocapacitive contribution from oxygen functionalities.

Nitrogen-enriched carbons through co-carbonisation

Nitrogen-enriched carbon materials have been produced by a different procedure where a polymeric precursor is simultaneously carbonised alongside a nitrogen-containing organic compound that has been impregnated throughout the structure of the precursor [**203**, **227**]. This method has been used to produce materials in the investigation of nitrogen functional groups with respect to their catalytic activity [**227**] and in the field of CO_2 capture [**203**]. Carbon materials containing up to 10 wt.% nitrogen with surface areas in the region of 300 - 400 m^2g^{-1} were produced by 'co-pyrolysis' of *m*-phenylene diamine (*m*PDA) and a phenol-formaldehyde resin. Previous investigations into the catalytic activity of nitrogen-enriched carbons were

hindered by the presence of mineral matter, which was avoided in this investigation through the use of a polymeric carbon precursor. The structure of *m*PDA is shown in Figure 2.29 and was chosen as the nitrogen source due to the presence of an "aromatic ring that should easily get involved in ring condensation" during the carbonisation process. *m*PDA contains approximately 26 wt.% nitrogen, and the nitrogen content of the final material was controlled by adjusting the mass fraction of *m*PDA added to the carbon precursor. The catalytic activity in the reduction of NO with NH_3 was found to correlate well with the surface nitrogen content of the carbon materials.

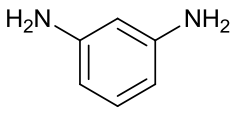

Figure 2.29: Structure of *m*-phenylene diamine (*m*PDA)

A subsequent study into the use of nitrogen-enriched carbon materials as an adsorbent for CO_2 capture used resorcinol-formaldehyde xerogels as the carbon precursor due to the ease with which different pore structures can be imparted on the resultant carbon. Initially, amines were used as a catalyst in the synthesis of the RF gels in an effort to incorporate nitrogen groups into the structure, however this only resulted in *ca.* 0.4 wt.% nitrogen being found in the carbon materials [**203**]. Therefore, simultaneous carbonisation of the RF gels impregnated with suitable nitrogen-containing compounds was explored as a method produce suitable nitrogen-enriched carbon materials for study.

In this case, *m*PDA as well as diphenylenimine (DPI) was added to the gels after drying, and underwent simultaneous carbonisation to create a range of materials with varying structural characteristics and nitrogen contents (up to 7 wt.%). As with previous studies it was found that as the mass fraction of nitrogen precursor was increased, the surface area of the materials decreased due to the blocking of pores. In addition, *m*PDA was found to enrich the nitrogen content of the resultant materials to a greater degree than DPI.

2.7.5 Objectives

Investigations into the use of nitrogen-enriched carbon materials in EC electrodes indicate a beneficial effect of nitrogen-enrichment on the specific capacitance of EC electrodes, however the extent of any improvements in comparison with conventional carbon materials is uncertain, and the mechanisms through which any benefits arise have yet to be fully elucidated.

From the preceding discussion of the related literature it is clear that investigations into the electrochemical behaviour of nitrogen-enriched carbon materials are complicated by several related factors. The aim of this work was to clarify the role that nitrogen groups play in the storage of charge in ECs by decoupling the capacitive contribution from nitrogen groups with that from oxygen groups, and also from the effects of changing the pore characteristics and specific surface area of the carbon electrode materials.

The use of different physical and electrochemical characterisation techniques could hopefully provide some insights into the mechanisms by which nitrogen groups enhance the specific capacitance of carbon materials, and indicate if there is any practical benefit to using these materials in high-power EC electrodes.

As RF gels have a pore structure that can be controlled easily through the synthesis conditions and the nitrogen content of the materials can be tailored through simultaneous carbonisation with *m*PDA, this was seen as a convenient method to create various nitrogen-enriched carbon materials with no electrochemically active oxygen groups for use in EC electrodes.

3 Characterisation

In this work various methods were used to investigate and characterise electrode materials for use in ECs. These can broadly be separated into the physical/ chemical and electrochemical characteristics of each material and the following section introduces some of the theory behind each technique.

Nitrogen adsorption data has been used to estimate the specific surface area and porosity of the materials, which has been compared with the results from small-angle neutron scattering experiments. Also, the skeletal density of some carbon materials was determined using helium pycnometry. Thermal Gravimetric Analysis (TGA) was used to develop a suitable method to produce porous carbons and to determine the amount of ash contained in the samples.

The chemical composition of the materials was determined using combustive elemental analysis which was compared with the results obtained using X-ray photoelectron spectroscopy (XPS). The use of XPS allowed the chemical composition of the surface layer of the sample to be determined and the types of functional groups present to be identified and quantified.

Electrochemical characterisation was carried out to investigate the use of the carbons in EC electrodes. Electrochemical Impedance Spectroscopy (EIS) was used to determine the specific capacitance and resistances associated with cells using the materials. The complementary techniques of Galvanostatic cycling and cyclic Voltammetry were also used to develop an understanding of how the physical/chemical characteristics of the materials influence their electrochemical behaviour in EC cells that use aqueous electrolytes.

3.1 Physical/ Chemical Characterisation

3.1.1 Nitrogen adsorption/ desorption

Gas adsorption measurements are useful in the determination of the surface areas and pore size distributions of porous solids. In this work, nitrogen adsorption data has been used to characterise the carbon materials produced. Many different treatments of adsorption data are available to characterise porous materials, with non-local density functional theory (NLDFT) being regarded as state of the art [**256**]. The nuances of different NLDFT treatments complicate comparisons between findings and more established data treatments allow for direct comparison with the relevant literature.

The well known Brunauer-Emmett-Teller (BET) equation [**257**] is widely used to evaluate the specific surface areas of electrode materials in ECs, and is a useful tool that allows for comparisons to be easily made. The Barrett-Joyner-Halenda (BJH) method [**258**], an extension of the Kelvin equation, has been used to define the pore size distribution of carbon materials in the mesopore range. In the course of this research it became apparent that a more detailed analysis of the micropores present in the samples would be necessary, requiring the use of the Dubinin-Astakov [**259**] treatment of a low-pressure adsorption isotherm.

Adsorption is defined as the enrichment of a component in the interfacial layer between a gas and solid. In the context of adsorption the free gas is referred to as the *adsorptive* and the solid under study as the *adsorbent*. The interfacial layer is thought to comprise of two layers, the *surface* layer and the *adsorption space*, which is a volume that can be occupied by the adsorptive. When the gas is in the adsorbed state it is referred to as the *adsorbate*. In addition, *adsorption* is used to describe the accumulation of adsorptive in the interfacial layer whereas *desorption* is used to describe a decrease in the total quantity of adsorbate in this layer [**170**].

The adsorption of a gas can occur due to *physisorption* or *chemisorption*. Chemisorption involves a transfer of electrons between the adsorbate molecule and sample surface, whereas physisorption occurs purely due to van der Waals' forces.

Chemisorption is therefore limited to a single layer of adsorbed molecules on the adsorbent surface while multiple layers of adsorbate molecules are formed during physisorption. These mechanisms can be differentiated between based on their heats of adsorption, as chemisorption usually has a significantly greater associated energy than that of physisorption (although an exception to this may be found when studying molecular sieves). As chemisorption occurs due to chemical reactions, there is an activation energy required for adsorption to occur and there may be an increase in the amount of adsorbed gas with increases in temperature. Physisorption is a reversible and spontaneous mechanism where the heat of adsorption is of similar magnitude to the latent heat of condensation of the adsorbate.

In the case of physisorption (which occurs when nitrogen is adsorbed on porous carbons) the specific amount of gas adsorbed is a function of the system temperature, *T*, pressure, *P*, and interaction potential between the adsorbent and adsorptive, *E*. This is indicated in Eq. 3.1. The amount of gas adsorbed, *W*, is expressed as the mass of adsorbate per gram of adsorbent, however this is also frequently expressed as a volume of gas (at STP) adsorbed per gram of adsorbent [**260**].

$$W = f(T, P, E) \qquad \textbf{Eq. 3.1}$$

The interaction potential *E* is a measure of the resultant force of attraction between adsorbent and adsorptive, and is also dependent on the extent of adsorption. In the case of physical adsorption, the interaction potential is dominated by the attractive dispersion forces that arise due to the synchronisation of the oscillating dipole moments of molecules in close proximity (*London forces*). Other forces affecting the interaction potential include ion-dipole, ion-induced dipole, dipole-dipole, and quadrapole interactions; these forces are similar to those that result in the condensation of vapours.

3.1.1.1 Potential Theory

The potential theory of adsorption [**171**, **261**, **262**] considers an adsorbed molecule to be compressed by the forces of attraction acting from the surface into the surrounding space. When the space above the surface of an adsorbent is thought to consist of a number of 'surfaces' of equal adsorption potential, an adsorbed molecule is considered to be confined to the volume between the adsorbent surface and the equipotential surface where the adsorption potential is zero. Therefore, the interaction potential field varies with the geometric and chemical nature of the adsorbent.

In porous materials the potential fields from the pore walls combine to produce an appreciably larger adsorption potential, and this effect increases when potential fields overlap in smaller pores as illustrated in Figure 3.1 [**263**].

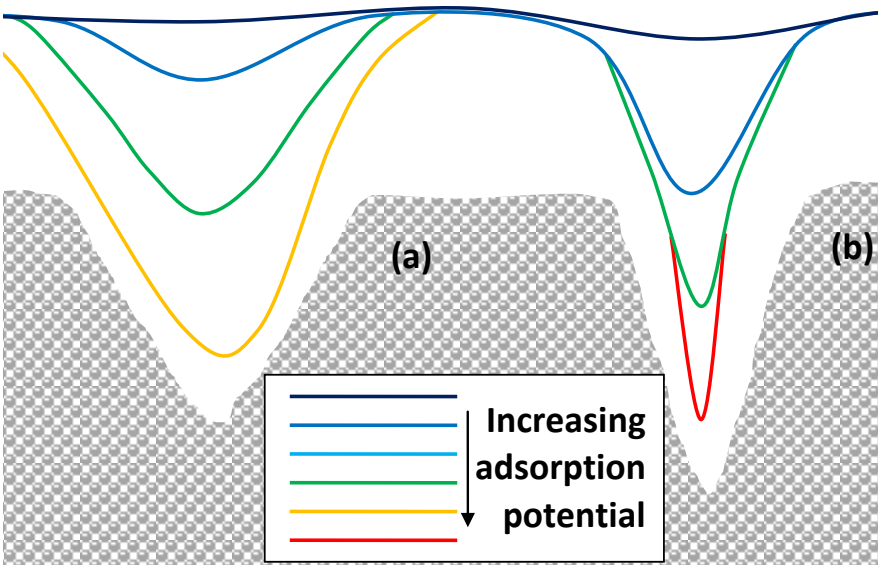

Figure 3.1: Adsorption potential fields (a) increasing near a pore and (b) overlapping in a narrow pore

When using gas adsorption to characterise porous materials it is usual to maintain a constant temperature and measure the amount of gas adsorbed by the sample over a range of pressures; a plot showing how the amount of adsorbate varies with pressure is known as an *adsorption isotherm*. The system pressure is more usefully expressed as a *relative pressure* (P/P_0), as shown in Eq. 3.2, where P_0 is the saturation vapour pressure of the adsorbate at the system temperature, T.

$$W = f(P/P_0)_{T,E} \qquad \textbf{Eq. 3.2}$$

3.1.1.2 Adsorption Mechanisms

Isotherm plots are unique for each system under consideration and can be classified according to their shape. The type of isotherm gives an indication of the adsorption processes involved, which can be categorised as *monolayer adsorption*, *multilayer adsorption*, *capillary condensation* and *micropore filling* [**170**].

Monolayer adsorption is defined as occurring when the entire adsorbent surface is covered by a layer of adsorbate molecules, each of which is in contact with the solid surface. The *monolayer capacity* is defined as the quantity of adsorbate required to form a single complete layer of adsorbed molecules and can be used to estimate the surface area of the adsorbent by considering the cross-sectional area of an adsorbed molecule.

When the adsorption space has the capacity for more than a monolayer of adsorbate and all adsorbed molecules are not in direct contact with the adsorbent surface *multilayer adsorption* is said to have occurred. Adsorbents frequently support multiple layers of adsorbate at some adsorption sites before completion of a single layer of adsorbate is in contact with the adsorbent surface. Figure 3.2(a) represents monolayer adsorption and Figure 3.2(b) represents multilayer adsorption.

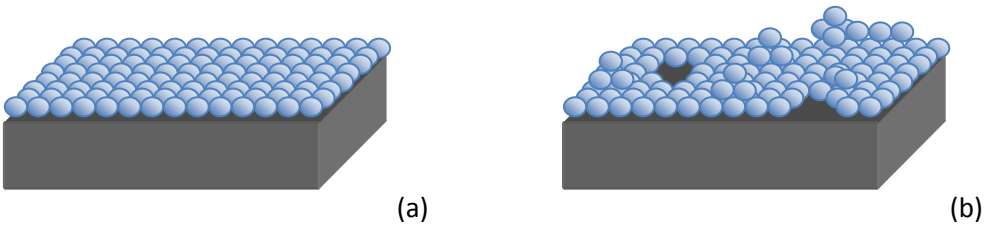

Figure 3.2: Adsorption on a plane surface (a) monolayer adsorption and (b) multilayer adsorption

Capillary condensation occurs after multilayer adsorption has taken place and adsorbate occupies the remaining pore space, separated from the adsorptive by menisci. When adsorption occurs by this mechanism the adsorption and desorption isotherms are found to differ (*hysteresis*). This is illustrated in Figure 3.3 (a) and (b). Figure 3.3(a) represents a cylindrical pore during the adsorption process where multilayer adsorption has taken place. The red line indicates the region available for adsorptive molecules to enter the adsorption space and be adsorbed. Figure 3.3(b) represents the same pore during the desorption process where capillary condensation has occurred, in this case the red line indicates the region available for molecules to leave the adsorption space and be desorbed. The difference in these adsorption and desorption 'areas' results in different rates for the respective processes, and is seen as hysteresis loops on the isotherm plot.

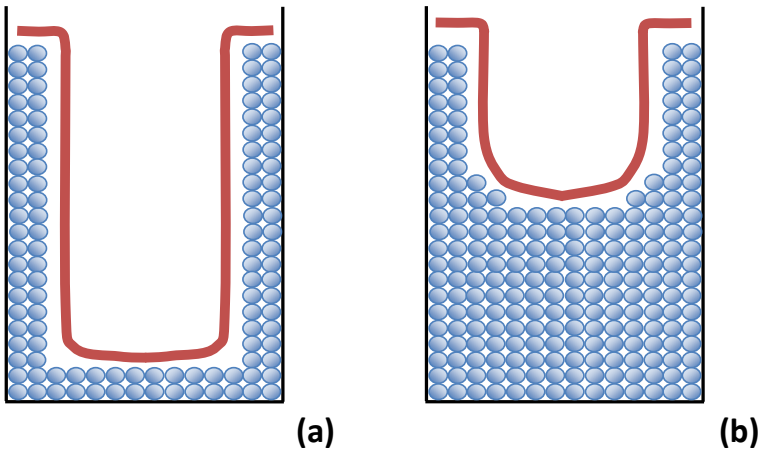

Figure 3.3: Capillary condensation (a) during adsorption (b) during desorption. (The red line is indicative of the surface area available for adsorption/desorption processes to occur)

Micropore filling describes the process that occurs when the diameter of a pore is too small for a meniscus to be formed. In the micropore range, adsorption cannot be described in terms of adsorbed layers, as tight packing of molecules is hindered by the pore walls. As a result, the surface area associated with micropores cannot be reliably determined by considering the cross sectional area of an adsorbed molecule.

The type of adsorption processes that occur are indicative of the pore structure possessed by the adsorbent, and the form of the adsorption isotherm can give an indication of the types of adsorption process taking place. Commonly encountered isotherm forms are shown in Figure 3.2 [**170**].

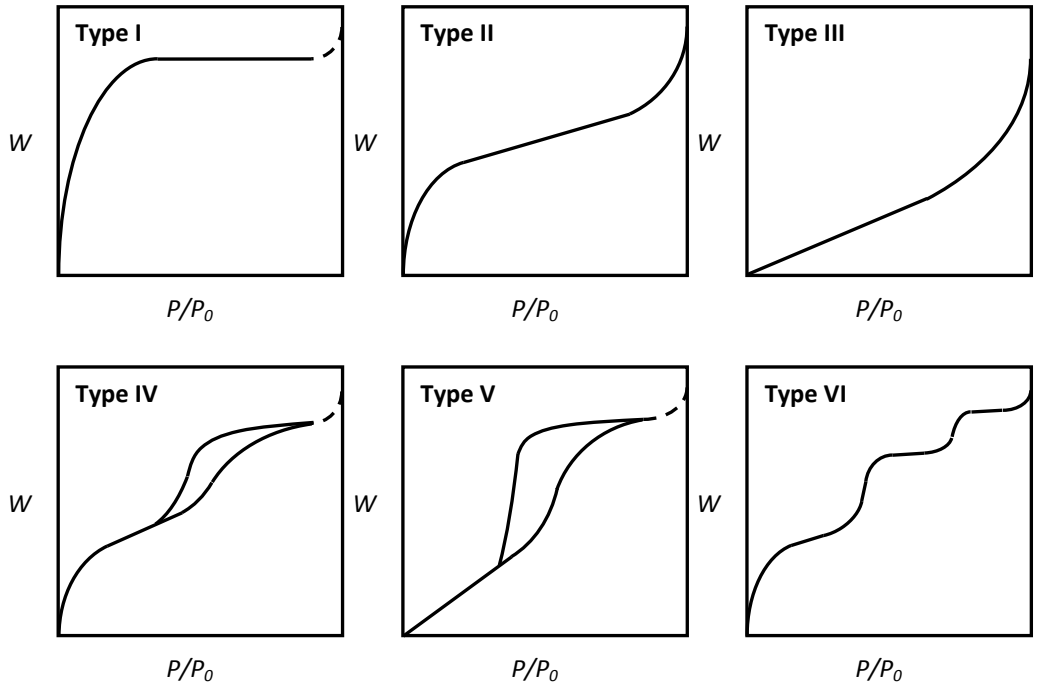

Figure 3.2: Adsorption isotherm classification. *W* represents the mass of adsorbate and P/P_0 is the relative pressure.

The first five types of adsorption isotherm in Figure 3.2 were defined by Brunauer, Deming, Deming, and Teller (BDDT) [**264**] by considering many experimental isotherms. Type I isotherms are reversible and approach a limiting value as the equilibrium relative pressure approaches the saturation pressure of the adsorbate. Isotherms of this type are obtained when the sample possesses a large degree of micropores (*e.g.* zeolites, certain porous oxides) as the limiting factor for adsorption

is the micropore volume rather than internal surface area [**170**]. Chemisorption processes also produce Type I isotherms as adsorption only occurs on active surface sites.

Type II isotherms are also fully reversible and are observed when the adsorbent is non-porous. This type of isotherm occurs due to both monolayer and multilayer adsorption, with the shift towards multilayer adsorption being indicated by the point of inflection on the isotherm.

Type III isotherms are uncommon and are produced when the interactions between adsorbate and adsorbed molecules are stronger than those between the adsorbate and adsorbate. This type of isotherm does not permit a reliable estimate of surface area or pore size distribution to be made [**251**].

Type IV isotherms are characterised by the presence of a hysteresis loop where the adsorption and desorption isotherms differ significantly. At low relative pressures the isotherm takes the form of the Type II isotherms, indicative of the presence of micropores, where the point of inflection is associated with monolayer coverage. Deviations from Type II behaviour occur at higher pressures where capillary condensation takes place, producing the hysteresis loop, and a limiting amount of adsorption is observed when the relative pressure approaches unity. This type of isotherm is indicative of an adsorbent possessing micropores and mesopores.

Type V isotherm is also characterised by a hysteresis loop; however it is more closely related to a Type III isotherm where the interactions between adsorbate molecules are stronger than the adsorbent-adsorbate interactions. As with Type III isotherms, this type of adsorption behaviour is seldom observed in practice [**170**].

Type VI isotherms are uncommon but were added to the BDDT classification system to allow for the formation of adsorbate layers on a non-porous, energetically uniform adsorbent. The formation of each layer is represented by a step on the isotherm with increasing relative pressure.

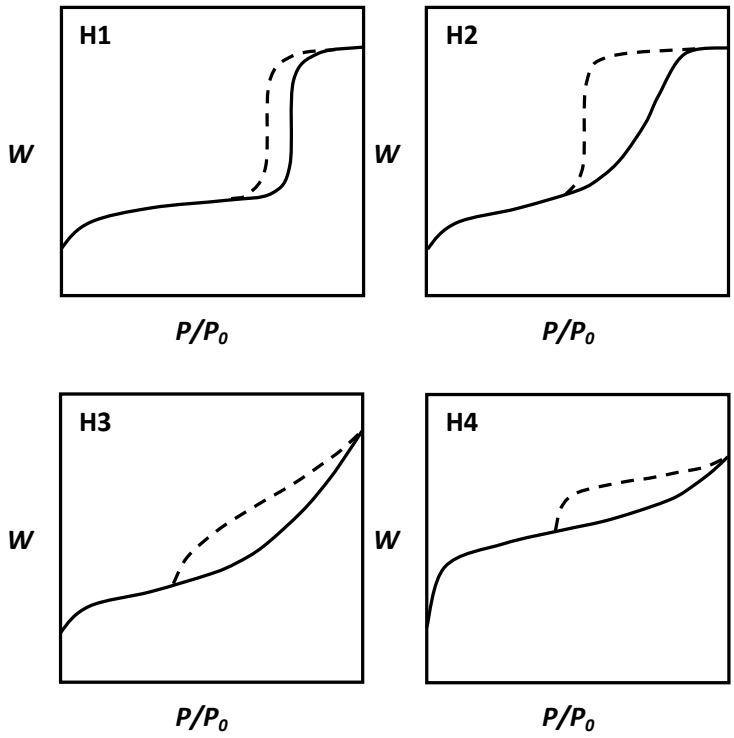

Figure 3.3: Hysteresis loop classification. *W* represents the mass of adsorbate and P/P_0 is the relative pressure.

The dashed line in isotherms of Types I, IV and V shows an increase in the amount adsorbed as the adsorbate pressure approaches the saturation vapour pressure of the adsorbate.

Different forms of hysteresis loop are associated with the Type IV and V isotherms and occur due to the difference in adsorption and desorption behaviour of capillary condensation in mesoporous solids. The relative pressure at which the desorption curve meets the adsorption curve is dependent on the adsorptive and occurs at *ca.* 0.42 when using nitrogen at 77K [**170**]. Hysteresis loops have been categorised into four main types, illustrated in Figure 3.3 [**170**].

Type H1 loops are associated with a small range of relative pressure, whereas H4 loops are spread over a relatively broad range. H2 and H3 loops can be considered as intermediate forms of the H1 and H4 loops. The different types of loop have been found to be associated with specific features of the porous materials being studied. H1 loops are associated with agglomerates of relatively uniform spheres with a narrow pore size distribution. H2 loops are frequently obtained and have been

ascribed to the presence of 'ink-bottle' pores (see Figure 2.16) however it has also been proposed that a network of interconnected pores may result in the same type of hysteresis. Type H3 loops show no limiting uptake as the pressure approaches saturation and have been proposed to result from slit-shaped pores that arise due to plate-like particles, and H4 loops are similar but associated with narrower slit-shaped pores.

3.1.1.3 Surface Area Determination

The Brunaeur-Emmett-Teller method is a commonly applied technique used in the determination of the surface area associated with porous solids. The BET method is an extension of the Langmuir theory which relates the coverage of molecules on a solid surface to the pressure of a gaseous adsorptive above the surface at a fixed temperature *i.e.* an adsorption isotherm.

The derivation of the Langmuir equation is based on several simplifying assumptions; namely, that the adsorbate covers the surface up to a complete monolayer, each adsorption site on the surface has equivalent energy and can only accommodate one adsorbed molecule, the adsorption of a molecule does not prevent a molecule being adsorbed at an adjacent site and there are no lateral interactions between adsorbed molecules.

3.1.1.3.1 Langmuir Adsorption Theory [265, 260]

The Langmuir theory is based on the kinetic theory of gases under the assumption that the rates of adsorption and desorption of molecules are equal at equilibrium. A derivation of the Langmuir equation is given in Appendix B, which can be rearranged to yield Eq. 3.3.

$$\frac{P}{W} = \frac{1}{\kappa W_m} + \frac{P}{W_m} \qquad \textbf{Eq. 3.3}$$

Applying Eq. 3.3 to an experimental isotherm allows for the determination of the mass of adsorbate in a complete monolayer, W_m, because a plot of P/W against P produces a linear slope of gradient $1/W_m$ with an intercept of $1/\kappa W_m$ (where κ is a constant).

The surface area of the adsorbent, S, can then be calculated as the product of the number of molecules in a saturated monolayer, N_m, and the apparent cross-sectional area of a single adsorbate molecule, σ, as shown in Eq. 3.4 where N_A represents Avogadro's constant and M the molecular weight of the adsorbate.

$$S = N_m\sigma = \frac{W_m N_A \sigma}{M} \qquad \textbf{Eq. 3.4}$$

When nitrogen is used as the adsorptive at a temperature of 77K, it is generally assumed that the cross sectional area, of an adsorbed molecule is equal to that of nitrogen in the liquid state (*i.e.* σ = 16.2 Å^2).

The Langmuir theory can be applied to Type I isotherms, but does not allow for multilayer adsorption or capillary condensation, and overestimates the surface area of adsorbents displaying other forms of isotherm. It should also be noted that the relationship in Eq. 3.4 relies on the assumption that there is a uniform packing of the adsorbate molecules and that the apparent cross-sectional area of a single adsorbate molecule is a constant in the system.

3.1.1.3.2 Brunauer-Emmett-Teller Theory [257, 260]

The BET method follows on from the Langmuir theory by allowing for the formation of multiple layers of adsorbate, under the assumption that the top layer of adsorbed molecules is in equilibrium with the adsorptive. Similar assumptions to those made in the Langmuir method are maintained (*i.e.* an energetically uniform surface, no lateral interactions between adsorbed molecules *etc.*) although the inclusion of multilayer adsorption required a few more assumptions to be made. Specifically, it

was assumed that the energy associated with adsorption in layers not in direct contact with adsorbent is a constant, and is equal to the heat of condensation as the molecules were deemed to be sufficiently far from the surface to be considered as being in the liquid state.

A summary of the BET method is given in Appendix C, which can be summarised by the linear form of the BET equation, given in Eq. 3.5. As with the Langmuir equation (Eq. 3.3) W_m represents the mass of adsorbate in a monolayer and W represents the mass adsorbed at a pressure of P. P_0 represents the saturation pressure of the adsorptive (P/P_0 is referred to as the relative pressure) and C is the BET constant.)

$$\frac{1}{W\left(\left({}^{P_0}/_{P}\right)-1\right)}=\left(\frac{1}{W_mC}+\frac{(C-1)\left({}^{P}/_{P_0}\right)}{W_mC}\right) \qquad \textbf{Eq. 3.5}$$

From this equation, a plot of $1/W[(P_0/P)-1]$ against P/P_0 (known as a BET plot) yields a straight line over a discrete range of relative pressures. The slope of the line from the BET plot, s, and the intercept, i, are then used to solve for the mass of an adsorbed monolayer, W_m, and the BET constant, using Eq. 3.6 and Eq. 3.7.

$$W_m=\frac{1}{s+i} \qquad \textbf{Eq. 3.6}$$

$$C=\frac{s}{i}+1 \qquad \textbf{Eq. 3.7}$$

The calculated mass of an adsorbed monolayer can then be used to obtain the total surface area using Eq. 3.4 (the same relationship used with the Langmuir equation). The fact that monolayer coverage may not occur but the amount of adsorbate in a theoretical monolayer can be calculated using the BET method enables the surface area of porous solids that do not display Type I isotherms to be quantified.

Typically, when an adsorption isotherm is expressed as a BET plot, a straight line is obtained for relative pressures between 0.05 and 0.35. Deviations from linearity at low relative pressures can occur due to the presence of very high adsorption potentials associated with microporous adsorbents [**260**].

3.1.1.4 Pore Size Characterisation

3.1.1.4.1 Barrett-Joyner-Halenda Method [258]

The Barrett-Joyner-Halenda (BJH) technique is a method that can be used to analyse the pore size distribution in materials that exhibit mesoporosity. This technique considers a pore that has been filled through capillary condensation to consist of two distinct regions, which is illustrated in Figure 3.4 where multilayer adsorption occurs on the pore walls, and condensation occurs in the remaining space ('inner capillary volume').

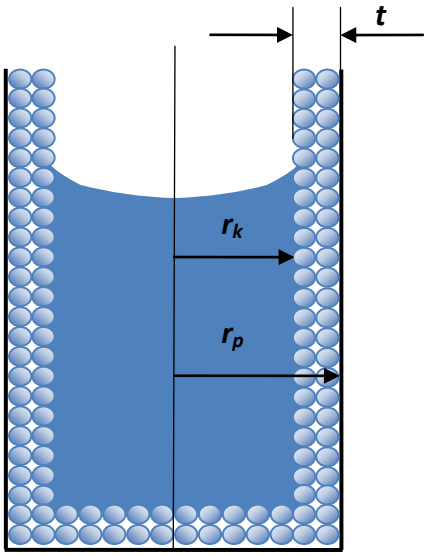

Figure 3.4: Capillary condensation within a cylindrical pore. *t* represents the multilayer adsorption thickness, r_p is the pore radius and r_k is the inner capillary radius.

The thickness of the adsorbed layer, *t*, can be calculated using a statistical models of the forms proposed by Halsey (Eq. 3.8 [**266**]) or Harkins and Jura [**267**] and, the

inner capillary volume is then assumed to behave according to the Kelvin equation [**268**]. In Eq. 3.8 the parameters *A*, *B*, and *C* represent adsorbate dependent constants that have been determined experimentally.

$$t = A\left[\frac{B}{\ln\left(\frac{P}{P_0}\right)}\right]^C \qquad \textbf{Eq. 3.8}$$

In this work, where nitrogen is used as the adsorbate, the Halsey equation takes the form shown in Eq. 3.9, and the thickness has units of Ångstroms.

$$t_{[\text{Å}]} = 3.54\left[\frac{5}{\ln\left(\frac{P}{P_0}\right)}\right]^{\frac{1}{3}} \qquad \textbf{Eq. 3.9}$$

Capillary condensation is observed in mesoporous materials when liquid adsorbate in a pore is separated from gaseous adsorbate by a meniscus, as is illustrated in Figure 3.4. The radius of a capillary, r_k, can be related to the relative pressure (P/P_0) through the Kelvin equation (Eq. 3.10 [**268**]) where γ represents the surface tension of liquid adsorbate, V the molar volume of the adsorbate, R the gas constant, T the absolute temperature, and θ the contact angle between the liquid adsorbate and solid surface.

$$\ln\left(\frac{P}{P_0}\right) = \frac{-2\gamma V}{r_k RT}\cos\theta \qquad \textbf{Eq. 3.10}$$

The BJH technique is particularly useful in the determination of the pore size distribution of the adsorbent as it does not assume a standard mathematical distribution of pore sizes, nor is it assumed that the thickness of the physically adsorbed layer is constant. As with other models used to determine pore size distribution a standard geometry is assumed, in the case of the BJH model it is assumed that pores are cylindrical and rigid.

A summary of the derivation of the BJH method is given in Appendix D, and the typical output is a plot of differential pore volume against pore width. Although the derivation of this method considers the desorption process, the adsorption curve of an isotherm should be used to determine the pore size distribution due to complications arising from networks during desorption [**170**].

By including the Kelvin equation, the range of relative pressures over which the BJH model is applicable is limited to relative pressures greater than 0.3. At lower pressures the formation of a meniscus by a liquid in a cylinder of the corresponding radius is unlikely; the BJH model is therefore used only to characterise the mesoporous structure of an adsorbent.

3.1.1.5 Micropore Volume

3.1.1.5.1 Dubinin-Radushkevitch Model [260]

In the analysis of microporous materials the Dubinin-Radushkevitch model (DR) assumes that the adsorbate in is in the liquid state, therefore this theory is limited to systems where the temperature is significantly lower than the critical temperature of the adsorbate ($T < 0.8\ T_c$).

In such a system the volume of pores filled with adsorbate, V, is defined as the mass of adsorbate, W, divided by the density of the adsorbate in the liquid state, ρ, as shown in Eq. 3.11, and as with the previous models, this assumption does not allow for any variation in adsorbate density with adsorption potential.

$$V = \frac{W}{\rho} \qquad \textbf{Eq. 3.11}$$

The adsorption potential, ϵ, is defined as the isothermal work required to compress adsorbate from equilibrium pressure, P, to saturation pressure, P_0, in the liquid state and is calculated according to Eq. 3.12.

$$\epsilon = RT \ln\left(\frac{P_0}{P}\right) \qquad \textbf{Eq. 3.12}$$

The affinity coefficient, β, relates the adsorption potential for the adsorbate to that of a reference adsorbate, ϵ_0, as shown in Eq. 3.13. (For carbon material adsorbents the reference adsorbate is usually benzene [**260**]).

$$\beta = \frac{\epsilon}{\epsilon_0} \qquad \textbf{Eq. 3.13}$$

In adsorbents where adsorption potentials are enhanced by the overlapping fields of extremely narrow pore walls, the occupied adsorption space has been found to be a function of adsorption potential as shown in Eq. 3.14.

$$V = V_0 e^{-\kappa {\epsilon_0}^2} \qquad \textbf{Eq. 3.14}$$

V_0 represents the limiting micropore volume, and the parameter κ is a constant that reflects the pore size distribution of the adsorbent with respect to pore volume. Substitution of β and ϵ in Eq. 3.14 yields Eq. 3.15, which can be combined with Eq. 3.11 to produce a linear form, Eq. 3.16.

$$V = V_0 e^{-\kappa\left(\frac{RT}{\beta}\ln\left(\frac{P_0}{P}\right)\right)^2} \qquad \textbf{Eq. 3.15}$$

$$\ln W = \ln(V_0\rho) - \kappa\left(\frac{RT}{\beta}\right)^2\left[\ln\left(\frac{P_0}{P}\right)\right]^2 \qquad \textbf{Eq. 3.16}$$

Therefore a linear plot of $\ln W$ vs $[\ln(P_0/P)]^2$ will have an intercept of $\ln(V_0\rho)$ allowing for calculation of the micropore volume. Linear plots are usually found at relative pressures lower than 0.1, and generally require adsorption data at relative pressures as low as 10^{-5}.

3.1.1.5.2 Dubinin-Astakov Model [259, 260]

The Dubinin-Astakov (DA) model is a modification of the DR model where the function relating occupied adsorption volume to adsorption potential is replaced by Eq. 3.17, where *n* is known as the heterogeneity parameter and provides an indication of the sharpness of the pore size distribution. Values of *n* greater than 3 correspond to pores of a well-defined width (*e.g.* zeolites, carbide derived carbons) whereas values less than 2 indicate a broadly distributed range of pore size (*e.g.* biomass-derived activated carbons) [**260**].

$$V = V_0 e^{-\kappa \epsilon_0{}^n} \qquad \textbf{Eq. 3.17}$$

The corresponding linear form of the DA equation is given by Eq. 3.18.

$$\ln W = \ln(V_0 \rho) - \kappa \left(\frac{RT}{\beta}\right)^n \left[\ln\left(\frac{P_0}{P}\right)\right]^n \qquad \textbf{Eq. 3.18}$$

From the DA method, the characteristic energy, *E*, of the system can be determined and along with the value of the heterogeneity parameter, this allows for a quantification of the pore size distribution indicated by adsorption data. A simple method that yields the modal pore width of the pore size distribution was proposed by Medek [**269**] and is given in Eq. 3.19, where *k* represents the interaction constant.

$$r_{mode} = \left[\left(\frac{3n}{3n+1}\right)^{1/n} \frac{k}{E}\right]^{1/3} \qquad \textbf{Eq. 3.19}$$

Alternative treatments of low pressure adsorption isotherms are available with that proposed by Horvath and Kawazoe [**270**] being encountered occasionally, but the DR and DA method appear more frequently in reports concerning materials for ECs.

The *t*-plot method [**271**] can also be used to indirectly determine the surface area associated with micropores, by considering a model of adsorbed film thickness, such as the Halsey equation, although it strictly determines the surface area of the sample

after micropore filling is complete (*'external' surface area*). A similar method is the α_s-plot [**251**] where a reference isotherm obtained using a non-porous sample of a similar material to the sample under study is used rather than a model of film thickness.

In some reports, adsorption at 273K of carbon dioxide is used to overcome the diffusion limitations that occur when using nitrogen at 77K. However, under these conditions the analysis temperature of the adsorbate is much closer to the critical temperature of the adsorbate and there is also a degree of uncertainty regarding specific interactions between CO_2 molecules and the surface functional groups present on porous carbons.

3.1.2 Gas Pycnometry

The density of a material, δ, is defined as the mass of the material, *m*, divided by the volume occupied by that mass, *v*. This relationship is represented by Eq. 3.20.

$$\delta = \frac{m}{v} \qquad \textbf{Eq. 3.20}$$

However, when considering particles and porous materials there are many different definitions of density, each based on a different method of determining the sample volume. Several different volumes are defined, which are; the volumes occupied by the solid material, the pores present in the sample, closed porosity, interstitial voids arising from the spaces between particles, and voids due to surface irregularities. When all of these volumes are included in the calculation of density, it is referred to as the *bulk* density (Figure 3.5(a)) and when the interstitial volume is excluded the density is referred to as the *envelope* density (Figure 3.5(b)). The *skeletal* (or *apparent*) density excludes the volumes that are available to an external fluid (Figure 3.5(c)) whereas the *absolute* (or *true*) density is based solely on the volume occupied by the solid phase (Figure 3.5(d)).

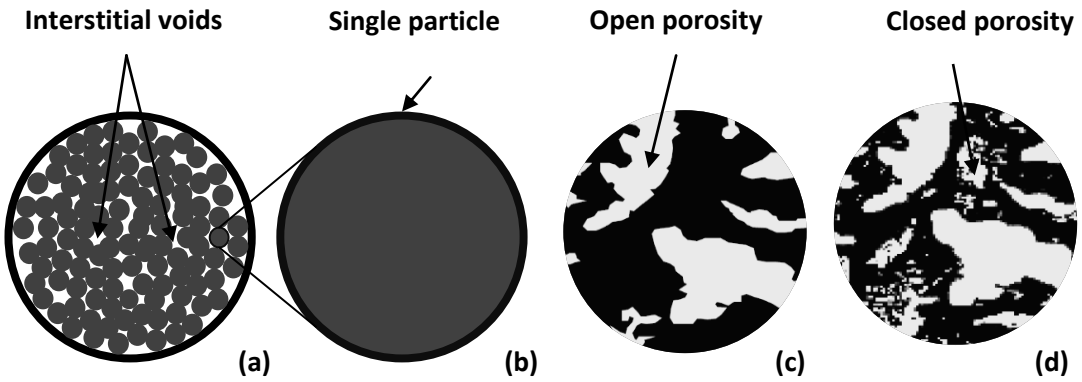

Figure 3.5: Representations of the different volumes used in the determination of density.

A gas pycnometer measures the change in pressure resulting from the displacement of a gas by a solid; a diagram of a simple measurement system is given in Figure 3.6. A known mass, *m*, of solid sample, whose volume, V_X, is placed into a sample chamber of known volume, V_S. After sealing the chamber, flushing the system with analysis gas and allowing the system to equilibrate, the pressure in the sample chamber, *Ps*, is measured. The sample is required to be flushed with analysis gas to remove any moisture or adsorbed species that could contribute to errors, and to allow sufficient time for diffusion of the analysis gas into the pore structure of the sample.

The isolated reference chamber (of known volume, V_R) is then charged to a known pressure which is greater than that of the sample chamber, P_R. The valve between the two chambers is then opened and the pressure (P_T) measured after a suitable equilibration time.

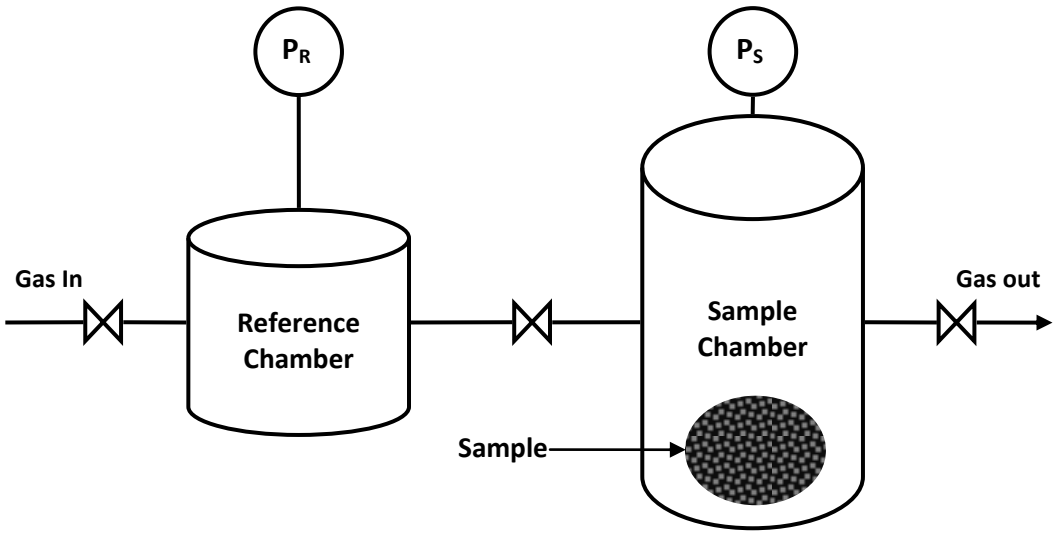

Figure 3.6: Schematic representation of a gas pycnometer system. P_R and P_S represent the pressure in the fixed volume reference and sample chambers respectively.

The volume of the sample is determined by applying the gas law under the assumptions that there is no change in temperature during the measurement and that the system is well-sealed (*i.e.* the number of gas molecules in the system is constant during each measurement).

Before the valve is opened, the system can be represented by Eq. 3.21 where *n* is the number of gas molecules in the system, *R* is the gas constant, and *T* is the system temperature.

$$P_S(V_S - V_X) + P_R V_R = nRT \qquad \textbf{Eq. 3.21}$$

After equilibration of the system, the system can be represented by Eq. 3.22.

$$P_T(V_S + V_R - V_X) = nRT \qquad \textbf{Eq. 3.22}$$

As the number of gas molecules is identical for both conditions, Eq. 3.21 and Eq. 3.22 can be combined to give Eq. 3.23.

$$P_S(V_S - V_X) + P_R V_R = P_T(V_S + V_R - V_X) \qquad \textbf{Eq. 3.23}$$

Eq. 3.23 can be rearranged to determine the volume occupied by the sample, as shown in Eq. 3.24.

$$V_X = \frac{1}{(P_T - P_S)}(P_T(V_R + V_S) - P_S V_S - P_R V_R) \qquad \textbf{Eq. 3.24}$$

Sample density is then determined using Eq. 3.20. As a gas pycnometer allows for the analysis gas to access any open porosity in the sample, this method provides a way to characterise the skeletal density of a porous sample, *i.e.* the volume of solid material and any closed porosity is used in the calculation of material density. Helium is typically used in a gas pycnometer as it readily diffuses into the pore structure of the sample; other gases may be used to investigate effect of molecule size on accessible volume, or how gases react with a sample surface.

3.1.3 TGA/ Proximate analysis

Thermal gravimetric analysis (TGA) is a technique that measures the change in weight of a sample with changes in temperature under a controlled atmosphere. TGA can be used to characterise materials with respect to their composition, and is used to investigate the processes that occur during carbonisation. At a constant heating rate under an inert atmosphere the weight loss profile of a sample can give an indication of the temperatures where bonds in the sample are broken. The derivative of the weight loss profile of a sample can be used to identify the points where the rate of weight loss is highest.

TGA can also be used to perform proximate analysis where the composition of coals and cokes can be defined on the basis of moisture, volatiles, fixed carbon and ash content. In this procedure, the moisture is removed from the sample and the mass recorded. The sample is then heated under an inert atmosphere to remove any volatile components until a constant mass is recorded. Finally the analysis gas is changed to oxygen and the mass lost in this step through combustion is equivalent to the fixed carbon content of the sample. The remaining incombustible component of the sample is referred to as the ash content of the sample.

3.1.4 X-ray Photoelectron Spectroscopy

X-ray Photoelectron Spectroscopy (XPS) is a quantitative technique that is used to measure the elemental composition of a sample surface. A major advantage of this technique is that all elements bar hydrogen and helium are detectable. From the obtained spectra, the binding state of the elements on the sample surface can also be determined, which allows for quantification of the surface functional groups present.

The sample under analysis is irradiated with soft X-rays (wavelength>0.1nm) and core electrons are ejected. The number of photo-emitted electrons is detected and their kinetic energy measured. XPS is performed under an ultra-high vacuum to prevent interference from gas molecules with photoelectrons before they are analysed. XPS is a surface specific technique as only the photoelectrons that originate from within the top 10 nm of the sample can escape into the instrument vacuum and be detected.

Under the assumption that the photoemission process is elastic in nature, the kinetic energy of the photoemitted electrons, E_K, is equal to the energy of the incident photons ($h\nu$) less the binding energy of the electron, E_B, and the work function of the surface φ, as shown in Eq. 3.25 and Figure 3.8.

$$E_K = h\nu - E_B - \varphi \qquad \textbf{Eq. 3.25}$$

E_B the binding energy of the electron is conventionally measured with respect to the Fermi level of the sample. (The precise value of the work function φ is dependent on the sample and spectrometer set-up)

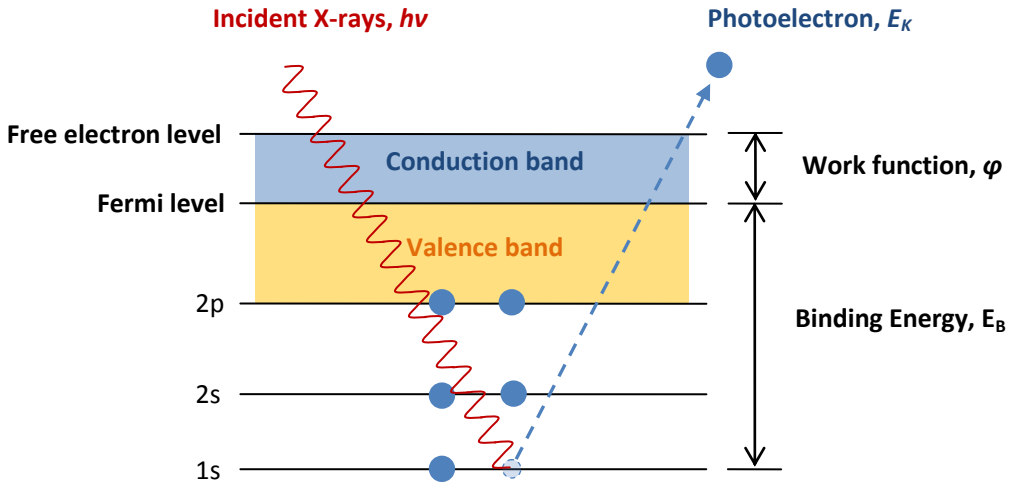

Figure 3.8: Photoelectron emission by X-rays

The output from an XPS experiment is usually a spectrum of the binding energy of electrons detected. The energy of emitted electrons is determined using a concentric hemispherical analyser (CHA) where photoelectrons are focussed into the gap between two concentric hemispheres that have a known potential difference between them. The resulting electric field allows only electrons of a narrow energy band to pass through the analyser to the detector. This 'pass' energy is fixed during the recording of a spectrum, and can be altered to allow for better resolution of complicated spectral regions. The instrument set up is illustrated in Figure 3.7.

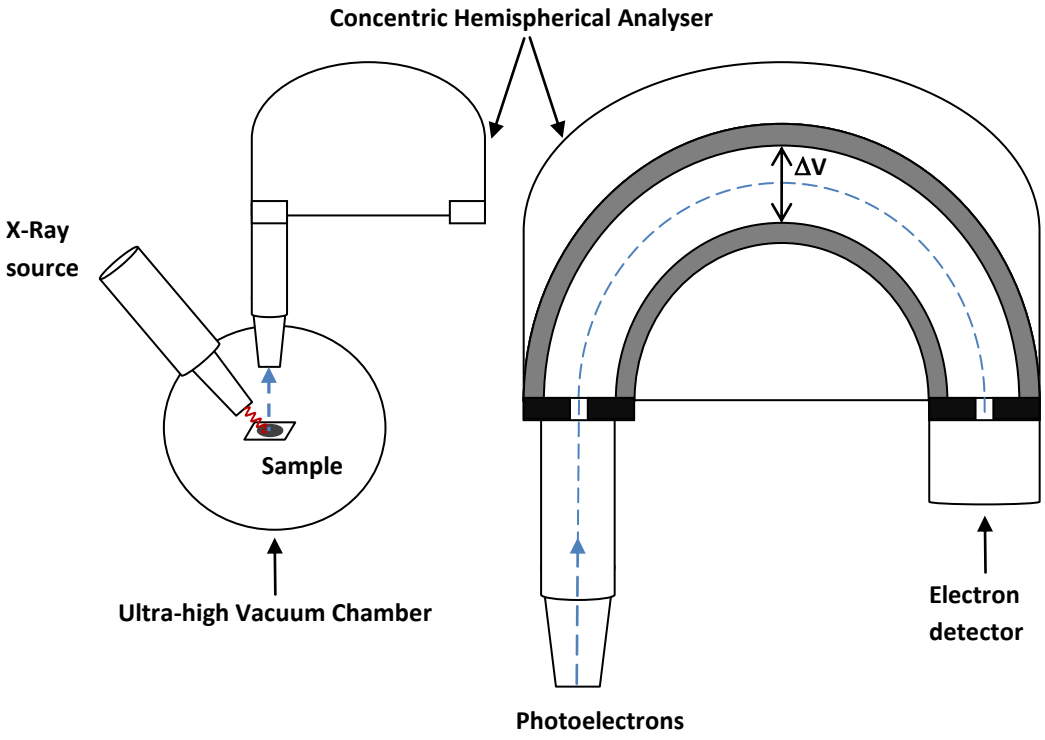

Figure 3.7: XPS instrument schematic with Concentric Hemispherical Analyser

The most widely employed X-ray sources in XPS systems emit Mg Kα or Al Kα radiation as these types produce narrow lines (<1.0 eV wide) that do not limit the resolution of the detector. The energies associated with these types of radiation are 1253.6 and 1486.6 eV respectively, which is large enough to eject a suitable amount of core electrons for analysis.

The spectrum from an unmonochromatised X-ray source consists of a principal characteristic line, but there are also 'satellite' characteristic lines and a continuous background, known as '*bremsstrahlung*', which is due to inelastic scattering of electrons. Satellite lines create additional features in the spectrum and need to be taken into account when analysing spectra.

In the absence of a monochromatised X-ray source, the continuous background can be subtracted from the spectra using several methods. This is an important aspect of the data analysis process as incorrect subtraction alters the intensity and position of peaks. One method is linear subtraction where the background is treated as a straight line between the first and last points in a spectrum. This can be used when a relatively small change in background is found in the region of interest and is commonly used when studying polymers. An alternative method (Shirley's method), suitable for conductive samples, assumes that each electron is associated with a flat background of losses. In Shirley's method the background is calculated to be proportional to the intensity of the total peak area above the background by iteration and produces a curved background over the region being analysed. More accurate methods of background subtraction have been developed by considering the losses associated with inelastic scattering. In the calculation of surface composition of nitrogen-enriched carbons, Shirley's method of background subtraction is the most commonly used [**255**, **272**].

Each element has a characteristic spectrum with peaks at specific values of binding energy that correspond with electron configuration. This allows for the identification of the elements present on a sample surface; some line positions when Mg-X-Rays are used as the excitation source are given in the table below. It should be noted that

the values given indicate a range where characteristic peaks can be found, as they shift in binding energy due to sample charging and the chemical state of the element.

Element	Line Position [eV]
C	281 - 293
N	396 - 408
O	529 - 534
F	684 - 695
Na	1071 - 1079

Table 3.1: 1*s* photoelectron line positions from Mg X-Rays [272]

Quantification of the elements present in the sample can be performed using XPS as the number of electrons detected in each of the spectral peaks is directly related to the amount of each element within the 'irradiated volume'. To convert the XPS signal to atomic percentage, the area under each principal peak is corrected using an empirically derived relative sensitivity factor, (given in Table 3.2 [**272**]) and is normalised to give elemental composition values that are sensitive to roughly 0.1 atomic percent.

Element	Relative Sensitivity Factor
C	0.25
N	0.42
O	0.66
F	1.00
Na	2.3

Table 3.2: Empirically derived atomic sensitivity factors relative to F 1*s* [272]

Shifts in the spectral peaks away from the characteristic core values provide information about the chemical state of the element. In nitrogen containing carbon materials there are many possible binding states, each with a different binding energy, which produces a spectral peak that is the result of several smaller peaks overlapping. Some of the nitrogen forms found in carbon materials are shown in Figure 3.9, along with binding energies (B.E.) that were determined using carbonised model compounds and model calculations [**255**].

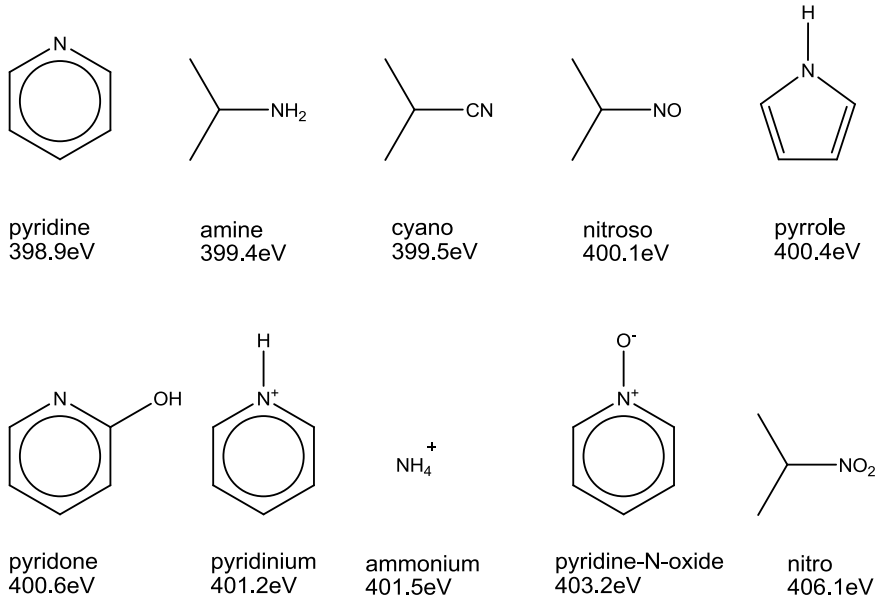

Figure 3.9: N 1*s* electron binding energy of groups found in carbon materials

Using high resolution scans over the N1*s* range (*ca.* 396-408 eV), the resultant peaks can be analysed to quantify the existence of different groups of nitrogen forms. Deconvolution is usually carried out by curve fitting, where the summation of several theoretical curves is fitted to the raw data using the least squares approach. However when the accuracy of XPS measurements is considered (typically ±0.1 eV) several groups cannot be differentiated between, and the nitrogen groups found in carbon materials are commonly reported [**255**] as consisting of four groups, roughly defined by the binding energies in Table 3.3. For example, the N-5 group is a combination of the pyrrolic (B.E. 400.4 eV) and pyridonic (B.E. 400.6 eV) contributions which cannot be reliably separated into distinct peaks. The binding energies in Table 3.3 were chosen based on values used in related literature **[145, 209, 210, 228, 230-234,**

236, 237, 240-242, 244-246, 248, 249, 255, 282] to allow for comparisons with previous work.

Group	Binding Energy [eV]
N-5: *pyrrolic*	400.6
N-6: *pyridinic*	398.7
N-Q: *quaternary*	401.2
N-X: *oxidised*	403.0

Table 3.3: Binding Energies of Nitrogen Groups

Quaternary nitrogen, N-Q, represents nitrogen that has been incorporated into the graphitic structure of the carbon material and is usually found to be fitted with a relatively broad curve in comparison with N-5 and N-6 curves. This indicates that slightly different forms of quaternary nitrogen exist in these materials. An even broader curve of low intensity is usually found to fit the N-X group which is associated with pyridinic N-oxides.

3.1.5 Neutron Scattering

Neutrons have unique characteristics that allow them to penetrate very deeply into matter, which makes them extremely useful in the study of porous materials [**274**]. Neutrons have neutral charge, an imperceptibly small electric dipole moment and, in contrast with other probes typically used to study matter (electrons and X-rays), interact with atoms through the residual strong force rather than the electromagnetic force. Considering the mode of interaction, solid matter is not dense from the point of view of neutrons as the distance between nuclei is many orders of magnitude greater than the size of the nuclei themselves. Therefore neutrons can travel relatively large distances into matter without being absorbed or scattered.

There are two different processes that can be used to produce neutrons suitable for scattering experiments. The first requires a nuclear reaction where each fission event

of uranium-235 releases a few neutrons. An example of this type of reactor used for research is the 58.3 MW high-flux reactor at the Institut Max von Laue-Paul Langevin (ILL) which produces the most intense continuous neutron flux currently available.

An alternative approach is used at spallation sources where neutrons are produced through the use of particle accelerators and synchrotrons that generate intense proton beams. The high energy protons are directed at a target containing heavy nuclei which disintegrate to release neutrons. Spallation is used at the ISIS pulsed source, where a beam of high-energy protons from the synchrotron are directed at a tantalum target. In comparison with the flux of X-rays available at synchrotron facilities, the values of neutron flux available from both reactor and spallation sources are miniscule and the neutron scattering is a signal limited technique that requires many different instruments tailored to the study of one aspect of neutron scattering.

In both of these arrangements, free neutrons are directed towards a moderator material to reduce the kinetic energy associated with the neutrons to a useful value. Liquid hydrogen and deuterium are common moderator materials in neutron scattering experiments, and the temperature of the moderator defines the average energy of the neutrons available for scattering experiments. Neutrons are then guided towards specific instruments in the form of a collimated beam.

The mode of operation for instruments using the different neutron sources differs although the results are often similar. At reactor sources, a continuous stream of neutrons leave the moderator with a spectrum of energies, although in most experiments the neutrons need to be reduced to narrow band of energies through the use of a monochromator crystal. On the other hand, at spallation sources the entire energy spectrum of neutrons can be used due to the pulsed nature of the neutron beam. By measuring the time that it takes from neutrons leaving the moderator to detection, the *time-of-flight*, the wavelength of each neutron can be determined.

There are several different techniques that can be used to provide information relating to the structure of a sample using neutrons, and at a neutron source there are typically many different instruments designed to make use of these techniques.

Spectroscopy and diffraction can be used to investigate the relative positions of atoms whereas larger length scales can be studied using small angle scattering techniques. In this work, small angle neutron scattering has been used to investigate the surface area of the carbon materials under study.

3.1.5.1 Small Angle Neutron Scattering (SANS)

The theory and mathematical foundations of small angle neutron scattering are extensive treatments and are discussed in several textbooks [**274-276**]. Only a brief introduction to the relevant theory is given in this section.

In a SANS experiment the sample under study is placed in the path of a collimated neutron beam. Incident neutrons are isotropically scattered by the nuclei in the sample and scattered neutrons are detected at a distance L from the sample. This is illustrated in Figure 3.10 where the parameters associated with a SANS experiment are indicated [**276**]. The scattered neutrons of wavelength λ are detected at a scattering angle of θ. Neutrons are elastically scattered in SANS experiments, where no transfer of energy occurs as a result of the scattering event.

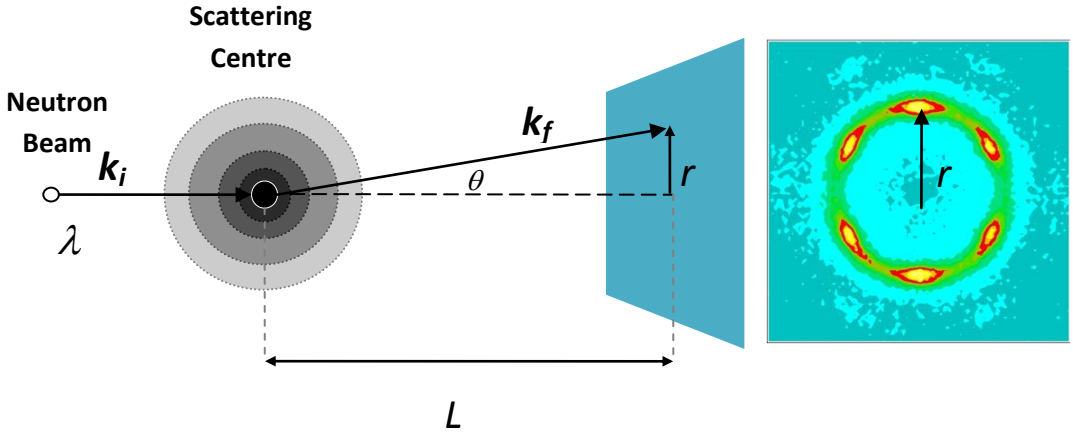

Figure 3.10: SANS experiment. Incident neutrons of wavelength λ are scattered isotropically and are detected at a distance *L* from the sample.

The wavelength, λ, of the incident neutrons can be calculated from their velocity using the de Broglie relationship given in Eq. 3.26, where *h* represents Planck's constant (6.6261×10^{-34} Js), *m* the mass of a neutron (1.6749×10^{-27} kg) and *v* the velocity of the neutron.

$$\lambda = \frac{h}{mv} \qquad \textbf{Eq. 3.26}$$

The incident neutrons have a wavevector of $\boldsymbol{k_i}$ (in the direction of *v*) whose magnitude depends on the de Broglie wavelength and can be calculated using Eq. 3.27.

$$k_i = \frac{2\pi}{\lambda} \qquad \textbf{Eq. 3.27}$$

Scattered neutrons have a wavevector of $\boldsymbol{k_f}$ and the scattering vector, $\boldsymbol{Q}$, is equal to the momentum transferred in the scattering event *i.e.* the resultant between the incident and scattered wavevectors as shown in Eq. 3.28.

$$\boldsymbol{Q} = \boldsymbol{k_f} - \boldsymbol{k_i} \qquad \textbf{Eq. 3.28}$$

The modulus of $\boldsymbol{Q}$, *q*, is the independent variable in a SANS experiment and can be determined from the de Broglie wavelength using Eq. 3.29 where *n* is the neutron refractive index, which is assumed to be unity.

$$q = \frac{4\pi n}{\lambda} \sin\left(\frac{\theta}{2}\right) \qquad \textbf{Eq. 3.29}$$

In the case of SANS instruments, the scattering angle is small and the value of $\sin(\theta/2)$ is approximately equal to (r/L). This produces an equivalent form of Eq. 3.29, when the scattering angle is small, Eq. 3.30.

$$q = \frac{4\pi n}{\lambda}\frac{r}{L} \qquad \textbf{Eq. 3.30}$$

Bragg's law of diffraction relates the wavelength of the incident neutrons to the scattering angle and a distance, *d*, which is a property of the sample [**277**], in the manner shown in Eq. 3.31.

$$\lambda = 2d\ sin\left(\frac{\theta}{2}\right) \qquad \textbf{Eq. 3.31}$$

Substituting the de Broglie wavelength of a neutron into Bragg's law shows that the distance *d* can be related to the wave vector through Eq. 3.32.

$$d = \frac{2\pi}{q} \qquad \textbf{Eq. 3.32}$$

The relationship in Eq. 3.32 provides an indication of the length scales that can be probed in SANS experiments by considering the available '*q*-range' of the instrument [**276**]. (Although this is sometimes erroneously taken as a direct measure of the interatomic distances in real space, it defines the spacing in reciprocal space.)

The *q*-range of an instrument is related to the type of neutron source, as different measurements and modes of operation are required to make use of steady-state (reactor) or pulsed (spallation) sources. At a reactor source the neutron beam used in scattering experiments is of fixed wavelength (*i.e.* monochromatic) and different values of *q* are measured by altering the distance between the sample and detector. Therefore fixed wavelength instruments are suited to experiments requiring data over a narrow *q*-range. Pulsed neutron sources on the other hand, usually supply an instrument that has a fixed geometry, and by measuring the time of flight for the neutrons, a relatively wide *q*-range can be investigated in one scattering run. In addition, the *q*-resolution at fixed geometry instruments is usually better than that found at instruments supplied with a monochromatic beam.

The instrument chosen for use in this work, LOQ at the ISIS pulsed source, has a *q*-range of roughly 0.006 to 1 $Å^{-1}$ which allows length scales between 0.6-100 nm to be investigated using the time-of-flight method.

3.1.5.1.1 Scattering Cross-Sections

The probability of a neutron being scattered by a single scattering centre can be described in terms of a cross-section that represents the effective area of the scattering centre presented to a passing neutron. If a neutron 'collides' with this cross section it is either absorbed or scattered with equal probability in any direction. The *absorption cross-section*, σ_{abs}, is an indication of the likelihood that a neutron will react with the scattering centre. The *coherent scattering cross-section*, σ_{coh}, represents the probability of a neutron being scattered that has the ability to interfere with other scattered neutrons, whereas the *incoherent scattering cross-section*, σ_{inc}, represents the occurrence of scattered waves that cannot interfere with each other.

The absorption, coherent scattering and incoherent scattering cross-sections of selected nuclides relevant to this work are given in Table 3.4 [**278**].

Nuclide	σ_{coh} [$\times 10^{-24}$ cm^2]	σ_{inc} [$\times 10^{-24}$ cm^2]	σ_{abs} [$\times 10^{-24}$ cm^2]
Hydrogen (^{1}H)	1.75	80.26	0.333
Deuterium (^{2}H)	5.59	2.05	0.0005
Carbon (C)	5.55	0.001	0.0035
Nitrogen (N)	11.01	0.50	1.90
Oxygen (O)	4.23	0.000	0.0002
Argon (Ar)	0.46	0.225	0.675

Table 3.4: Coherent, incoherent and absorption neutron scattering cross-sections of relevant nuclides [278]

Neutrons are unique when compared to light or X-rays as the scattering cross-sections with these methods increases in direct proportion to the number of electrons, whereas neutron scattering cross sections vary irregularly with increasing atomic

number. A major strength of neutron scattering occurs due to the difference seen in the coherent scattering cross-section between hydrogen and deuterium. Not only can neutrons detect different isotopes of hydrogen (that cannot be detected using X-rays), but the ability to distinguish between them is also extremely useful.

3.1.5.1.2 Scattering Equations

The flux of neutrons detected in a SANS experiment, *I(q)*, can be represented as the product of several different components as indicated in Eq. 3.33 [**276**].

$$I(q) = I_0(\lambda)\Delta\Omega\,\eta(\lambda)\,T(\lambda)\,V_s\,\frac{\partial\Sigma}{\partial\Omega}(q) \qquad \textbf{Eq. 3.33}$$

I_0 represents the incident flux, $\Delta\Omega$ is the solid angle element, η the detector efficiency, T is the transmission of the sample and V_s is the illuminated volume of the sample. The solid angle element is defined by the size of a detector pixel, and the detector efficiency depends on the type of detector used therefore these parameters, as well as the incident flux, are instrument specific. The illuminated volume, V_s, is simply the product of the area of the incident neutron beam and the thickness of the sample. Different designs of cuvette are used to hold samples in the neutron beam, however a small path length (1 - 2 mm) is required to ensure that multiple scattering does not occur and to minimise transmission losses as far as possible. Sample transmission, T, is dependent on the sum of the coherent, incoherent and absorption cross sections of the sample and allows for the events where incident neutrons do not reach the detector.

$d\Sigma/d\Omega$ represents the differential scattering cross section which is the measured quantity in a SANS experiment and is specific to the material under study. This quantity contains all of the information relating to the size, shape, and interactions between the scattering centres within the sample, represented by Eq. 3.34 [**276**].

$$\frac{\partial\Sigma}{\partial\Omega}(q) = N\,V^2\,(\Delta\rho)^2 P(q)S(q) + B \qquad \textbf{Eq. 3.34}$$

In Eq. 3.34 N represents the numerical concentration of scattering centres, V the volume of one scattering centre, $(\Delta\rho)^2$ is the system contrast, $P(q)$ the form factor and $S(q)$ the interparticle structure factor. B is any background signal present in the scattering data due to incoherent scattering, which can usually be subtracted from the scattering data as it contains no information pertaining to the sample structure.

The form factor, $P(q)$, and structure factor, $S(q)$ contained in the first term of Eq. 3.34 are the result of coherent scattering. The form factor is a dimensionless function that describes how the differential scattering cross-section is modulated by interference effects between neutrons scattered by different parts of the same scattering body. The form factor is therefore dependent on the size and shape of the scattering centre and different analytic expressions for commonly encountered shapes such as spheres, discs and rods have been developed. In the situation where these scatterers vary in size, the form factor can be adjusted to take a suitable size distribution function into account.

As an example, in the case of some porous materials, a suitable form factor has been fitted to experimental data by considering the voids in the material to consist of polydisperse, interpenetrating spheres [**279**].

The structure factor describes how the differential scattering cross-section is modified by interference effects between neutrons scattered by different scattering bodies in the same sample. The structure factor is dependent on the degree of local order in the sample and usually takes the form of a damped oscillating density distribution function that approaches unity as q tends to infinity. In dilute systems the structure factor is generally assumed to be equal to one [**280**], however in the case of porous materials it is inappropriate to consider the concentration of scattering centres as being dilute and a suitable structure factor is required. In the case of materials that exhibit scattering from a mass fractal, a structure factor incorporating the fractal dimension and an appropriate cut-off length has been found to adequately model the observed scattering [**281**].

3.1.5.1.3 Contrast and Coherent Scattering Length Density

The system contrast, $(\Delta\rho)^2$, is dependent on the existence of a difference between the scattering length density of two phases in the sample, specifically the contrast between two materials of different scattering length densities, ρ_α and ρ_β, is defined by Eq. 3.35 [**276**].

$$(\Delta\rho)^2 = (\rho_\alpha - \rho_\beta)^2 \qquad \textbf{Eq. 3.35}$$

The neutron scattering length density, ρ, can be determined using Eq. 3.36 where b_c is the bound coherent scattering length of i^{th} of n atoms in a molecule with molecular volume v_m.

$$\rho = \frac{1}{v_m}\sum_{i=1}^{n} b_c \qquad \textbf{Eq. 3.36}$$

The molecular volume can be expressed in terms of the sample density, δ, as shown in Eq. 3.37 where MW is the molecular weight of the sample and N_A represents Avogadro's constant, ($6.022 \times 10^{23} mol^{-1}$).

$$v_m = \frac{MW}{\delta N_A} \qquad \textbf{Eq. 3.37}$$

Selected coherent neutron scattering lengths, b_c, and atomic weights used in the calculation of scattering length densities in this work are given in Table 3.5 [**278**].

Nuclide	b_c [fm]	Atomic Weight [u]
Hydrogen (^{1}H)	-3.7423	1.00794
Deuterium (^{2}H)	6.674	2.0141
Carbon (C)	6.6484	12.0107
Nitrogen (N)	9.362	14.00674
Oxygen (O)	5.805	15.9994
Argon (Ar)	1.909	39.948

Table 3.5: Coherent Neutron Scattering Lengths and Atomic Weights of relevant nuclides [278]

3.1.5.1.4 Data analysis

The output from a SANS experiment is a plot of the differential scattering cross section varies *versus* scattering vector and, when plotted on a logarithmic scale, can provide an indication of the structures present in the sample. This becomes clear in a log-log plot as linear regions correspond to power law behaviour (*i.e.* $d\Sigma/d\Omega \propto q^{-n}$), and the value of n indicates the type of structures present in the sample. For example, when n=1 the scattering structures have been found to be rods or filaments whereas surface fractals have been found to fit n=4 behaviour. *Fractal* is a term used to describe an object that displays the same type of structure at all length scales, and scattering from a fractal structure results in linear behaviour over several orders of magnitude of q.

Porod's Law

For samples that consist of two distinct phases, scattering at high q values is inversely proportional to q^4 (*i.e.* $d\Sigma/d\Omega \propto q^{-4}$). This relationship is known as Porod's Law, and is usually seen when the interface between the phases is well defined and relatively smooth [**282**]. Porod's Law indicates the existence a limiting value, K, for the product of q^4 and the differential scattering cross-section as q tends to infinity.

The value of the constant, *K*, is dependent on the volumetric surface area between the two phases present in the sample, S_v, and the system contrast as shown in Eq. 3.38.

$$K = \lim_{q\to\infty} q^4 \frac{d\Sigma}{d\,\Omega}(q) = 2\pi\,(\Delta\rho)^2 S_v \qquad \textbf{Eq. 3.38}$$

Porod's Law does not apply to some porous materials where the interface between phases is poorly defined or cannot be considered as smooth. These situations can be attributed to the existence of a finite surface region in the solid phase exhibiting a variable scattering length density or where highly convoluted surfaces are present, for example in fractal structures. In the case of porous carbon materials analysed in the presence of air it is reasonable to assume that the phase boundary is well defined and that Porod scattering can be observed at high values of *q*.

The Porod Invariant

The Porod Invariant is defined as the integral of the differential scattering cross section over reciprocal space, as represented in Eq. 3.39, and is independent of the structural features present in the sample [**282**].

$$Q = \int_0^\infty q^2 \frac{d\Sigma}{d\,\Omega}(q)dq \qquad \textbf{Eq. 3.39}$$

Practically, the integral cannot be determined for the limits indicated in Eq. 3.39, as experimental limits are imposed by the *q*-range of the instrument. Clearly, as wide a *q*-range as possible should be used to determine the value of *Q* in a scattering experiment although several extrapolation methods have been used to approximate the 'actual' value of the Porod Invariant on an absolute scale.

To evaluate the integral in the low-*q* region, the differential scattering cross section has been extrapolated to *q*=0 either linearly [**276**] or by fitting a fourth order polynomial [**283**]. When a plot of differential scattering cross section against the square of the scattering wave vector is linear at the lower end of the experimental *q*-range (*i.e.* $d\Sigma/d\Omega \propto q^2$), extrapolation provides an estimate of the value of $d\Sigma/d\Omega$ for *q*=0. This linear behaviour is known as the Guinier approximation, which also

allows for the calculation of the molecular weight and radius of gyration of polymer samples [**283**]. As the integral in Eq. 3.39 increases with q^2 and has a theoretical upper limit of infinity, it is necessary to introduce an upper integral limit, although the selection of an actual value is somewhat arbitrary.

The Porod Invariant is directly related to the contrast in the system, and for scattering systems that consist of two phases (*e.g.* porous materials) Q can be expressed in terms of the phase volume, φ. As with Porod's Law, the relationship between these quantities, given in Eq. 3.40, is only applicable when the interface between the two phases is distinct and relatively smooth.

$$Q = 2\pi^2(\Delta\rho)^2\varphi(1-\varphi) \qquad \textbf{Eq. 3.40}$$

The system contrast and phase volume can be ascertained using alternative techniques to provide a theoretical value of the Porod Invariant. (The system contrast can be estimated using the procedure described previously and the phase volume can be ascertained using adsorption/intrusion techniques.) The Porod Invariant can therefore be used as an indicator of the relative interfacial surface areas of samples having the same composition [**284**].

More detailed analysis of scattering data can be carried out by fitting an appropriate model to the experimental data. For example, the fully penetratable polydisperse spheres model [**285**] has been successfully fitted to scattering data to give an indication of the pore size distribution and surface area of porous carbon materials [**286**].

SANS is uniquely suited to the study of microporous materials as a finite electron density is likely to be found in these regions which is known to influence the results of techniques such as X-ray scattering or gas adsorption [**287**].

SANS is a rarely encountered technique in literature relevant to ECs although it has been used to characterise the changes in surface area introduced through oxidation in thin sheets of low surface area pyrolytic carbon (*ca.* 3.5 m^2g^{-1}) and to compare this with the effects on specific capacitance [**180**]. SANS has also been used to study the

pore structure of RF aerogel derived carbons [**288**] and hypercrosslinked resin derived carbons [**263**]. In these studies, Porod's Law has been used to provide an indication of the relative surface areas possessed by materials of similar composition.

3.1.5.1.5 Contrast-Matching

The strength of neutron scattering techniques is in the ability of the scattering length density of solvents to be adjusted through partial deuteration. This is possible because the coherent scattering length of hydrogen and deuterium differ in sign and therefore the scattering length density of solvents can be controlled by mixing a conventional solvent with a known fraction of the deuterated form of the solvent.

As the measured differential scattering cross section is proportional to the contrast between the phases present in the sample, (Eq. 3.34) by matching the scattering length density of two phases, scattering can provide information about the structure of another particular phase. This technique is known as contrast-matching SANS (CM-SANS) and has been used to investigate and quantify the degree of closed porosity in a variety of porous materials including coals [**283**, **289**, **290**] and polymer derived chars [**263**, **277**, **286**]. In this case the contrast-matched solvent is assumed to occupy all open porosity, and any residual scattering can be ascribed to the presence of closed porosity.

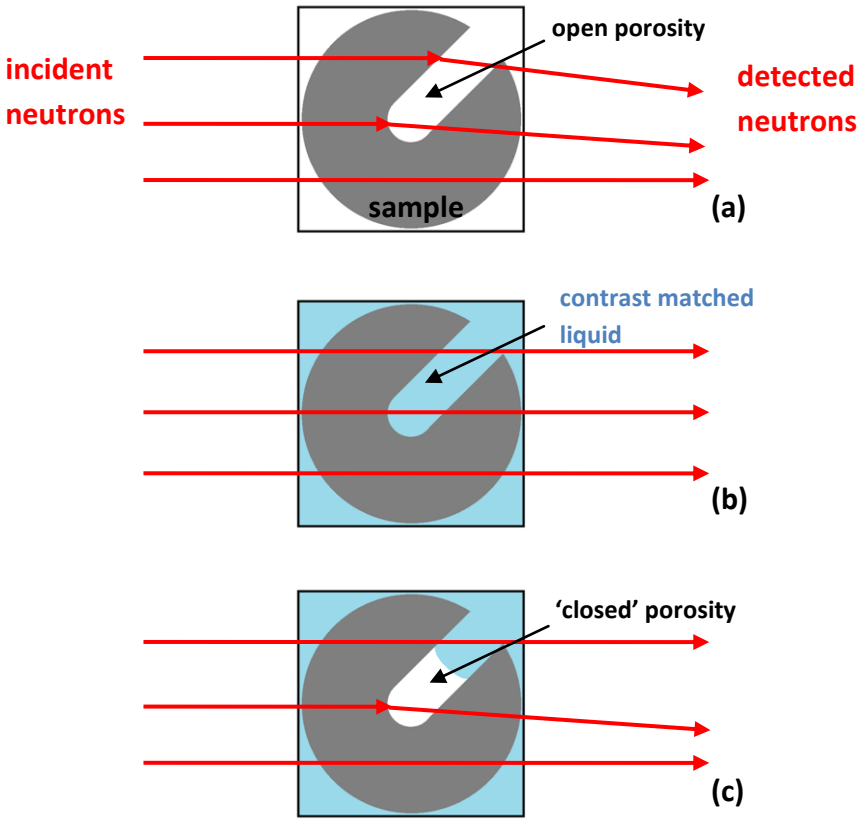

Figure 3.11: Contrast-matching SANS showing scattering from (a) a porous sample, (b) a porous sample completely filled with a liquid of the same scattering length density and (c) a porous sample partially filled with contrast-matching liquid.

CM-SANS is illustrated in Figure 3.11 where (a) represents the scattering from a porous sample measured in the presence of air. Figure 3.11(b) represents the situation where all of the open porosity in the sample is filled with a liquid of the same scattering length density (*i.e.* contrast-matched) and no scattering occurs. In this event any closed porosity will scatter in the same manner as in the conventional or 'dry' SANS run.

As any regions of porosity that are accessible to nitrogen during adsorption measurements, but not accessed by electrolyte are effectively closed porosity, it was proposed that CM-SANS could be used to investigate the degree of porosity that is not accessed by electrolyte in porous carbon materials for use in EC electrodes. This situation is illustrated in Figure 3.11(c) where a portion of the porosity is unfilled by contrast-matching liquid and scatters in the same way as in the 'dry' SANS run, which is the same as the behaviour of closed porosity.

3.2 Electrochemical Characterisation

Different electrochemical techniques to evaluate the behaviour of ECs are widely used, each being suitable for the determination of different cell parameters. Of importance in the design of ECs are the operating conditions, associated resistances, rate dependent performance, self-discharge, cycling behaviour and of course, the capacitive performance of the materials being investigated.

3.2.1 Electrode systems

A three-electrode cell (*3e*) consists of a working electrode containing the material under study, a counter electrode, and a reference electrode. The counter electrode is usually a platinum ribbon or nickel mesh, and is required to maintain neutral charge over the entire cell. It is assumed that the capacitance of the counter electrode is very much greater than that of the working electrode, and the capacitance determined in a three-electrode system is equivalent to the capacitance of the working electrode.

Using an unpolarised reference electrode permits the study of individual electrodes under positive or negative charging. Reference electrodes such as the standard hydrogen electrode (0.0 V), saturated calomel electrode (+0.242 V) or silver/silver chloride electrode (+0.197 V) and are suitable for use with different combinations of electrode and electrolyte.

However real devices consist of two electrodes, and the electrochemical behaviour observed in a three-electrode cell may not be achievable in practice. Measurements made on two-electrode cells better represent the charge/discharge performance that can be realised in EC systems.

3.2.1.1 3-electrode and 2-electrode cells

An important distinction in the reporting of capacitance values arises from the use of three electrode cells using a reference electrode when compared to values obtained from practical devices [**212**].

The capacitance determined in a three electrode cell, C_{3e}, is equivalent to the capacitance of the electrode material, and the *3e*-specific capacitance can be calculated by dividing by the mass of the electrode, *m*, as shown in Eq. 3.41.

$$c_{3e-spec} = \frac{C_{3e}}{m} = \frac{C}{m} \qquad \textbf{Eq. 3.41}$$

In a practical device, equivalent to a two-electrode cell, the measured capacitance, C_{2e}, is equal to the capacitance of each electrode connected in series, and can be calculated using the relationship shown in Eq. 3.42.

$$\frac{1}{C_{2e}} = \frac{1}{C_+} + \frac{1}{C_-} \qquad \textbf{Eq. 3.42}$$

For symmetrical cells where the capacitive contribution from each electrode is equal, the capacitance from one electrode, *C*, is equal to the measured three-electrode capacitance and this results in the relationship shown in Eq. 3.43.

$$\frac{1}{C_{2e}} = \frac{2}{C} \qquad \textbf{Eq. 3.43}$$

Under the assumption that the specific capacitance (and therefore mass) of each electrode is identical, the specific capacitance of the material on a two electrode basis is given by Eq. 3.44.

$$c_{2e-spec} = \frac{C_{2e}}{2m} = \frac{C}{4m} \qquad \textbf{Eq. 3.44}$$

Therefore the specific capacitance reported with respect to a three-electrode cell is equal to 4 times that reported for a two-electrode cell. Although a two-electrode cell was used in the determination of cell capacitances in this work, all values of specific capacitance are reported with respect to a three-electrode cell to allow for comparison with the relevant literature.

3.2.2 Electrochemical Impedance Spectroscopy

Electrochemical Impedance Spectroscopy (EIS) is commonly used in the determination of capacitances, resistances and frequency dependent behaviour of ECs. The potential across the cell is subjected to a small amplitude sine wave over several decades of frequency and the resulting alternating current response is measured. Through comparison of the impedance associated with the current response and a suitable equivalent circuit, fundamental cell parameters can be determined.

3.2.2.1 Impedance

Electrical resistance is a measure of the ability of a circuit to oppose the flow of electrical current [**291**]. Ohm's law and the idea of resistance is applicable only to ideal resistors, where the value of resistance is independent of signal frequency and alternating current-voltage signals are in phase. Impedance (Z) is a concept analogous to resistance but applies to a wider range of circuit elements and is defined by Eq. 3.45.

$$Z = \frac{E}{I} \qquad \textbf{Eq. 3.45}$$

For a small-amplitude (E_0) sinusoidal potential, the response is pseudo-linear (*i.e.* a sine wave of the same frequency, ω, but exhibiting a phase shift, ϕ). For an ideal resistor, no phase shift is observed and the impedance is simply equal to resistance.

An excitation signal can be represented by Eq. 3.46 and the current response of a capacitor is defined by Eq. 3.47.

$$E(t) = E_0 \cos(\omega t + \phi) \quad \textbf{Eq. 3.46}$$

$$I(t) = C\frac{dE}{dt} \quad \textbf{Eq. 3.47}$$

The derivative of Eq. 3.46 can be substituted into Eq. 3.47 to give Eq. 3.48, which can also be expressed in the form shown in Eq. 3.49.

$$I(t) = C(-\omega E_0 \sin(\omega t + \phi)) \quad \textbf{Eq. 3.48}$$

$$I(t) = C\left(\omega E_0 \cos\left(\omega t + \phi + \frac{\pi}{2}\right)\right) \quad \textbf{Eq. 3.49}$$

As the amplitude, phase-shift and angular frequency are independent of time, the relationships in Eq. 3.46 and Eq. 3.49 can be expressed in the form of phasors, shown in Eq. 3.50 and Eq. 3.51 respectively, with only the real component being relevant. (When dealing with electrical circuits j is used to represent $\sqrt{-1}$ to avoid confusion with instantaneous current, usually denoted by i.)

$$\boldsymbol{E} = E_0 e^{j\phi} \quad \textbf{Eq. 3.50}$$

$$\boldsymbol{I} = \omega C E_0 e^{j(\phi+\frac{\pi}{2})} \quad \textbf{Eq. 3.51}$$

$$\boldsymbol{I} = j\omega C E_0 e^{j\phi} \quad \textbf{Eq. 3.52}$$

Using the simplified form of the current phasor shown in Eq. 3.52 (since $j = e^{j(\pi/2)}$) the impedance can then be defined as shown in Eq. 3.53.

$$\boldsymbol{Z} = \frac{\boldsymbol{E}}{\boldsymbol{I}} = \frac{E_0 e^{j\phi}}{j\omega C E_0 e^{j\phi}} = \frac{1}{j\omega C} \quad \textbf{Eq. 3.53}$$

Therefore, the phase shift between the voltage and current in an ideal capacitor is $-\pi/2$ (*i.e.* imaginary) and the impedance is a function of the frequency of the

excitation signal. ***Z*** can be divided into two components, the real and imaginary, which are typically represented on the complex plane in the form of a Nyquist plot.

3.2.2.2 Resistance

In real cells many different factors contribute to the values of resistance exhibited by ECs. This resistance is termed the equivalent series resistance (ESR) and is of practical importance as the maximum power output of the cell is dependent on the value of the ESR (Eq. 2.4). The factors that affect the ESR of the cell are the resistances encountered by the flow of current from one electrode to another; this includes the resistances imparted by the current collector, electrode, separator, electrolyte and the interfaces between these components. The inherent resistance of carbon electrodes is in turn affected by several factors including particle size, relative degree of graphitisation, micropore volume and the presence of heteroatoms, which was discussed previously.

3.2.2.3 Equivalent Circuits

In the analysis of EIS data, a suitable equivalent circuit that represents the components in an EC is usually fitted to the experimental data to determine the different cell parameters. An ideal capacitor generates a complex plane frequency response that exhibits no real impedance component at all frequencies, and the imaginary component tends towards zero with increasing frequency as shown in the Nyquist plot given in Figure 3.12.

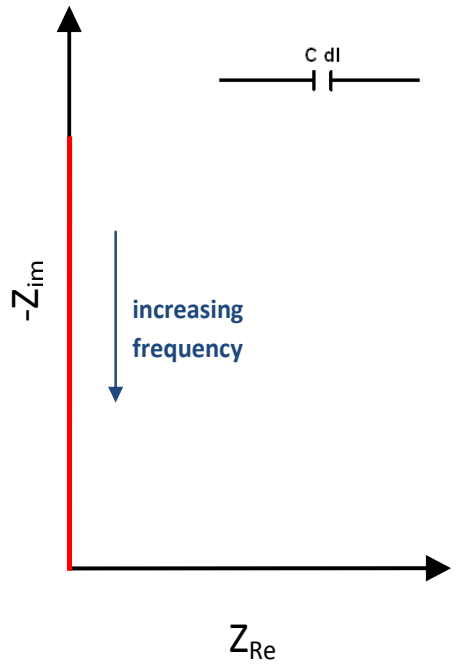

Figure 3.12: Nyquist plot for an ideal capacitor

Incorporating a resistor in series with an ideal capacitor, to represent the impedance arising from the electrolyte, results in the same frequency response plot described for the capacitor but shifted along the real axis by the value of this resistance *i.e.* the real component of impedance is a constant at all frequencies. This is shown in Figure 3.13.

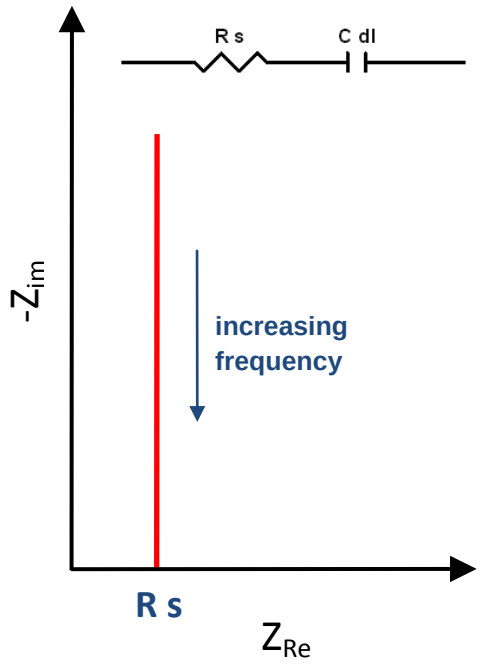

Figure 3.13: Nyquist plot for a resistor and capacitor in series. R_S represents the solution resistance in an EC

The addition of a resistor in parallel to the capacitor in the aforementioned circuit (to represent a leakage resistance) produces a markedly different complex-plane response. This arrangement can be used to describe the behaviour of a non-ideally polarisable interphase where a small current is required to maintain a constant potential across the cell. When the value of this resistance is sufficiently large, the Nyquist plot generated is similar to that seen for the series circuit in Figure 3.13, whereas for relatively small values of leakage resistance a semicircular plot, as shown in Figure 3.14, is observed. The maximum real component value is obtained as the frequency tends towards zero, which is equal to the sum of both resistances. As the frequency is increased the plot follows a semicircular path in the negative imaginary region, tending towards a real impedance value that is equivalent to the series resistor.

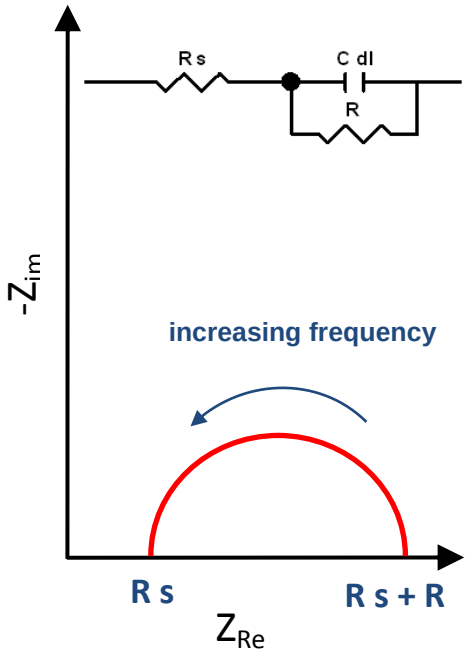

Figure 3.14: Nyquist plot for a resistor and capacitor (with parallel leakage resistance) in series. R_S represents the solution resistance and R the ionic resistance in an EC

If the value of the parallel resistor is dependent on potential and impedance spectra are recorded at different values of applied potential, the diameter of the semi-circle is altered accordingly. A real, non-ideally polarisable interphase generates a current response somewhere between that of a pure resistor and a pure capacitor (*i.e.* the phase angle is between 0° and -90°) and is manifested as a slope in the low frequency range on the Nyquist plot.

The complex plane responses from the above models cannot be reliably fitted to the experimental data obtained using porous electrodes. The equivalent circuit of a pore has been modelled as consisting of network of parallel RC circuits ('transmission line') that represent the distribution of resistance and capacitance down the length of an ideal pore [**10**, **292**]. The frequency response behaviour of the 'transmission line' model produces a characteristic phase angle of -45° that is independent of frequency. Although being a relatively simple model, this approach introduces the concept of different charging rates being present in porous electrodes as well as allowing the introduction of a different element with a phase angle between that of an ideal

capacitor and resistor into equivalent circuits. An electrode containing pores of uniform distribution results in the frequency response indicated in Figure 3.15 [**10**].

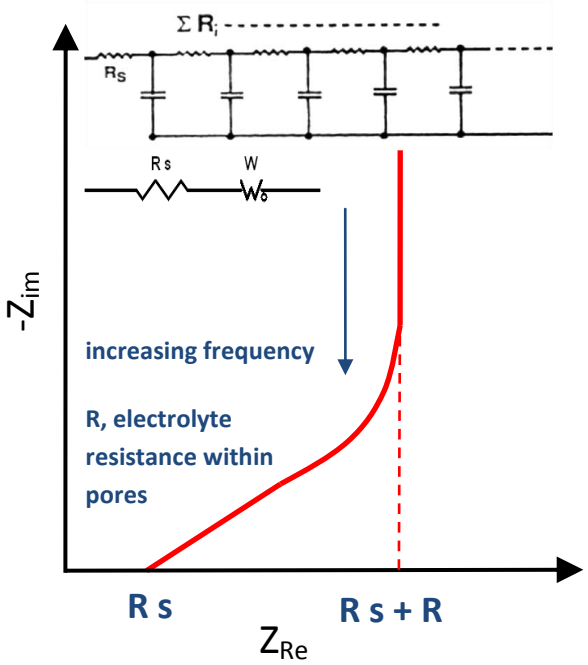

Figure 3.15: Nyquist plot for a 'Transmission Line'/ Resistor and Warburg element in series. R_S represents the solution resistance in an EC

The frequency response of an RC transmission line has been shown to be similar to the behaviour of a Warburg diffusion impedance element at a planar electrode. In a finite-length Warburg element, behaviour is modelled based on the diffusion of reactive species and produces a phase angle of -45°, as both the capacitance and resistive impedance components vary with the square root of frequency over a finite frequency region. However, as the fitted parameters are not relevant to the systems under study but only used to approximate the porous behaviour of the electrode, details of the Warburg impedance element are not given here, but a comprehensive derivation is given in [**291**].

An equivalent circuit that is frequently used to represent the impedance of an EC incorporates a Warburg impedance element in parallel with the double layer capacitance and is known as Randles' circuit [**10**, **254**], this is represented in Figure 3.16, alongside a schematic of the frequency response. In this work Randles' circuit was fitted to EIS results to determine the cell parameters such as solution resistance, charge transfer resistance and cell capacitance.

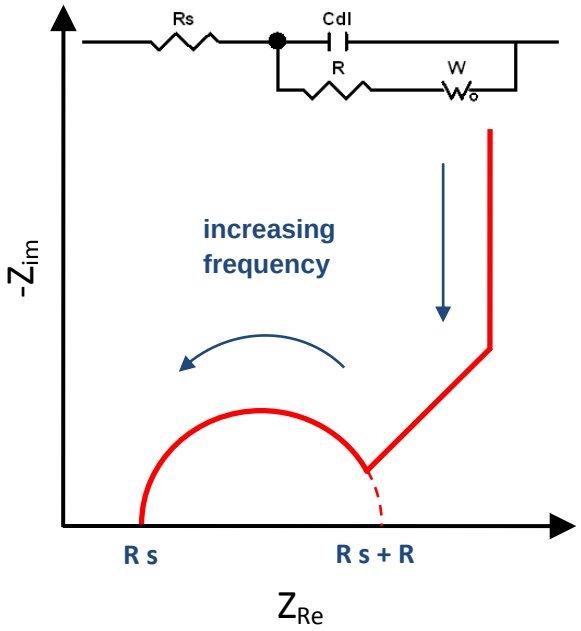

Figure 3.16: Nyquist plot for Randles' Circuit. R_S represents the solution resistance and R the ionic resistance in an EC

An indication of the cell capacitance, *C*, was found by the value of imaginary impedance, Z_{im}, at a low frequency of value, *f*, using the relationship seen in Eq. 3.54.

$$C = \frac{1}{2\pi f Z_{im}} \qquad \textbf{Eq. 3.54}$$

3.2.3 Galvanostatic Charge-Discharge

Charge/discharge cycling is a technique that can replicate the operating conditions of an EC and is widely used in the determination of cell performance. Current is added

to or drawn from the cell at a constant rate, *i*, (*i.e.* Galvanostatically) between two cut-off limits usually determined by the decomposition of the electrolyte. The range between these limits is known as the operating voltage of the cell. Constant current cycling is usually employed in preference to constant potential or constant power cycling, as the electrical control systems required in such systems are usually simpler [**10**]. Figure 3.17 represents the changes in current and potential with time for two cycles at a constant current, *i* between the cut-off limits, V_{min} and V_{max}.

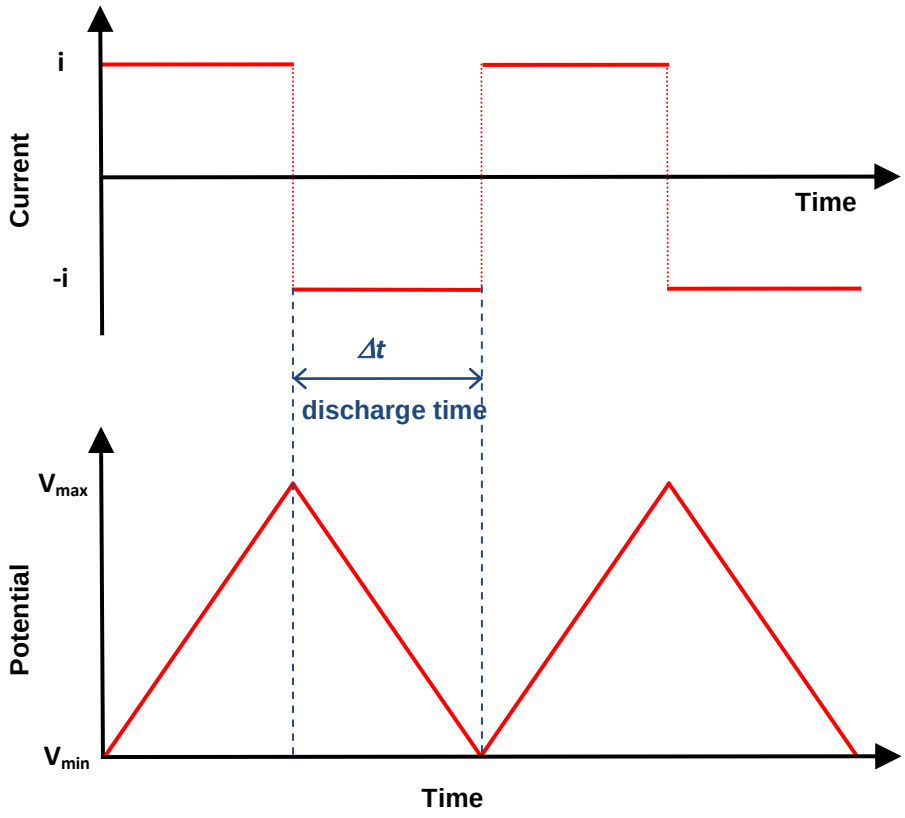

Figure 3.17: Variation of current (top) and potential (bottom) with time for Galvanostatic charge/ discharge process

When the discharge profile of a cell is fairly linear, as seen in Figure 3.17, the total capacitance of the cell under study can be calculated over a discharge cycle by determining the quantity of charge transferred and then dividing this by the voltage drop during discharge, as shown in Eq. 3.55.

$$C = \frac{Q}{\Delta V} = i\frac{\Delta t}{(V_{max} - V_{min})} \qquad \textbf{Eq. 3.55}$$

The ESR of an EC can be measured using the voltage response to Galvanostatic cycling. The drop in voltage measured on the reversal of the current direction from charge to discharge is referred to as the *iR* drop, indicated in Figure 3.18, and can be used to calculate the ESR according to Ohm's law, represented by Eq. 3.56, where the equivalent series resistance is denoted by R_{ESR}, the *iR* drop by ΔV_{iR}, and the current by *I*.

$$R_{ESR} = \frac{\Delta V_{iR}}{I} \qquad \textbf{Eq. 3.56}$$

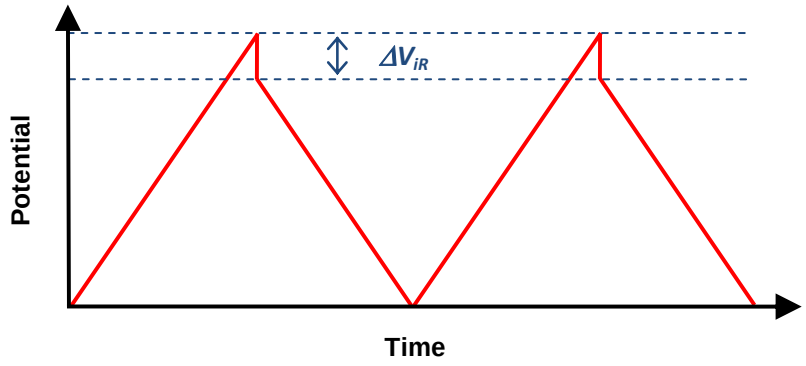

Figure 3.18: Variation of potential with time for Galvanostatic charge/ discharge process exhibiting *iR* drop

The amount of energy that can be stored at different rates of charge/ discharge has been found to vary significantly depending on the rate used, with the highest values of specific capacitance being obtained at the lowest rates of charge (or current density). It is therefore important that the rates used in the determination of capacitive performance reflect the operating conditions in a practical device.

Changes in capacitance with repeated cycling are usually investigated using Galvanostatic charge/ discharge cycling over many thousands of cycles, as the stability of capacitive behaviour determines the lifetime of the device. Where pseudocapacitance contributes significantly to the specific capacitance of carbon electrodes, an appreciable fade in capacitance with repeated cycling is usually observed.

3.2.4 Cyclic Voltammetry

Linear-sweep Voltammetry, also known as cyclic Voltammetry (CV) when applied repetitively, is used to study the potential dependent behaviour of ECs and is particularly useful in the study of materials displaying pseudocapacitance. Cyclic Voltammetry is usually employed as the first linear-sweep can produce a significantly different response in comparison with subsequent sweeps.

In this procedure the variation of current with applied potential and time is measured at a constant sweep rate between two cut-off potentials. The sweep rate, *s*, represents the change in potential with time (*dV/dt*) and is usually of the order mVs^{-1}. The direction of the observed current is dependent on the direction of the sweep rate which reverses periodically when a cut-off potential is reached. The limiting potentials are defined by the decomposition limits of the electrolyte being used, or a cut-off current associated with electrolyte decomposition can be applied to determine the operating voltage of new electrolytes such as ionic liquids [**195**, **196**].

Results are usually displayed in a plot of *i vs V* known as a cyclic Voltammogram, illustrations of which are given in Figure 3.19 and Figure 3.20. For constant values of cell capacitance, rectangular current responses similar to that seen in Figure 3.19(a) that are roughly symmetrical around the zero-current axis are generated. Deviations from the rectangular shape at the cut off potentials are usually indicative of electrolyte decomposition.

The capacitance of a cell under study can be estimated from a cyclic Voltammogram using the relationship(s) in Eq. 3.57.

$$C = \frac{\int idt}{\Delta V} = \frac{I(t)}{s} \qquad \textbf{Eq. 3.57}$$

For an ideally polarisable interphase the only process occurring in a given potential region is double layer charging which generates a Voltammogram of the form seen in Figure 3.19(a) [**293**]. In the case of a non-ideally polarisable interphase, illustrated in Figure 3.19(b) the leakage current may cause a skewing of the current response to produce a parallelogram shaped cyclic Voltammogram, especially when measured at relatively low sweep rates.

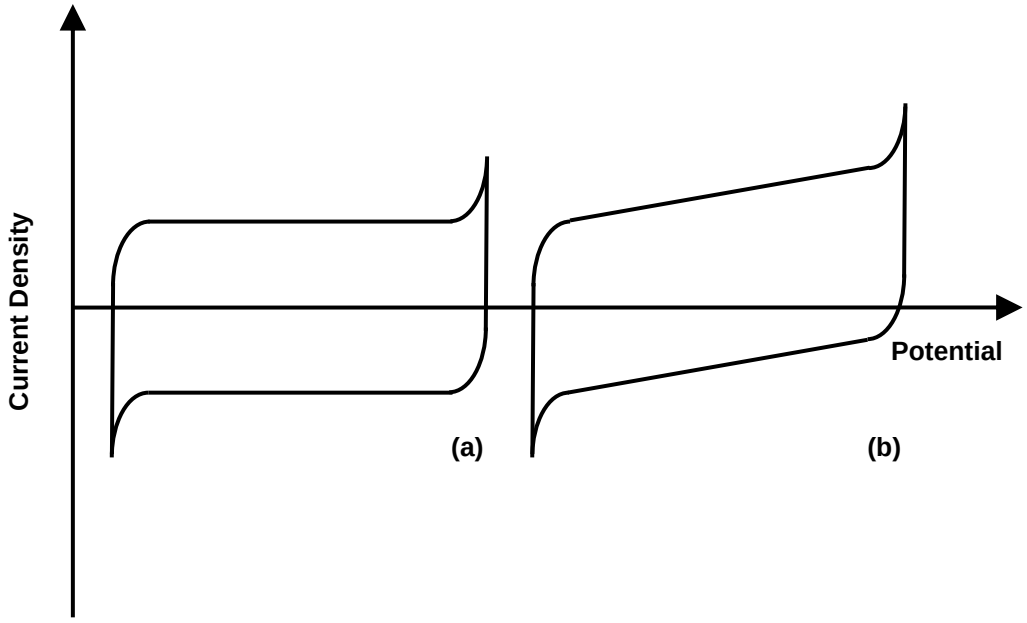

Figure 3.19: Cyclic Voltammograms for (a) an ideally polarisable interphase and (b) a non-ideally polarisable interphase

In many electrode systems however, the cell capacitance is not constant with changes in potential due to the influence of kinetic or diffusion limited currents. In the case of a pseudocapacitive system, significant deviations from the rectangular, or parallelogram-shaped, response are generated. Peaks in the current response occur at the potential where specific interactions become thermodynamically favourable and result in a change in the rate of charge acceptance with changes in potential. The derivative that occurs from this change is equivalent to a capacitance, as indicated by Eq. 3.58.

$$C = \frac{dQ}{dt}\frac{dt}{dV} \qquad \textbf{Eq. 3.58}$$

For example, the highest reported values of specific capacitance have been found in the study of thin films of hydrous ruthenium dioxide, the cyclic Voltammograms of which show the presence of three distinct peaks, each corresponding to a particular reaction, as indicated by Figure 3.20 [**10**].

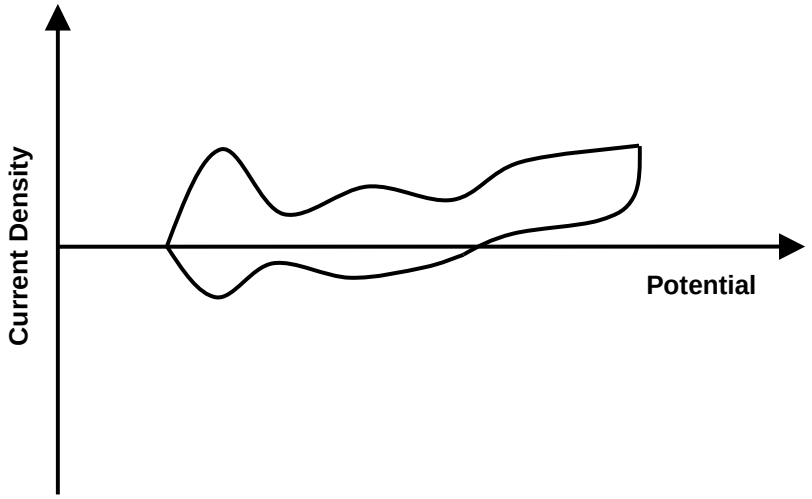

Figure 3.20: Cyclic Voltammogram indicating pseudocapacitance associated with thin-film RuO_2

To a lesser extent, pseudocapacitance can augment the double layer capacitance in carbon based ECs through the reaction of certain surface functional groups.

3.2.5 Self-Discharge

When fully charged, ECs have high free energy in relation to an uncharged device which is equivalent to a driving force for self-discharge. This has a detrimental effect on the performance of ECs as the voltage across the cell decreases fairly quickly after charging. The self-discharge of ECs is of practical importance as the useful energy and power densities are adversely affected by the mechanism, which results in a substantial degree of redundant energy storage capacity. Also, additional hardware may be required to provide a float current to counteract the self-discharge process.

Self-discharge can be investigated relatively easily by charging the cell up to the maximum operating potential and recording the voltage decay over time, although determination of the current required to maintain a steady potential can also provide a measure of self-discharge of a cell (*leakage current*). Different self-discharge mechanisms have been identified based on the relationship found between cell potential and time.

Activation controlled Faradaic processes have been shown to follow Eq. 3.59.

$$i(\eta) = i_0 \, e^{\left[\frac{\alpha \eta F}{RT}\right]} \qquad \textbf{Eq. 3.59}$$

In Eq. 3.59, $i(\eta)$ represents the current density at an overvoltage represented by η, i_0 is the exchange current density and α is known as the transfer coefficient. This can be expressed in terms of the voltage across the cell at any instant, V_t, as a proportion of the initial voltage, V_i, where t represents the time that the cell has been under open circuit conditions, and A and τ are constants in Eq. 3.60.

$$V_t = V_i - A \log(t - \tau) \qquad \textbf{Eq. 3.60}$$

The relationship in Eq. 3.60 shows that under these circumstances a plot of the decline in cell voltage against log (time) yields a straight line.

In this case the leakage current can be attributed to a Faradaic potential dependent reaction, the rate of which decreases as the self-discharge process progresses. For example, this applies to the decomposition of electrolyte by overcharging as the species involved can be considered at a high concentration. This is also applicable to redox reactions occurring between electrolyte species and surface functionalities [**294**].

It has also been shown that the process of charge redistribution, a consequence of uneven charging in porous electrodes, results in a linear relationship between the decline in cell voltage and log (time) [**295**].

An alternative relationship is found when species present in a low concentration are involved in Faradaic self-discharge mechanisms. In this case the leakage current does not follow Eq. 3.59, but is controlled by the diffusion of reactive species that participate in Faradaic reactions within the operating potential of the cell. These species are typically impurities in the electrolyte solution that can act like a shuttle between the two electrodes with the reduced and oxidised forms of the species interchanging and diffusing in both directions. Iron ions are a typical example of depolarising shuttle species, however dissolved oxygen species in the electrolyte can also undergo redox reactions and discharge the cell [**10**].

The diffusion of redox species can be shown to yield the self-discharge relationship given in Eq. 3.61 where z represents the amount of charge transferred according to the discharge reaction stoichiometry, D is the diffusion coefficient of the species, the initial concentration of which is $c_{0,}$ A represents the electrochemically active surface area and C again represents the cell capacitance.

$$V_t = V_i - \frac{2\,z\,FA\,D^{½}\pi^{½}c_0}{C}\,t^{½} \qquad \textbf{Eq. 3.61}$$

The relationship in Eq. 3.61 shows that under diffusion controlled self-discharge a plot of the decline in cell voltage against $(\text{time})^{½}$ yields a straight line.

4 Experimental

4.1 Carbon Material Production

4.1.1 Precursor Synthesis

Organic hydrogels were synthesised in a manner similar to those used in many previous investigations [**183**, **194**-**197**, **203**] where the polycondensation of an aqueous solution of resorcinol (R) with formaldehyde (F) was catalysed by the addition of sodium carbonate (C).

A typical synthesis procedure involved the dissolution of 0.10 moles of resorcinol (1,3-dihydroxybenzene, Aldrich, 99%) in 110 cm^3 of deionised water (W). The desired mass of sodium carbonate (Na_2CO_3, Aldrich, >99.5%) was added to the solution under stirring to increase the pH, a crucial factor determining the structure of the resultant gel [**198**]. 0.20 moles of formaldehyde (CH_2O, Aldrich, 37 wt.%, stabilised by 10 - 15 wt.% methanol) were added by volume under stirring, which was carried out for a further 45 mins to obtain an homogenous solution. The R/F molar ratio was kept constant at 0.50 and R/W was maintained at 0.10 g cm^{-3}. R/C molar ratios between 100 and 500 were initially investigated. The solution was sealed in a bottle to prevent solvent evaporation and kept at 85ºC for 3 days. The colour of the gels was found to vary with R/C ratio and this was more noticeable at the early stages of gelation, as evident in the photographs given in Figure 4.1.

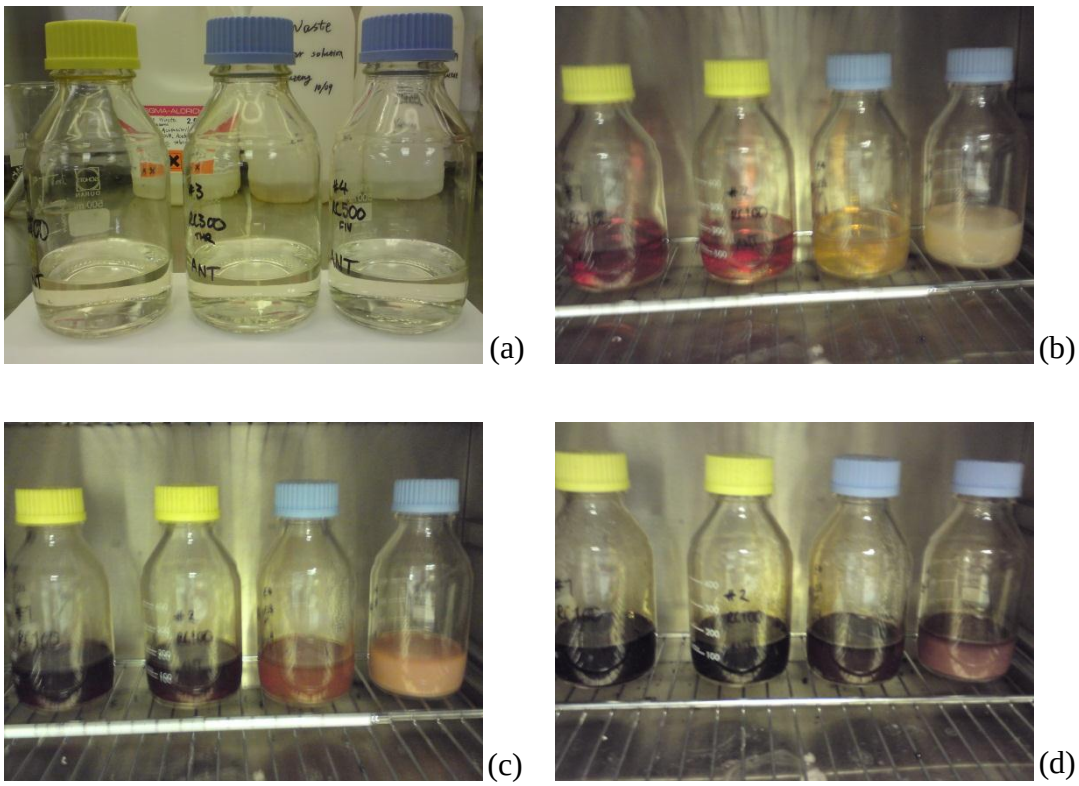

Figure 4.1: RF gels at various stages throughout gelation (l-r) RC100 (yellow caps), 300 and 500 (a) after mixing (b) after 1h at 85°C (c) after 3h at 85°C (d) after 24h at 85°C

The resultant RF hydrogels were cooled to room temperature and drained of liquid before maceration into pieces roughly 10 mm in diameter. Gels were then rinsed thoroughly with approximately 100 cm^3 acetone (Fluka, 98%) before being submerged in approximately 200 cm^3 of fresh acetone. Solvent exchange was carried out over a period of 3 days in an orbital shaker maintained at 25°C.

The required mass of *m*-phenylenediamine (1,3-phenylenediamine, Aldrich, ≥99%) was solvated in roughly 100 cm^3 acetone and added to the drained gel, which was then sonicated for 15 mins to encourage the thorough impregnation of *m*PDA solution. Impregnated gels were then agitated for a further 3 days. In samples where no *m*PDA was added, the same procedure using pure acetone was performed.

Gels were then heated to 55-60°C in a water bath under a fume hood, to evaporate the majority of acetone present without removing any *m*PDA, before being dried to

constant mass at 80°C under vacuum. Dried xerogels were prepared for carbonisation by milling for 5 mins in a bench-top ball mill using a tungsten carbide vial and balls.

4.1.2 Carbonisation

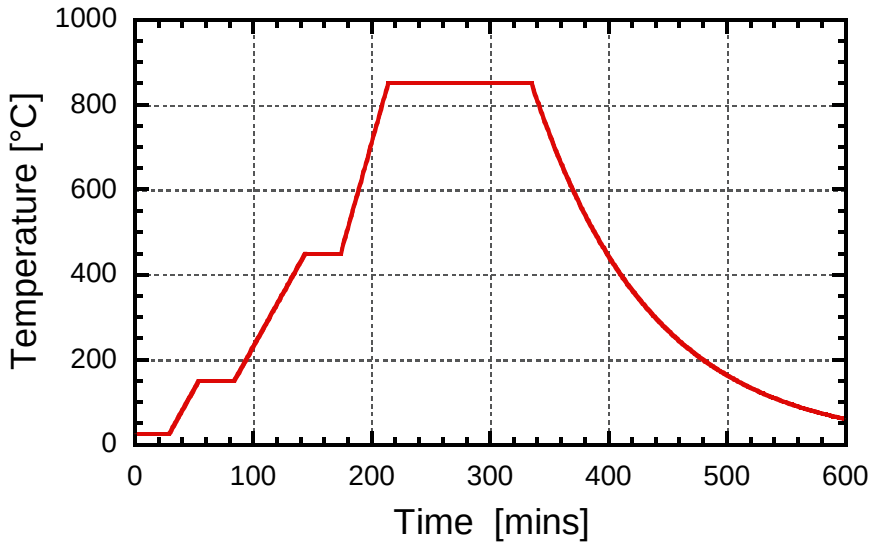

Figure 4.2: Carbonisation temperature schedule

Carbonisation was carried out in a Carbolite 2408 tube furnace under argon flowing at 300 cm^3 min^{-1}. Roughly 4 g of milled carbon precursor was added to a ceramic crucible which was then placed in the centre of the furnace tube. The tube was purged with argon for 30 mins to remove oxygen before heating commenced. A heating schedule developed for the carbonisation of resorcinol-formaldehyde xerogels [**197**] was used (with minor modifications) and is illustrated in Figure 4.2.

The temperature was raised to 150°C at a rate of 5°C min^{-1} and soaked for 30 mins, then raised to 450°C at a rate of 5°C min^{-1} and again soaked for 30 mins. The temperature was then raised to the final carbonisation temperature of 850°C at 10°C min^{-1} where it was maintained for 120 mins. The furnace was allowed to cool slowly to room temperature under flowing argon. The alterations to the heating schedule are discussed at the beginning of the following chapter.

4.1.3 Activation

Activation was carried out to open up the porosity contained in carbonised samples. The furnace was heated to the activation temperature at a rate of 10°C min^{-1} in an argon atmosphere, and carbonised samples were then activated in CO_2 flowing at 200 cm^3 min^{-1} for 60 mins at 850°C. The furnace was allowed to cool slowly to room temperature under flowing argon.

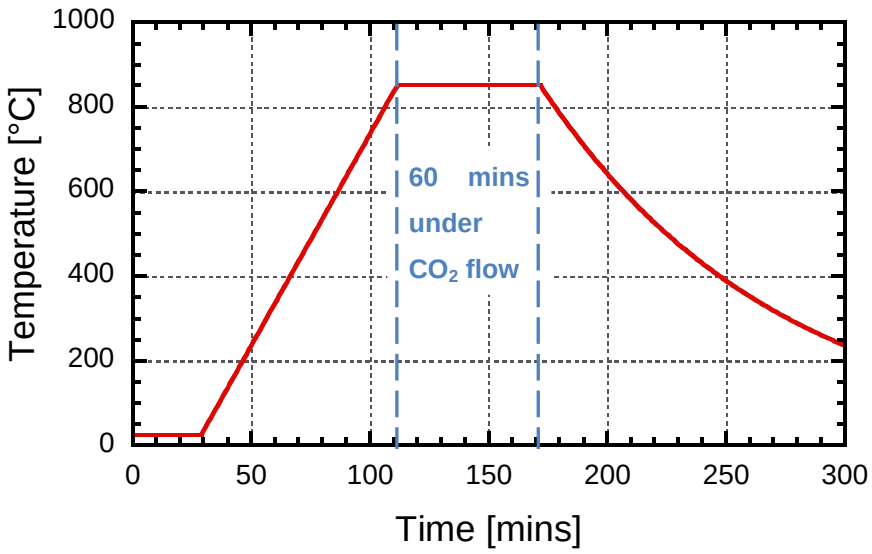

Figure 4.3: Activation temperature schedule

4.1.4 Hydrogen Treatment of Carbon Materials

Nitrogen groups were removed from the sample surface by heating to 1000°C in a hydrogen atmosphere. Approximately 1 g of carbon material was added to a ceramic crucible which was then placed in the centre of the furnace tube. The tube was purged with hydrogen for 120 mins prior to heating to ensure all oxygen was removed from the tube. The furnace was heated to 1000°C at a rate of 10°C min^{-1} under hydrogen flowing at 200 cm^3 min^{-1}. The sample was then soaked at 1000°C for 120 mins before being allowed to cool slowly to room temperature under flowing argon. This procedure was repeated under an argon atmosphere to provide a suitable material for comparison. An intermediate material was produced using the same procedure where the gas fed to the furnace was switched from hydrogen to argon

after the material had been soaked for 60 mins at 1000°C in order to maintain the same thermal treatment conditions.

4.1.5 Milling of Carbon Materials

Particle size was reduced to <38 μm by milling the activated carbon materials for 60 mins in a SPEX SamplePrep 8000M Mixer/Mill using a silicon nitride vial and balls. Samples were added to the vial under argon in a glove box (Saffron Scientific Equipment Ltd.) to prevent oxidation of the carbon materials during high-energy milling.

4.2 Physical/ Chemical Characterisation

4.2.1 Thermal Gravimetric Analysis (TGA)

Thermal gravimetric analysis was carried out using a Mettler Toledo TGA/DSC1 STARe instrument. Approximately 20 mg of sample was transferred to an alumina crucible and placed alongside a reference crucible at the appropriate position on the horizontal balance. The sample mass was recorded as the furnace was heated from room temperature to 1000°C at a rate of 5°Cmin^{-1} under flowing nitrogen.

Proximate analysis was performed using the same instrument. Samples were heated to 400K at a rate of 100Kmin^{-1} under nitrogen flow, and this temperature was maintained for 10 mins. The temperature was then increased to 1200K at 100Kmin^{-1}, and the sample was soaked at this temperature for 5 mins to allow for complete removal of volatile species. The furnace was cooled to 1100K and the gas was switched to oxygen for a period of 30 mins to ensure complete combustion of the carbon in the sample. The furnace was then cooled back to room temperature. As with previous TGA experiments, the results were corrected using data from an experimental run using an empty sample pan.

4.2.2 Nitrogen adsorption/ desorption

Nitrogen adsorption/desorption isotherms were obtained using a Micromeritics ASAP 2420 instrument at the temperature of liquid nitrogen (77K) from a helium/ nitrogen mixture. (Physical adsorption of helium does not occur as the analysis temperature is significantly greater than the critical temperature of helium.)

Carbon materials were dried for several days at 50°C before being transferred to a clean sample tube that was weighed accurately. Roughly 0.2 g of sample was used for each analysis. Samples were degassed under an initial slow vacuum to 5 mmHg at room temperature to remove the majority of physically adsorbed molecules. A fast vacuum was then applied until a pressure of 10 μmHg was obtained. The sample was heated to a temperature of 50°C and held for 30 mins, before raising the temperature to 200°C which was maintained for 10 h. Degassed samples were cooled to room temperature and backfilled with analysis gas before re-weighing to ascertain the 'degassed' sample mass.

Samples were analysed using two different methods. An initial isotherm was produced for each material for relative pressures between roughly 0.05 and 1.0, (consisting of 40 adsorption and 30 desorption points). In this method a filler rod was added to the sample tube after degas to accelerate analysis.

Selected samples underwent a more rigorous analysis over the relative pressure range of 0.005 - 1.0, using a low dose rate of 3.0 cm^3g^{-1} per increment until a relative pressure of 0.1 was achieved. A further degassing step is advised for this method to ensure that all molecular species were removed, and was carried out on the analysis port. Filler rods were not added to the sample tube using this method but seal frits were used to prevent any particulates being carried over into the vacuum system. Samples were heated at 150°C under vacuum for a period of 2 hours and were not backfilled with analysis gas prior to analysis.

4.2.3 Pycnometry

Helium pycnometry was used to determine the skeletal density of carbon materials using a Micromeritics AccuPyc 1340 instrument. Roughly 0.25 g of sample was weighed accurately in the sample cup and transferred to the pycnometer. The system was flushed with helium prior to measurements being taken. Density measurements were taken using the Micromeritics software, using an equilibration cut-off of 0.0050 psig min^{-1} until a value within 1% error was obtained using four consecutive measurements.

4.2.4 Elemental Analysis

The carbon, hydrogen and nitrogen contents of the carbon materials were determined using a Perkin Elmer 2400 Series II CHNS/O Elemental Analyser. Approximately 2 mg of sample was weighed accurately in a tin capsule, which was then folded and transferred to the analyser. The capsule was heated to 925°C in oxygen and the products of combustion were catalysed and interferences removed. CO_2, H_2O and NO_2 were carried by helium to a gas chromatography column where they were separated. The detector signals were then converted to a percentage of the total sample mass by comparison with an acetanilide standard.

4.2.5 X-Ray Photoelectron Spectroscopy

XPS was performed in an ion pumped VG Microtech CLAM 4 MCD analyser system using 200 W unmonochromated Mg X-ray excitation (20 mA at a potential of 10 kV). The CLAM 4 has variable slits for small area analysis and the 5 mm slit was used in this case with no apertures selected. Milled carbon samples were supported on stubs using conductive carbon tape and were introduced to the instrument through a turbo molecular pumped entry lock. The entry lock was evacuated for about 15 mins before the sample was introduced into the analysis chamber. An annotated photograph of the instrument is given in Figure 4.4.

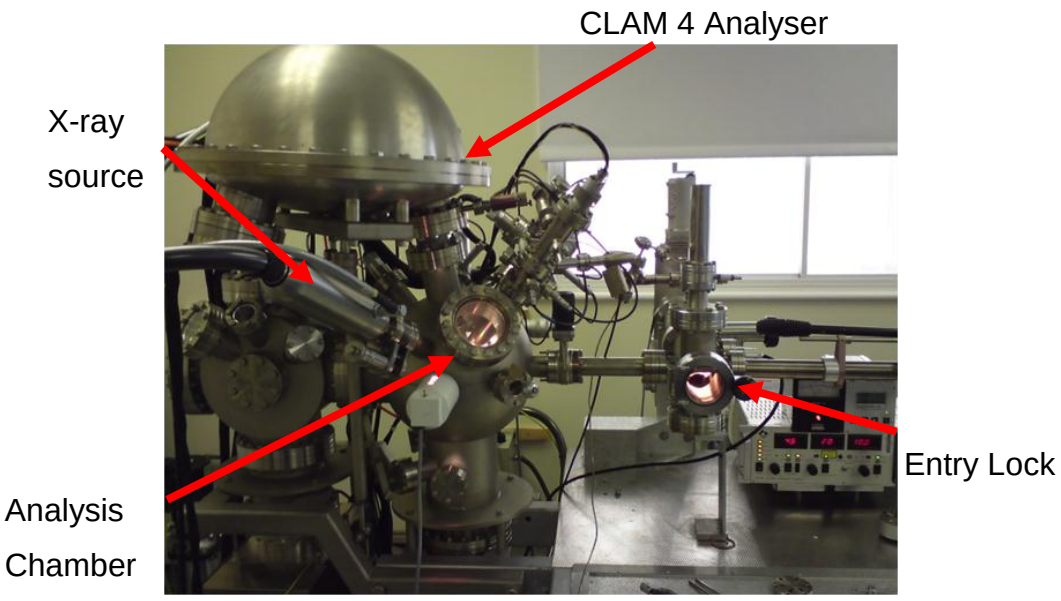

Figure 4.4: XPS setup (Dept. of Materials, University of Oxford, U.K.)

The analyser was operated at constant pass energy of 100 eV for wide scans and 20 eV for detailed scans. Sample charging was not observed. Data was obtained using SPECTRA version 8 operating system and data processing was performed using CASA XPS software. Peak areas were measured after satellite removal and background subtraction [**296**]. Elemental compositions were determined by dividing the obtained peak areas by their relative sensitivity factors given in Table 3.2 [**272**]. Deconvolution of the N1*s* peak was performed using the binding energies given in Table 3.3 with mixed 30% Gaussian-Lorentzian line shapes with a FWHM of 1.0 eV for the groups N-5, N-6 and N-Q, and the FWHM for N-X being in the range 1.5 - 2.0 eV to give the best fit.

4.2.6 Small Angle Neutron Scattering

Small-angle neutron scattering (SANS) was performed using the LOQ small-angle diffractometer at the ISIS Pulsed Neutron Source (STFC Rutherford Appleton Laboratory, Didcot, U.K.) [**297**, **298**]. A schematic of the LOQ instrument is given

in Figure 4.5 [**299**]. LOQ is a fixed-geometry "white beam" time-of-flight instrument which utilises neutrons with wavelengths between 0.2 and 1 nm. Data was simultaneously recorded using an 8mm diameter beam on two, 2-dimensional position-sensitive neutron detectors, to provide a simultaneous Q range of 0.08 - 16 nm^{-1}. Each sample was placed in a 2 mm path length, rectangular quartz cuvette (Hellma Analytics). Pure deuterium oxide (D_2O, Aldrich, 99.9 atom % D) was used for contrast-matching experiments, and samples underwent brief sonication to encourage the penetration of contrast-matching fluid into all accessible pores.

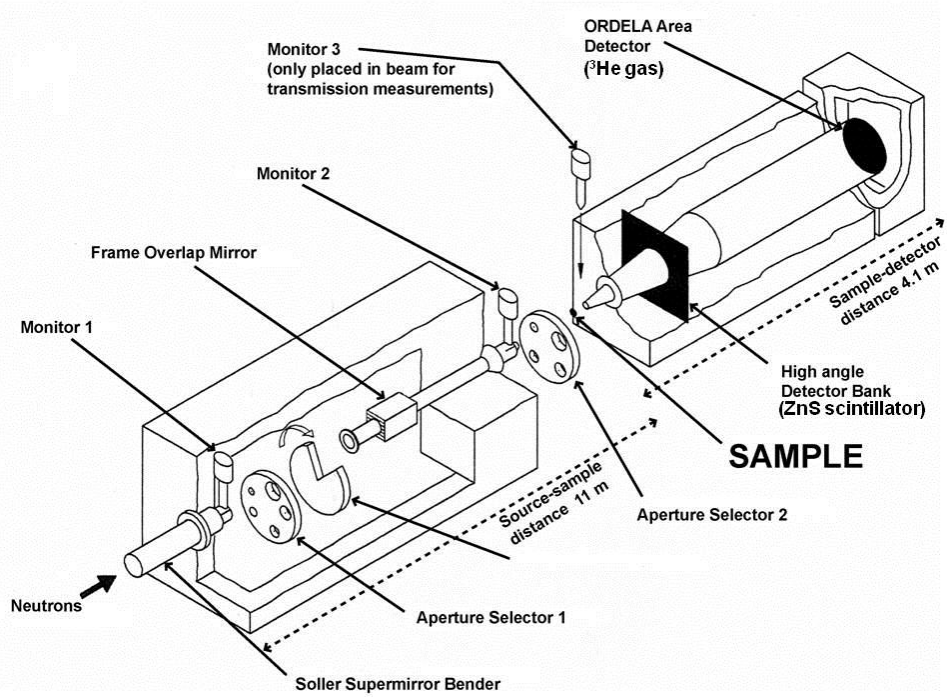

Figure 4.5: Schematic of the LOQ small-angle diffractometer at the ISIS pulsed neutron source. (STFC Rutherford Appleton Laboratory, Didcot, U.K.)

Transmission data was collected for 8 µAh, SANS for 60 µAh and CM-SANS for roughly 150 µAh in order to gather data of high statistical precision. SANS experiments were carried out for a shorter time than the CM-SANS runs to prevent saturation of the detector. Transmission data showed that no multiple scattering effects occurred.

Each raw scattering data set was then corrected for the detector efficiencies, sample transmission and background scattering, and was converted to scattering cross-

section data ($d\Sigma/d\Omega$ *vs* Q) using the instrument-specific COLETTE software. Results were placed on an absolute scale using the scattering data from a standard sample in accordance with established procedures [**300**].

4.3 Electrochemical Characterisation

4.3.1 Electrode Production

Electrodes were manufactured by mixing 240 mg of the material under study with 30 mg polymer binder (Kynar® 2801) and 30 mg milled carbon black (Cabot XC72), to give an 80/10/10 ratio by mass of sample/binder/carbon black[2]. Carbon black was milled for 60 mins before use to ensure that uniform sheets of electrode were cast. 1.7 cm^3 acetone was added to the dry powder and an homogenous slurry was formed by stirring in a closed sample vial for 4 hours. The slurry was then cast onto a glass plate and spread to a wet film thickness of 500 µm using a micrometer adjustable gap paint applicator (RK Print Coat Instruments, Ltd.). Electrode sheets were dried by heating overnight in an oven at 85°C. This facilitated the removal of the electrode from the glass by causing the polymer binder to soften slightly. Electrode sheets were removed using a wide, flat blade and, if the electrode was found to curl excessively, it was pressed overnight in an oven at 85°C between two small glass plates. Discs 13 mm in diameter were pressed from the flat sheet and any discs with noticeable defects (cracks, irregular edges, pinholes *etc.*) were discarded. It is estimated that the thickness of the dried electrode sheets is 100 - 250 µm. Electrode discs were weighed and matched as closely as possible to a counter electrode of the same composition. The average electrode mass was roughly 10 mg, and paired electrodes differed in mass by 0.1 mg at most.

Pairs of electrodes were soaked in potassium hydroxide solution (Aldrich, 28.5 ± 0.5 wt.%) and sonicated for 15 mins to encourage electrolyte diffusion into the smallest

[2] This procedure was found to produce mechanically stable electrodes where the pore volume of the sample was less than 0.5 cm^3g^{-1}. For greater pore volumes, a larger proportion of binder was found to be necessary.

pores[3]. Electrodes were soaked in electrolyte for at least three days prior to cell manufacture.

Symmetric two-electrode EC cells were constructed using a modified version of a test cell used in previous investigations [**195**, **301**, **302**, **196**]. A schematic of the cells used is given in Figure 4.6 [**195**]. 13 mm diameter discs of 50 µm thick nickel foil (Goodfellow, >99.99%) were used as current collectors to protect the steel components from corrosion. A 13 mm diameter disc of glass fibre filter paper was used to separate the electrodes and was soaked in electrolyte before being inserted into the cell to ensure that an excess of electrolyte was available. The plunger screw was finger-tightened to ensure good contact between the electrodes, current collectors and external plates.

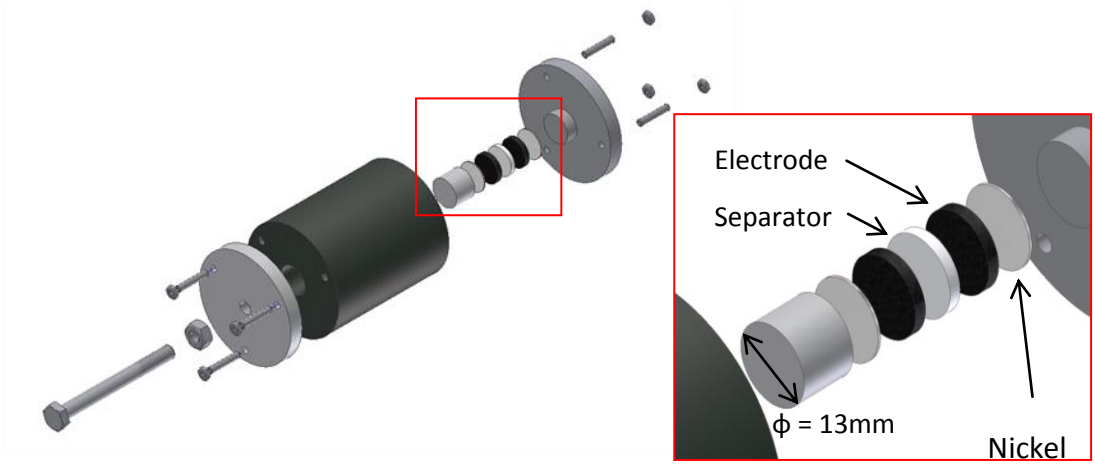

Figure 4.6: Test cell with symmetric electrode arrangement (inset)

Electrochemical tests were carried out using a Solartron Analytical 1470E Multichannel Potentiostat/ Galvanostat with 1455A Frequency Response Analyser and MultiStat *v*1.1b software, (Scribner Associates, Inc.). The cell temperature was maintained at 25°C (± 0.1°C) using a Friocell temperature control cabinet.

Cells were initially conditioned by cycling 10 times between 0.0 and 1.0 V (*vs* OCP) at a rate of 100 mA. The cell was subsequently charged to 1.0 V at 10 mA and

[3] A modified test cell to enable vacuum filling of the cell chamber was manufactured, however the electrodes were not mechanically strong enough to withstand the flow of electrolyte through the chamber.

switched to open circuit for 10 mins. These 'break-in' steps were found to be necessary to produce reproducible results.

4.3.2 Galvanostatic Charge/ Discharge

Cells were cycled between 0.0 and 1.0 V (*vs* OCP) at rates of 100, 64, 32, 16, 8, 4 and 2 mA (roughly 0.1 to 5 A g^{-1}, depending on the actual mass of the electrodes used) for twenty charge/ discharge cycles. The value of cell capacitance was calculated on the tenth discharge cycle at each rate.

4.3.3 Electrochemical Impedance Spectroscopy

Electrochemical impedance spectra were obtained at a potential bias of 0.1 V (*vs* OCP) using a 10 mV signal over the frequency range 100 kHz to 10 mHz. Each spectrum was measured twice, as the data from the initial runs were found to be erratic. The value of cell capacitance was obtained at 10 mHz from the imaginary component of the impedance using the relationship given in Eq. 3.54. Nyquist plots and equivalent circuits were evaluated using ZView software (Scribner Associates, Inc.).

4.3.4 Cyclic Voltammetry

Cyclic Voltammetry was performed between 0.0 and 1.0 V (*vs* OCP) at sweep rates of 10 mV s^{-1} (for 2 cycles) and 100 mV s^{-1} (for 10 cycles). Cell capacitance was obtained using the magnitude of the average current response to a particular sweep rate.

4.3.5 Self-discharge

Cells were charged to 1.0 V (*vs* OCP) at a constant current of 50 mA and switched to open circuit for 60 mins to monitor the voltage decay resulting from self-discharge mechanisms.

4.3.6 Galvanostatic Cycling

Further charge/ discharge cycles between 0.0 and 1.0 V (*vs* OCP) were carried out at a constant current of 100 mA with the specific capacitance being determined periodically. EIS and self-discharge measurements were repeated after 1000 and 10000 cycles.

5 Results & Discussion

To ascertain if there is any practical benefit in the addition of nitrogen groups to carbon materials used in the manufacture of aqueous based EC electrodes, materials were produced using the method of simultaneous carbonisation outlined in the previous chapter. As the pore structure of RF xerogels can be easily controlled and the nitrogen content of carbon materials can be tailored through the impregnation of *m*-phenylene diamine into the xerogels before carbonisation, this process was explored as a method to investigate the influence of nitrogen content on the specific capacitance of carbon materials.

The development of the method used to produce carbon materials for study is outlined at the start of this chapter, and the reasons for carrying out future experiments in a particular manner are discussed.

The electrochemical behaviour of some of these materials is discussed with respect to their physical and chemical characteristics, and it was found that several of the same problems seen in the literature were also applicable to the interpretation of the results in this work.

In an effort to clarify the role that nitrogen heteroatoms play in the mechanism(s) that affect the electrochemical behaviour of these materials, it was proposed that further thermal treatment under hydrogen could be used to selectively remove nitrogen groups from the materials without influencing the physical structure to any great extent. These materials are then discussed with respect to their physical and chemical characteristics.

Additionally, contrast-matching small angle neutron scattering (CM-SANS) has been put forward as a technique that can be used to investigate the degree of inaccessible porosity in electrode materials.

5.1 Adjustment of synthesis procedure

A reproducible method for the production of RF xerogels has been previously established and these materials have been well characterised [**195**, **197**]. However, it should be noted that the addition of *m*PDA requires an additional processing step that can be expected to adversely affect the pore characteristics of the resultant materials. Typically, *m*PDA in solution (ethanol [**227**] or acetone [**203**]) is added to the precursor and the solvent is removed through evaporation. In the production of RF gels the solvent exchange step offers an opportunity to insert *m*PDA into the pore structure of the gel before drying, and as the volume of the gel shrinks substantially during drying, a more thorough impregnation of *m*PDA into the precursor can be expected.

Additionally, preliminary experiments where *m*PDA was added to the RF xerogel after drying produced a sticky material that was difficult to handle. When adding *m*PDA before drying the precursor, the established drying procedure [**195**, **197**] required a slight alteration. In the usual method, excess solvent is decanted or filtered off whereas, to ensure that all *m*PDA remains in the precursor, all of the solvent was removed through evaporation in this work.

5.1.1 Development of Carbonisation Schedule

From TGA data obtained using different formulations of RF xerogel, it has been seen that the removal of volatile components is virtually complete at temperatures greater than 800°C [**195**, **197**, **198**]. The mass loss profiles of RF gels at a heating rate of 10°C min^{-1} is almost identical for R/C ratios between 100 and 500 [**195**].

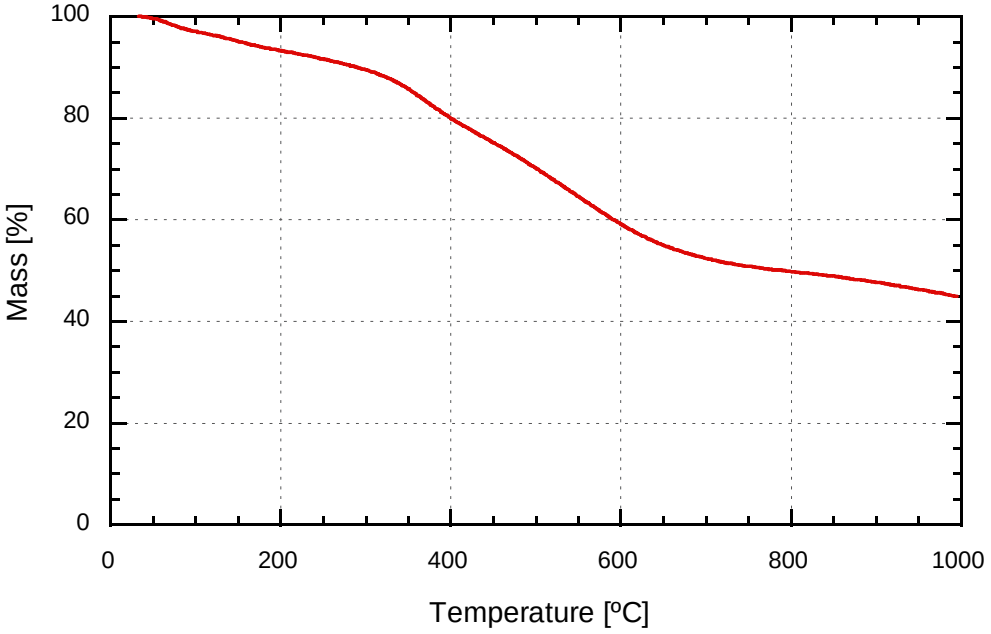

Figure 5.1: TGA profile of RF xerogel (R/C = 500) heated at a rate of 5°C min^{-1} to 1000°C under nitrogen

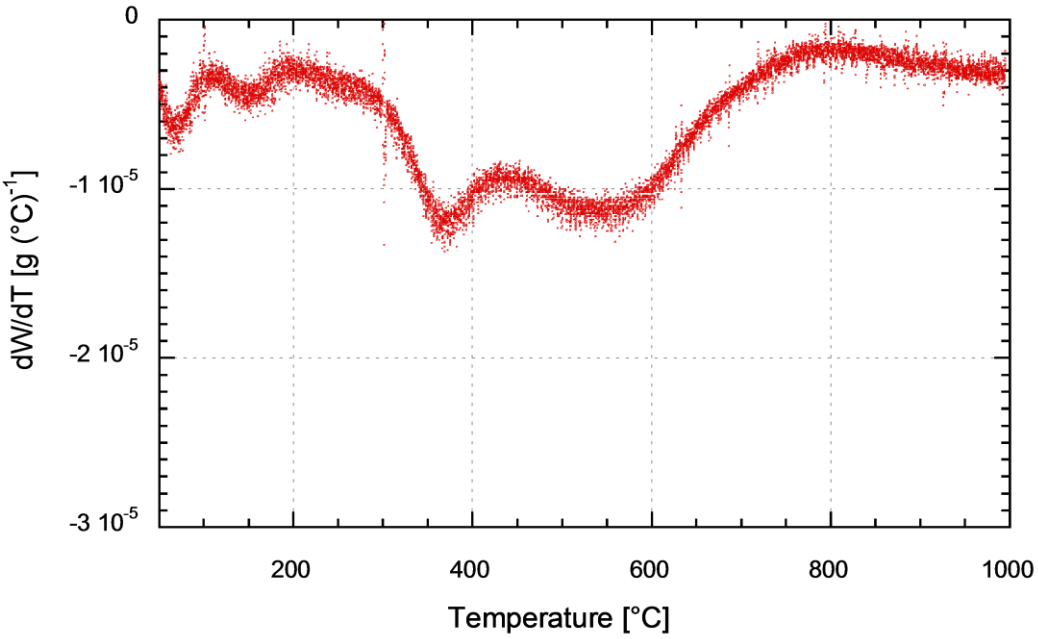

Figure 5.2: DTGA profile of RF xerogel (R/C = 500) heated at a rate of 5°C min^{-1} to 1000°C under nitrogen

The mass loss profile obtained for a sample RF xerogel is shown in Figure 5.1 and, when considered alongside the derivative curve in Figure 5.2, can be broken down into four distinct sections. At temperatures less than 300°C, mass loss is attributed to the removal of any residual solvents from the structure. Despite drying the gel under vacuum at 80°C until a constant mass was obtained, there is likely to be a small amount of solvent in the sample that can only be liberated by further heating due to the strong adsorption potential present in micropores. Approximately 10% of the total sample mass is due to the removal of residual solvents and/or species adsorbed from the atmosphere. An increased rate of mass loss is observed over the temperature range of 300 - 800°C, with two distinct derivative peaks appearing in this region. The derivative curve approaches maxima at values of 380°C and 550°C and indicates that there are two different decomposition processes associated with carbonisation. It has been postulated that the peaks are associated with the cleavage of C-O bonds at the lower temperature and C-H bonds at the higher temperature [**198**]. The first mechanism seems to be complete at a temperature of 450°C as the derivative curve approaches a constant value at this point. The removal of volatiles is virtually complete at a temperature of around 800°C. (The small amount of mass loss observed at temperatures greater than 800°C in Figure 5.1 is not seen in the literature but is likely to be due to the slower heating rate used.)

Considering the different processes that occur during carbonisation, a phased heating program was developed that allowed more time for these reactions to complete before progressing to the next stage [**197**]. This allows volatiles to evolve slowly and to be removed from the sample before further reactions occur to leave an accessible porous network in the resultant char.

Samples were also analysed using a heating schedule analogous to that used in the carbonisation process, an example of which is shown in Figure 4.2. This indicates that under this carbonisation schedule, mass loss is complete after a final isothermal step lasting roughly 120 mins at a temperature of 850°C. The char yield resulting from this procedure is roughly 43% based on the mass of sample after vacuum drying. When carbonised in a tube furnace, the yield achieved was 52.7%. The disparity between the yields produced by the two methods may be down to a

combination of several factors; for example, the gas used in the TGA experiments was nitrogen whereas the tube furnace was operated under argon, the yield was calculated based on the sample mass at 850°C in the TGA and at room temperature in the tube furnace, and the ratio of gas flow to sample mass is very much greater in the TGA when compared to that in the tube furnace.

5.1.2 Carbonisation Temperature

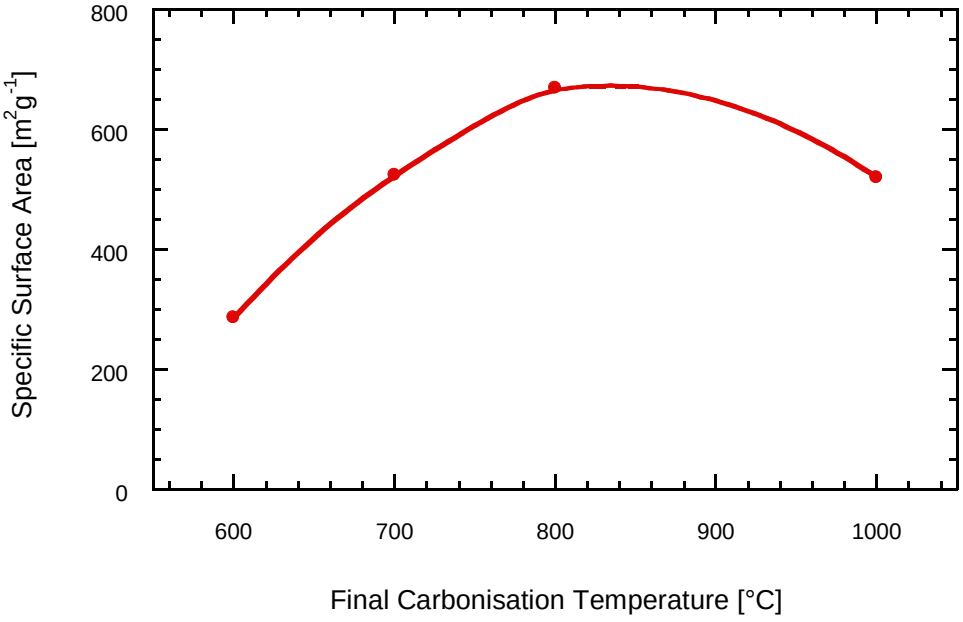

Figure 5.3: Specific surface area against final carbonisation temperature for R/C = 100 RF xerogel [197]

The maximum temperature used in the carbonisation process affects the final pore structure and surface area of the char, as well as influencing the electrical conductivity of the material. Using the phased heating program illustrated in Figure 4.2, the effect of the final temperature on the specific surface area of the char was investigated [**197**] and the result is shown in Figure 5.3.

Figure 5.3 shows that the maximum specific surface area of the char is obtained when a carbonisation temperature of 800 - 900°C is used. A similar trend to that shown in Figure 5.3 was found in a different study using a more concentrated gel precursor solution (R/W ~ 0.3 g cm^{-3}) [**203**], and in this case a maximum specific

surface area of the char was observed at the lower temperature of 700°C. In other studies, a decrease in specific surface area with increasing carbonisation temperature has been observed [**303**] but in the majority of cases, results are not directly comparable as there are too many differences in the experimental conditions (*e.g.* different R/W, drying methods, heating rates *etc.*)

From several studies into the relationship between the carbonisation temperature and electrochemical performance of carbonised RF gel electrodes, results indicate that temperatures in the region of 800 - 900°C produce the highest values of capacitance on a gravimetric and volumetric basis. A typical example of this relationship is shown in Figure 5.4 [**207**]. This is probably a consequence of the relatively large specific surface area developed at these temperatures in combination with the fact that complete carbonisation has occurred to leave behind a material with a reasonable amount of graphitisation that can be expected to be highly electrically conductive. For the aforementioned reasons, a final carbonisation temperature of 850°C was chosen for use in this study.

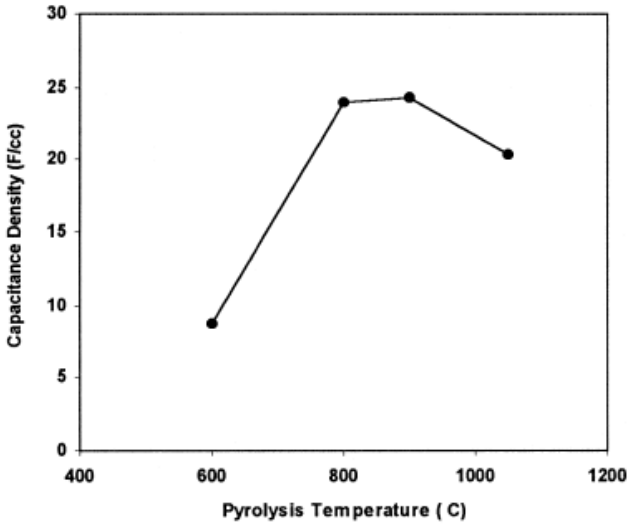

Figure 5.4: Capacitance density *vs* carbonisation temperature for R/C 200 RF aerogel [207]

5.1.3 Variation of R/C Ratio

To evaluate whether the adjustments to the synthesis and carbonisation procedures significantly affects the pore characteristics of the chars obtained, carbonised RF xerogels were produced using the procedure described previously at R/C ratios of 100, 200, 300 and 500 (with no *m*PDA added). From nitrogen adsorption isotherms, specific surface areas and pore characteristics were determined and are summarised in Table 5.1. The experimental errors associated with the calculation of specific surface areas for these samples has been determined to be less than ±15 m^2g^{-1} and the pore volumes given have an error of ±0.01 cm^3g^{-1}. For comparison, data reported for xerogels produced using comparable techniques (*i.e.* same R/W, drying method *etc.* but carbonised at 800°C for 180 mins) are also included in Table 5.1.

R/C	Specific surface area [m^2g^{-1}]	Total Pore Volume [$cm^3\ g^{-1}$]	Micropore Volume [$cm^3\ g^{-1}$]	Mesopore Volume [$cm^3\ g^{-1}$]	Average pore diameter* [nm]	[Ref.]
100	515	0.28	0.18	0.07	2.1	[this work]
200	625	0.43	0.18	0.25	2.8	[this work]
300	590	0.56	0.17	0.39	3.8	[this work]
500	615	1.10	0.18	0.82	7.1	[this work]
100	670	0.38	0.33	0.05	2.2	[**197**]
200	700	0.71	0.18	0.53	6.6	[**197**]
500	645	1.23	0.21	1.01	21.7	[**197**]
100	410	0.21	0.18	0.04	2.2	[**195**, **196**]
200	615	0.42	0.20	0.23	3.5	[**195**, **196**]
300	655	0.64	0.18	0.46	4.9	[**195**, **196**]
500	640	0.92	0.19	0.73	8.9	[**195**, **196**]

Table 5.1: Surface area and pore volumes of carbonised RF xerogels (*modal pore widths are reported for this work and refs [195, 196] whereas the mean is reported in ref [197])

Similar trends in the pore volume data are seen for each R/C series and comparable values of surface area are produced using the altered synthesis procedure. For each

R/C ratio the altered synthesis procedure produces smaller values of average pore diameter but the same trend with increasing R/C ratio is observed. The narrowing of the average pore diameter may be due to increased capillary forces during the evaporation of the solvent, but it is more probable that the increased carbonisation temperature is responsible for this effect. (It is also likely that the particle size differs for each of the R/C series in Table 5.1, as it has been found that the specific surface area and pore volumes attributed to carbonised RF xerogels decrease with reductions in average particle size [**195**].)

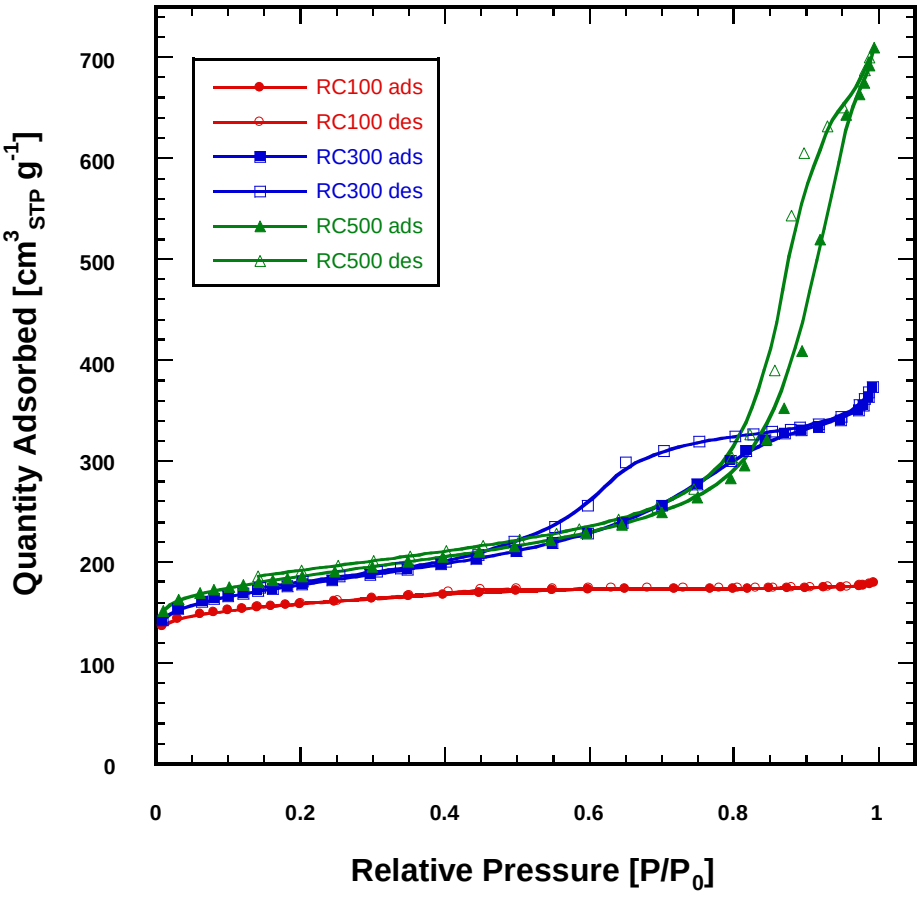

Figure 5.5: Nitrogen Adsorption Isotherms (at 77K) of carbonised RF xerogels (R/C = 100, 300 and 500)

The nitrogen adsorption isotherms in Figure 5.5 show that the materials produced vary in their degree of porosity and pore structure. There is a similar quantity of nitrogen adsorbed at low relative pressure for all samples (*ca.* 140 cm^3_{STP} g^{-1}) which

suggests that the micropore volume does not vary greatly with R/C ratio. The carbonised R/C = 100 RF xerogel displays a type I isotherm that is usually seen when the adsorbent is predominantly microporous [**170**]. A typical type IV isotherm is exhibited by the R/C = 300 material and the observed difference between adsorption and desorption isotherms is indicative of mesoporosity. The hysteresis loop is best approximated by the type H2 loop (see Figure 3.3) which indicates that a network of interconnected pores is present in the adsorbent [**170**]. This type of hysteresis loop has also been linked to the presence of open-ended cylindrical pores [**304**].

A type IV isotherm is also obtained using the R/C = 500 derived material, however the hysteresis loop differs from the H2 type as a definite limiting uptake is not observed at high relative pressures. The loop is perhaps better described as belonging to the H3 type which is associated with adsorbents that are composed of agglomerated plate-like particles that form slit shaped pores [**170**].

Figure 5.5 illustrates the diversity of the pore structures that are produced through the carbonisation of RF xerogels. These isotherms also reflect the change in reaction rates with R/C ratio; at R/C = 100 the formation of primary particles is dominant whereas at lower catalyst concentrations primary particles are produced at a slower rate and form loose agglomerates before gelation. The differences between the pore structures are more obvious in Figure 5.6 where the quantity adsorbed relative to the total uptake is plotted against the relative pressure. These plots give a better indication of the pore size distribution present in the materials. For example the pore volume of the R/C = 100 material consists largely of micropores as the uptake is almost 80% at low relative pressure, whereas the R/C = 500 material shows only 20% of the total uptake at the same relative pressure, and can be presumed to be predominantly mesoporous.

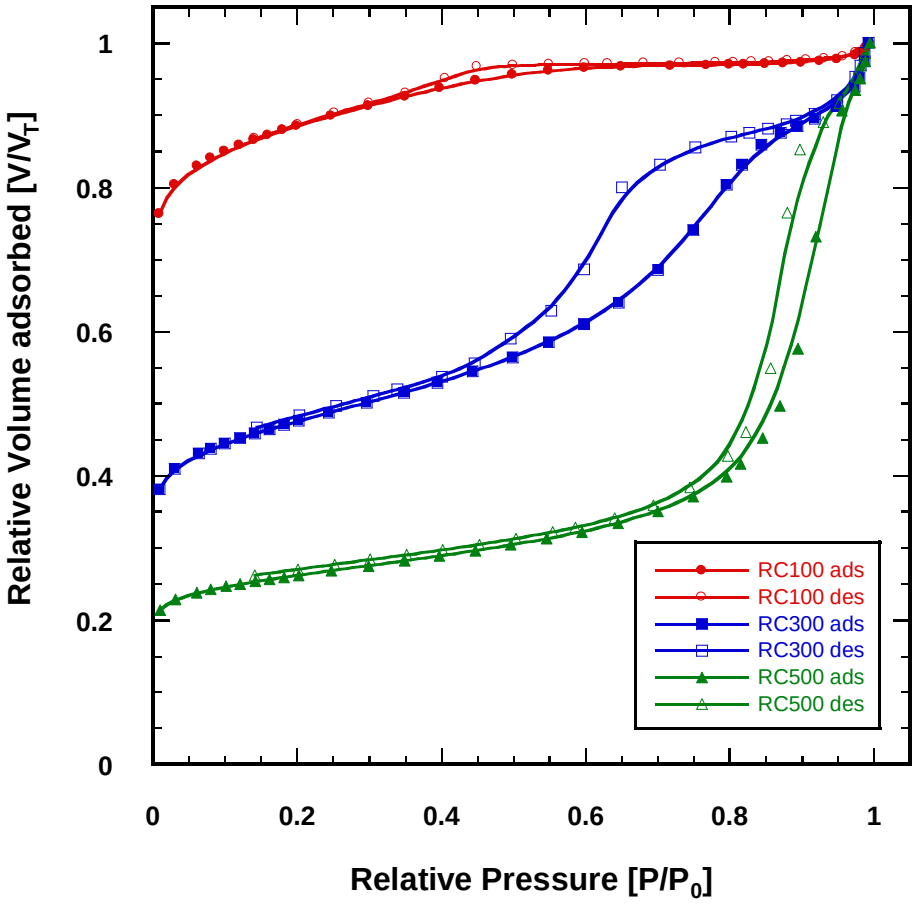

Figure 5.6: Nitrogen Adsorption Isotherms (at 77K) of carbonised RF xerogels (R/C = 100, 300 and 500) normalised to volume adsorbed at maximum uptake

From the nitrogen adsorption data, the mesopore size distribution was determined using the BJH method for each of the materials produced using the altered synthesis procedure, and are shown in Figure 5.7. Despite the apparent narrowing of the average pore diameter, control over the pore size distribution by adjusting the R/C ratio was still maintained using the altered synthesis procedure, and similar structural characteristics to published results were obtained.

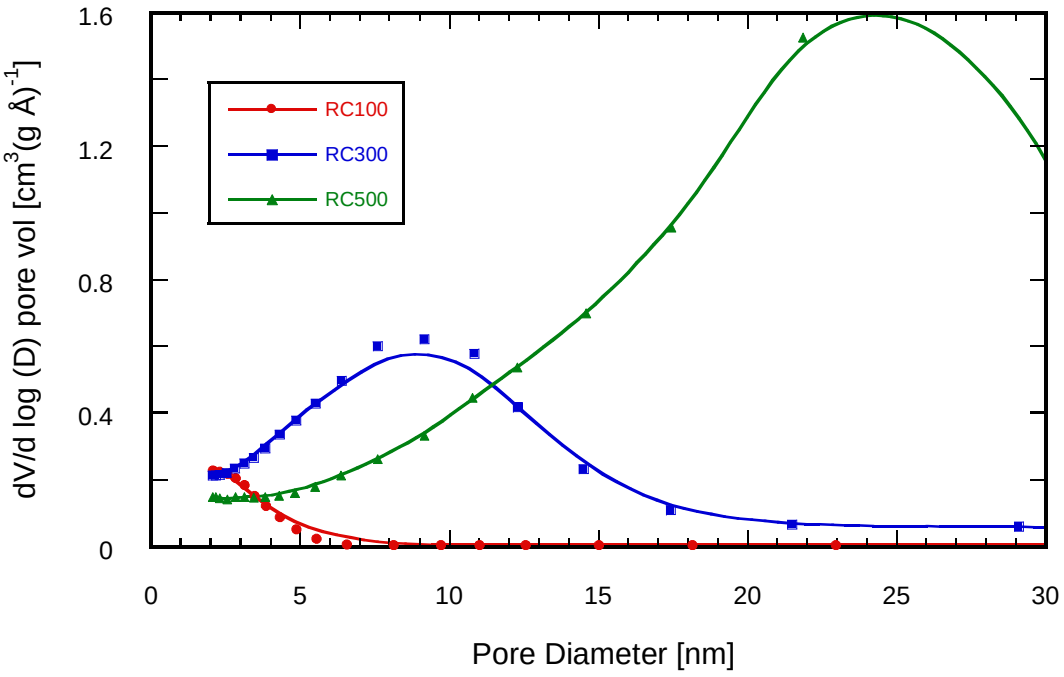

Figure 5.7: Mesopore size distribution of carbonised RF xerogels (R/C=100, 300 and 500)

5.2 Addition of mPDA

The degree to which the co-carbonisation mechanism affects the carbonisation process was investigated using the same TGA method described previously for a sample that was impregnated with 40% by mass of *m*PDA. Figure 5.8 shows the rate of mass loss as the temperature of the sample is increased to 1000°C (alongside the TGA profile of pure RF xerogel from Figure 5.1), and the corresponding derivative curve is given in Figure 5.9. Pure *m*PDA under the same conditions begins to decompose at around 150°C and is removed completely by 200°C [**203**]. In a comparison of the derivative curves (Figure 5.2 and Figure 5.9) it is clear that the co-carbonisation process shows a substantially different mass loss profile, especially with the absence of the dip centred at 550°C. This results in the majority of mass loss occurring before 400°C in the sample co-carbonised with *m*PDA, whereas a larger proportion of mass loss occurs at temperatures greater than 400°C during the carbonisation of pure RF xerogels. This indicates that the presence of *m*PDA inhibits

the carbonisation of RF xerogels, which could be expected to some extent as the pores present in the carbonisation precursor are occupied by *m*PDA. As with the pure RF xerogel, carbonisation is virtually complete at a temperature of 800°C. When the impregnated sample was carbonised using the same procedure as that in Figure 4.2, the yield was roughly 40% and the mass loss profile is shown in Figure 5.10. For comparison, the same procedure in a tube furnace achieved a yield of 51.4%.

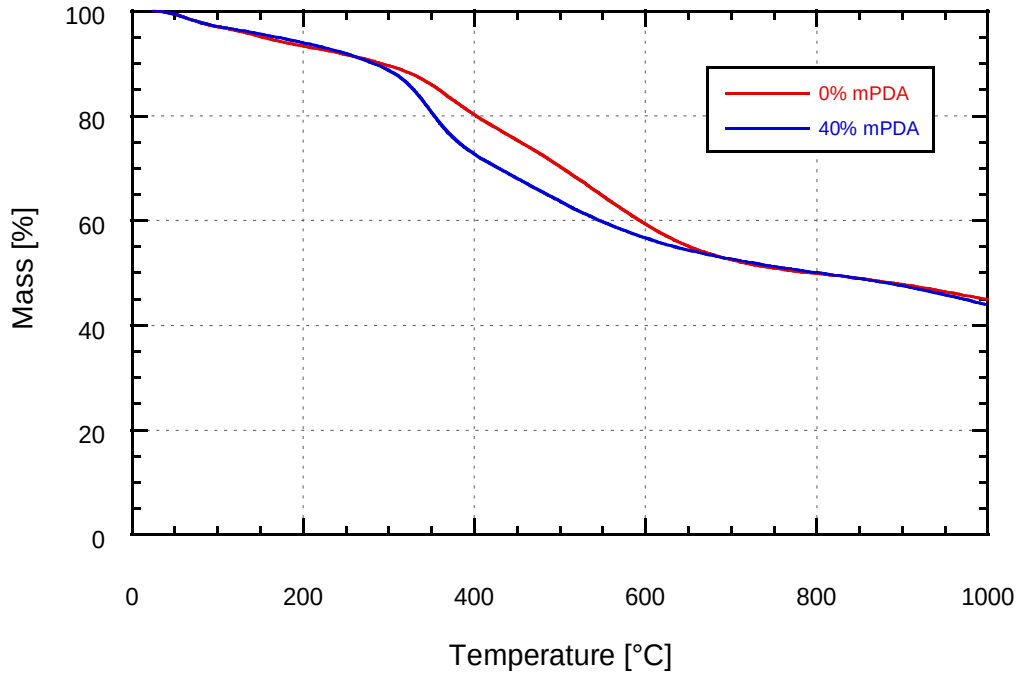

Figure 5.8: TGA profiles of R/C = 500 RF xerogel and R/C = 500 RF xerogel impregnated with 40% *m*PDA by mass, heated at a rate of 5°C min^{-1} to 1000°C under nitrogen

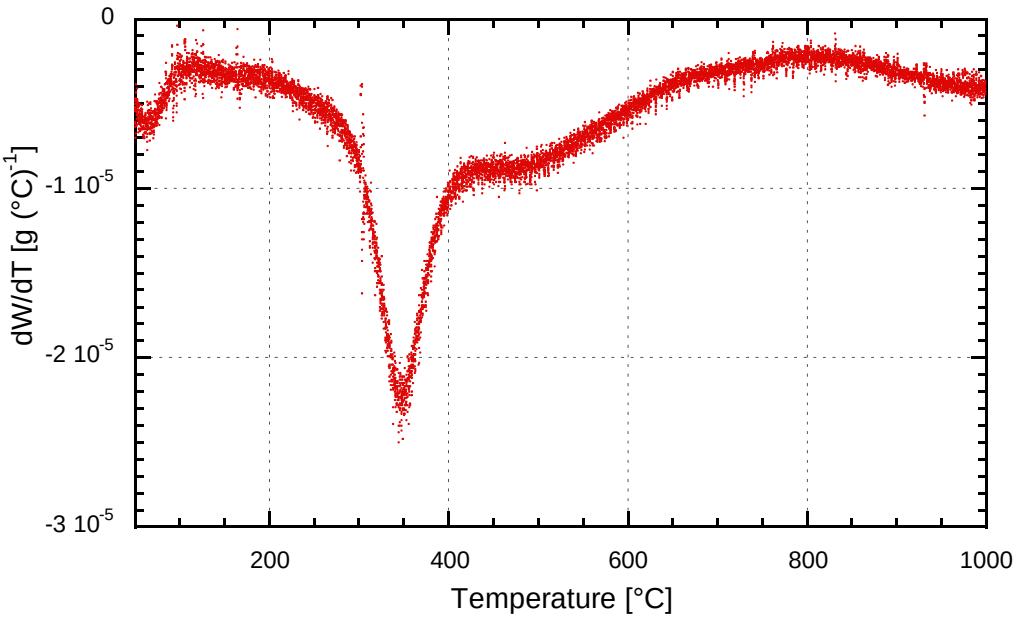

Figure 5.9: DTGA profile of R/C = 500 RF xerogel impregnated with 40% *m*PDA by mass, heated at a rate of 5°C min^{-1} to 1000°Cunder nitrogen

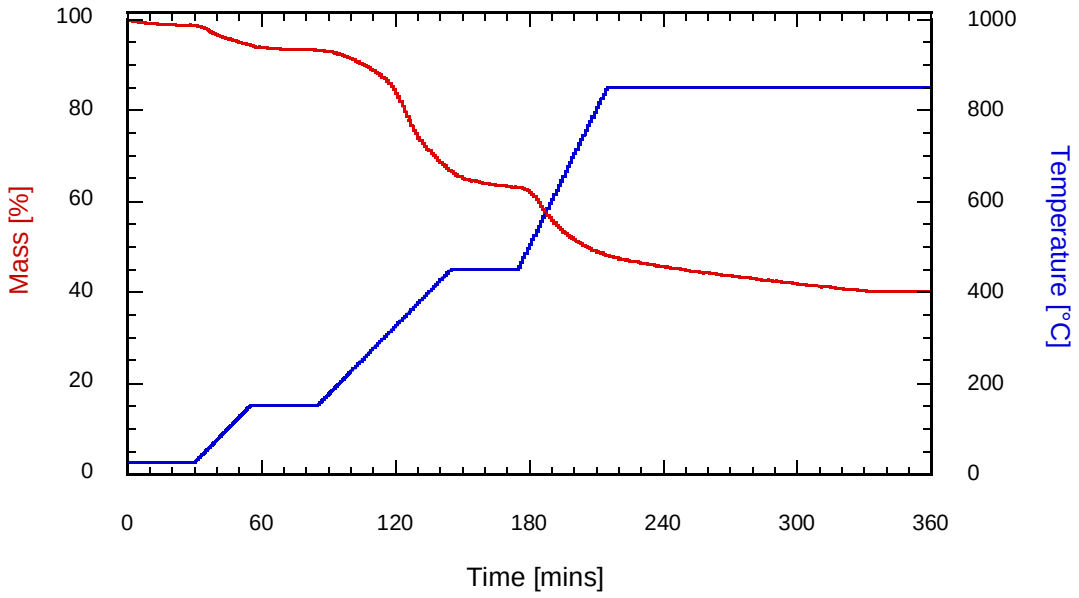

Figure 5.10: TGA profile of R/C = 500 RF xerogel impregnated with 40% *m*PDA by mass, using the indicated heating schedule under nitrogen

When compared to previous results, where the same materials were carbonised but *m*PDA was added after drying the RF gel, there is a much smaller amount of mass loss at temperatures less than 300°C [**203**]. This indicates that by adding *m*PDA

during solvent exchange, a more thorough impregnation into the pore structure was achieved, which should create a more homogenous distribution of nitrogen throughout the material.

The melting point of *m*PDA is 63°C so it can be expected that during the first stage of carbonisation (heating to 150°C at 5°C min^{-1}), or even during the drying of the gel, *m*PDA would form a liquid phase and agglomerate in the pores of the impregnated RF xerogels. The presence of *m*PDA may hinder the second phase of the carbonisation process by trapping volatiles inside the pores of the RF gel and thereby preventing the removal of heteroatoms from the RF gel.

5.2.1 Physical Characterisation

Carbonised RF xerogels were produced using the procedure described in the experimental section at R/C ratios of 100, 300 and 500, each being impregnated with 10, 20, 30 and 40% of *m*PDA (based on the mass of dried gel with no *m*PDA added). From nitrogen adsorption isotherms the surface area and pore volumes were determined, and are summarised in Table 5.2.

R/C	*m*PDA [%]	Specific surface area [m^2g^{-1}]	Total Pore Volume [$cm^3\ g^{-1}$]	Micropore Volume [$cm^3\ g^{-1}$]	Mesopore Volume [$cm^3\ g^{-1}$]	Average pore diameter [nm]
100	**0**	515	0.28	0.18	0.07	2.1
100	**10**	385	0.22	0.14	0.05	2.3
100	**20**	200	0.13	0.07	0.04	2.6
100	**30**	46	0.04	0.02	0.01	3.7
100	**40**	27	0.03	0.01	0.01	4.3
300	**0**	590	0.56	0.17	0.39	3.8
300	**10**	525	0.56	0.14	0.40	4.3
300	**20**	455	0.53	0.12	0.40	4.7
300	**30**	395	0.41	0.11	0.28	4.1
300	**40**	335	0.35	0.10	0.24	4.1
500	**0**	615	1.10	0.18	0.82	7.1
500	**10**	525	0.80	0.17	0.63	6.1
500	**20**	440	0.70	0.13	0.55	6.3
500	**30**	335	0.61	0.09	0.50	7.3
500	**40**	245	0.48	0.07	0.39	7.8

Table 5.2: Surface Areas and Pore Volumes of RF xerogels co-carbonised with *m*PDA

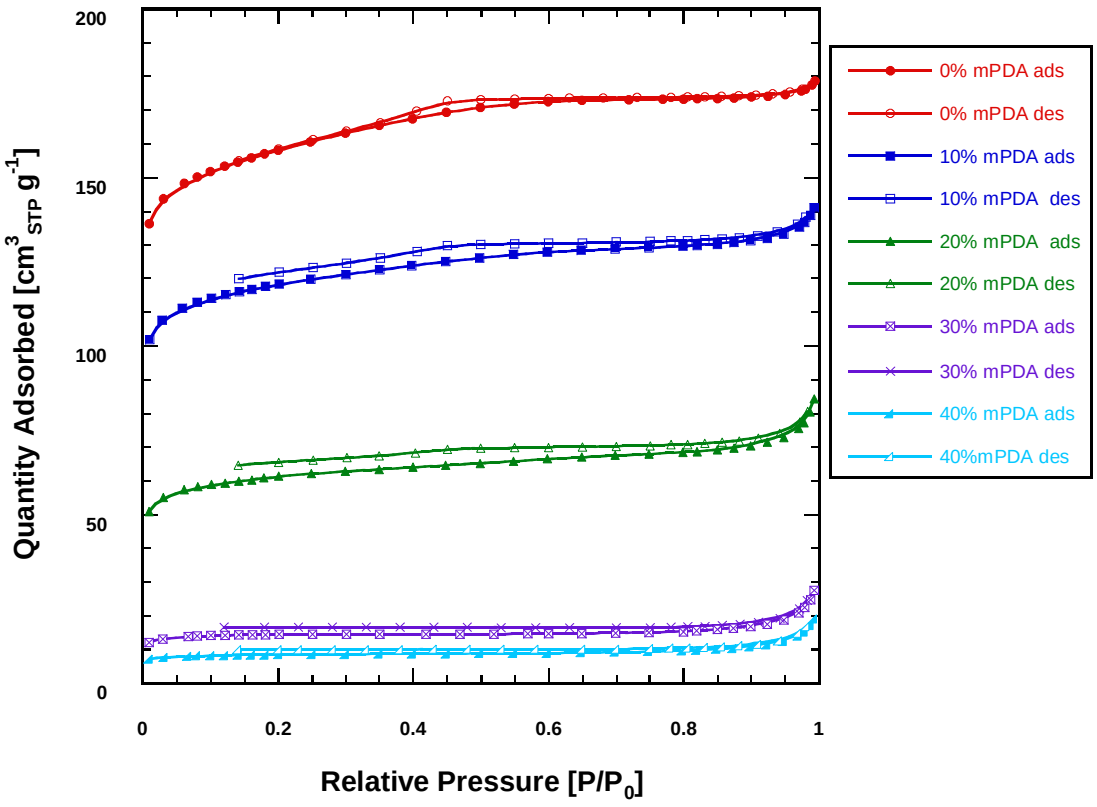

Figure 5.11: Nitrogen Adsorption Isotherms (at 77K) for R/C=100 RF xerogels co-carbonised with *m*PDA

The nitrogen adsorption isotherms for the R/C = 100 derived materials are shown in Figure 5.11. The general form of the isotherms is the same for each of the materials although the initial uptake at low relative pressure decreases with increasing fraction of *m*PDA. Therefore co-carbonisation can be seen to inhibit the generation of micropores and the extent of this effect increases with increasing fraction of *m*PDA added. The isotherms are best categorised as a combination of type I and type IV forms, although the degree of hysteresis is very small. At relative pressures less than P/P_0 = 0.42 the discrepancy between the adsorption and desorption isotherms is due to the presence of strongly adsorbing micropores in the samples [**170**].

The pore size distributions of the materials, illustrated in Figure 5.12, are also similar in form but the pore volumes corresponding to each sample decrease with increasing fraction of *m*PDA.

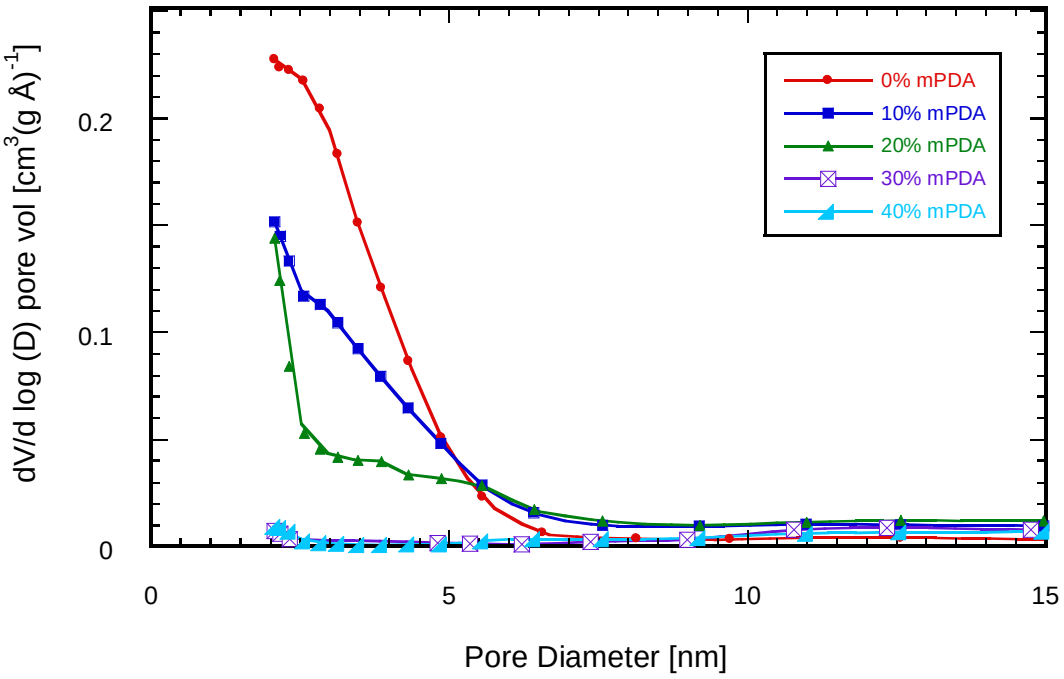

Figure 5.12: Mesopore Size Distributions for R/C=100 RF xerogels co-carbonised with *m*PDA

The nitrogen adsorption isotherms for materials produced using R/C = 300 RF xerogels are shown in Figure 5.13. Each of these isotherms is of a similar form that can be described as belonging to the type IV category, which is indicative of the presence of mesoporosity [**170**]. As with the R/C = 100 derived materials, the volume of nitrogen adsorbed at low relative pressures decreases with increasing fraction of *m*PDA added. The hysteresis loops in Figure 5.13 are best described as belonging to the H2 type and are of remarkably similar form. This can be taken to indicate that the co-carbonisation process influences the mesoporous structure to the same extent, especially for added *m*PDA fractions up to 20% by mass.

Mesopore size distributions from the nitrogen adsorption isotherms are given in Figure 5.14 and show that *m*PDA addition influences the pore characteristics of the materials, particularly by shifting the modal pore width irregularly with increasing mass fraction of *m*PDA added.

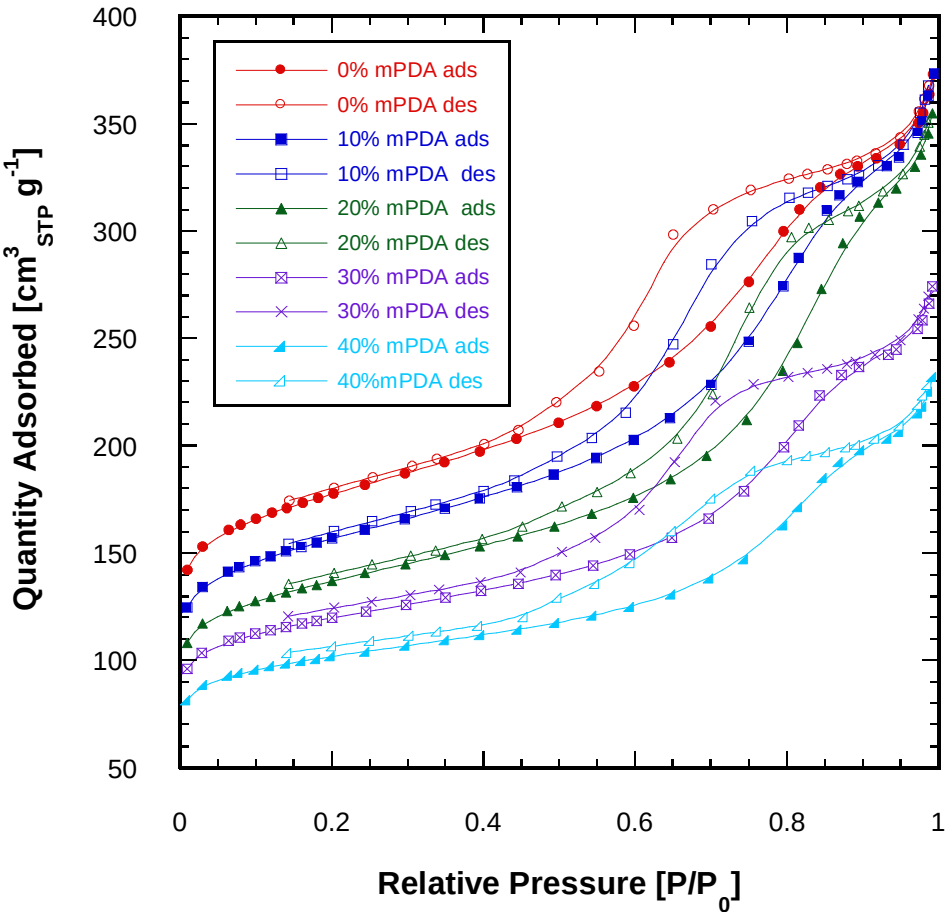

Figure 5.13: Nitrogen Adsorption Isotherms (at 77K) for R/C=300 RF xerogels co-carbonised with *m*PDA

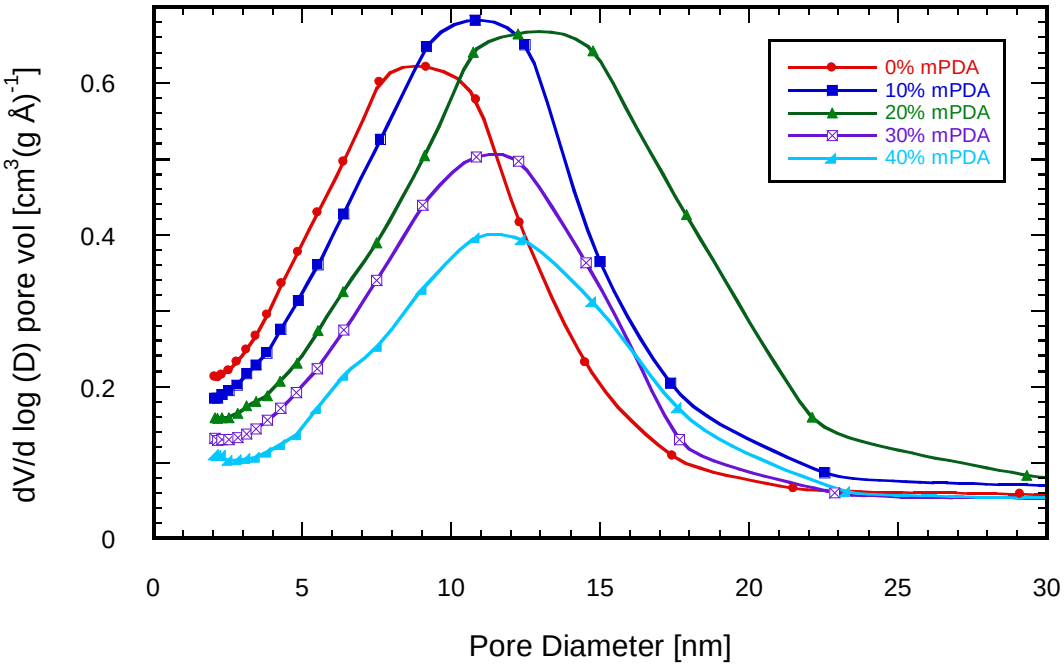

Figure 5.14: Mesopore Size Distributions for R/C=300 RF xerogels co-carbonised with *m*PDA

The nitrogen adsorption isotherms for materials produced using R/C = 500 RF xerogels are shown in Figure 5.15. In a manner similar to that seen in the isotherms produced using R/C = 100 and 300 derived materials (Figure 5.11and Figure 5.13) the uptake at low relative pressures decreases with increasing *m*PDA addition, signifying that microporosity is blocked in proportion with the amount of *m*PDA added. Again, as observed with R/C = 100 and 300 derived materials the isotherms are of a similar type IV form, but in this case the hysteresis loop is present over a much narrower range of relative pressures and is better categorised as belonging to the H3 type. Figure 5.16 shows the mesopore size distribution obtained from the nitrogen adsorption isotherms.

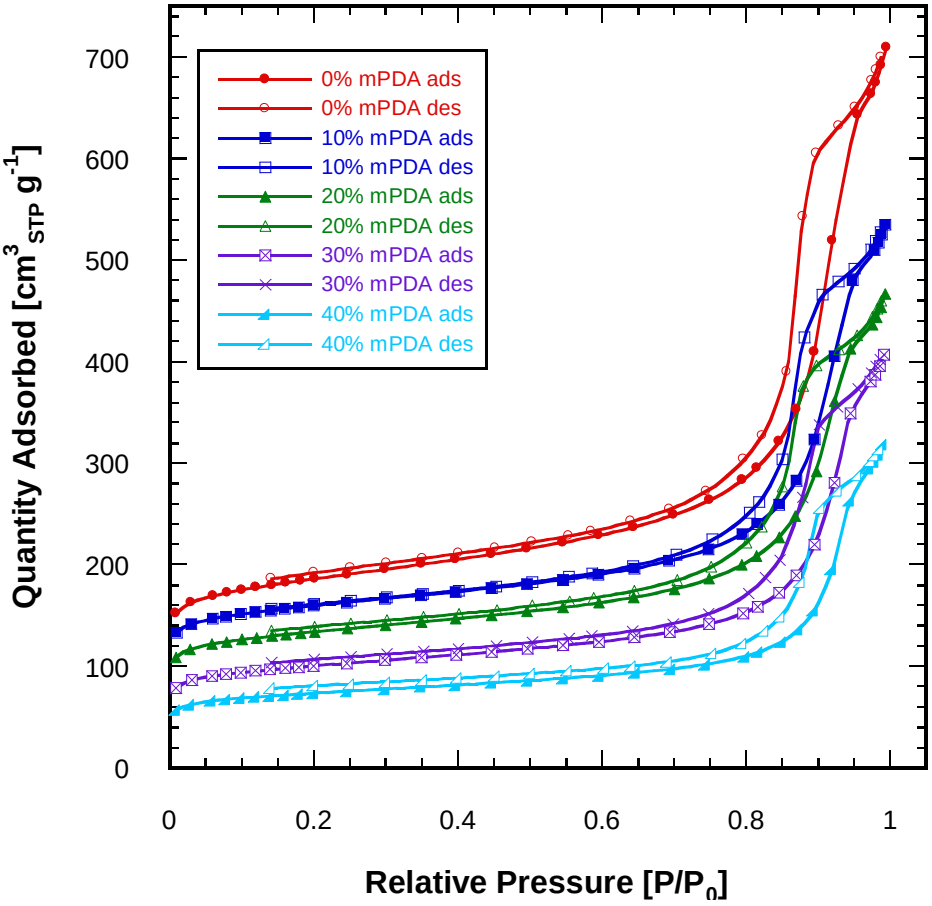

Figure 5.15: Nitrogen Adsorption Isotherms (at 77K) for R/C=500 RF xerogels co-carbonised with *m*PDA

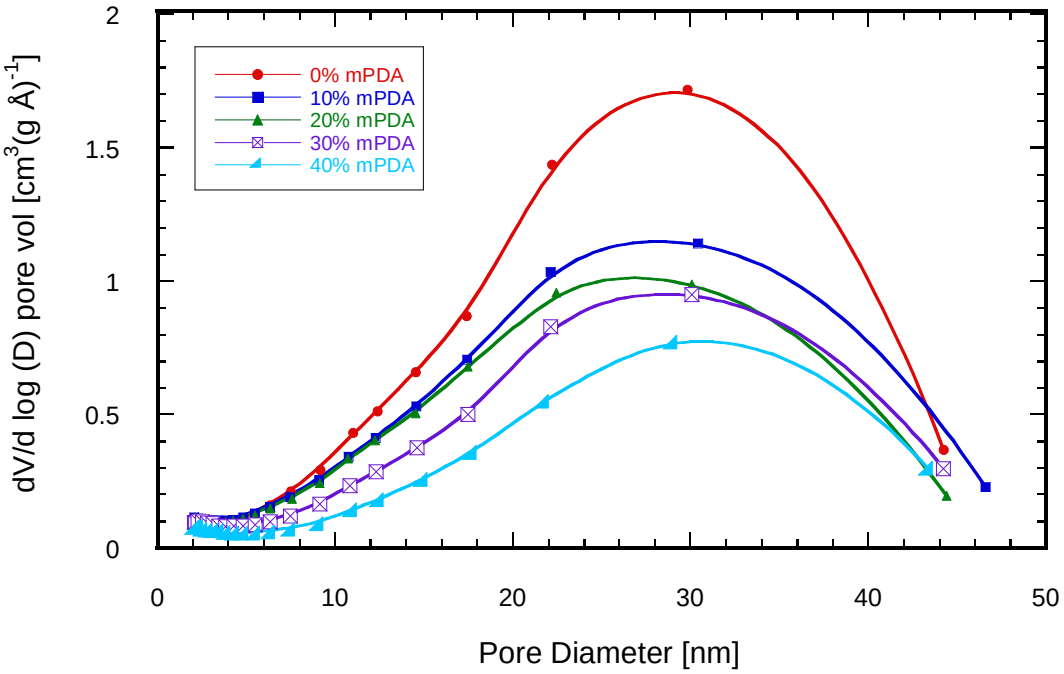

Figure 5.16: Mesopore Size Distributions for R/C=500 RF xerogels co-carbonised with *m*PDA

From the nitrogen adsorption isotherms and derived data it is clear that materials with varying pore characteristics were produced, and that isotherms are of the same general form for a particular R/C ratio. Co-carbonisation mainly influences the nitrogen uptake at low relative pressures indicating that the micropore volume of materials is reduced with increasing fraction of *m*PDA added. It should also be noted that in the cases of R/C = 300 and 500 derived materials the pore size distribution is bimodal, whereas R/C = 100 derived materials are best described as being unimodal.

Considering these results it would seem that specific capacitance values for materials produced using the same R/C ratio could be usefully compared to investigate the effect of electrode nitrogen content, but the uncertainty over the influence of pore size distribution on capacitance does not allow for comparisons between materials produced using different R/C ratios. In the cases of R/C = 300 and 500 derived materials the addition of *m*PDA alters the distribution of pore sizes significantly, which also influences the electrochemical behaviour of the materials.

5.2.2 Electrode manufacture

In the study of carbon materials for use in ECs it is typical to add a small quantity of polymer binder (*ca.* 10%) to the carbon and to form a pellet electrode through compaction. Using this method it is likely that the polymer is forced into the pores of the carbon and can block a great deal of surface area.

An alternative method, based on a technique used in battery production, has been developed which allows for the production of thin, flexible films that can be used in EC cells [**195**]. This method involves the mixing of the carbon material under study with polymer binder and carbon black in an 80:10:10 ratio (by mass) and forming a slurry with a small volume of acetone. It was found that stirring the slurry for at least 4 hours and a fine carbon particle size (< 38 μm) produced uniform, mechanically stable films when cast on an aluminium foil current collector. The acetone evaporates quickly from the cast slurry to leave behind a thin electrode film that reflects the pore characteristics of the carbon material under study. Also, the removal of acetone in this manner indicates that an accessible porous network exists within the film.

However, this method was developed for use with ionic liquid electrolytes and required some modification for use with corrosive aqueous electrolytes. The sheet of aluminium current collector was replaced with nickel foil to permit the use of KOH electrolyte but the electrode film was found to spall when discs were punched from the foil. (This problem was encountered when using several different thicknesses of nickel foil and could be attributed to the differences in the ductility and malleability of nickel when compared with the aluminium foil.) It was therefore decided to cast the slurry directly onto a glass plate and form electrodes from the freestanding film. The production of nitrogen-enriched carbon materials for use in ECs is summarised in Figure 5.17 from the synthesis of the carbon precursor through to electrochemical testing.

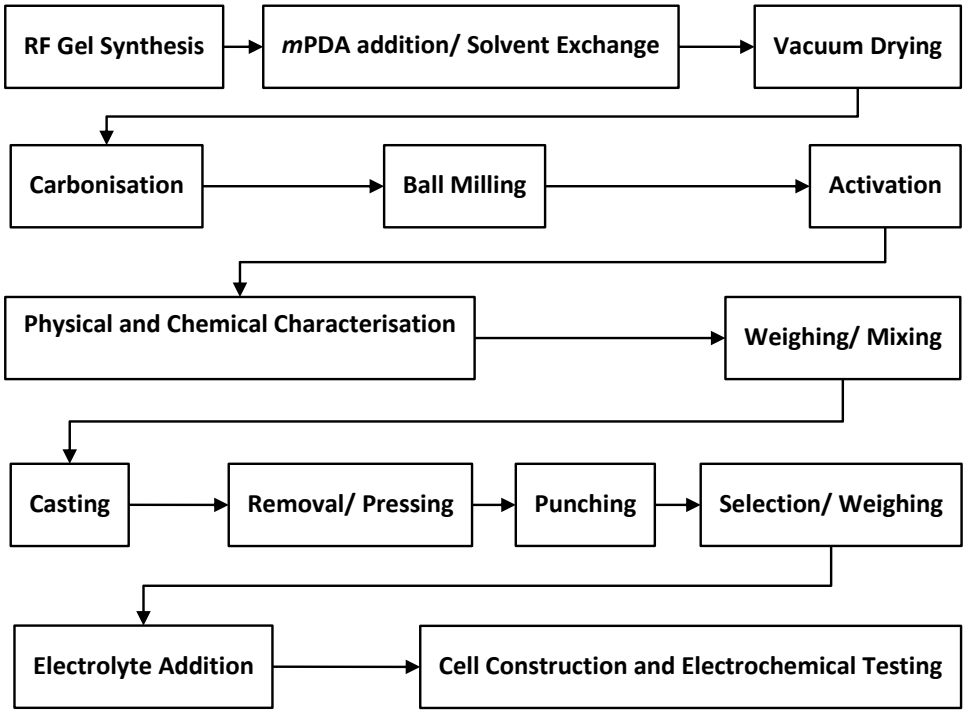

Figure 5.17: Electrode production process block diagram

Different proportions of binder and acetone were used to produce electrodes with the carbon materials described in Table 5.2. Using 10% binder in the slurry, only R/C = 100 xerogels produced electrodes stable enough for use in the test cell; the majority of R/C = 300 and 500 electrodes fractured and disintegrated during the production of test cells. Considering the total pore volumes related to each material (see Table 5.2) and the integrity of the electrodes formed using this method, it was seen that stable electrodes could not be produced when the total pore volume was greater than around 0.5 $cm^3 g^{-1}$.

Increasing the amount of binder to 25 - 30% produced mechanically strong films for all of the carbon materials tested, but during electrochemical tests relatively large values of resistance were observed and this overwhelmed the response from the carbon material being investigated. With an increasing volume of binder in the electrode it can be expected that a greater amount of pore blocking would occur, and the pore characteristics of the electrode may not reflect that of the material under study. Also bearing in mind that ECs are used in high power applications, it is desirable to keep the resistance of the cell, and therefore the binder content, as low as

possible. In hindsight it may be more appropriate to add binder on a volumetric rather than a gravimetric basis when investigating different carbon materials with a highly variable bulk density to allow for the disproportionate reduction in electrode conductivity that arises from the addition of polymer binder.

As materials with total pore volumes up to 0.5 cm^3 g^{-1} could be used to produce reliable electrodes, R/C = 100 RF xerogels co-carbonised with up to 40% *m*PDA chars were activated in CO_2 for 60 mins to open up some porosity and increase the specific surface area. This was necessary because the relatively small specific surface areas of the materials produced using higher loadings of *m*PDA resulted in very low electrical responses which were difficult to measure. Burn-off was typically less than 20% of the original sample mass. A greater degree of burn-off was undesirable as the nitrogen content was found to decrease with increasing burn-off, and the oxygen content of activated carbon materials can be expected to increase with increasing activation.

The surface area and pore volumes of the activated materials derived from nitrogen adsorption isotherms are summarised in Table 5.3. Hereafter, all RF xerogels were produced at R/C = 100, the amount of *m*PDA added before carbonisation is referred to, and their subsequent thermal treatment is indicated; for example "X30CA" denotes the carbon material obtained through the co-carbonisation and activation of R/C = 100 RF xerogel impregnated with 30% by mass *m*PDA.

Sample	Specific surface area [m^2g^{-1}]	Total Pore Volume [$cm^3\ g^{-1}$]	Micropore Volume [$cm^3\ g^{-1}$]	Mesopore Volume [$cm^3\ g^{-1}$]	Average pore diameter [nm]
X00C	515	0.28	0.18	0.07	2.1
X10C	385	0.22	0.14	0.05	2.3
X20C	200	0.13	0.07	0.04	2.6
X30C	46	0.04	0.02	0.01	3.7
X40C	27	0.03	0.01	0.01	4.3
After activation at 850°C in CO_2 for 60 mins					
X00CA	775	0.43	0.30	0.08	2.2
X10CA	430	0.25	0.16	0.06	2.3
X20CA	420	0.26	0.16	0.06	2.5
X30CA	310	0.18	0.13	0.03	2.4
X40CA	150	0.11	0.06	0.03	2.9

Table 5.3: Surface Areas and Pore Volumes of Activated R/C=100 RF xerogels co-carbonised with *m*PDA

From Table 5.3 it can be seen that the activation process increases the micropore volume of the materials and is accompanied by an associated increase in surface area. When the isotherms of the activated carbons, given in Figure 5.18, are compared with those obtained from carbonised materials it is clear that the same shape of isotherm is present with a larger uptake of adsorbate in the low relative pressure region. However, activation does not affect each material to the same degree. The nitrogen adsorption isotherms indicate greater uptakes at each value of relative pressure, and this is most noticeable in the difference between X30CA and X40CA. Rather surprisingly, the isotherms produced for X10CA and X20CA almost lie directly on top of one another, suggesting a near identical pore structure, and produce more or less identical values of BET surface area. Despite undergoing the same activation process, X00CA shows an increase in total pore volume by around 15%, whereas the increase is almost 100% for X20CA. These results indicate that there is a degree of closed porosity in the materials produced *via* co-carbonisation that becomes accessible during activation. It can be expected that as the amount of

*m*PDA used in co-carbonisation increases, the volume of disordered regions (that are easily removed during activation) increases. Also, it can be expected that the rate of gasification increases with the specific surface area of the sample and that these effects both influence the pore structure of the final activated carbon materials.

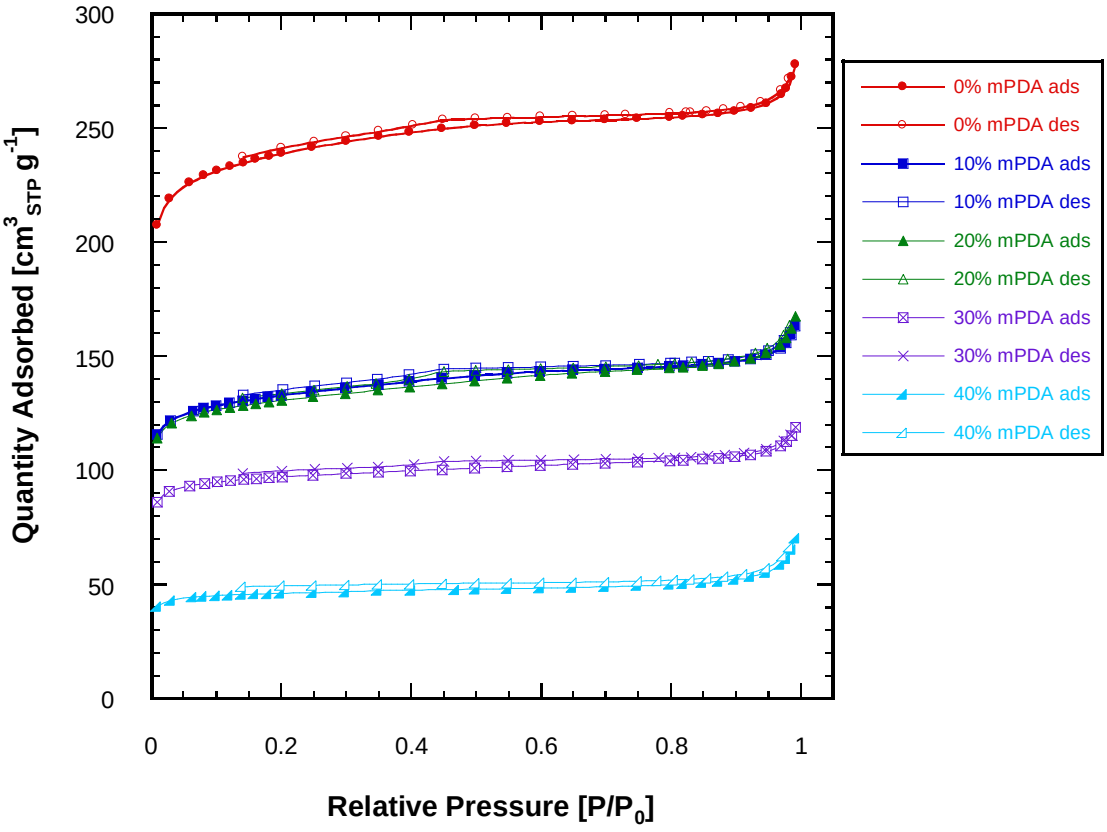

Figure 5.18: Nitrogen Adsorption Isotherms (at 77K) for Activated R/C=100 RF xerogels co-carbonised with *m*PDA

The mesopore size distribution of the activated materials is given in Figure 5.19 and shows a similar form to that seen in the carbonised materials (Figure 5.12) with each material being predominantly microporous and with the values of pore volume at any given pore width decreasing with increasing amount of *m*PDA added. (The small peak at *ca*. 3nm seen for the sample where 40 wt.% *m*PDA was added is an artefact of the method used to determine pore size distribution, as the incremental volumes involved are very small.)

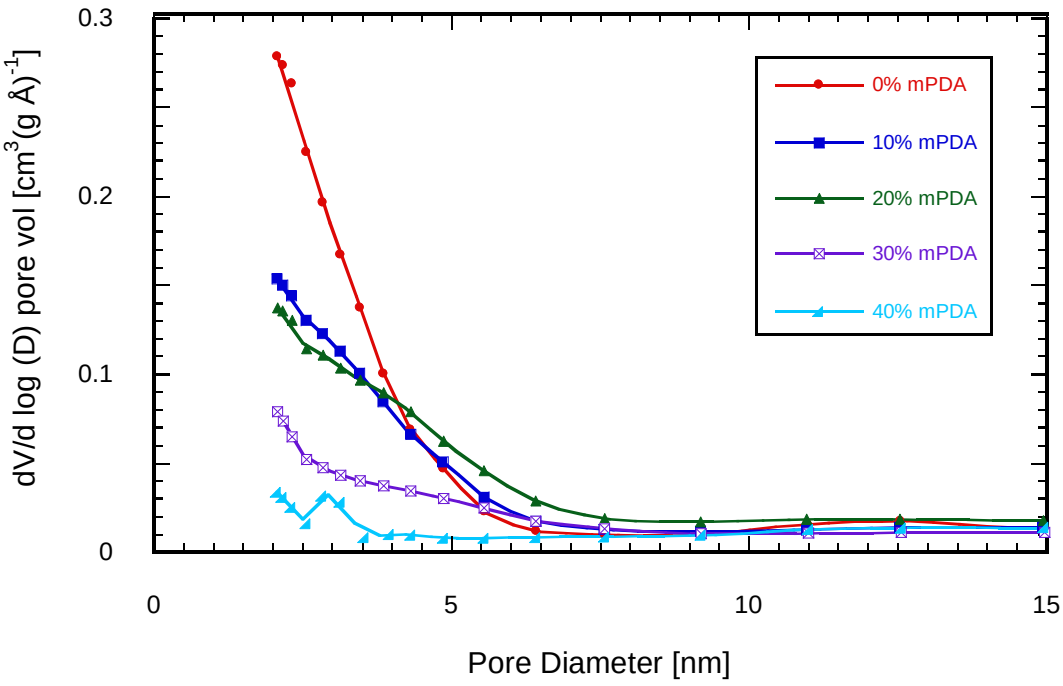

Figure 5.19: Mesopore Size Distributions for Activated R/C=100 RF xerogels co-carbonised with *m*PDA

5.2.3 Chemical Characterisation

Using elemental analysis the ratio of carbon: hydrogen: nitrogen present in each material was determined and is expressed as a weight percentage of the total sample mass as given in Table 5.4. Naturally, the nitrogen content of the co-carbonised materials was found to increase with increasing *m*PDA addition.

Sample	C [wt.%]	H [wt.%]	N [wt.%]	balance [wt.%]
X00CA	83.9	1.3	0.2	14.6
X10CA	79.7	1.7	2.3	16.3
X20CA	79.5	1.6	3.6	15.3
X30CA	77.4	1.8	4.6	16.2
X40CA	78.5	1.5	5.5	14.5

Table 5.4: Elemental composition (wt.%) of activated R/C=100 RF xerogels co-carbonised with *m*PDA on a dry basis

When using elemental analysis it is usually assumed that the remainder of the sample mass ("**balance [wt.%]**" in Table 5.4) is due to the oxygen content of the sample, however proximate analysis of the samples indicates a small but significant amount of incombustible material present (*i.e.* ash), and XPS measurements revealed a significant sodium contribution present in each sample. This arises from the catalyst used in the synthesis of the RF gel and, from a rough estimate, it can be expected that 1.0 - 1.5% of the sample mass after activation can be attributed to the presence of sodium[4]. An acid wash stage could be added to the synthesis procedure to remove some sodium from the materials prior to carbonisation, but it is likely that sodium is deeply embedded within the RF xerogel structure.

[4] For a typical xerogel formulation at this R/C ratio, roughly 46 mg of sodium is present in approximately 14g of xerogel, which is reduced to *ca.* 5.6 g after carbonisation and *ca.* 4.5 g after activation.

Proximate analysis was carried out to determine the amount of incombustible matter present in the samples, and the results on a dry basis are given in Table 5.5.

Sample	Volatiles [wt%]	Fixed Carbon [wt%]	Ash [wt%]
X00CA	6.4	91.8	1.8
X10CA	6.1	88.2	5.7
X20CA	6.6	92.3	1.1
X30CA	5.4	88.9	5.6
X40CA	5.1	93.3	1.5

Table 5.5: Composition (wt.%) of activated R/C=100 RF xerogels co-carbonised with *m*PDA on a dry basis determined by proximate analysis

As the ash content of the materials in some cases is greater than the value that can be ascribed to the presence of sodium of the sample, another source of incombustible matter in the sample is present. It is likely that this contamination occurred during the ball milling of the sample, and it was noted that the two samples with the highest ash content were milled at a different time, corresponding to a period when it was noticed that the silicon nitride balls were deteriorating at a faster rate than usual. It is estimated that after 60 mins of milling approximately 1 g of carbon material, 30 mg was lost from the mass of the balls.

Using the ash contents from Table 5.5, the data in Table 5.4 was corrected to quantify the composition on a dry ash-free basis, and the oxygen content was calculated by difference; the results are given in Table 5.6.

Sample	C [wt.%]	H [wt.%]	N [wt.%]	O (by difference) [wt.%]
X00CA	85.5	1.4	0.2	12.9
X10CA	84.5	1.8	2.5	11.2
X20CA	80.4	1.6	3.7	14.3
X30CA	82.0	1.9	4.9	11.2
X40CA	79.7	1.5	5.6	13.2

Table 5.6: Elemental composition (wt.%) of activated R/C=100 RF xerogels co-carbonised with *m*PDA on a dry, ash-free basis

Through quantification of the X-ray photoelectron spectra as described previously, a different elemental composition of the materials is obtained, and is described in Table 5.7.

Sample	C [at.%]	N [at.%]	O [at.%]	Na [at.%]
X00CA	89.9	trace/nil	8.7	1.4
X10CA	85.2	2.0	11.2	1.5
X20CA	88.6	3.1	8.3	trace/nil
X30CA	83.9	3.7	11.2	1.2
X40CA	83.5	5.1	10.0	1.4

Table 5.7: Elemental Composition (at.%) of activated R/C=100 RF xerogels co-carbonised with *m*PDA on a dry basis determined by XPS

As the quantification of XPS data produces an elemental composition as an atomic percentage of the top 1 - 2 nm of the carbon particles, to make comparisons with the combustive elemental analysis results, the data in Table 5.7 was expressed as a weight percentage using the atomic weights and densities of the elements present [**278**] and is given in Table 5.8.

Sample	C [wt.%]	N [wt.%]	O [wt.%]	Na [wt.%]
X00CA	86.3	trace/nil	11.1	2.6
X10CA	80.8	2.2	14.1	2.9
X20CA	85.8	3.5	10.7	trace/nil
X30CA	79.6	4.1	14.2	2.1
X40CA	79.2	5.6	12.6	2.6

Table 5.8: Elemental Composition (wt.%) of activated R/C=100 RF xerogels co-carbonised with *m*PDA on a dry basis determined by XPS

Differences between the two methods can be attributed to several factors including the surface specific nature of XPS (which may be responsible for the discrepancy in sodium/ ash content), that XPS is unable to detect the presence of hydrogen atoms, and that oxygen content is not measured directly by elemental analysis, but evaluated by difference. Additionally, small discrepancies may arise from the fact that XPS is performed under a vacuum whereas in the microanalysis procedure the samples were exposed to the atmosphere and considering their microporous nature have a propensity to adsorb moisture/ gases. For all samples, excluding X20CA, it appears that there is a greater concentration of sodium atoms in the surface layer of the material which suggests that sodium diffuses towards the surface during treatment at elevated temperatures. Quantification of the broad XPS spectra revealed only trace amounts of sodium present in X20CA, which corresponds to the low ash content of this material determined by proximate analysis but also contradicts the above finding that sodium is concentrated in the surface layer of the material after thermal treatment. It is possible that a greater proportion of sodium was removed from the wet xerogel during synthesis of X20CA, as the sodium content of the water decanted from gels before solvent exchange was not determined.

There also seems to be a correlation between the values of oxygen content as X10CA and X30CA yield higher values than average when determined by XPS (*i.e.* in the surface region) and lower than average when determined using combustive elemental analysis. This could also be indicative of the migration of oxygen atoms towards the

surface during high temperature treatment, but it is more likely to be associated with the high concentrations of ash determined for these samples and may be an artefact of the corrections made to the data to obtain the composition on a dry ash-free basis. Nevertheless, the values of nitrogen content obtained are generally comparable and within the bounds of experimental error. (The error associated with the determination of nitrogen content by elemental analysis is ± 0.3 wt.% and ± 0.1 at.% by XPS).

Deconvolution of the nitrogen spectra was achieved by fitting four curves centred on the binding energies of nitrogen bound to carbon in different configurations (see Table 3.3). An example of the deconvolution process is illustrated in Figure 5.20 and the deconvolution analyses for X10CA, X20CA and X30CA are given in Appendix E.

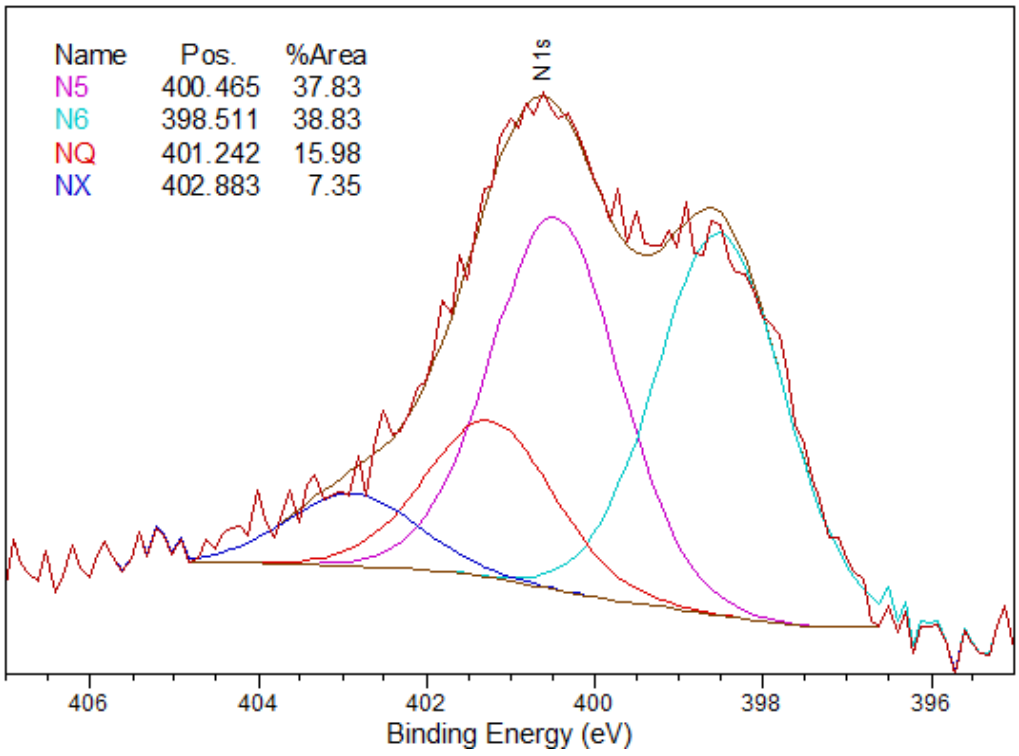

Figure 5.20: N1*s* X-ray photoelectron spectra for X40CA (with deconvolution analysis)

The composition of the nitrogen content derived by deconvolution of XPS data for each of the samples is given in Table 5.9.

Sample	N-5 [at.%]	N-6 [at.%]	N-Q [at.%]	N-X [at.%]
X10CA	36.9	36.6	18.7	7.8
X20CA	37.7	34.2	16.9	11.2
X30CA	37.4	35.9	15.4	11.3
X40CA	37.8	38.8	16.0	7.4

Table 5.9: Nitrogen group composition for activated R/C=100 RF xerogels co-carbonised with *m*PDA

The values given in Table 5.9 should only be considered as indicative of the 'actual' value because the curve fitting process is dependent on many different factors such as the curve type chosen for fitting (*e.g.* Gaussian, Lorentzian *etc.*), the values of FWHM used, and of course the fact that the experimental spectra are not smooth.

The relative proportions of each nitrogen group are broadly comparable at each value of *m*PDA loading, which allows for the electrochemical behaviour of these materials to be directly compared. The most significant deviation seen is the presence of more N-X groups is in X20CA and X30CA, which signifies a greater amount of nitrogen groups that are bound to oxygen atoms. It is likely that more oxygen becomes bound with nitrogen during activation with CO_2, as the larger values of N-X correspond to the samples that underwent a greater degree of activation (see Table 5.3) and should theoretically display a greater amount of surface oxygen.

5.2.4 Electrochemical Characterisation

5.2.4.1 Electrochemical Impedance Spectroscopy

EIS measurements were made using the cells described previously and the parameters determined using the appropriate relationships. The spectra are shown in Figure 5.21. Cell capacitance values were calculated at a frequency of 10mHz and are expressed as specific capacitances based on the mass of electrochemically active

material in one electrode (*i.e.* capacitances are expressed on a three-electrode basis). The maximum specific power was calculated based on the ESR determined at 1 kHz, and the total mass of the electrodes in the cell (*i.e.* including binder and carbon black). (It is noted that this determination of specific power does not take into account the mass of electrolyte, separator, current collectors, packaging *etc.* and it has been estimated that these values can be reduced by a factor of 4 to 10 to give an indication of the specific power realisable in a useful cell.) The values given in Table 5.10 are averages obtained from at least three cells, and the maximum deviation from the average specific capacitance in cells assembled using the same material was less than 2.3%.

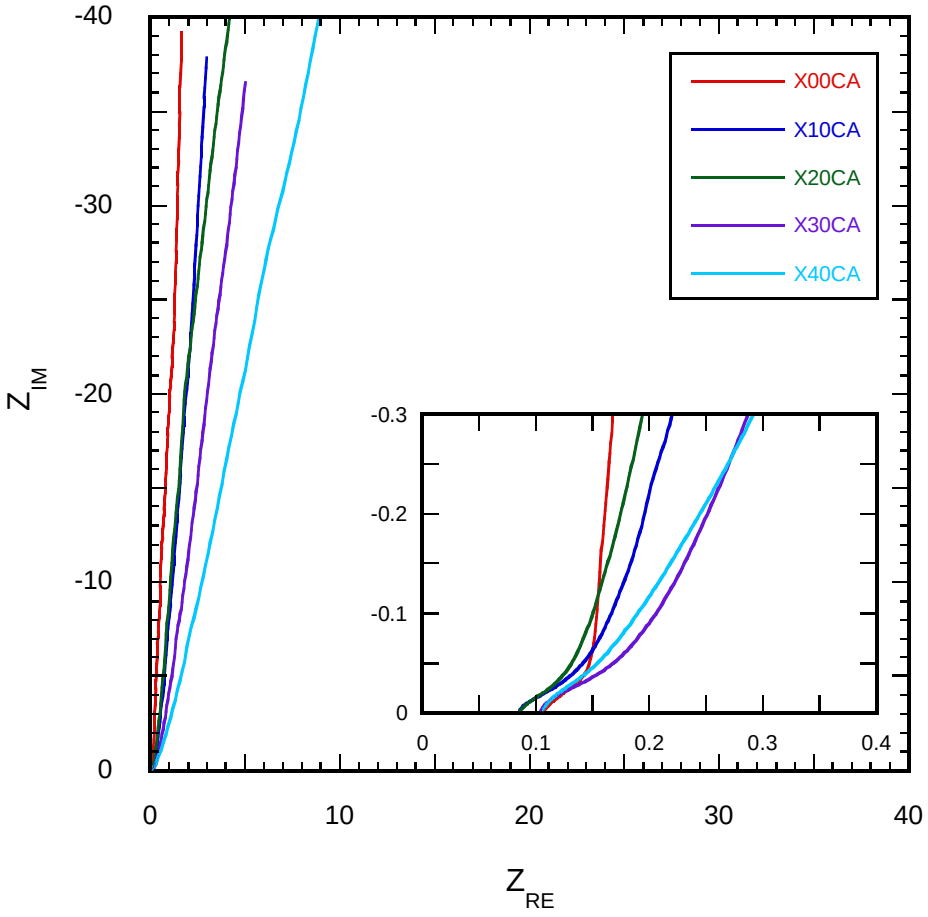

Figure 5.21: Nyquist Plots for cells using activated R/C=100 RF xerogels co-carbonised with *m*PDA

Sample	EIS Specific Capacitance (at 10mHz) [F g^{-1}]	EIS Specific Capacitance / BET surface Area [µF cm^{-2}]	Max. Power density [kW kg^{-1}]
X00CA	128.7	16.6	124
X10CA	109.2	25.4	153
X20CA	114.5	27.3	154
X30CA	96.1	31.0	101
X40CA	66.3	44.2	110

Table 5.10: Specific capacitance and maximum capacitance density from EIS using activated R/C=100 RF xerogels co-carbonised with *m*PDA

The Nyquist plot of the real and imaginary impedance components over the whole frequency range given in Figure 5.21, shows that all of the cells have a capacitive nature at low frequencies but are not equivalent to a pure capacitor element. The presence of a phase angle at low frequencies shows that the interphase between the electrode and electrolyte is not ideally polarisable, and that the deviation from ideal capacitor behaviour increases when larger amounts of *m*PDA are used in co-carbonisation. The extent to which each material is ideally polarisable may be influenced by their composition; however the presence of binder complicates the interpretation of the impedance response associated with each material.

The resistances measured for each cell are influenced by the binder content of the composite electrodes. As the porosity of the materials decreases with increasing *m*PDA addition it can be assumed that the bulk density of the samples increases. Binder was added on a gravimetric basis which would result in a greater proportion of binder being present in lower porosity materials on a volumetric basis. This has a detrimental effect on the conductivity of the electrode. On the other hand, a material with lower degree of porosity could be expected to display a higher electrical conductivity due to the increased density of electron percolation pathways. These competing effects manifest themselves in the variation seen in the values of specific power, which initially increases with increasing *m*PDA addition before decreasing

for X30CA and X40CA. With the benefit of hindsight, the conductivity of the electrode would be less affected if binder was added on a volumetric basis.

The higher frequency behaviour, illustrated in the inset of Figure 5.21, shows a similarity to those of the models that describe transmission line behaviour and that of Randles' circuit which is used to describe EC behaviour [**10**, **254**]. For all samples there is a short frequency region that has a phase angle of -45° (Warburg-type behaviour), and there is a small degree of curvature for all samples as they approach the real axis. The plots are best approximated by that described for electrode materials with a well-defined unimodal pore size distribution [**10**] and from plots of this form the resistance of the electrolyte within the pore is defined as the value of the real impedance component as the frequency approaches zero. However, as the electrode is not ideally polarisable, the value of the real impedance component does not approach a constant value at low frequencies and the impedance associated with the electrolyte in the pores and that associated with the polarisability of the interphase cannot be separated.

The values of solution resistance, determined by the intercept of the spectra with the real axis, vary little with the electrode materials and no trend with any measured physical characteristics could be found. Essentially, the solution resistance could be considered to be a constant when the variations in cell assembly are taken into account[5].

[5] To ensure that the electrolyte solution could be considered constant for the duration of electrochemical testing, electrical conductivity was tested periodically and dropped from 580 mS cm^{-1} to 575 mS cm^{-1} over the entire testing period due to reaction with atmospheric CO_2.

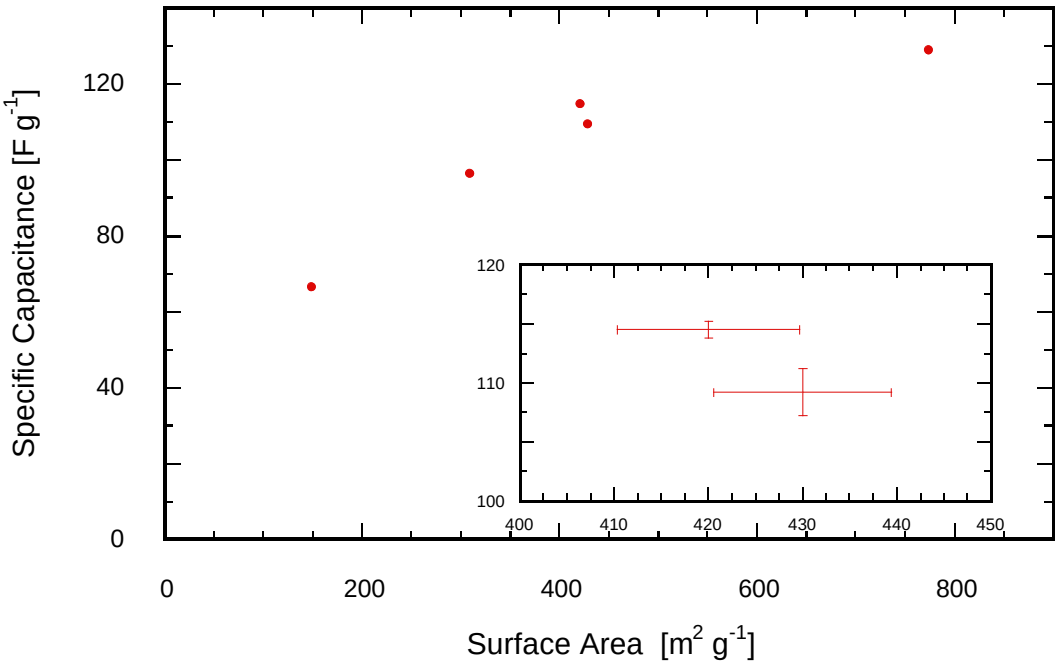

Figure 5.22: EIS specific capacitance against specific surface area (BET) for activated R/C=100 RF xerogels co-carbonised with *m*PDA and (inset) approximate errors for X10CA and X20CA

From Figure 5.22 it can be seen that the materials do not follow the relationship in Eq. 2.2, namely that specific capacitance does not increase with surface area. It should be noted that each of the points represents a different material with not only different nitrogen contents, but also dissimilar pore size distributions. This highlights the problem identified in the discussion of related literature with normalisation of capacitance on the basis of specific surface area, as this approach tacitly assumes that Eq. 2.2 is valid.

In the inset of Figure 5.22, it is seen that the sample with a surface area of 420 m^2 g^{-1} produces a higher specific capacitance than the sample possessing a marginally larger surface area of 430 m^2 g^{-1}. Firstly, it should be stressed that using the BET method to determine surface area has an associated error of roughly 10 m^2 g^{-1}, which is of the same order as the difference in values being discussed. (Repetition of these measurements resulted in similar values of surface area.) It is also noted that the values of specific capacitance are in close proximity and may be considered to be within the margin of error. Repetition of the EIS measurements for different samples produced fairly well defined values of specific capacitance, indicated by the error

bars in the inset of Figure 5.22 that represent the maximum spread of the values used to determine the average specific capacitance.

Also, if it is assumed that the ash contained in the materials is not electrochemically active and is likely to have a negligible surface area but significant mass, the values of specific capacitance in Table 5.10 can be adjusted for the presence of ash to estimate the behaviour of uncontaminated materials. As the ash contents of X10CA and X20CA differ, the result is that both materials have a specific capacitance of 115.8 F g^{-1}.

The discrepancy in specific capacitance between the two samples of similar pore structure and surface area indicates that the chemical composition of the material influences the electrochemical behaviour of the electrodes with respect to EIS measurements.

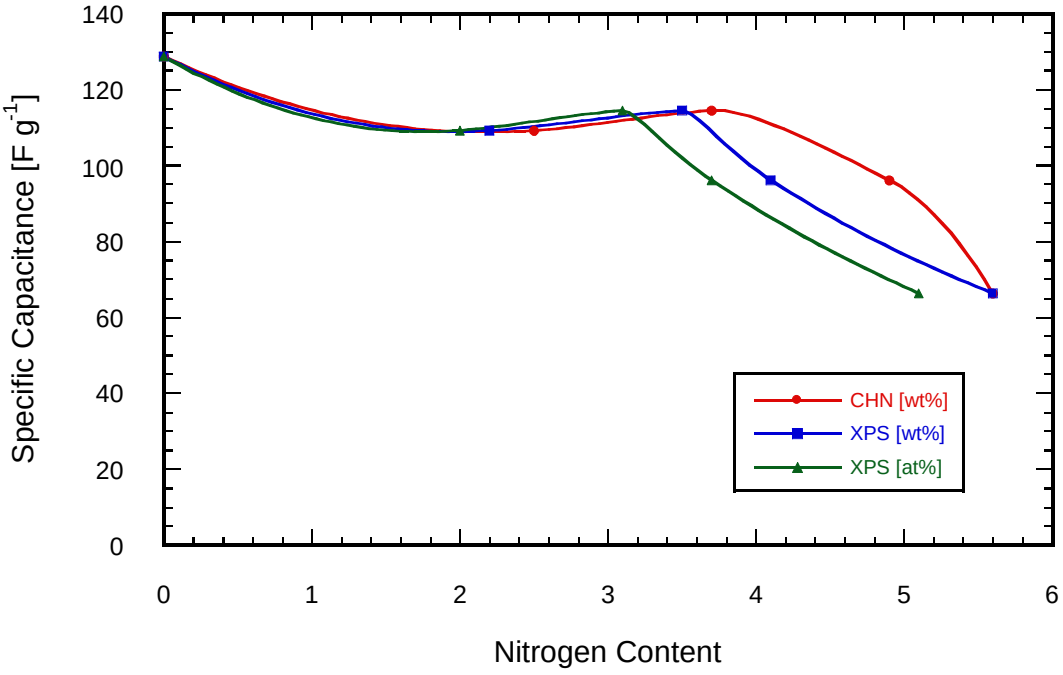

Figure 5.23: EIS specific capacitance against nitrogen content for activated R/C=100 RF xerogels co-carbonised with *m*PDA

Figure 5.23 shows that specific capacitance generally decreases with increasing nitrogen content and also highlights the difference between the nitrogen content as determined using XPS and elemental analysis. The surface specific nitrogen content is also expressed in terms of atomic percentage (at.%) as this better reflects the

proportion of atoms available in direct contact with electrolyte. Despite the highest value of specific capacitance being associated with X00CA, a small beneficial effect of increased nitrogen content is seen when comparing samples X10CA and X20CA.

As was discussed earlier, the surface area of the samples decreases with increasing nitrogen content and, in an effort to decouple the influence of surface area on the capacitance of the material, values of capacitance are usually normalised on the basis of BET surface area. These values are indicated in Table 5.10 and plotted against nitrogen content in Figure 5.24.

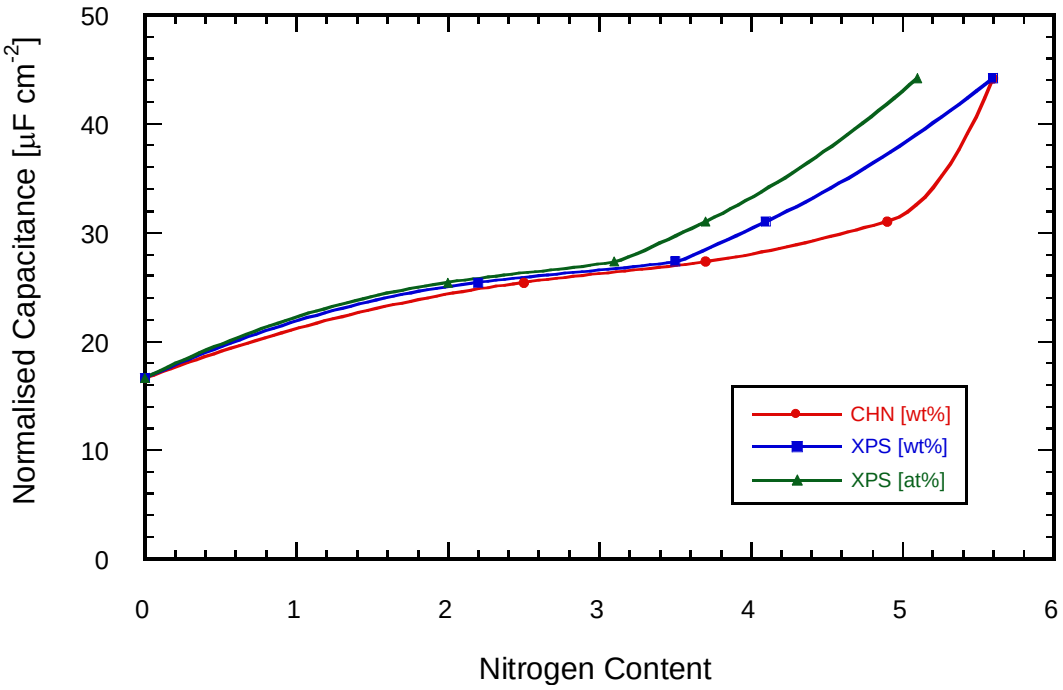

Figure 5.24: Surface area normalised EIS specific capacitance against nitrogen content for activated R/C=100 RF xerogels co-carbonised with *m*PDA

The trend seen in Figure 5.24 roughly agrees with those previously reported and seems to indicate that a larger nitrogen content increases the amount of energy stored per unit surface area of carbon electrode materials. From results like this, it initially appears that the presence of roughly 5 wt.% of nitrogen in the composition of EC electrodes can result in a twofold increase in the amount of energy stored when compared to a material of the same specific surface area but containing no nitrogen. Unfortunately, a practical difficulty is encountered as the surface area of materials generally diminishes as more nitrogen is added to the material. Activated carbons

with specific surface areas in the region of 1000 m^2g^{-1} are commonplace but a method that can reliably produce materials with an equivalent surface area, and a uniform distribution of nitrogen heteroatoms (but no oxygen heteroatoms) has not yet been found.

However any analysis on the basis of surface area normalisation relies on several assumptions. Normalisation of data on the basis of surface area assumes that all of the surface area determined by the BET method is electrochemically active, and that all of the surface area behaves in an identical manner with respect to the quantity of charge stored. These have been proven to be inaccurate for various reasons, from the unreliability of BET surface area estimation, to the fact that pores of different sizes are best modelled by different charge storage mechanisms. In addition, it is commonly assumed that values of surface area normalised specific capacitance in excess of roughly 30 $\mu F\ cm^{-2}$ indicates the occurrence of charge transfer reactions, but this definition is far from rigorous and the presence of electrode reactions is better identified through the use of cyclic Voltammetry.

The behaviour of X10CA and X20CA reveal an interesting effect where an increase in nitrogen content is accompanied by an increase in specific capacitance and surface area normalised capacitance. Galvanostatic cycling was employed to better reflect the operating conditions encountered in a functional device, and to establish whether or not the difference in behaviour observed between X10CA and X20CA has any practical benefits.

5.2.4.2 Galvanostatic Cycling

At all values of discharge current, all materials largely follow the linear charge-voltage relationship displayed by an ideal capacitor (as shown in Figure 3.17). An example of the charge/ discharge profile ('chronopotentiograms') for each of the materials at a rate of 2 mA (0.2 A g^{-1}) is given in Figure 5.25. The data has been adjusted to reflect a constant single electrode mass of 10.0 mg (including binder and carbon black) to allow for comparisons between materials to be made.

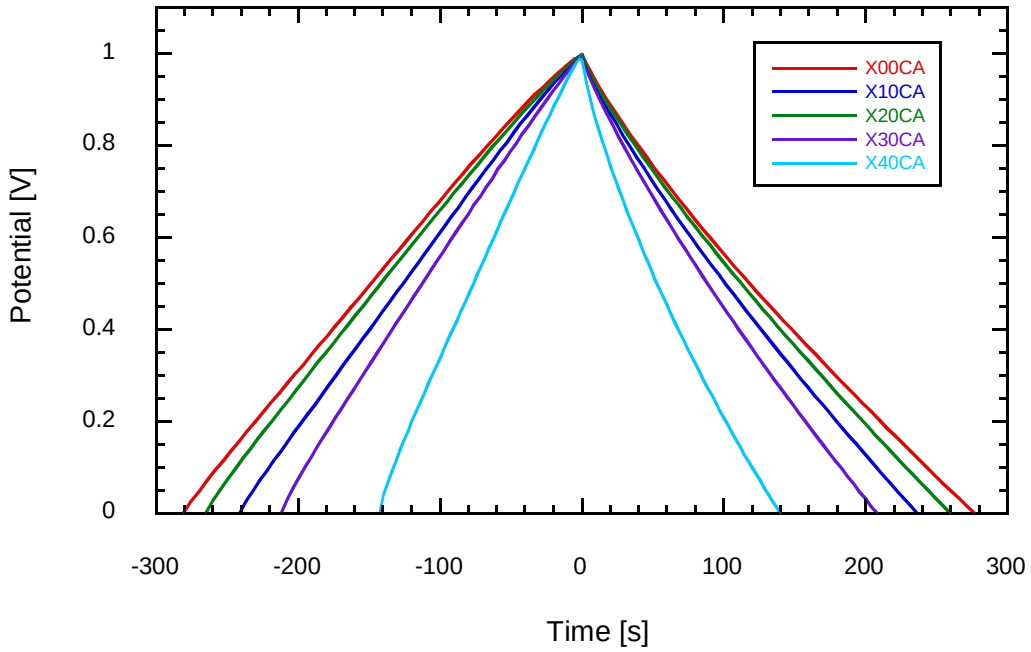

Figure 5.25: Charge/ Discharge profiles for activated R/C=100 RF xerogels co-carbonised with *m*PDA at 2 mA (electrode mass is normalised to 10.0 mg)

By calculating the area under each profile, the energy supplied to the cell during charging and that drawn from the cell during discharge can be determined and the efficiency of the cell determined. For the profiles shown in Figure 5.25, the efficiency of each charge/ discharge cycle is roughly 84%, with the exception of X40CA which has an efficiency of 78%. These efficiencies seem to be very low in comparison with those usually claimed for ECs (*ca.* 99%), but this is probably due to the low charge/ discharge rate used (which resulted in a discharge time between 140 and 280 s), and that the cell design had not been optimised. The low efficiency can be attributed to the existence of a small leakage current which can be approximated by a value of 0.016 A g^{-1} at this rate of charge. The leakage current may be associated with the degree of polarisability of the electrode, self-discharge mechanisms, cell resistances *etc.*

As ECs are typically applied to processes that have a time scale in the region of 1 - 10 s (see Figure 1.1) substantially greater rates of charge and discharge are used in a functional device, and Figure 5.26 shows examples of the charge/ discharge profile obtained at 100 mA (10 A g^{-1}).

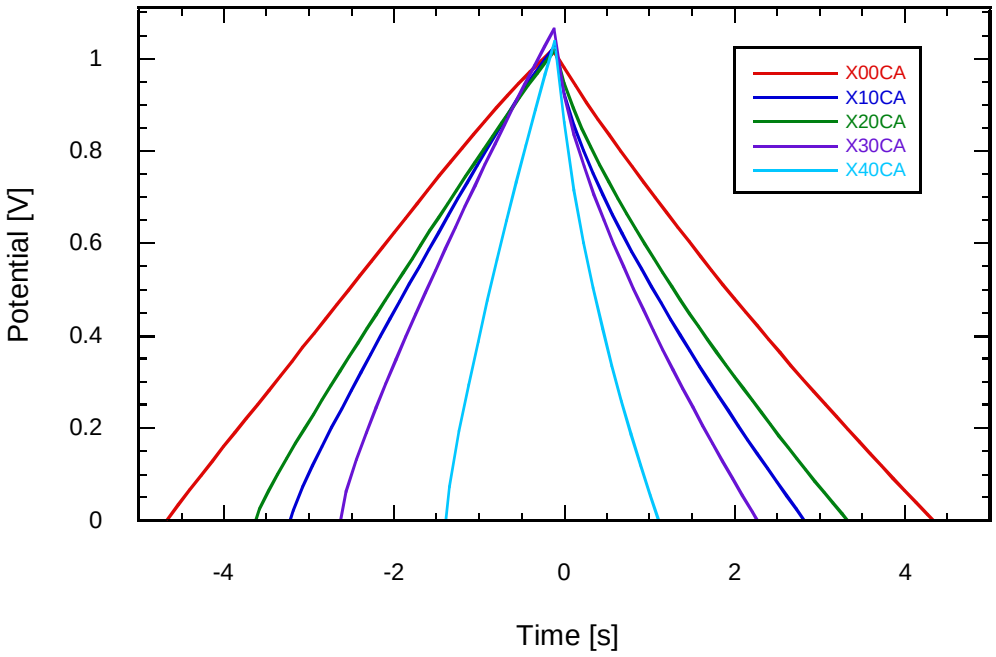

Figure 5.26: Charge/ Discharge profiles for activated R/C=100 RF xerogels co-carbonised with *m*PDA at 100 mA (electrode mass is normalised to 10.0 mg)

Specific capacitances were calculated at several discharge rates to determine if there was any rate-dependent behaviour associated with nitrogen content. The values of specific capacitance obtained at each discharge rate are given in Table 5.11, and are averages obtained from at least three cells. The maximum deviation from the average specific capacitance in cells assembled using the same material was 9.0% at a rate of 2 mA and 4.6% at 100 mA, but the typical deviation was *ca.* 2.5%.

Sample	Galvanostatic discharge specific capacitance [F g⁻¹]						
	2 mA	4 mA	8 mA	16 mA	32 mA	64 mA	100 mA
X00CA	140.3	135.0	129.9	125.2	121.1	117.6	113.6
X10CA	104.7	99.8	98.6	95.0	90.2	83.8	76.3
X20CA	123.2	117.9	112.0	105.8	99.4	93.2	86.3
X30CA	101.2	94.7	87.6	80.4	73.2	66.1	59.8
X40CA	69.2	62.0	55.3	49.3	44.0	38.8	33.4

Table 5.11: Specific capacitance obtained by Galvanostatic discharge at different rates for activated R/C=100 RF xerogels co-carbonised with *m*PDA

At each value of discharge current, the specific capacitance is seen to follow the same trend as those obtained using EIS measurements at 10 mHz. In general, a discharge current lower than 1 A g^{-1} produced values of specific capacitance which are similar to the values determined using EIS. Each material shows the same behaviour with increasing discharge current, namely that the highest values of specific capacitance are obtained at the lowest rate, and reduces to an approximately constant value as the rate increases. Plots of this form are typical of EC cells. The data in Table 5.11 is plotted in Figure 5.27 where the discharge current is expressed in A g^{-1} based on the average mass of one electrode.

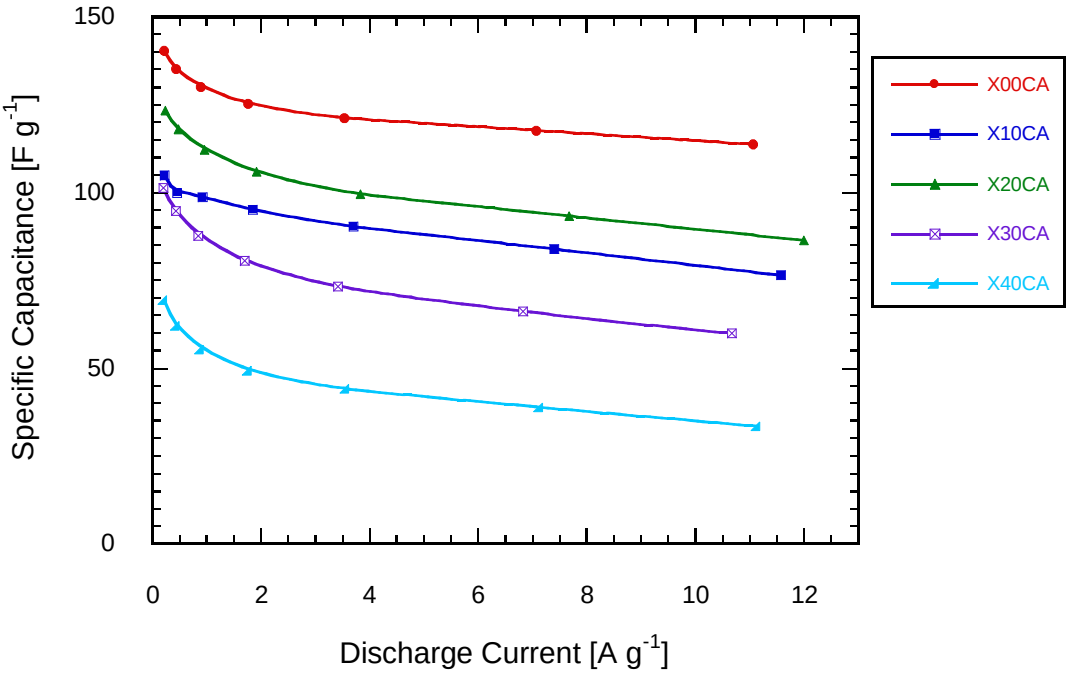

Figure 5.27: Galvanostatic discharge specific capacitance against discharge current for activated R/C=100 RF xerogels co-carbonised with *m*PDA

As with the values obtained by EIS, the specific capacitance of X20CA is larger than that of X10CA, and this is seen at all values of discharge current. However, unlike the EIS measurements a difference is maintained after the values have been adjusted to take the ash content of the electrodes into account. The data obtained from these samples is given in Figure 5.28 in both the 'as obtained' and adjusted forms with the error bars indicating the spread of data used to calculate the average value.

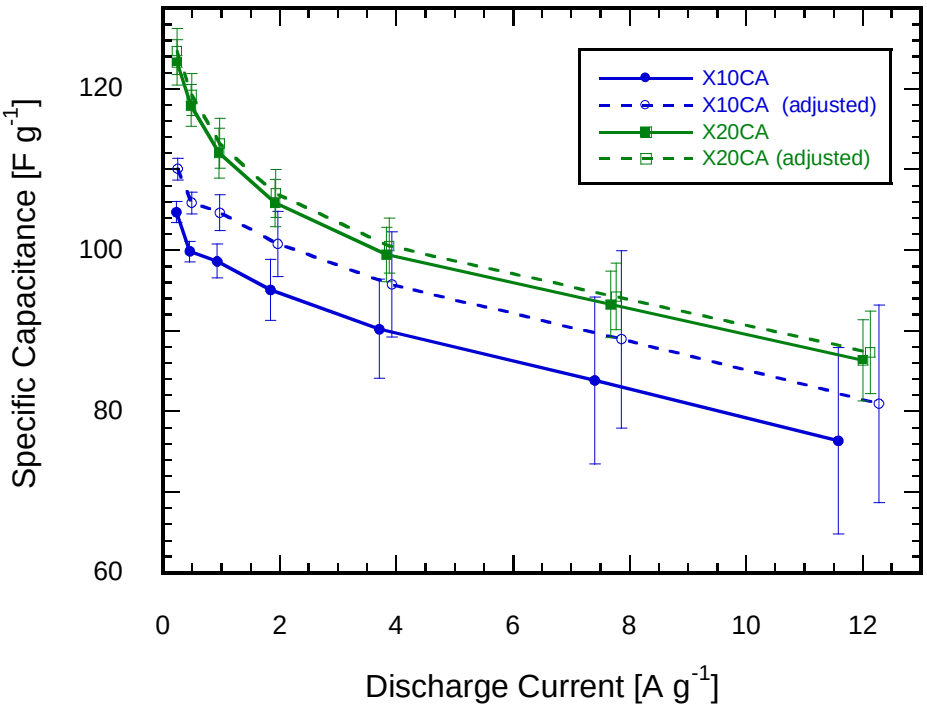

Figure 5.28: Galvanostatic discharge specific capacitance against discharge current (with error bars) for X10CA and X20CA

It is clear that the spread of the data increases with increasing discharge current which may be due to the accuracy with which the potential can be determined at each step. Initially, the potential was found to frequently exceed the limit stated for the cell at higher rates due to the frequency of measurements. The time between measurements was therefore reduced when using higher rates, nevertheless a greater amount of variability occurs at higher rates due to the collection of less data points (usually more than 1000 points were obtained during discharge at low rates, and less than 100 were available at higher rates).

Discharge rates less than 2 A g^{-1} X20CA produce average specific capacitances that are about 10% larger than those obtained using X10CA, and the spread of the values used in their calculation is sufficiently narrow to state that differences in the composition of the electrodes is responsible for the difference in their electrochemical behaviour. For rates greater than 2 A g^{-1}, a broadly similar relationship between the average values is seen (*i.e.* larger average values) but the spread of values makes the difference less definite.

When the data in Table 5.11 is normalised on the basis of BET surface area and plotted against the surface nitrogen content (from XPS measurements) as shown in Figure 5.29, a similar behaviour as seen in Figure 5.24 (using specific capacitance values obtained using EIS) is displayed at low rates (2 – 8 mA), however as the rate is increased the surface area normalised capacitance seems to be less affected by nitrogen content. The value of surface normalised capacitance seems to approach a constant value that is independent of nitrogen content as the rate increases, and the difference between the values of surface area normalised capacitance obtained at high rate and that obtained at low rate, increases with increasing nitrogen content. This behaviour implies that the presence of nitrogen in the electrodes enhances the specific capacitance measured at low rates to a greater extent than at high rates. This apparent rate dependent behaviour could indicate that the nitrogen content contributes to the capacitance of the material to a greater extent as the rate decreases, and that a pseudocapacitive reaction may occur.

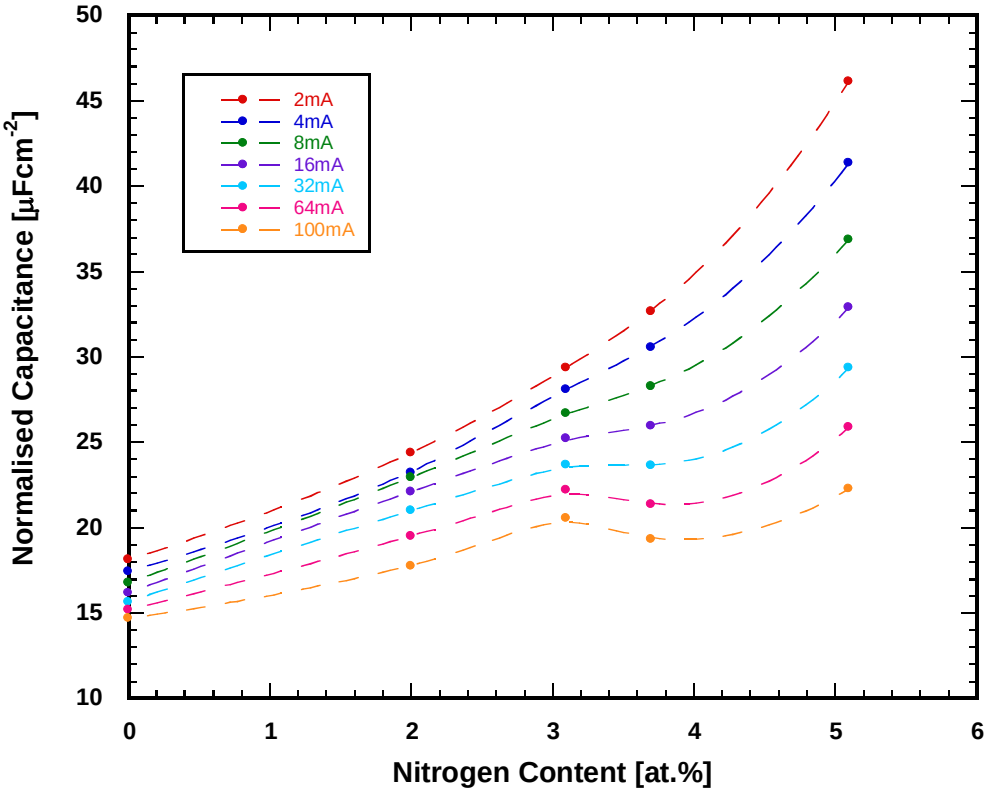

Figure 5.29: Surface area normalised capacitance against nitrogen content (XPS) for activated R/C=100 RF xerogels co-carbonised with *m*PDA

An alternative explanation for this apparent rate dependent behaviour could be that the effects of pore structure in the samples with varying nitrogen content influences the electrochemical results. As there is a reduction in the amount of micropore volume with increasing nitrogen content it can be anticipated that the rate response will be poorer in more microporous materials.

Also, as there is a relationship between nitrogen content and surface area as well as a correlation with the specific capacitance of the materials, Figure 5.29 cannot be considered as proof that reactions with nitrogen groups occur. The uncertainty over these results again serves to highlight the problem encountered when data is normalised on the basis of surface area for materials where the pore characteristics are noticeably dissimilar.

5.2.4.3 Cyclic Voltammetry

A common method used in the determination of pseudocapacitive reactions is cyclic Voltammetry, where the current induced by a changing potential is measured as a function of the applied potential. In this situation the presence of pseudocapacitive reactions are usually identified by a broad but distinct peak.

Cyclic Voltammograms obtained at a sweep rate of 10 mVs^{-1} are illustrated in Figure 5.30 and have been adjusted to reflect a constant single electrode mass of 10.0 mg (including binder and carbon black) to allow comparisons between materials to be made. The form of each of the current responses is similar for each material and takes the shape of that expected from an ideal capacitor.

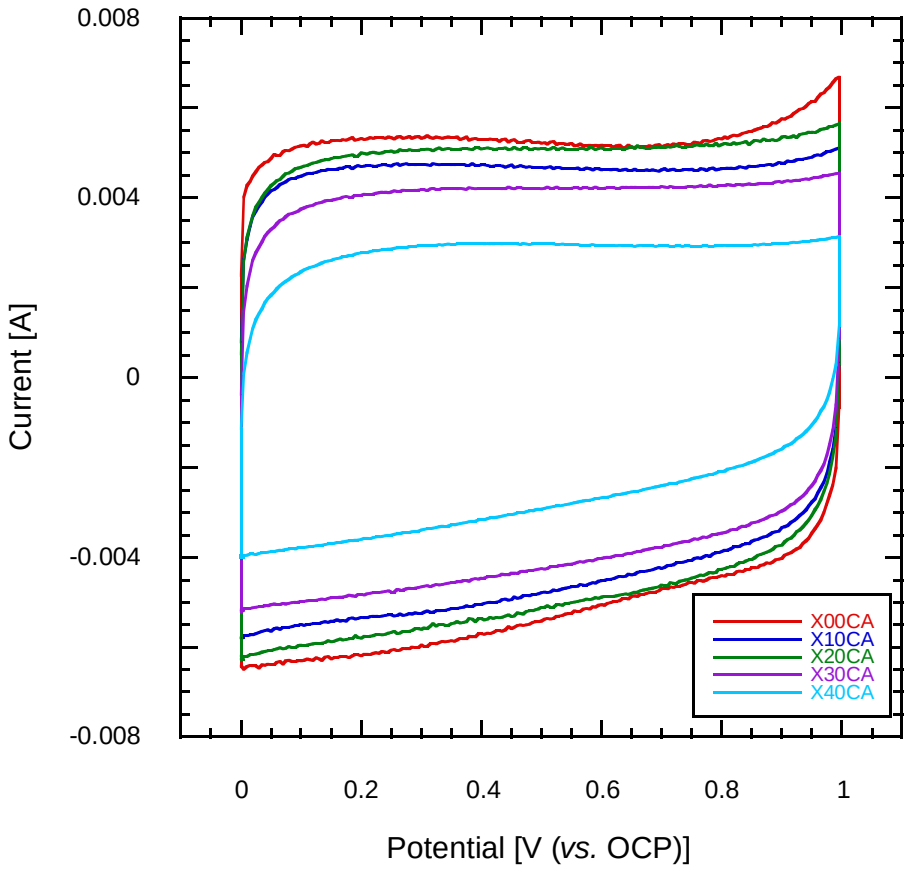

Figure 5.30: Cyclic Voltammograms at 10 mV s^{-1} for activated R/C=100 RF xerogels co-carbonised with *m*PDA (electrode mass normalised to 10.0 mg)

No discernible peaks that would indicate pseudocapacitance are evident over the operating potential of the cell and, if the presence of nitrogen does enhance the specific capacitance of an electrode material, an alternative mechanism may be responsible. The possibility remains that a Faradaic reaction which is favourable over the entire operating potential occurs between nitrogen heteroatoms and the electrolyte, however it is unlikely that a single reaction is responsible for the response seen, as the majority of pseudocapacitive reactions occur over a fairly narrow range of potential (*e.g.* quinone/hydroquinone *ca.* 0.4V [**10**, **221**]) In the highly unlikely event that different nitrogen functional groups react with the electrolyte in overlapping regions of potential to produce a roughly constant current response, (*e.g.* in RuO_2 three separate reactions are superimposed over 1V), further experimental evidence where the type of functional group is altered would be required to disprove this hypothesis.

In several reports the term ‘pseudocapacitance’ has been used to describe cases where the double-layer capacitance is apparently augmented to some degree, (usually on the basis that surface area normalised capacitance values are in excess of that reported for activated carbons) whereas it should be reserved for cases where the extent of charge acceptance varies with changes in potential (*dQ/dV*) and charge is passed across the double-layer. Also, this is usually on the basis of increased normalised specific capacitance with increasing nitrogen content which assumes that all of the surface area accessible to nitrogen is accessible to electrolyte. The behaviour seen in Figure 5.30 and Figure 5.31 is better described by the double-layer mechanism operating over different surface areas, or with an enhanced amount of charge displaced through the double-layer mechanism.

Of particular interest is the difference in specific capacitance seen between X10CA and X20CA which display comparable surface areas and pore size distributions, and all other things being equal, can be expected to have a similar value of accessible surface area. As the nitrogen content of these samples differs, a reasonable hypothesis is that hydrophilic groups attract electrolyte into otherwise inaccessible pores and can enhance the electrochemically active surface area. Using the values of specific capacitance obtained from CV at $10mVs^{-1}$, the normalised specific capacitance could be used as an indicator of the relative utilisation of surface area with X10CA showing approximately 90% of the surface area utilisation seen in X20CA. If this is the case, the values of resistance associated with each material could be expected to differ due to the presence of unfilled voids within the electrode. From the measurements made, it is difficult to discern the origin of the different resistances in these materials and an alternative technique to probe the degree of electrochemically active surface area is necessary.

At the higher sweep rate of 100 mV s^{-1} seen in Figure 5.31, the differences between each material become more apparent and the values of specific capacitance follow the same trend as those obtained at 10 mV s^{-1}. The form of the Voltammogram at the higher sweep rate is nearly identical to that recorded at the lower rate for X00CA and as the quantity of *m*PDA added is increased, the difference between the 10 mVs^{-1} and 100 mVs^{-1} Voltammograms become larger.

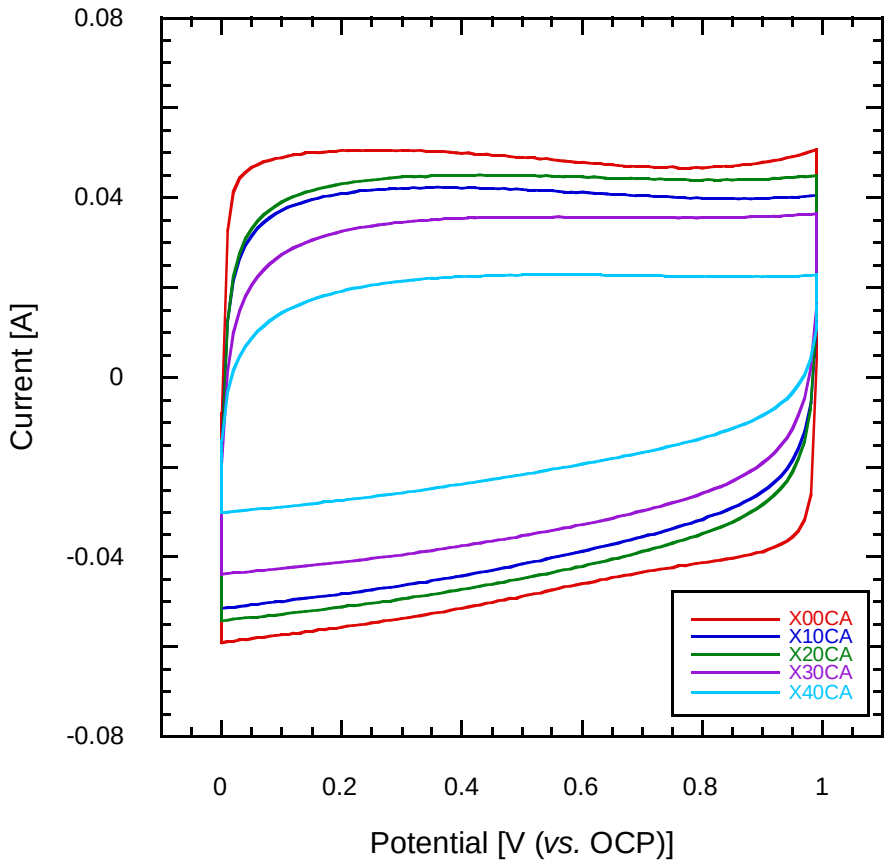

Figure 5.31: Cyclic Voltammograms at 100 mV s^{-1} for activated R/C=100 RF xerogels co-carbonised with *m*PDA (electrode mass normalised to 10.0 mg)

The values of specific capacitance calculated for the discharge step of each Voltammogram in Figure 5.30 and Figure 5.31 are given in Table 5.12.

Sample	CV Specific Capacitance [F g⁻¹]		[μF cm⁻²]	
	10 mVs^{-1}	*100 mVs^{-1}*	*10 mVs^{-1}*	*100 mVs^{-1}*
X00CA	130.9	120.0	16.9	15.5
X10CA	115.0	98.5	26.7	22.9
X20CA	124.5	106.1	29.6	25.3
X30CA	102.5	82.5	33.1	26.6
X40CA	70.4	50.7	46.9	33.8

Table 5.12: Specific capacitance determined by Cyclic Voltammetry for activated R/C=100 RF xerogels co-carbonised with *m*PDA

As the values of specific capacitance derived from the cyclic Voltammograms in Figure 5.30 are in the region of those obtained from Galvanostatic discharge at 2 - 4 mA (see Table 5.11) it is not unreasonable to suggest that any proposed reactions involving nitrogen would also occur under the conditions used during cyclic Voltammetry.

A similar effect between the differences in specific capacitance obtained at high and low sweep rates with those obtained by Galvanostatic charge and discharge at high and low sweep rates is evident, namely that the difference increases with increasing nitrogen content.

5.2.4.4 Summary

In this study of nitrogen-enriched carbon materials as EC electrodes a similar trend to those previously published between the surface area normalised capacitance of the materials was found, but the mechanism by which this occurs was not clear. It remains possible that reactions between nitrogen functional groups and electrolyte ions occur, however this is highly unlikely as cyclic Voltammograms show no evidence that pseudocapacitive reactions occurred.

Interestingly, one sample that possessed more nitrogen but a (marginally) smaller surface area was found to produce a specific capacitance that was larger than that recorded for a similar material with a lower nitrogen content. This difference, though small, is indicative of a practical use for nitrogen-enriched carbons in ECs that use KOH electrolyte and is a seldom seen instance where a higher specific capacitance can be attributed to the presence of nitrogen in the material rather than changes in surface area or the presence of oxygen functionalities. Further studies into this effect were designed in an attempt to decouple the effects of surface area and electrode composition, to clarify the difference in behaviour seen between nitrogen-enriched samples, and to perhaps gain an insight into the mechanism(s) by which any changes in specific capacitance occur.

5.3 Hydrogen Treatment

From the previous experiments it became clear that there are several difficulties encountered when studying nitrogen-enriched carbons for use in EC electrodes. In particular it is difficult to control both the nitrogen content and pore structures of the materials under study.

In the studies discussed previously, there is usually a complicated relationship between the nitrogen content and surface area associated with each material. As has been discussed previously, the electrochemical behaviour of such materials is usually normalised on the basis of surface area which is based on several flawed assumptions. Ideally, materials with the same pore structure and varying chemical composition would be produced to investigate this further, however it was proposed that further treatment of the samples already studied could have a similar result. By treating a nitrogen-enriched carbon at an elevated temperature under a hydrogen atmosphere, it was proposed that surface nitrogen groups could be selectively removed while leaving behind a carbon material with a similar pore structure. Sample X20CA was chosen for further study as it possessed a reasonable nitrogen content while retaining a significant amount of surface area and produced a sizeable specific capacitance. However, to remove nitrogen from the materials, a temperature

of 1000°C was used which resulted in a significant change in the pore structure and surface area of the material. As this temperature is significantly greater than that used during carbonisation and activation (*i.e.* 850°C) further structural changes occur in the sample during treatment which cannot be attributed solely to the removal of nitrogen groups, but are due to graphitic reordering processes as illustrated in Figure 2.15 ('Transformation of a graphitisable carbon [**148**]'). Also, the oxygen content diminishes from *ca.* 11% to *ca.* 8% when the samples are subjected to further thermal treatment, which implies that a substantial change in physical structure has occurred.

Therefore, the values of specific capacitance obtained using this new material cannot be directly compared to those previously discussed due to the substantial difference in the structure and composition of the materials. The same thermal treatment was carried out under an inert gas (argon), and under a mixed atmosphere to provide materials for comparison.

5.3.1 Physical Characterisation

The nitrogen adsorption isotherms for these samples are shown in Figure 5.32, and the surface area and pore characteristics derived from these isotherms are summarised in Table 5.13. (X20CA H refers to the material produced by treating X20CA in hydrogen at 1000°C. X20CA Ar and X20CA H_Ar refer to materials produced under argon, and under a mixture of hydrogen and argon, respectively.)

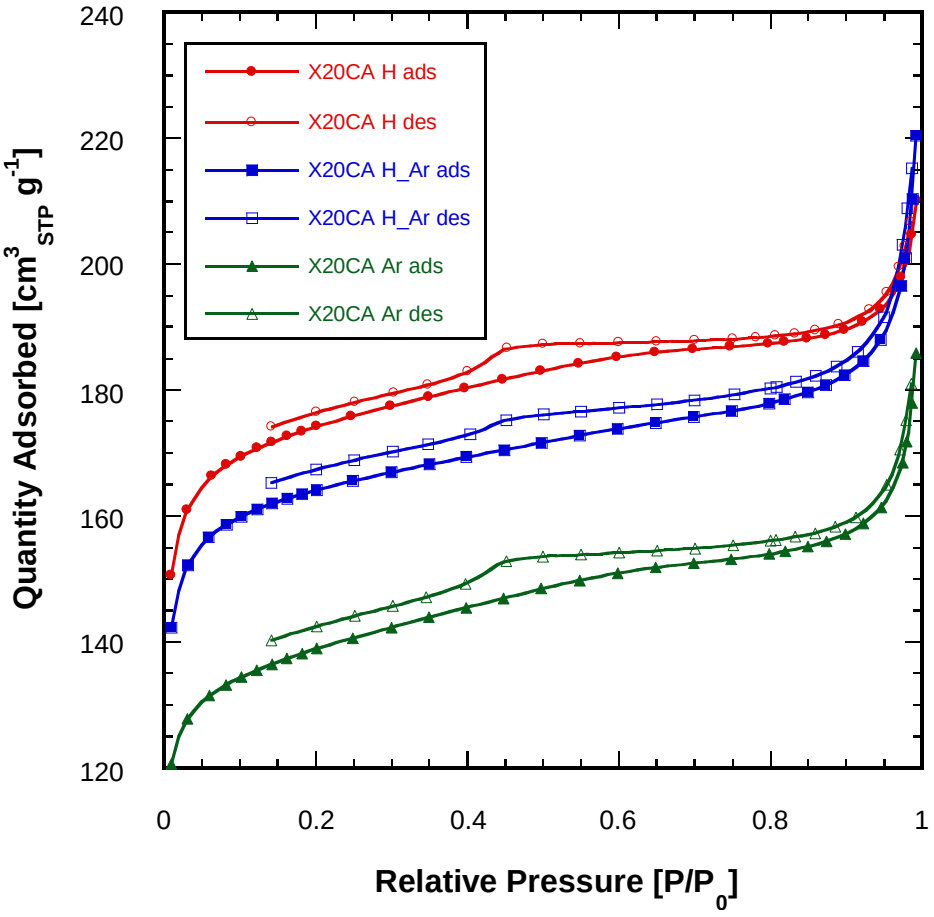

Figure 5.32: Nitrogen Adsorption Isotherms (at 77K) of X20CA treated at 1000°C in different atmospheres

The nitrogen adsorption isotherms for the materials treated at 1000°C are of similar form and can be categorised as type IV isotherms. The uptake at low relative pressures differs for each sample which indicates that the micropore volume of the sample varies depending on the gas used in the high temperature step. The hysteresis behaviour of the samples can be classified as type H3 as no limiting uptake is observed as the relative pressure approaches unity. This type of loop is associated with slit shaped pores [**170**] and may indicate that some degree of graphitisation has occurred during thermal treatment. A kink is evident in all desorption isotherms at a relative pressure of roughly 0.45 which is typical when using nitrogen as an adsorbent, and the hysteresis seen at lower relative pressures arises from the microporosity in the sample.

Sample	Specific surface area [$m^2\ g^{-1}$]	Total Pore Volume [$cm^3\ g^{-1}$]	Micropore Volume [$cm^3\ g^{-1}$]	Mesopore Volume [$cm^3\ g^{-1}$]	Average pore diameter [nm]
X20CA H	580	0.33	0.22	0.08	2.3
X20CA H_Ar	535	0.33	0.21	0.08	2.4
X20CA Ar	465	0.28	0.18	0.08	2.4
X20CA	420	0.26	0.16	0.06	2.5

Table 5.13: Surface Areas and Pore Volumes of X20CA treated at 1000°C in different atmospheres

From Table 5.13 it can be seen that by treating X20CA at 1000°C the micropore volume and surface area are enlarged, with this effect being more pronounced with increasing hydrogen concentration. Considering that X20CA is a product of co-carbonisation, it is likely that some micropores are blocked by small crystallites or tars which are subsequently removed by treatment at high temperature. It is also likely that some micropore volume is rendered inaccessible by the presence of nitrogen groups which are then abstracted through reaction with hydrogen.

The isotherm obtained using the material that was produced using a mixture of hydrogen and argon is closer to the isotherm of X20CA H than that of X20CA Ar in terms of quantity adsorbed. This may be due to an increase in reaction rate as more surface area becomes accessible during the process or may be a result of the procedure used (rather than using a 50:50 feed stream, the furnace was flushed with hydrogen and the gas was switched to argon after 1 hour at 1000°C).

The mesopore size distributions given in Figure 5.33 have a very similar shape for X20CA H and X20CA Ar, however the sample treated in a mixed atmosphere shows a slightly different form and exhibits the lowest value of mesopore volume. This may be a consequence of the greater amount of contamination identified in this sample (determined *via* proximate analysis).

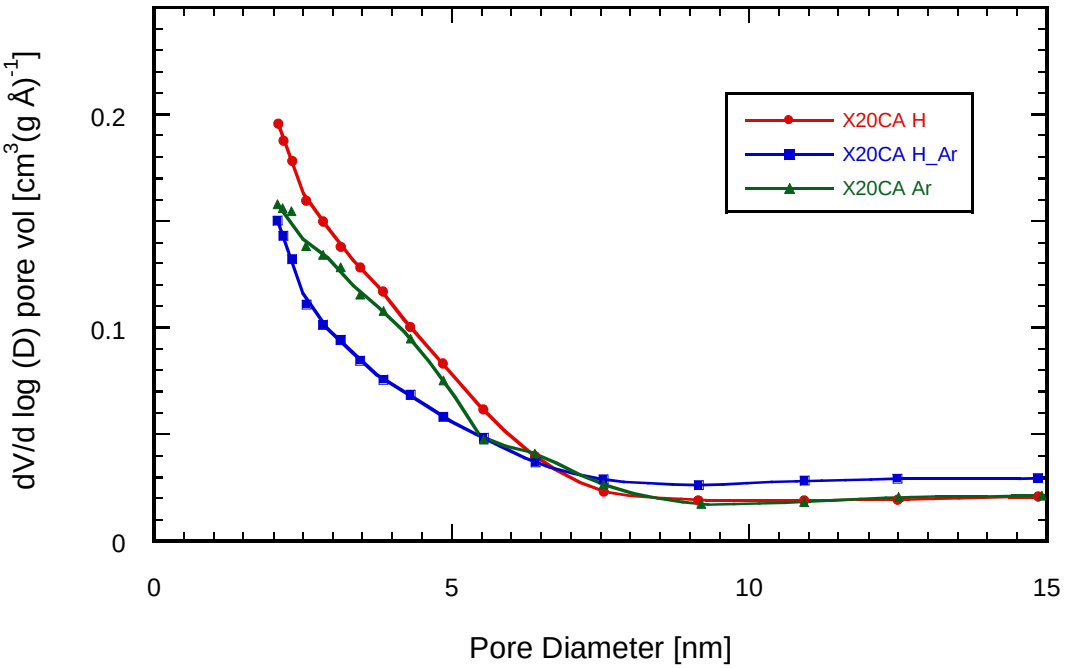

Figure 5.33: Mesopore Size Distributions for X20CA treated at 1000°C in different atmospheres

To ascertain the pore size distribution below 2 nm, the Dubinin-Astakhov method was applied to isotherms obtained at a low dose rate. These isotherms are of almost identical form to those given in Figure 5.32, with many more points being taken in the low pressure region. Linear fits (R^2>0.995) for the DA method were found over relative pressures in the range 10^{-5}<P/P_0<0.1 and the relevant calculated quantities are given in Table 5.14.

Sample	Limiting micropore volume [cm³ g^{-1}]	Heterogeneity parameter, *n*	Modal equivalent pore width [nm]
X20CA H	0.24	2.72	1.40
X20CA H_Ar	0.23	2.75	1.40
X20CA Ar	0.21	2.39	1.37
X20CA	0.20	2.15	1.31

Table 5.14: Micropore characteristics of X20CA treated at 1000°C in different atmospheres

In a comparison of the micropore volumes calculated for the materials treated at 1000°C by the *t*-plot method (Table 5.13) and those calculated using the DA method (Table 5.14) the values are slightly different but the same trend is seen, with the values for X20CA H and X20CA H_Ar being comparable and roughly 20% larger than that obtained for X20CA Ar. The discrepancy between the *t*-plot and DA values is possibly due to the method used to obtain the different isotherms. Many more equilibrations at low pressure were used to obtain the isotherms used in the calculation of micropore volume using the DA method which may have facilitated a greater degree of micropore filling.

The untreated material possesses a lower value of micropore volume than those treated at 1000°C which confirms that the structure of the material changes through heat treatment alone.

The heterogeneity parameter from DA analysis is also lower for the untreated material which indicates a slightly broader distribution of pore sizes than the other samples. A narrowing of pore size distribution occurs during heat treatment and the larger values of heterogeneity parameter seen for materials treated in hydrogen possibly reflects the fact that surface groups are removed from the material which is also seen by a shift in the peak position. For the material treated in argon the differential pore volume distribution peaks at a pore width of 1.31 nm shifts to 1.37 nm due to reordering of the graphitic regions in the carbon material. Treatment with hydrogen results in a marginally larger value of modal pore width of 1.40 nm for both X20CA H and X20CA H_Ar.

5.3.2 Chemical Composition

Using the same technique as before, the ratio of carbon: hydrogen: nitrogen present in each material was determined and is expressed as a weight percentage of the total sample mass in Table 5.15.

Sample	C [wt.%]	H [wt.%]	N [wt.%]	balance [wt.%]
X20CA H	91.9	0.5	1.1	6.5
X20CA H_Ar	89.0	0.7	1.6	8.7
X20CA Ar	89.3	0.4	2.3	8.0

Table 5.15: Elemental composition (wt.%) of X20CA treated at 1000°C in different atmospheres on a dry basis

As anticipated, the quantity of nitrogen present in each of the samples decreases with hydrogen concentration during treatment at 1000°C. This shows that treatment with hydrogen at a high temperature provides a useful method by which to control the amount of nitrogen in nitrogen-enriched carbon materials. The nitrogen content of the untreated material was determined to be 3.6 wt.% (from Table 5.4) and the reduction to 2.3 wt.% seen in X20CA Ar indicates that some nitrogen is removed during treatment at 1000°C in an inert atmosphere. This was to be expected as the temperature is greater than that used during both carbonisation and activation, and the gasification of some material was recorded (*ca.* 10 wt.%).

Previously, it was found that the carbon materials contained a small amount of mineral matter from the sodium carbonate used during synthesis and contamination from the ball milling process. Proximate analysis was carried out to determine the amount of incombustible material present in each of the materials treated at 1000°C, and the results on a dry basis are given in Table 5.16.

Sample	Volatiles [wt.%]	Fixed Carbon [wt.%]	Ash [wt.%]
X20CA H	4.5	94.0	1.5
X20CA H_Ar	4.9	87.9	7.2
X20CA Ar	5.3	92.9	1.8

Table 5.16: Composition (wt.%) of X20CA treated at 1000°C in different atmospheres on a dry basis, determined by proximate analysis

Proximate analysis shows that the samples X20CA H and X20CA Ar show comparable amounts of ash present which is slightly larger than that of the precursor material which contained 1.1 wt.% ash (Table 5.5). This is to be expected as roughly 10 wt.% is lost during treatment at 1000°C, and the mineral matter effectively becomes concentrated in the carbon material.

A substantially larger ash content was found for X20CA H_Ar which may correspond to a greater amount of contamination from ball milling due to the different times at which materials were prepared. The relatively high ash content of this material clearly influences the results of physical and electrochemical characterisation, and therefore data has been adjusted where possible to take the ash content into account; however a degree of uncertainty over the composition of this specific sample remains.

The values in Table 5.15 were adjusted to give the composition of the materials on a dry, ash-free basis and are shown in Table 5.17.

Sample	C [wt.%]	H [wt.%]	N [wt.%]	O (by difference) [wt.%]
X20CA H	93.4	0.5	1.1	5.0
X20CA H_Ar	95.8	0.8	1.7	1.6
X20CA Ar	91.0	0.4	2.3	6.3

Table 5.17: Elemental composition (wt.%) of X20CA treated at 1000°C in different atmospheres on a dry, ash-free basis

The compositions indicated in Table 5.17 remain affected by the ash content as the oxygen content of the mineral matter was not determined, but was assumed to be oxygen-free to permit calculation of the values in Table 5.17. This is reflected by the relatively low value of oxygen content associated with X20CA H_Ar as it can be expected to have a value between that obtained for X20CA H and X20CA Ar (*i.e.* 5.0 - 6.3 wt.%). Nevertheless, the adjusted values still show that the quantity of nitrogen present in each of the samples decreases with the hydrogen concentration during treatment at 1000°C.

5.3.2.1 X-Ray Photoelectron Spectroscopy

X-ray spectra from the materials were quantified to provide a measure of the composition of their surface layer. The results are shown in terms of atomic % in Table 5.18 which were converted to wt.% (given in Table 5.19) to allow for comparison with elemental analysis results.

Sample	C [at.%]	N [at.%]	O [at.%]	Na [at.%]
X20CA H	92.1	0.8	6.5	0.6
X20CA H_Ar	93.6	1.1	5.0	0.3
X20CA Ar	92.3	1.9	5.5	0.3

Table 5.18: Elemental Composition (at.%) of X20CA treated at 1000°C in different atmospheres on a dry basis determined by XPS

Sample	C [wt.%]	N [wt.%]	O [wt.%]	Na [wt.%]
X20CA H	89.6	0.9	8.4	1.1
X20CA H_Ar	91.7	1.3	6.4	0.6
X20CA Ar	90.1	2.2	7.1	0.6

Table 5.19: Elemental Composition (wt.%) of X20CA treated at 1000°C in different atmospheres on a dry basis determined by XPS

The elemental composition determined by XPS shows the same trend as that found by combustive analysis, namely that the nitrogen content is diminished by reaction with hydrogen.

As was noted previously, the sensitivity of each technique is limited as oxygen content is unable to be ascertained through combustive analysis, and XPS is unsuitable for the determination of hydrogen content. It is therefore inevitable that

there are some differences between the values obtained using both techniques. Notwithstanding, the disparity between the bulk and surface composition may be taken to indicate that the majority of nitrogen present in the samples is contained in the surface region of the material. The oxygen concentration determined by XPS is higher than that obtained by elemental analysis and can be attributed to valencies created by high temperature treatment reacting with oxygen on exposure to the atmosphere, however there is no systematic variation seen between samples.

Detailed spectra were obtained for the materials over a range of binding energies between 395 – 407 eV which corresponds to the presence of nitrogen groups.

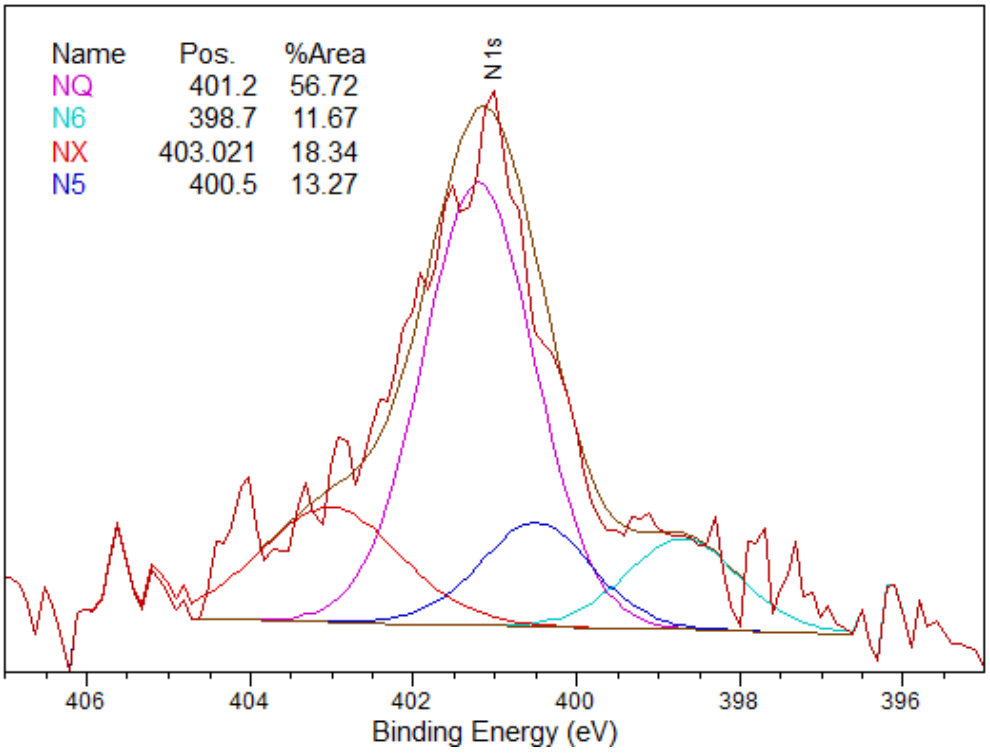

Figure 5.34: N1*s* X-ray photoelectron spectra for X20CA H

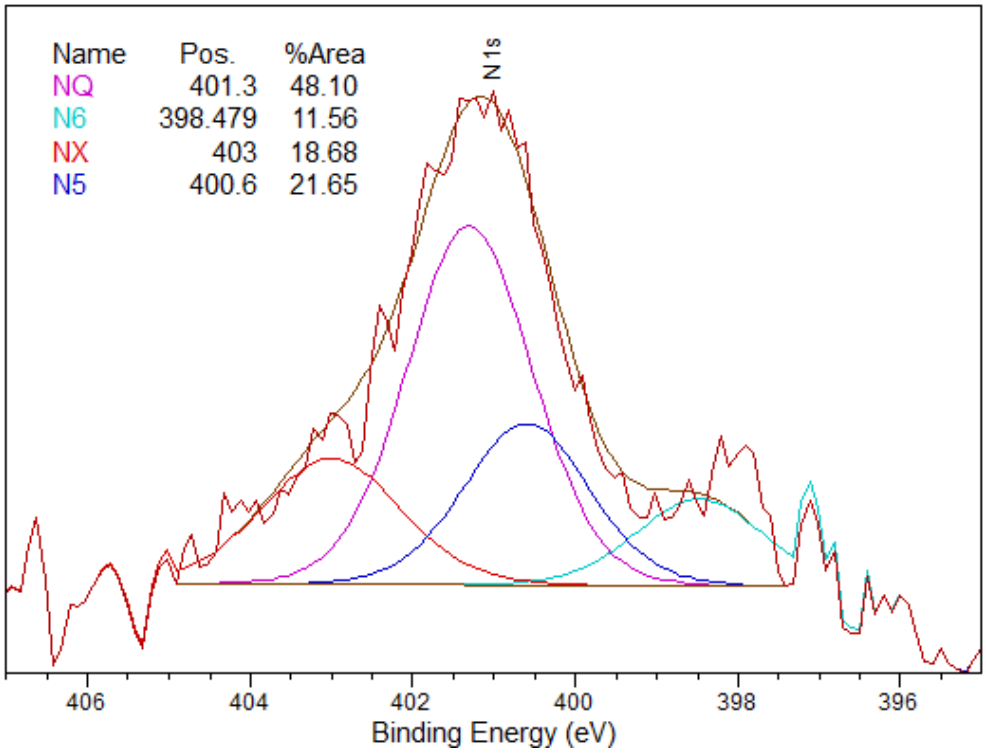

Figure 5.35: N1*s* X-ray photoelectron spectra for X20CA H_Ar

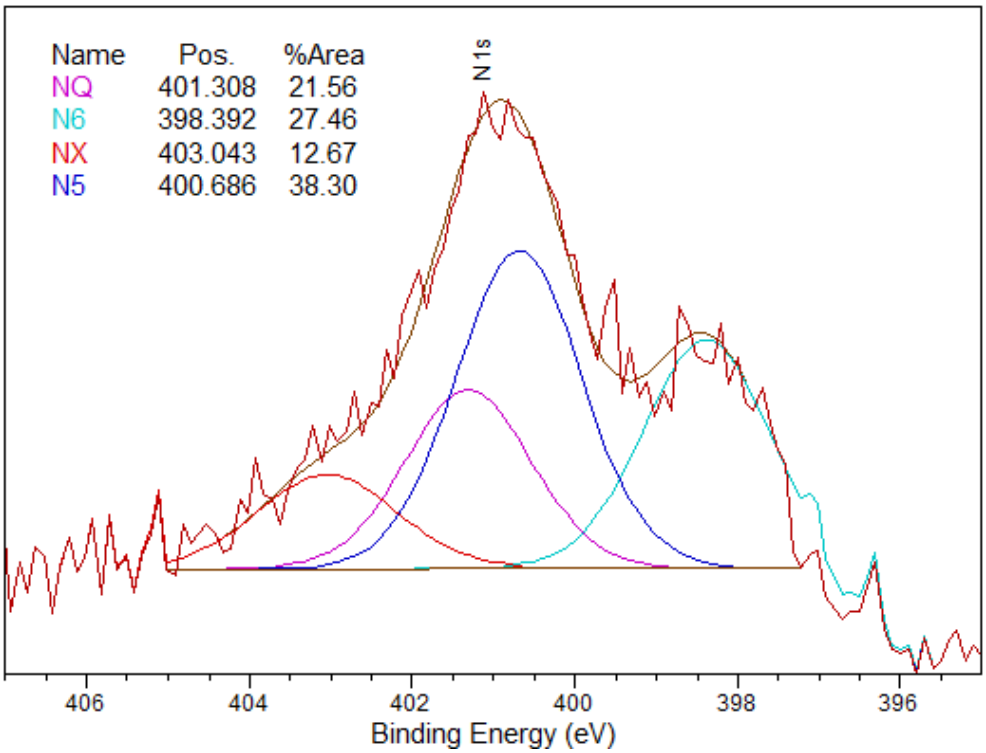

Figure 5.36: N1*s* X-ray photoelectron spectra for X20CA Ar

In contrast to the spectra obtained for the co-carbonisation products (Figure 5.20 and Appendix E) that have a very similar form, Figure 5.34, Figure 5.35 and Figure 5.36 show that treating the material with hydrogen removes certain nitrogen groups disproportionately, specifically the peak at a binding energy of 398.4 eV (N-6) is markedly diminished when hydrogen is present during thermal treatment.

Deconvolution of these spectra was performed in the same manner as before and the results are expressed as a percentage of the total nitrogen composition in Table 5.20.

Sample	N-5 [%]	N-6 [%]	N-Q [%]	N-X [%]
X20CA H	13.3	11.7	56.7	18.3
X20CA H_Ar	21.7	11.6	48.1	18.7
X20CA Ar	38.3	27.4	21.6	12.7

Table 5.20: Nitrogen group composition for X20CA treated at 1000°C in different atmospheres

The absolute concentrations of nitrogen groups were determined by multiplying the atomic percentage of the N1*s* peak by the relative compositions from Table 5.9 and Table 5.20; the results are given in Table 5.21.

Sample	N-5 [at.%]	N-6 [at.%]	N-Q [at.%]	N-X [at.%]
X20CA H	0.1064	0.0936	0.4536	0.1464
X20CA H_Ar	0.2387	0.1276	0.5291	0.2057
X20CA Ar	0.7277	0.5217	0.4096	0.2407
X20CA	1.1681	1.0618	0.5236	0.3463

Table 5.21: Nitrogen group concentration for X20CA treated at 1000°C in different atmospheres

The presence of all nitrogen groups is diminished through heat treatment at 1000°C. Significant reductions in the amount of edge nitrogen groups (N-5, N-6 and N-X) accompany thermal treatment, and quaternary groups are less affected. Of particular interest is the disproportionate removal of N-5 and N-6 groups that corresponds to the presence of hydrogen during thermal treatment. Also, the larger quantity of quaternary nitrogen seen in X20CA H and X20CA H_Ar suggests that some nitrogen atoms located at the edge of graphene sheets are converted into quaternary nitrogen during thermal treatment under hydrogen. It has been reported that pyrrolic (N-5) and pyridinic (N-6) nitrogen groups undergo a gradual conversion to quaternary nitrogen at temperatures in excess of 600°C [**255**].

By comparing the types of nitrogen groups present in samples X20CA Ar and X20CA H it is reasonable to propose that differences in the electrochemical behaviour seen between these two materials arises mainly from the significantly greater concentrations of nitrogen edge groups in X20CA Ar.

5.3.3 Pycnometry

The skeletal density of the carbon materials was estimated using helium pycnometry to allow for the calculation of the scattering length densities of the samples for SANS experiments. The skeletal density of X20CA H_Ar was not determined but it is reasonable to assume that the value lies between that obtained for X20CA H and X20CA Ar.

The slightly higher skeletal density of X20CA H in comparison with X20CA Ar indicates that less ordered regions of the material are removed by reaction with hydrogen. Also, as the value of skeletal density approaches that of theoretical pure graphite (2.267 g cm^{-3} [**149**]) it can be posited that the material exhibits a substantial degree of graphitisation and very little closed porosity.

		X20CA H	X20CA H_Ar	X20CA Ar
Skeletal Density	[g cm^{-3}]	2.19	-*	2.14

Table 5.22: Skeletal density for X20CA treated at 1000°C in different atmospheres (*not determined)

5.3.4 Small-Angle Neutron Scattering

Parameters relevant to the SANS experiments were determined using the pycnometry data (Table 5.22), elemental analysis results (Table 5.15) and the method described in Chapter 3.

		X20CA H	X20CA H_Ar	X20CA Ar
Coherent Scattering Length, b_c	[10^{-12} cm]	5.2203	5.0733	5.4243
Scattering Length Density, ρ_s	[10^{10} cm^{-2}]	6.884	6.546 -6.690*	6.764
System contrast, $(\Delta\rho)^2$	[10^{21} cm^{-4}]	4.733	4.280 - 4.470*	4.570
Max. Porod Invariant, Q_{max}	[10^{22} cm^{-4}]	2.3356	2.2058	2.2551

Table 5.23: Calculated neutron scattering parameters for X20CA treated at 1000°C in different atmospheres (*estimate using determined skeletal densities)

A plot of the scattering cross section versus wave vector for each of the SANS experiments is given in Figure 5.37.

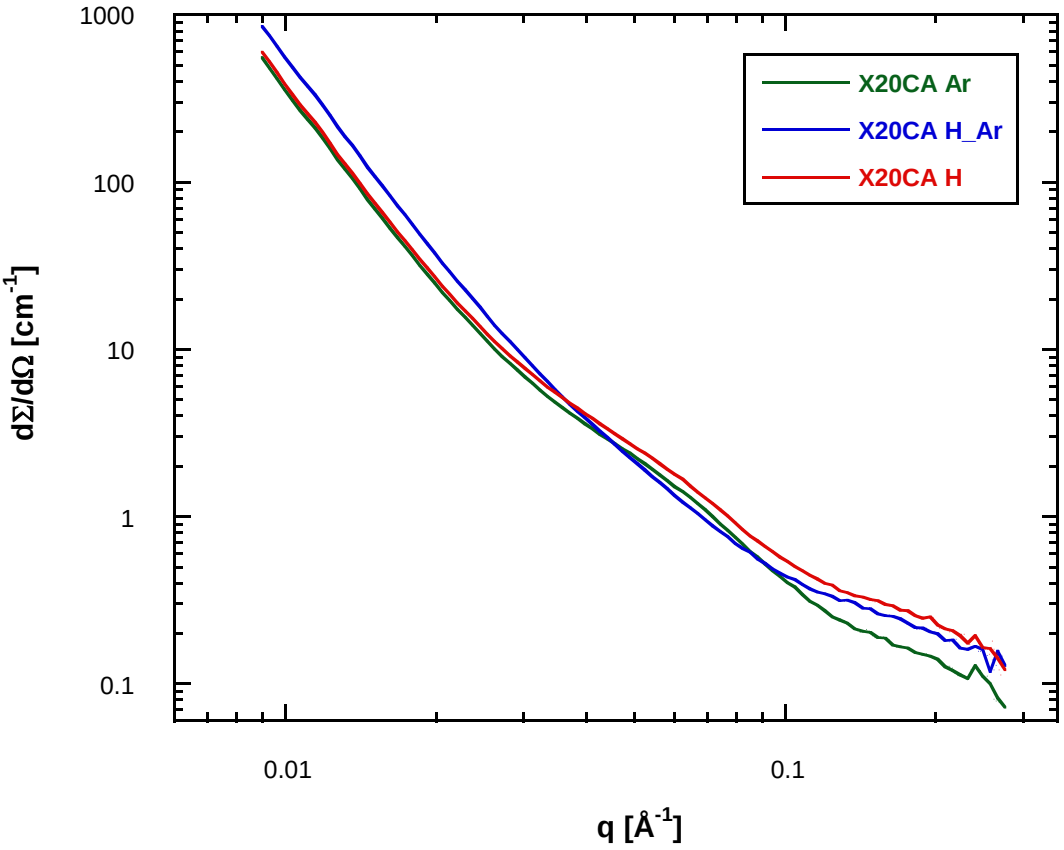

Figure 5.37: SANS plots for X20CA treated at 1000°C in different atmospheres

The form of the plots seen in Figure 5.37 is similar to that reported for other porous carbon materials [**263**, **284**, **286**, **287**] however the fitting of fractal models was deemed unsuitable for this data as power law behaviour over a significant *q* range was not present. (Linear behaviour over at least one decade of *q* is required for fitting fractal models.)

The subtle differences in the scattering between different samples in Figure 5.37 correspond to distinct features associated with the porous characteristics obtained using nitrogen adsorption isotherms. At low values of *q*, which correspond to larger pore sizes and particle size effects, the values of scattering cross section are similar for each of the materials with X20CA H_Ar showing the highest values. This corresponds to the mesopore size distribution generated using the BJH method for pore sizes greater than 10 nm (Figure 5.33) which indicates that there is a slightly greater volume associated with larger mesopores in X20CA H_Ar. As stated

previously, this may be an attributed to the relatively high level of contamination found by proximate analysis in this sample.

The differential scattering cross section associated with X20CA H becomes greater than the other samples at q ~ 0.03 $Å^{-1}$which corresponds to the increase in differential pore volume seen in Figure 5.33 for pores less than 6.5 nm. For samples X20CA H_Ar and X20CA Ar the cross section plots cross at q ~ 0.04 $Å^{-1}$ and q ~ 0.08 $Å^{-1}$ which corresponds to the changes in relative pore volume seen at values of roughly 5.5nm and 7.0 nm in Figure 5.33.

For values of q greater than 0.1 $Å^{-1}$, which corresponds to the micropore region [**284**], X20CA H and X20CA H_Ar indicate a significantly greater amount of scattering in comparison with X20CA Ar, which again correlates well with the micropore volumes determined from analysis of nitrogen adsorption isotherms.

Porod type behaviour, where the cross section varies with q^{-4}, is approached at the highest values of q studied. However, the errors associated with each value of differential scattering cross section increase with increasing wave vector, and in the region where Porod scattering is identified, the errors are of the same order of magnitude as the measured quantity. (The individual plots from Figure 5.37 with the associated errors are given in Appendix F.) For this reason, an upper limit of q = 0.275 $Å^{-1}$ was chosen to allow for a meaningful analysis of the experimental results. To obtain data with lower errors for $q > 0.275Å^{-1}$, experiments would need to be performed using an instrument with a different geometry.

5.3.4.1 Porod Invariant

The Porod Invariants were calculated using Eq. 3.39 for each of the samples over the range $0.009 < q < 0.275$ $Å^{-1}$ and are given in Table 5.24. The actual value of the Porod Invariant in these experiments is significantly larger than the values given in Table 5.24 due to the limited q-range analysed. As the integral in Eq. 3.39 has limits of $q = 0$ and $q = \infty$, scattering data over the entire range of q values would be necessary to accurately determine the Porod Invariant for the system, and only

qualitative information can be ascertained from the scattering data in Figure 5.37. Nevertheless, the Porod Invariant calculated over the analysed *q*-range can be used as an indicator of the volumetric surface area of the sample, and can be used to compare surface areas when the samples are of similar composition [**180**, **263**, **284**, **288**].

		X20CA H	X20CA H_Ar	X20CA Ar
Porod Invariant, *Q*	[arbitrary units]	2.201	2.089	1.552

Table 5.24: Experimental Porod Invariant values for X20CA treated at 1000°C in different atmospheres

The trend seen in the values of Porod Invariant is similar to that seen in Table 5.13, *i.e.* the specific surface area and Porod Invariant of X20 CA H > X20CA H_Ar > X20CA H. However, to quantify the volumetric surface area of the samples using Eq. 3.38, accurate determinations of the limiting values of $q^4 \cdot d\Sigma/d\Omega$ (the Porod constant) are needed. The scattering data appears to follow the Porod Law (*i.e.* $d\Sigma/d\Omega \propto q^{-4}$) in the high-*q* region, but as oscillations around the limiting value of $q^4 \cdot d\Sigma/d\Omega$ occur [**276**] and the errors are at their largest in this region, it was felt that more scattering data at larger values of *q* would be required to calculate the true limiting value of $q^4 \cdot d\Sigma/d\Omega$. Therefore further experimental runs using a different instrument geometry would be required to ascertain reasonably accurate values of volumetric surface area for these samples.

It is noted that X20CA H_Ar has a hydrogen content of 0.8 wt.% which is greater than the other samples (*ca.* 0.4 wt.%) and that hydrogen has a relatively large incoherent scattering cross section (82.02×10^{-24} cm^2 [**278**]). Subtraction of incoherent scattering was deemed to be unnecessary as the amount of contamination was very small and carbon, nitrogen and oxygen have extremely small values of incoherent scattering cross section ($0.001 - 0.50 \times 10^{-24}$ cm^2 [**278**]).

Additionally the Porod identity may not be satisfied if the boundary between the two phases has a different density than the bulk solid, and the difference between the

chemical compositions determined using elemental analysis and XPS indicates that the materials are inhomogenous which could influence the scattering observed.

5.3.5 CM-SANS

As it has been proposed that the presence of nitrogen groups in a carbon material enhances the wettability of the electrode surface [**176, 231**, **236**, **238**, **240**, **242**, **243**, **247**, **248**], thereby increasing the electrochemically surface area in an EC, Contrast-Matching SANS (CM-SANS) could be used to probe the degree of inactive surface area in an electrode/ electrolyte system. CM-SANS has previously been used to investigate closed porosity in porous materials, and pores not filled with contrast-matching liquid effectively scatter in the same manner as closed porosity, therefore it was proposed that a comparison between SANS data for dry and contrast-matched samples could provide an indication of the inactive/ unaccessed surface area.

In contrast-matching experiments it is typical to obtain scattering data for the same sample using different liquid mixtures of controllable scattering length density and the optimum mixture is identified where the contrast between the solid and liquid phases is at a minimum [**283**]. However, from Table 5.23 it can be seen that the scattering length density of the carbon materials under study is *ca.* 6.7×10^{-10} cm^{-2} which is similar to that of deuterium oxide (6.40×10^{-10} cm^{-2}) which can be considered to represent an aqueous electrolyte solution. CM-SANS plots obtained using D_2O as the contrast-matching liquid for the carbon materials treated at 1000°C are given in Figure 5.38.

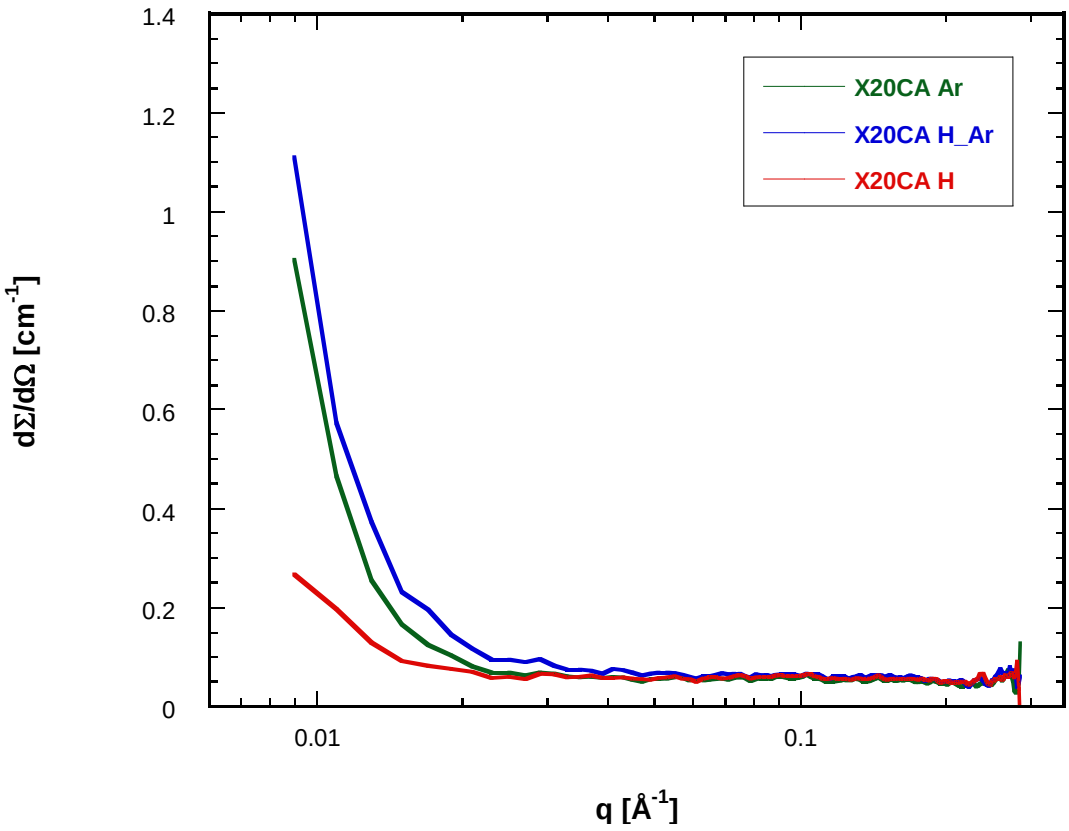

Figure 5.38: CM-SANS plots using D_2O for X20CA treated at 1000°C in different atmospheres

In comparison with the SANS data for the materials (Figure 5.37) the contrast-matching experiments (Figure 5.38) show that contrast-matching with deuterium oxide reduced the differential scattering cross-section by about three orders of magnitude in the low-*q* range. The effect of contrast-matching is clearer in Figure 5.39 where the scattering from dry and contrast-matched samples are displayed on the same plot.

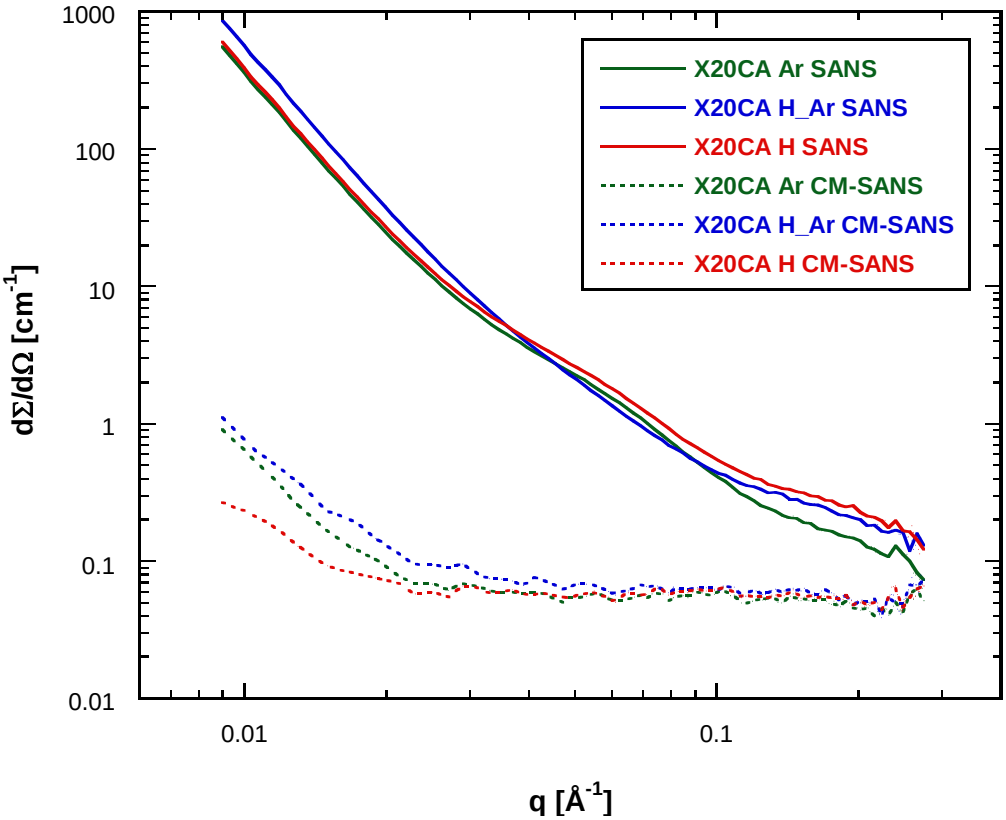

Figure 5.39: SANS and CM-SANS plots using D_2O for X20CA treated at 1000°C in different atmospheres

Also, the value of the differential scattering cross section is roughly constant for each material for *q* values between 0.04 and 0.22 $Å^{-1}$. This can be taken to indicate that the contrast-match between the solid and liquid phase is attained using D_2O, and that the porosity of all the samples is open and filled with the contrast-matching liquid.

It is possible that the slight differences between the CM-SANS curves arise from a residual contrast between the solid phase and D_2O, as the carbon materials have different compositions and skeletal densities. This is likely as the relationship in Eq. 3.34 shows that the differential scattering cross section varies with the square of the contrast between the two phases. However, contrast-matching experiments using different liquids to ascertain the ideal contrast-matching liquid composition were not carried out due to time constraints. Also, there is no correlation between the values of scattering length density (Table 5.23) and the differential scattering cross section, which suggests that this effect is negligible. It is noted that deuterated cyclohexane has a scattering length density closer to that calculated for the materials under study (6.70×10^{-10} cm^{-2}), however it was felt that D_2O better reflects the physical properties

of an aqueous electrolyte in an electrochemical capacitor. For example, it was noted that an organic-based electrolyte wetted electrodes rapidly in comparison with an aqueous solution.

Also, the small value of $d\Sigma/d\Omega$ seen in the CM-SANS experiments may be attributed to the existence of incoherent background scattering which increases with the hydrogen content of the materials. This would correlate well with the findings from elemental analysis (Table 5.17) where the hydrogen content of X20CA H_Ar is largest (0.8 wt.%) and X20CA Ar is lowest (0.4 wt.%).

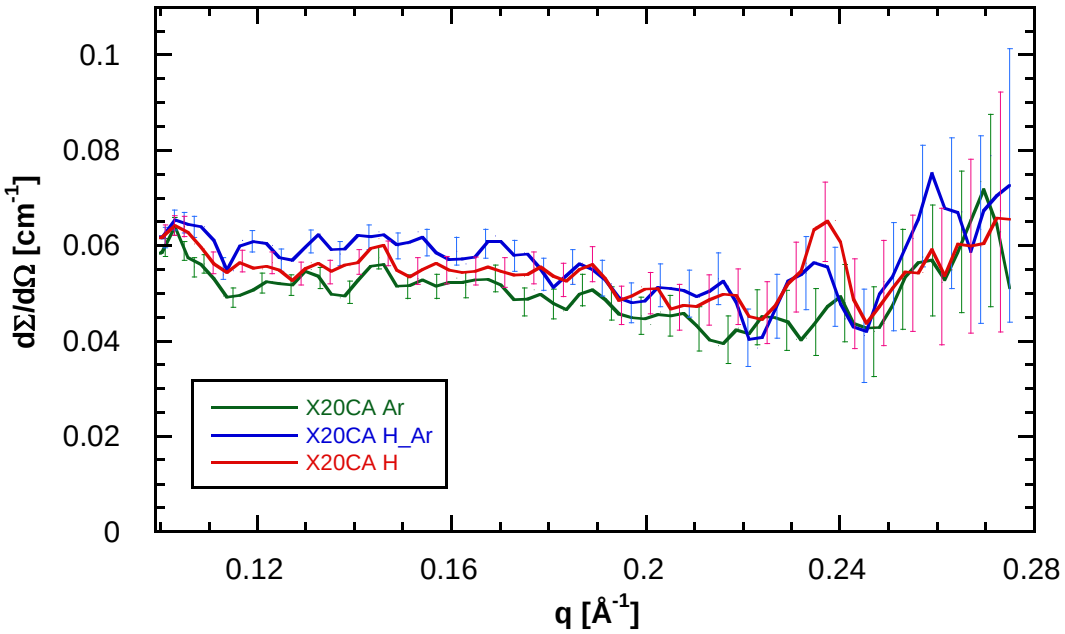

Figure 5.40: CM-SANS plots using D_2O for X20CA treated at 1000°C in different atmospheres in the 'high-q' range (with error bars)

At higher values of scattering wave vector in the range ~ 0.22 $Å^{-1} < q < 0.275$ $Å^{-1}$ (illustrated in Figure 5.40 with error bars) the difference in scattering between the 'dry' and contrast-matched samples is reduced by approximately a factor of 4. In this region the errors associated with the values are of similar order to the measured quantity but the data shows a slight upward trend, which may correspond to the presence of unfilled voids in the sample.

Although the absolute values of the differential scattering cross section for the CM SANS curves at all values of q are lower than those using dry samples, the upward deviation may be indicative of partial filling of the smallest pores (or in a similar

fashion to the adsorption of nitrogen, the assumption is made that the density of the liquid phase is unaffected by the proximity of the solid phase. This effect can be expected to occur to a greater extent as the size of the pores decrease).

Overall, there are no significant differences between the CM SANS curves for each of the samples which indicates that the amount of porosity accessed by D_2O is not influenced by the surface nitrogen concentration to any great extent.

5.3.6 Electrochemical Testing

5.3.6.1 Electrochemical Impedance Spectroscopy

EIS measurements and the calculation of cell parameters were made in the same manner as described previously. Examples of experimental spectra are shown in Figure 5.41 and the average values of capacitance and specific power are given in Table 5.25. The values given in Table 5.25 are averages obtained from at least three cells, and the maximum deviation from the average specific capacitance in cells assembled using the same material was less than 5.8%.

It is noted that the deviation for materials that had underwent treatment at 1000°C is larger than those discussed previously. During cell manufacture, markedly different behaviour on the addition of electrolyte was observed. Specifically, materials treated at 1000°C exhibited a more hydrophobic nature, and required immersion in electrolyte for a significantly longer time before sinking to the bottom of the container. Also, differences in the variation between cells were seen for materials heat treated in different atmospheres. The highest variation of 5.8% was seen when using X20CA Ar whereas a much smaller variation of 3.4% was seen for X20CA H (over a greater number of cells). This suggests that the material treated in hydrogen has a more homogenous structure and/or composition. Hydrophobicity also indicates that wetting of the entire solid surface with aqueous electrolyte may not occur, although the results from the CM-SANS experiments indicate that this is not problematic. It is also possible that the change in energy required to overcome hydrophobicity and fill the previously inaccessible volume occurs when the electrical

potential of the electrode is changed. This may account, at least partially, for the longer charge times observed during the first Galvanostatic cycle.

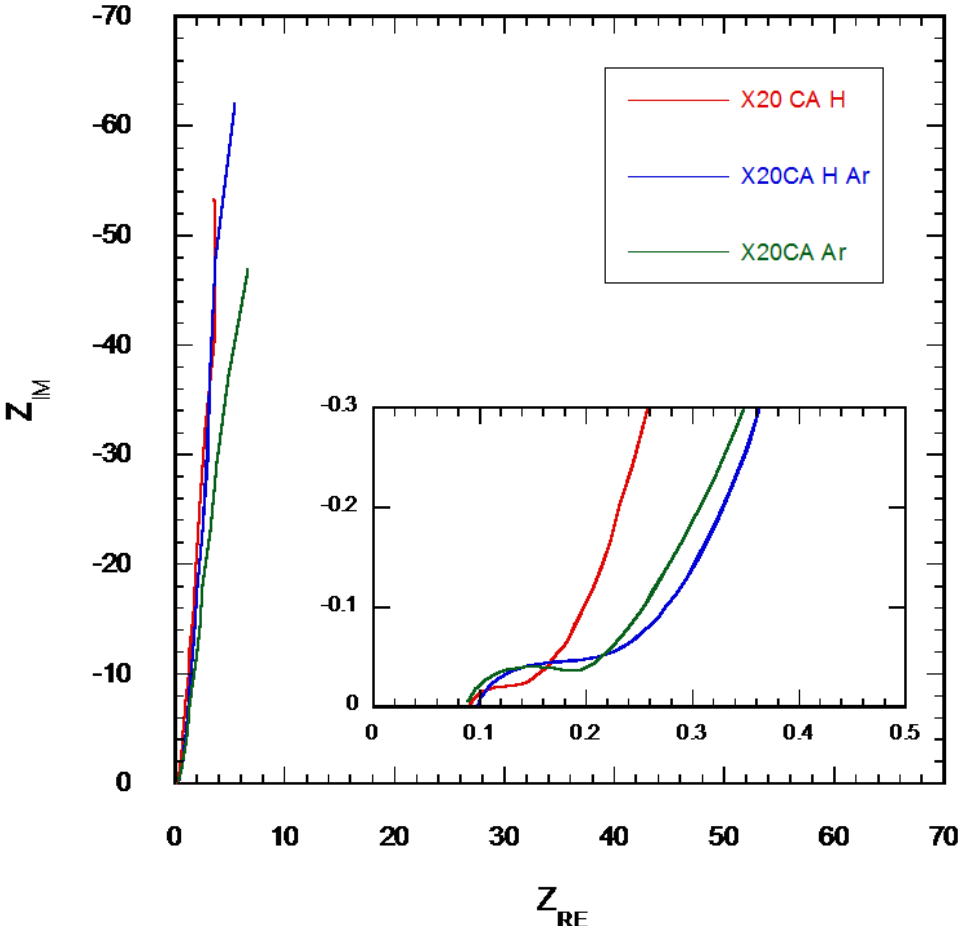

Figure 5.41: Nyquist plots for cells using X20CA treated at 1000°C in different atmospheres

Sample	EIS Specific Capacitance (at 10mHz) [F g^{-1}]	EIS Specific Capacitance / BET surface Area [μF cm^{-2}]	Max. Power density [kW kg^{-1}]
X20CA Ar	93.1	19.9	74.1
X20CA H_Ar	70.6	13.1	103.3
X20CA H	83.9	14.4	97.4

Table 5.25: Specific capacitance and maximum capacitance density from EIS for X20CA treated at 1000°C in different atmospheres

The Nyquist plot of the real and imaginary impedance components over the whole frequency range in Figure 5.41, shows that all of the cells have a capacitive nature at low frequencies but are not equivalent to a pure capacitor element. The low frequency behaviour is similar to that observed for the samples in Figure 5.21 with the presence of a phase angle at low frequencies indicating that the interphase between the electrode and electrolyte is not ideally polarisable.

The deviation from ideal capacitor behaviour decreases with increasing hydrogen concentration during thermal treatment. As stated previously, the extent to which each material is ideally polarisable may be influenced by their composition. In particular the surface nitrogen content (from XPS) seems to correlate well with the phase angle of the spectra at 10 mHz. This suggests that the degree of polarisability of the electrode is diminished by the presence of surface nitrogen groups, and indicates that charge is passed across the double layer during charge/ discharge to a greater extent with increasing nitrogen content [**10**].

The higher frequency behaviour, illustrated in the inset of Figure 5.41, shows a significantly different form to that previously observed, as the presence of a semi-circular section is quite clear. Moreover the apparent diameter of the semicircle varies with the gas used during treatment at 1000°C. X20CA H shows the most similar spectrum to that obtained for the untreated carbons tested previously, however the Warburg-type behaviour seen at higher frequencies is replaced by an arc segment that represents a parallel RC circuit. The arc becomes more pronounced for X20CA H_Ar and X20CA Ar, and the apparent diameter of the circle indicated by the arc increases with decreasing hydrogen concentration used during thermal treatment.

In the previously discussed samples it is possible that the resistance of the solid phase allows the Warburg component to dominate, whereas in the case of materials treated at 1000°C the resistance of the solid phase is likely to have decreased significantly (*via* graphitisation and/or the increase in quaternary nitrogen), reducing the influence of the Warburg component which reveals a circular aspect in the spectra.

All materials can be represented by Randles' circuit [**10**, **254**] over a finite frequency region (*ca*. 20 Hz - 20 kHz) and the equivalent resistances obtained by fitting this model to the experimental data are given in Table 5.26. At frequencies lower than roughly 20 Hz, the polarisability of the electrode seems to influence the experimental data unduly, rendering the data unsuitable for fitting to Randles' circuit.

Sample	Solution Resistance [Ω]	Faradaic Resistance [Ω]
X20CA Ar	0.093	0.0754
X20CA H_Ar	0.096	0.0450
X20CA H	0.094	0.0351

Table 5.26: Resistance values obtained by fitting Randles' circuit to EIS data for X20CA treated at 1000°C in different atmospheres

The values of solution resistance, as was observed in previous experiments, did not vary to any great extent when different electrode materials were used. The Faradaic resistances calculated by fitting Randles' circuit have an associated error of between 5.2% and 10.9% and show a clear dependence on the hydrogen concentration during thermal treatment. There is an apparent linear dependence between the Faradaic resistance of a material and the quantity of nitrogen present in the surface region of the material (determined by XPS) which is shown in Figure 5.42.

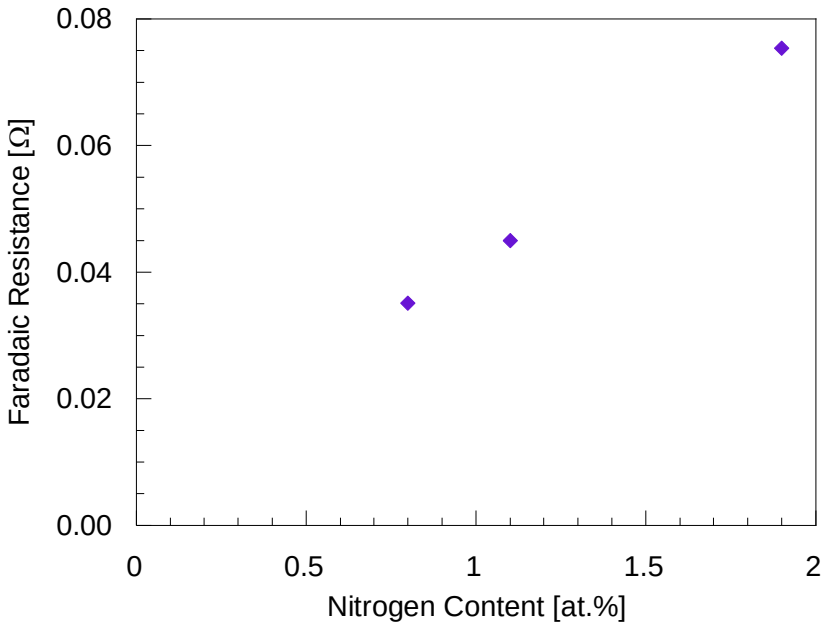

Figure 5.42: Faradaic Resistance against surface nitrogen content (XPS) for X20CA treated at 1000°C in different atmospheres (with linear fit)

This confirms the relationship indicated by the phase angle correlation, namely that the presence of nitrogen influences the polarisability of the electrode which results in charge crossing the double layer during charge/ discharge. This may be due to self-discharge mechanisms occurring during the charge and discharge processes.

Faradaic resistances suggest that a self-discharge mechanism is present or that pseudocapacitance is the predominant charge storage mechanism in the device [**10**]. It is highly unlikely that pseudocapacitance accounts for the majority of the amount of charge stored in cells using these materials. Firstly, the double-layer mechanism for carbon materials with BET surface areas of roughly 500 m^2g^{-1} can be expected to contribute a minimum of 50 F g^{-1} to the total specific capacitance, which accounts for the greater part of the specific capacitances given in Table 5.25. Also, the concentration of surface nitrogen is far lower than that of oxygen in the carbon materials mentioned previously, where the charge stored through pseudocapacitance has been estimated to account for 30% of the total capacitance at most. Self-discharge is far more likely to be responsible for the Faradaic resistances observed.

The Faradaic resistance does not have a direct influence on the ESR (and hence maximum power output) of the device as the real component of the impedance at

1kHz is closer to the value of solution resistance, but may have an adverse effect on the efficiency of the charge/ discharge process.

The values of specific capacitance in Table 5.25 determined using EIS are lower in comparison with values obtained using the previous materials (*i.e.* Table 5.10). Curiously, although treating X20CA at 1000°C increases the BET surface area, the values of specific capacitance decrease. However this has been shown to occur for other carbon materials treated at temperatures in excess of 900°C [**165**].

One possibility is that the density of the solid phase has increased after treatment at 1000°C which influences the ratio of phase volume to surface area. Also, by treating the materials at 1000°C it is likely that some degree of graphitisation occurs which increases the hydrophobicity of the electrodes, as was previously noted. It is then possible and that a fraction of micropores, and therefore surface area, may not be electrochemically active.

Another consideration is the influence that the polymer binder has on the pore characteristics of the electrode. It was previously mentioned that the binder adversely affects microporous materials disproportionately in comparison with predominantly mesoporous materials, and it is likely that this affects the results associated with materials treated at 1000°C. As the micropore volume associated with X20CA Ar, X20CA H_Ar and X20CA H has been shown to be larger than that of X20CA, and that the BET surface area is augmented markedly (Table 5.13) it is reasonable to assume that a greater amount of BET surface area arises from micropores in these samples. This results in a greater proportion of the total surface area being blocked by binder and therefore the electrochemical behaviour of materials treated at 1000°C cannot be directly compared to the behaviour of untreated materials.

Unfortunately, there was an insufficient quantity of sample remaining to allow for a useful nitrogen adsorption analysis of the tested electrodes, and it could be debated that the analysis procedure would yield unreliable results. For example, heating under vacuum to degas the sample may alter the distribution of binder, cooling to 77K for analysis may also affect the polymer (oscillations in the heat flow were

observed during DSC experiments which may be due to phase changes), and specific adsorption mechanisms between the adsorbate and polymer binder may complicate interpretation of the isotherms.

When considering the specific capacitance of treated materials it is possible to adjust the values to remove the influence of ash content (particularly in the case of X20CA H_Ar) under the assumption that the mineral matter is electrochemically inactive in the same manner as before. However there remains a degree of uncertainty over the extent to which the addition of binder influences the surface area of the composite electrode. Therefore the BET surface area of the carbon material has been used to normalise and compare the electrochemical results between samples despite being larger than the actual surface area of the electrodes tested. As the micropore volumes of the carbon materials after heat treatment are broadly similar, it is reasonable to assume that the binder influences each material to the same degree *i.e.* by blocking the same proportion of surface area in all samples.

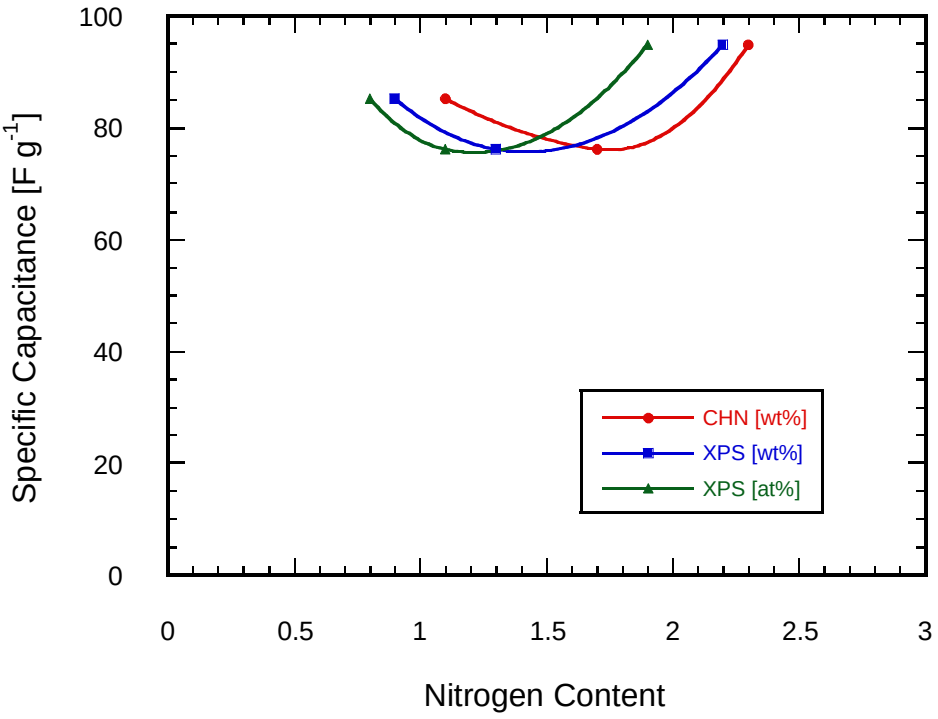

Figure 5.43: Specific capacitance against nitrogen content for X20CA treated at 1000°C in different atmospheres (data adjusted for ash content)

The relationship between specific capacitance and nitrogen content (determined by both elemental analysis and XPS) is seen in Figure 5.43 which shows that X20CA H has a specific capacitance of 85.2 F g^{-1}. The slight increase in nitrogen content of X20CA H_Ar in comparison with X20CA H is accompanied by a decrease in specific capacitance. It is possible that the lower surface area of X20CA H_Ar is responsible for the observed reduction in specific capacitance, however it is likely that the ash content has influenced the results.

A more interesting finding is that the gravimetric capacitance of X20CA Ar is greater than that of X20CA H and X20CA H_Ar despite these samples exhibiting larger BET surface areas. This is similar to the findings of the previous experiments using X10CA and X20CA and indicates that the presence of nitrogen groups can augment the specific capacitance of carbon materials, and moreover, this could be of practical benefit in the manufacture of ECs that use KOH electrolyte. However it is important to bear in mind that any increase in the amount of energy stored will probably be accompanied by an increase in Faradaic resistance.

The influence of nitrogen content on capacitance is more evident when the specific capacitance is normalised on the basis of BET surface area, as shown in Figure 5.44.

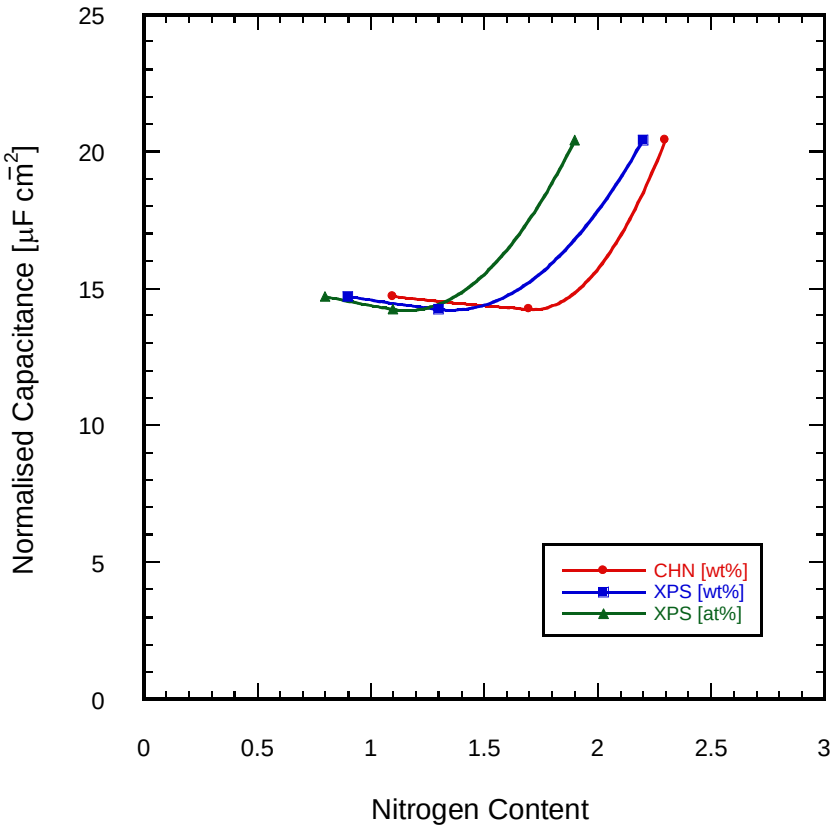

Figure 5.44: Surface area normalised capacitance against nitrogen content for X20CA treated at 1000°C in different atmospheres (data adjusted for ash content)

The surface area normalised specific capacitance for both X20CA H and X20CA H_Ar is approximately 14.4 μF cm^{-2} (when adjusted for ash content), whereas a value of 20.4 μF cm^{-2} is obtained for X20CA Ar.

A rough connection between the XPS spectra and the surface area normalised specific capacitance can be made, as the form of the nitrogen specific spectra are also grouped in this manner with only X20CA Ar showing an appreciable peak at the binding energy associated with pyridinic nitrogen groups. A plot of normalised specific capacitance *vs* the concentration of pyridinic groups in the surface region approximates a straight line, as indicated in Figure 5.45.

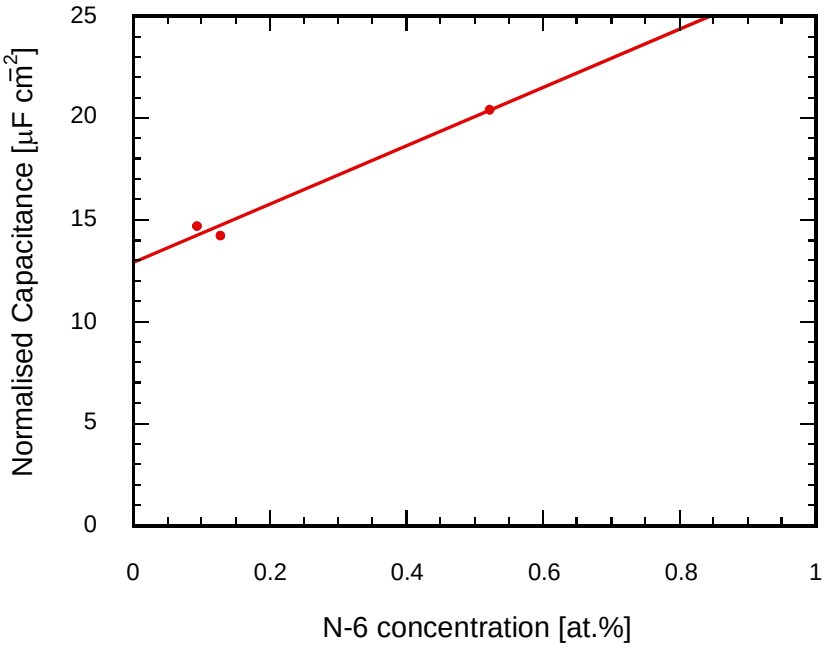

Figure 5.45: Surface area normalised capacitance against pyridinic nitrogen (N-6) concentration for X20CA treated at 1000°C in different atmospheres (data adjusted for ash content)

This finding indicates that the specific capacitance of these materials is enhanced by the presence of pyridinic nitrogen groups. The *y*-intercept of the fitted line suggests that a surface area normalised specific capacitance of 12.9 μF cm^{-2} corresponds to the double-layer capacitance of a carbon material with the same pore structure and degree of graphitisation, but no pyridinic nitrogen content.

It is noted that this treatment of results assumes that all of the surface area contributes to the specific capacitance uniformly, whereas it has been found that the pore size influences the mechanism by which charge is stored. However the pore size distribution and surface area of the materials being discussed are fairly similar which reduces the overall uncertainty associated with this assumption.

It is also possible that the N-5 groups are responsible for the increase in normalised specific capacitance as the quantities indicated in Table 5.21 correlate in a similar manner to the N-6 groups. However, the degree of correlation is reduced for this quantity and the N-5 group in XPS corresponds to two distinct nitrogen groups which can be expected to behave differently under charge/ discharge in an electrochemical capacitor. The presence of both pyrrolic and pyridonic nitrogen in an unknown ratio

is also complicated by the existence of three tautomeric forms of pyridine [**255**], which makes it unlikely that there is a linear relationship between the concentration of N-5 groups and surface area normalised specific capacitance. The apparent correlation seen may simply be a reflection of the fact that the absolute concentration of N-5 groups follows the same trend as that for N-6 groups, as they are both edge groups removed by the presence of hydrogen during thermal treatment.

5.3.6.2 Galvanostatic Cycling

Galvanostatic cycling was used to better reflect the operating conditions encountered in a functional device, and to establish whether or not the same differences in behaviour observed during EIS apply to practical cells.

An example of the charge/ discharge profile for each of the heat treated materials at a rate of 2 mA (~ 0.2 A g^{-1}) is given in Figure 5.46. The data has been adjusted to reflect a single constant electrode mass of 10.0 mg (including binder and carbon black) to allow for comparisons between materials to be made.

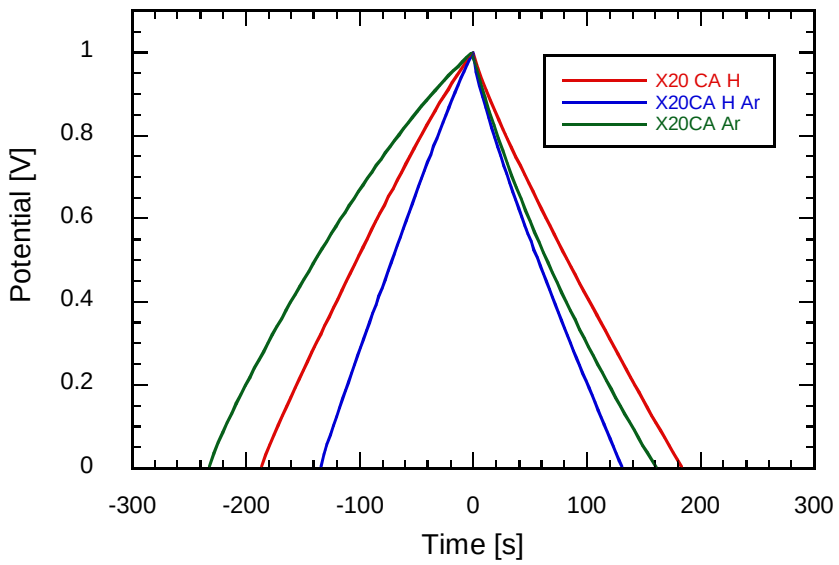

Figure 5.46: Charge/ Discharge profiles at 2 mA for X20CA treated at 1000°C in different atmospheres (electrode mass normalised to 10.0 mg)

The charge/ discharge efficiency associated with each material was determined for the profiles given in Figure 5.46 and a value of roughly 85% was found for X20CA H and X20CA H_Ar which is similar to that obtained for the previous materials. A significantly greater degree of asymmetry between the charge and discharge profiles for X20CA Ar is evident at this rate, and a significantly lower coulombic efficiency of 53% was determined for the profile in Figure 5.47. This may be a result of the higher Faradaic resistance (or degree of non-ideal polarisability) that was found for this sample, as a leakage current will adversely affect the charging efficiency of the cell.

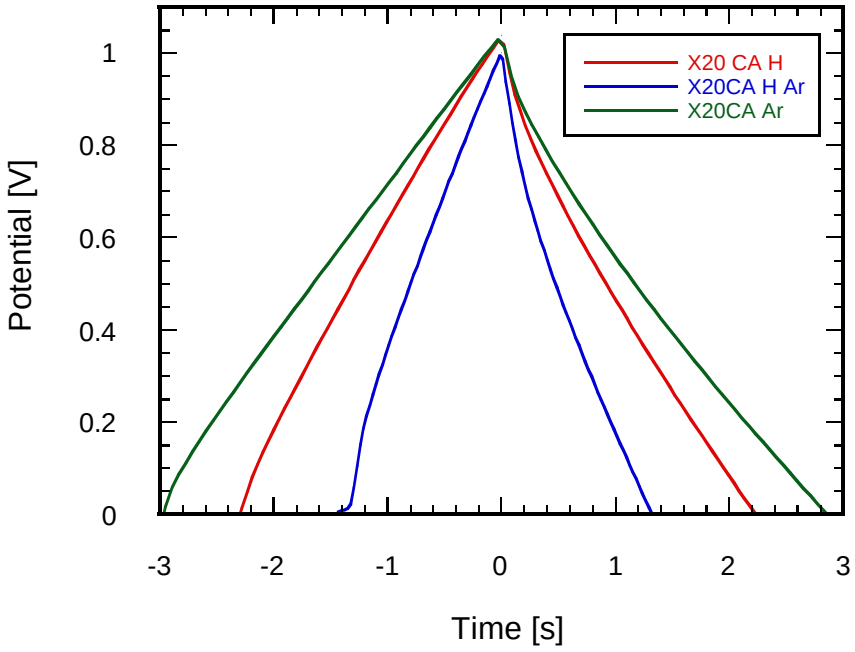

Figure 5.47: Charge/ Discharge profiles at 100 mA for X20CA treated at 1000°C in different atmospheres (electrode mass normalised to 10.0 mg)

Specific capacitances were calculated at several discharge rates to identify any rate-dependent behaviour associated with nitrogen content. The values of specific capacitance obtained at each discharge rate are given in Table 5.27, and are averages obtained from at least three cells. The maximum deviation from the average specific capacitance in cells assembled using the same material was 11.8% at a rate of 2 mA (for X20CA Ar) however a huge variation in the behaviour of X20CA H_Ar at 100

mA was found, and may be a consequence of inhomogeneous distribution of the contamination found in this particular material.

Sample	Galvanostatic discharge specific capacitance [F g^{-1}]						
	2 mA	4 mA	8 mA	16 mA	32 mA	64 mA	100 mA
X20CA H	89.6	83.5	77.9	72.8	67.8	63.2	58.2
X20CA H_Ar	69.9	66.3	61.9	57.5	53.5	47.1	42.7
X20CA Ar	88.0	87.7	85.1	81.5	77.5	74.3	71.0

Table 5.27: Specific capacitance obtained by Galvanostatic discharge at different rates for X20CA treated at 1000°C in different atmospheres

At rates of charge/ discharge greater than 4 mA the values of specific capacitance determined by Galvanostatic discharge follow the same trend as the EIS values in Table 5.25. Quantitatively, the values obtained by the two methods correlate well for a Galvanostatic discharge rate of 4 mA.

Anomalously, at the lowest rate of 2 mA (roughly 0.2 A g^{-1}), the specific capacitance of X20CA H is marginally larger than that of X20CA Ar. This is probably a consequence of the higher Faradaic resistance associated with this sample as the leakage current will have more influence at lower rates of charge/ discharge. This is clarified by a plot of specific capacitance against specific discharge current which is given in Figure 5.48.

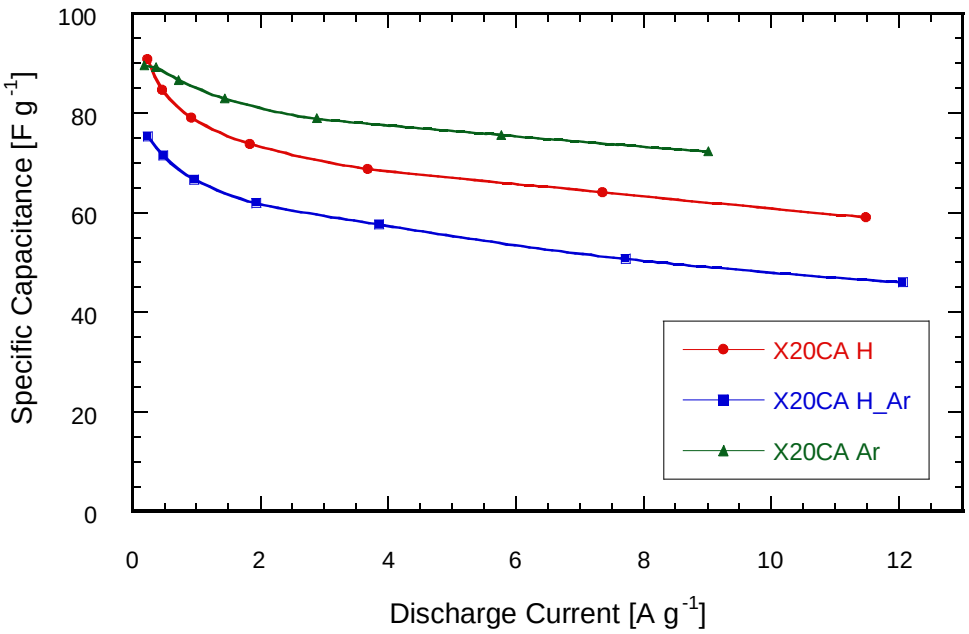

Figure 5.48: Galvanostatic discharge specific capacitance against specific discharge current for X20CA treated at 1000°C in different atmospheres

As with the materials discussed previously, these samples show similar behaviour with increasing discharge current where the highest values of specific capacitance are obtained at a low rate which reduces to an approximately constant value as the rate increases.

From Figure 5.48 it can be seen that X20CA Ar produces a significantly larger specific capacitance than the materials treated with hydrogen at rates of discharge greater than 0.3 A g^{-1} and, as the typical discharge time of ECs corresponds to rates well in excess of this value, this effect may be of practical use in devices using KOH electrolyte.

When the specific capacitance values obtained under Galvanostatic discharge are normalised on the basis of surface area (Table 5.28) and plotted against the specific discharge rate, the difference between the behaviour of X20CA Ar and the materials treated with hydrogen becomes more apparent as is indicated in Figure 5.49.

Sample	Normalised Galvanostatic discharge specific capacitance [μF cm^{-2}]						
	2 mA	4 mA	8 mA	16 mA	32 mA	64 mA	100 mA
X20CA H	15.7	14.6	13.6	12.7	11.9	11.1	10.2
X20CA H_Ar	14.1	13.4	12.5	11.6	10.8	9.5	8.6
X20CA Ar	19.3	19.2	18.6	17.8	17.0	16.3	15.5

Table 5.28: Specific capacitance obtained by Galvanostatic discharge at different rates for X20CA treated at 1000°C in different atmospheres (data adjusted for ash content)

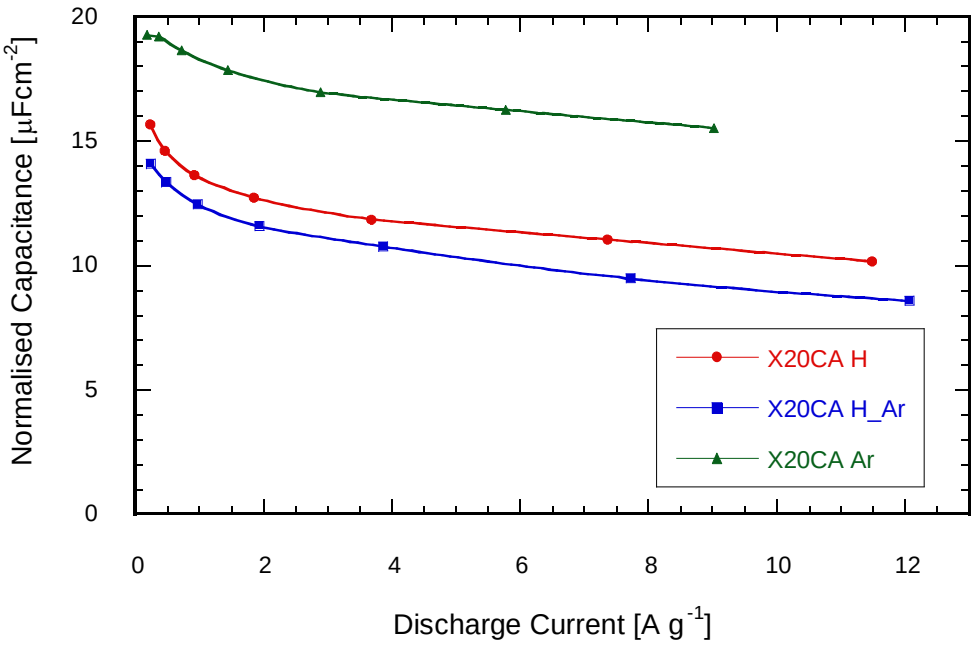

Figure 5.49: Surface area normalised specific capacitance against specific discharge current for X20CA treated at 1000°C in different atmospheres

Figure 5.50 shows a plot of normalised specific capacitance against the surface nitrogen content of the materials, at different rates of charge/ discharge. The plot has a similar form at all rates of Galvanostatic charge/ discharge, with the normalised specific capacitance values for each material decreasing with increasing rate.

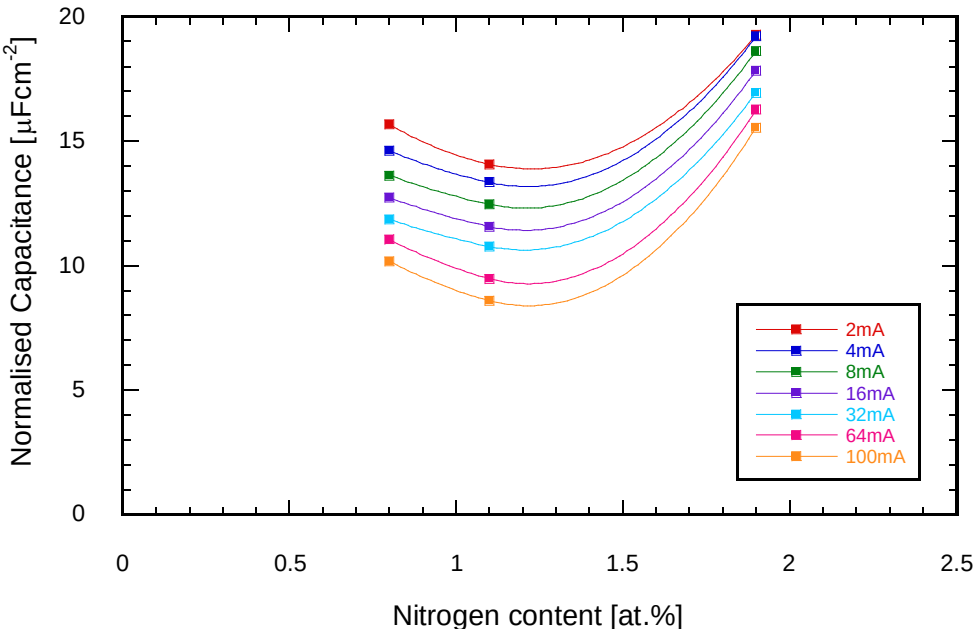

Figure 5.50: Surface area normalised specific capacitance at different rates against nitrogen content (XPS) for X20CA treated at 1000°C in different atmospheres

The lines in Figure 5.50 are also of similar form to the relationship seen using the data derived from EIS experiments (Figure 5.44) and confirm that there is a significant difference in the electrochemical behaviour of X20CA Ar in comparison with the materials treated with hydrogen at 1000°C. This again indicates that the concentration of pyridinic nitrogen groups has an influence on the specific capacitance of carbon materials using KOH electrolyte.

A plot of normalised specific capacitance at different rates of charge/ discharge against the concentration of pyridinic groups in the surface region approximate straight lines as indicated in Figure 5.51.

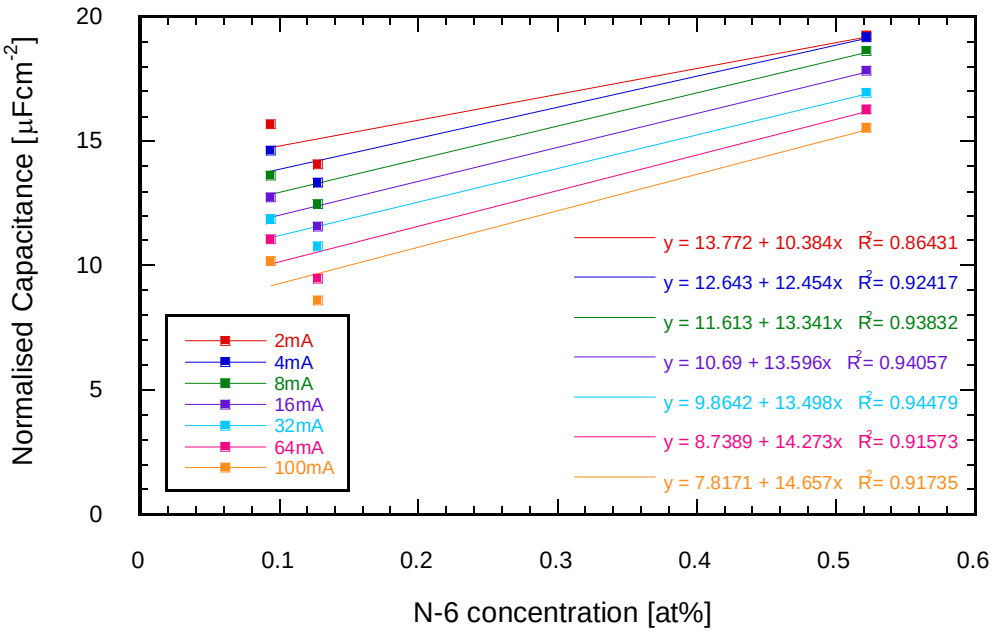

Figure 5.51: Surface area normalised specific capacitance against pyridinic nitrogen (N-6) concentration for X20CA treated at 1000°C in different atmospheres

Although the degree of correlation is not as good as the EIS data, the correlation coefficient increases with increasing rate. The *y*-intercept of the fitted lines decreases with increasing rate of charge which, if taken as an indicator of the double-layer capacitance arising from a pure carbon surface, could be attributed to the reduced time available for the charges in the electrolyte to diffuse toward the surface and form a densely packed layer. It seems reasonable to suggest that this is the case, as it is merely a reflection of the influence of the discharge rate used to determine specific capacitance. This behaviour is typical of plots of Galvanostatic discharge specific capacitance against discharge current where only the double-layer charging mechanism is present [**10**, **166**].

Also, if the gradient of the fitted lines is taken as a measure of the relative influence that pyridinic groups have on the normalised specific capacitance, it could be argued that these groups contribute a greater proportion of the total capacitance at higher rates. This could indicate that a reaction between the electrolyte and pyridine groups is unlikely as the extent of reaction (and hence charge transferred across the double-layer) would be expected to increase with the amount of time under charge. It is

possible that ions are preferentially adsorbed at pyridinic sites during charging and that a greater amount of charge is displaced at these sites through the double-layer mechanism.

In one study [**245**] it was claimed that N-Q and N-X type groups have a beneficial effect on capacitance on the strength of a correlation between the sum of these quantities (effectively the surface concentration of these groups) and a measure of surface area normalised capacitance. No such correlation was found using the results obtained in this work. In the aforementioned report, the sum of the N-Q and N-X type groups follows the same trend as the concentration of pyridinic groups which has a significantly better correlation with surface area normalised capacitance, and it is therefore possible that the trend seen is not due to the N-Q and N-X groups but is rather a consequence of pyridinic nitrogen augmenting the specific capacitance. There is also a sizeable contribution to the specific capacitance by quinone group pseudocapacitance, indicated by peaks in cyclic Voltammograms, which are more pronounced for samples with a larger oxygen content.

To investigate the possibility that oxygen pseudocapacitance contributes to the specific capacitance of the materials under study in this work, detailed XPS data was obtained over a range of binding energies between 527 - 540 eV. Each of the spectra is of similar form with one major peak centred at a binding energy of 532.6 eV. This indicates that all of the oxygen present in the samples is bound in the form of phenol or ether groups and that no electroactive quinone-type groups are present. Considering the synthesis method and treatment conditions used to produce the materials, it can be expected that oxygen bound in the form of ether groups would be found, as the resorcinol-formaldehyde xerogel is connected through ether bridges (Figure 2.17). Ether bonds are likely to be the most robust form of oxygen and not easily removed during thermal treatment.

5.3.6.3 Cyclic Voltammetry

To identify if the increased specific capacitance associated with the presence of N-6 groups arises from a pseudocapacitive reaction, cyclic Voltammetry was carried out on the materials over the operating potential range of the cell (*i.e.* 0.0 - 1.0 V).

Cyclic Voltammograms obtained at a sweep rate of 10 mV s^{-1} and 100 mV s^{-1} are illustrated in Figure 5.52 and Figure 5.53, and have been adjusted to reflect a constant single electrode mass of 10.0 mg (including binder and carbon black) to allow for comparisons between materials.

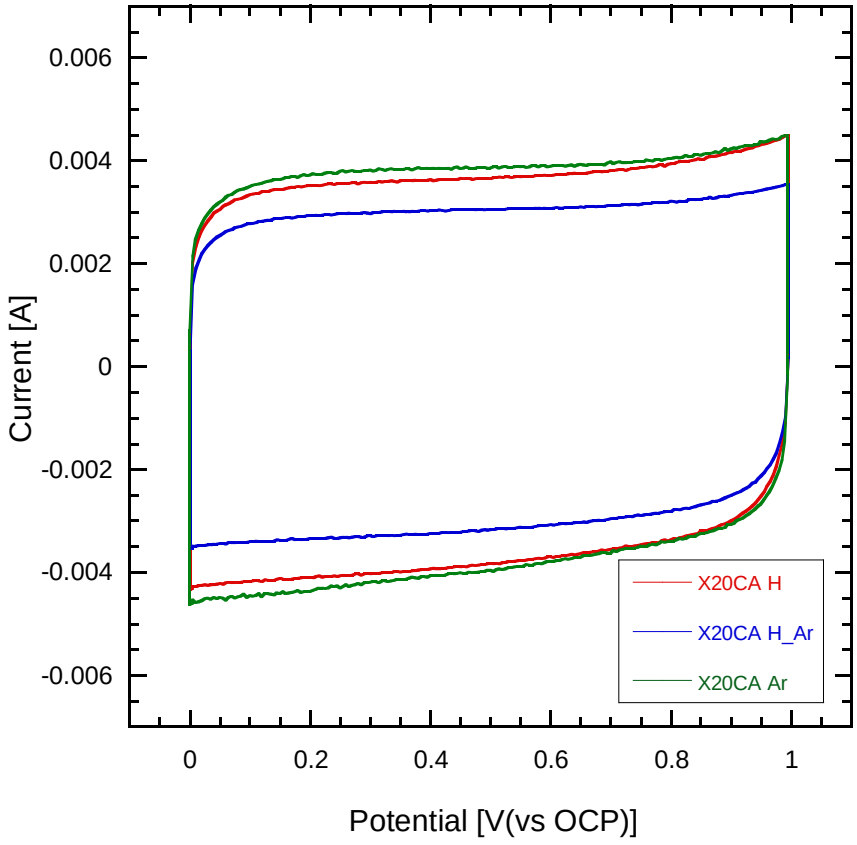

Figure 5.52: Cyclic Voltammograms at 10 mV s^{-1} for X20CA treated at 1000°C in different atmospheres (electrode mass normalised to 10.0 mg)

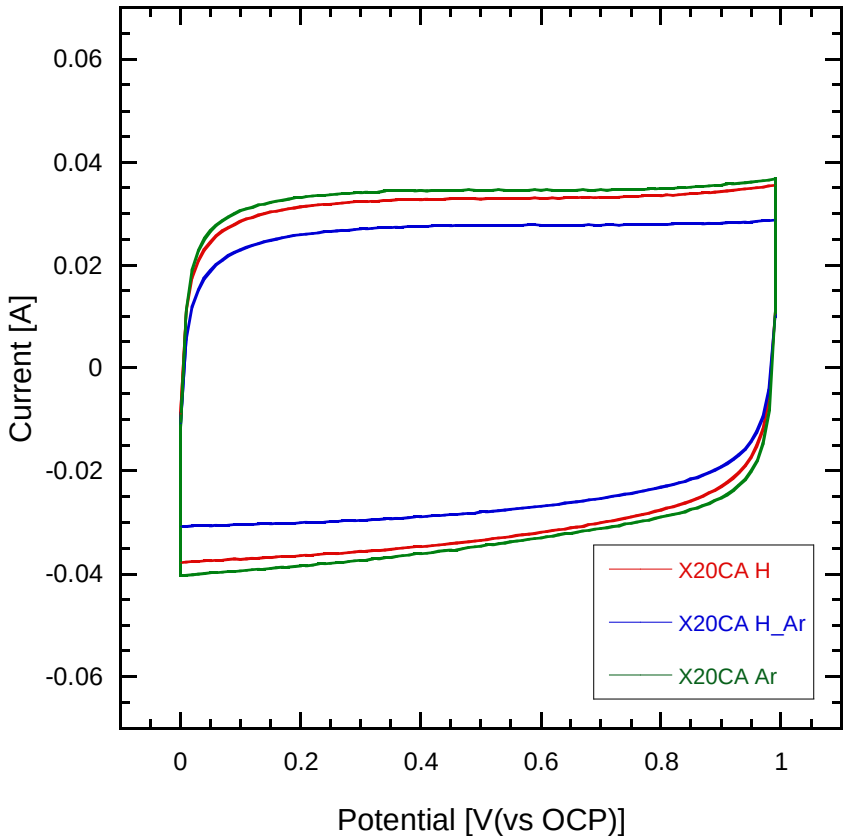

Figure 5.53: Cyclic Voltammograms at 100 mV s^{-1} for X20CA treated at 1000°C in different atmospheres (electrode mass normalised to 10.0 mg)

The form of each of the current responses is similar for each material and is a closer match to the response from an ideal capacitor in comparison with those obtained for the untreated materials (Figure 5.30 and Figure 5.31). The specific capacitances of the materials were calculated for the cyclic Voltammograms and are given in Table 5.29. The values determined at a sweep rate of 10 mV s^{-1} are in agreement with the values determined through Galvanostatic discharge at 2 mA (Table 5.27 and Table 5.28).

There are no distinguishable peaks over the operating potential of the cell and, if the presence of pyridinic groups enhance the specific capacitance of an electrode material, an alternative mechanism is probably responsible. It is unlikely that the enhancement of capacitance is due to a pseudocapacitive reaction, as it would be required to be favourable over the entire operating potential, and to influence the specific capacitance to the same extent independently of the potential across the cell.

Sample	CV Specific Capacitance [F g^{-1}]		[μF cm^{-2}]	
	10 mVs^{-1}	*100 mVs^{-1}*	*10 mVs^{-1}*	*100 mVs^{-1}*
X20CA H	90.9	79.9	15.7	13.8
X20CA H_Ar	75.7	66.6	14.1	12.4
X20CA Ar	91.7	78.1	19.7	16.8

Table 5.29: Specific capacitance obtained by cyclic Voltammetry discharge for X20CA treated at 1000°C in different atmospheres

An alternative mechanism that could explain the enhanced specific capacitance of X20CA Ar could be that this sample has a larger electrochemically active surface area in comparison with the other samples. It is also possible that surface regions containing pyridinic groups adsorb ions from the electrolyte in a different manner than occurs in the usual double-layer capacitance mechanism on pure carbon surfaces. For instance, a greater adsorption energy may occur due to pyridinic nitrogen (perhaps influenced by electron density) or there could be a difference in the solvation state of the adsorbed ions. In the latter case, an unsolvated ion would have a closer approach distance to the surface and a greater number of ions could be accommodated on the same surface.

5.3.6.4 Self-Discharge

The self-discharge behaviour of the cells was investigated by charging the cell to 1 V and recording the voltage decay over a period of 1 hour under open circuit conditions. A typical self-discharge profile (after roughly 100 cycles) is shown in Figure 5.54 and there is little difference between the self-discharge profile of the different materials. All cells that did not display short circuit behaviour (where ln$V$ varies directly with t, possibly created during cell manufacture) exhibited a drop in potential of roughly 25% after 1 hour, as given in Table 5.30

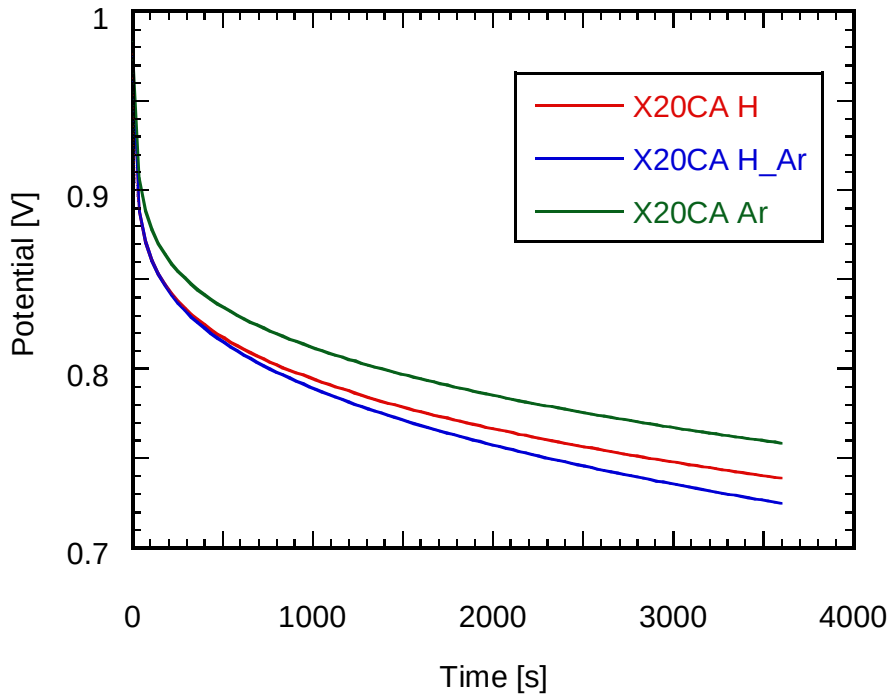

Figure 5.54: Self-discharge - Potential drop of a typical cell after 100 cycles for X20CA treated at 1000°C in different atmospheres

To determine the mechanism(s) responsible for the self-discharge of ECs it is useful to plot the cell voltage against log(t) and $t^{½}$. The typical cell data from Figure 5.54 is presented in these forms in Figure 5.55 and Figure 5.56 respectively.

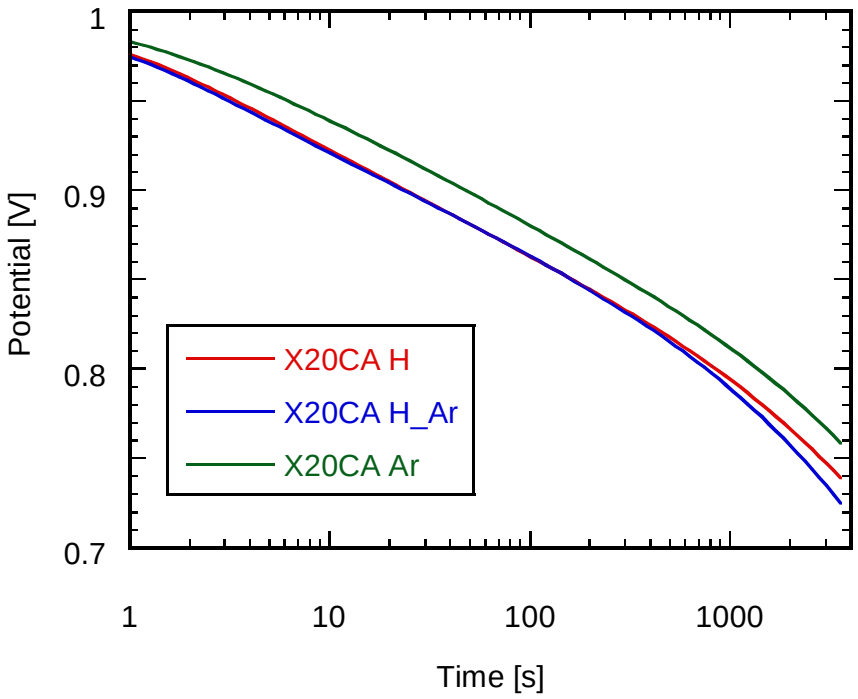

Figure 5.55: Self-discharge - Potential *vs* log(time) after 100 cycles for X20CA treated at 1000°C in different atmospheres

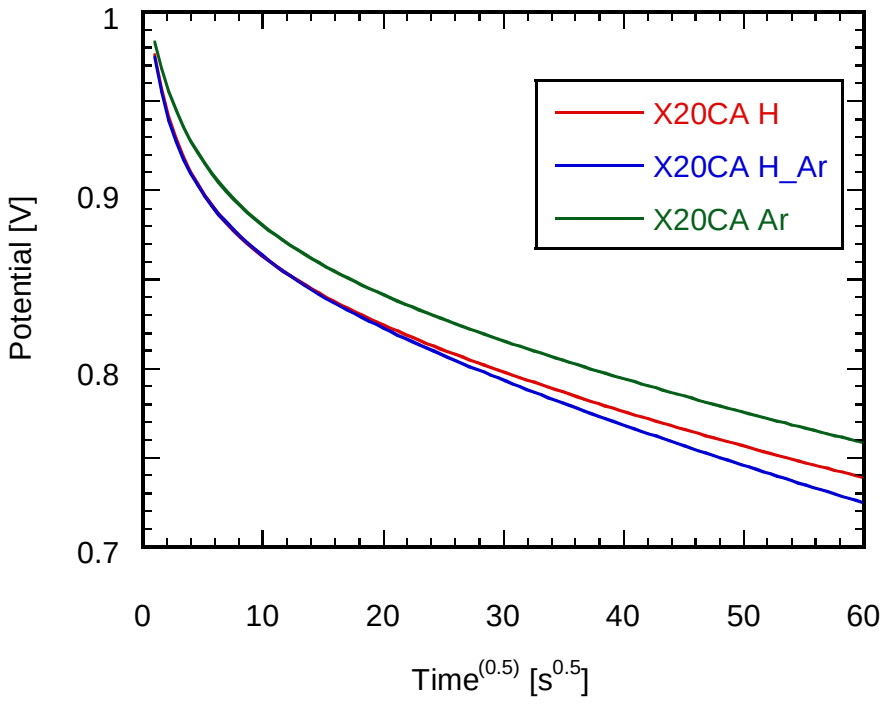

Figure 5.56: Self-discharge - Potential against (time)^{½} after 100 cycles for X20CA treated at 1000°C in different atmospheres

In Figure 5.55 it is seen that a fairly linear fit to the data is found for $t < 1000$ s which indicates that the self-discharge mechanism is either activation controlled, or is due to charge redistribution effects in this period [**295**]. This corresponds well with the behaviour seen in Figure 5.56 where a linear fit is suitable only after a time of 1000 s has elapsed, which suggests that the mechanism is diffusion controlled after this time. When the conditions under which the self-discharge profiles are considered it is most likely that the process of charge redistribution is responsible for the decline in voltage seen over the first 1000 s for each of the materials. As the carbon electrode materials are porous and no special measures were taken to counteract the effects of charge redistribution, (*e.g.* a potentiostatic charging period) the initial self-discharge profiles are likely to be affected by the uneven distribution of charge. The other sources of self-discharge in log *t* relationships are the decomposition of electrolyte or redox reactions involving surface functionalities. Cyclic Voltammetry (Figure 5.52 and Figure 5.53) shows that electrolyte decomposition is unlikely to occur between the limits of potential used, and also that no potential dependent redox reactions occur between the electrolyte and any surface groups present, therefore any log *t* dependent voltage drop is probably due to charge redistribution.

Sample	Potential Drop [V]
X20CA H	0.261
X20CA H_Ar	0.275
X20CA Ar	0.242

Table 5.30: Potential drop after 1h due to self-discharge after 100 cycles for X20CA treated at 1000°C in different atmospheres

The values of potential drop associated with each material shows that the largest drop is associated with X20CA H_Ar which may be attributed to the relatively large degree of contamination associated with this sample. It is possible that some of the impurities in the electrodes are solvated on contact with electrolyte and form self-discharge shuttle species. This is confirmed by the gradient of the line fitted to the

potential drop against $t^{½}$ plot being significantly larger for this sample (*ca.* 0.00260) than that obtained for X20CA H and X20CA Ar (*ca.* 0.0022).

To reduce the influence of charge redistribution effects, the same procedure was repeated after 1000 Galvanostatic charge/ discharge cycles at 100 mA were carried out and the resulting plots are given in Figure 5.57, Figure 5.58 and Figure 5.59.

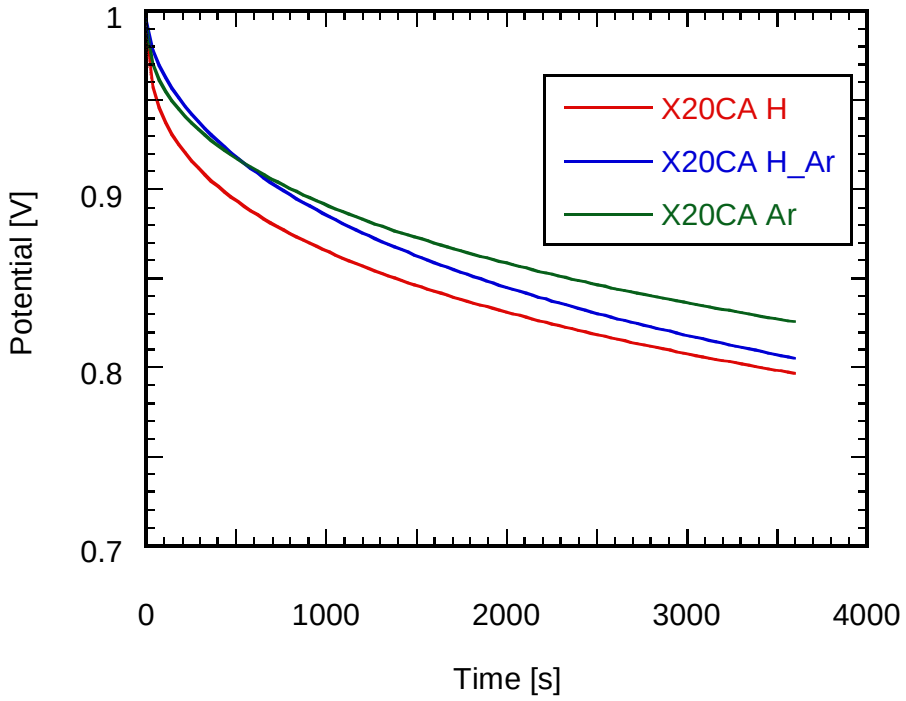

Figure 5.57: Self-discharge - Potential drop of a typical cell after 1000 cycles for X20CA treated at 1000°C in different atmospheres

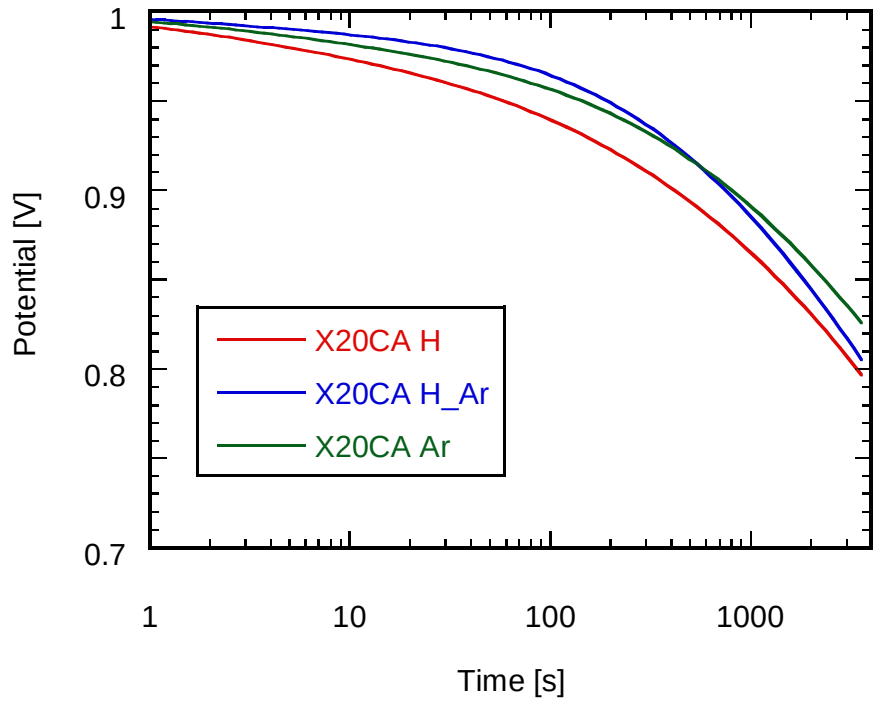

Figure 5.58: Self-discharge – Potential against log(time) after 1000 cycles for X20CA treated at 1000°C in different atmospheres

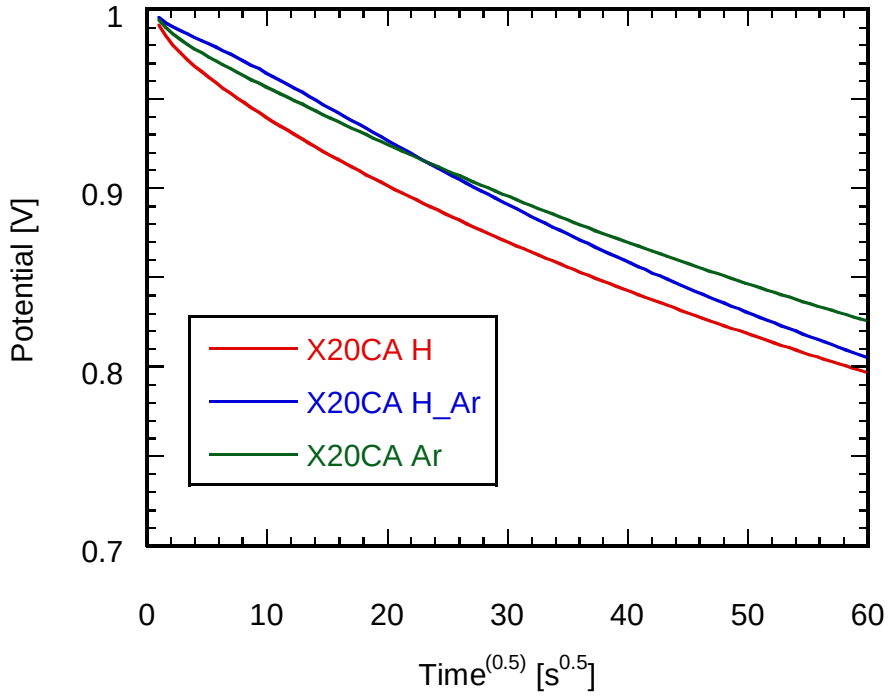

Figure 5.59: Self-discharge – Potential against (time)^{½} after 1000 cycles for X20CA treated at 1000°C in different atmospheres

The total decline in cell potential for each material in Figure 5.57 is reduced significantly in comparison with those seen in Figure 5.54, and the extent of linear behaviour in the log *t* plot (Figure 5.58) is drastically reduced.

It can be seen that the self-discharge profiles for X20CA Ar and X20CA H_Ar intersect at roughly 500 s which may be taken to indicate that more than one self-discharge mechanism is responsible for the drop in potential of the different materials. As found previously, the self-discharge mechanism of X20CA H_Ar electrodes is dominated by the relatively high level of impurities found in the carbon and is confirmed by the linearity of the profile against $t^{½}$ over the whole range of *t*.

Sample	Potential Drop [V]
X20CA H	0.203
X20CA H_Ar	0.195
X20CA Ar	0.175

Table 5.31: Potential drop after 1h due to self-discharge after 1000 cycles for X20CA treated at 1000°C in different atmospheres

This could indicate that the double-layer is more stable in X20CA Ar which may be attributed to the presence of pyridinic nitrogen groups or a consequence of reduced surface area for interaction with shuttle species.

5.3.6.5 Galvanostatic Cycling

To ascertain whether the enhancement of capacitance found for X20CA Ar is of practical use, Galvanostatic charge/ discharge cycling at 100 mA was performed on heat treated samples for 10000 cycles, and the specific capacitance determined periodically. A plot showing how the average specific capacitances vary with the number of cycles is shown in Figure 5.60.

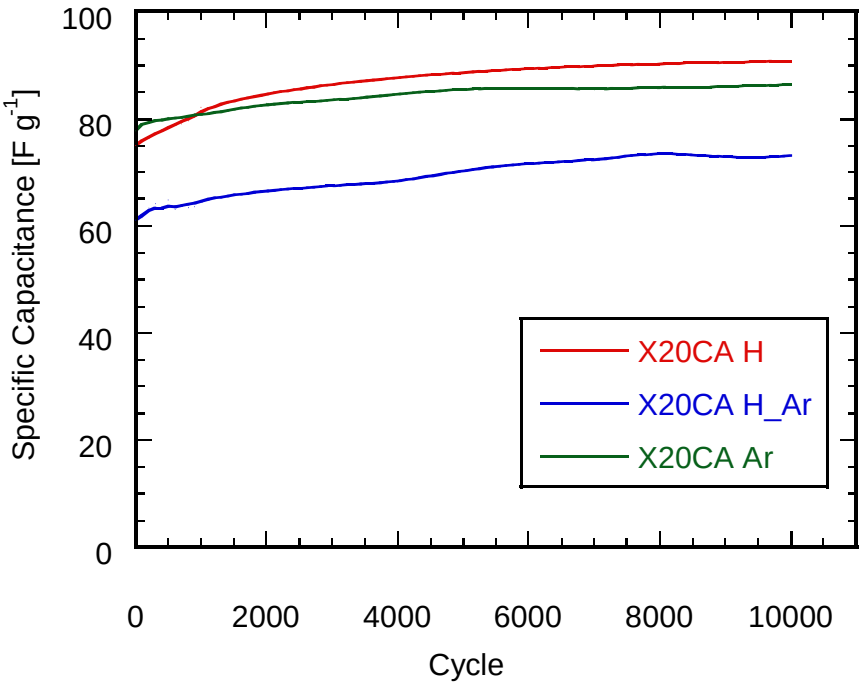

Figure 5.60: Specific capacitance against cycle number for X20CA treated at 1000°C in different atmospheres

An appreciable fade in the specific capacitance of ECs is usually seen on extended cycling, however the opposite trend is surprisingly evident in Figure 5.60, which shows that the initial value of specific capacitance determined for each material increases by 10 – 20% after 10000 cycles.

As the specific capacitance of all materials increases with cycle number it is possible that this results from the way in which cells are manufactured rather than being a characteristic of the materials under study. A source of chemical incompatibility is the use of Kynar® Flex 2801 as a polymer binder material, which has been employed successfully in cells using organic and ionic liquid based electrolytes. However, this material is attacked after prolonged exposure to strongly basic solutions which was confirmed by the occurrence of a noticeable colour change after roughly ten days immersed in electrolyte solution. This chemical incompatibility would necessitate the use of an alternative binder in devices that use strongly basic solutions as an electrolyte. In the context of an electrode component this is obviously undesirable, but offers an explanation for the increasing values of capacitance seen in Figure 5.60. Degradation of the binder exposed to KOH could be considered to open up

previously inaccessible porosity and increase the electrochemically active surface area of the electrode.

This may have influenced the interpretation of specific capacitance data associated with individual samples, particularly as the specific capacitance of X20CA H increases above that of X20CA Ar between 1000 and 2000 cycles. This could be taken as confirmation that a greater proportion of surface area is blocked in microporous materials through the addition of binder and the increase in specific capacitance observed after 10000 cycles is highest for the sample with the largest micropore volume (*ca.* 21%) and 19.6% for X20CA H_Ar and 11.1%.

This finding may cast doubt on the suitability of normalising capacitance data on the basis of surface area as the BET surface area of each material may not be proportional to the electrochemically active surface area of the electrode. Nevertheless, the same trends discussed previously between the surface area normalised capacitance of the materials are maintained over the 10000 cycles, as shown in Figure 5.61.

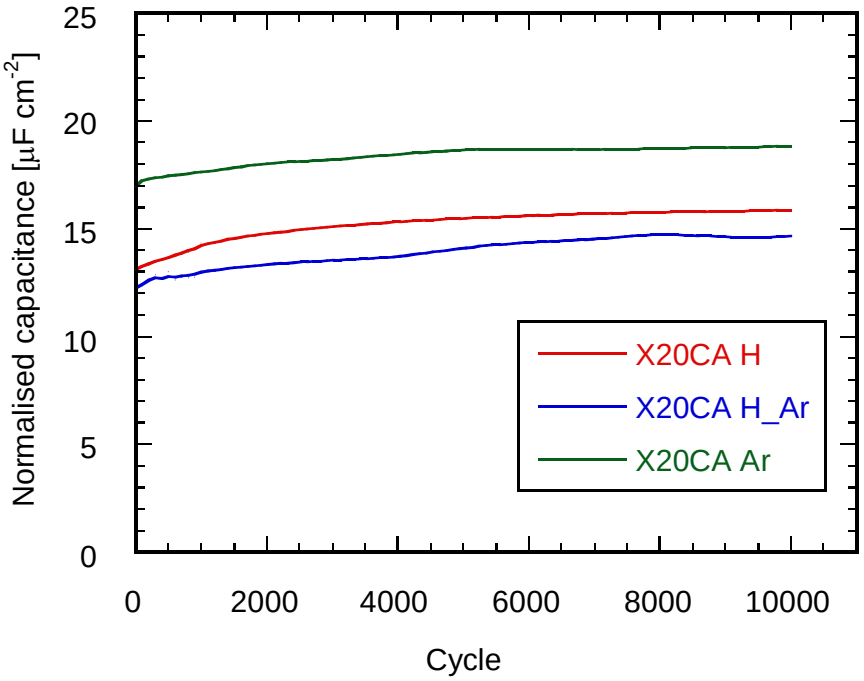

Figure 5.61: Surface area normalised specific capacitance against cycle number for X20CA treated at 1000°C in different atmospheres

Although the values of normalised specific capacitance are slightly different in comparison with those discussed previously, similar relationships between the values obtained for each material are evident. Namely, the normalised capacitance associated with X20CA Ar is significantly greater than that seen for X20CA H_Ar and X20CA H. This again highlights the difficulty in quantifying the influence of nitrogen heteroatoms in carbon electrode materials for ECs, and supports the conclusions drawn from the previous discussions on a qualitative basis.

6 Conclusions

From the review of literature presented in the first two chapters, it can be argued that storage technologies are of great benefit in the design of energy supply systems, and that electrochemical capacitors have unique characteristics that span the gap between capacitor and battery technology in terms of power and energy density for electrical systems. However, the use of ECs is not widespread due to their inadequate cost/performance ratio.

ECs can be categorised as either EDLCs or pseudocapacitors based on the predominant charge storage mechanism present in the device, and can be considered to form part of a charge transfer continuum. Current research has been directed towards combining the best features of these devices with the high specific surface area of carbon materials being accompanied by pseudocapacitance through electrically conducting polymers, metal oxides or surface functional groups. ECs can also be classified based on the type of electrolyte that they employ, which also gives an indication of the performance characteristics that can be expected from the device. Where aqueous electrolytes are used, a relatively high power density can be anticipated but this is at the expense of energy density. Comparatively high energy densities can be expected from ECs that use organic based, or ionic liquid electrolytes however this is accompanied by an increase in the equivalent series resistance of the device.

Many different types of carbon have been explored for use in ECs and surface functionality has been explored as a method by which to increase the capacitance of these devices. The pseudocapacitive reaction of quinone/hydroquinone groups has been found to augment the specific capacitance of carbon materials by as much as 30%, and the presence of oxygen functional groups has been found to increase the wettability of carbon materials. However it has also been shown that the oxygen content of carbon materials has an adverse effect on the resistance and self-discharge of EC electrodes. As a result, other surface functional groups have been explored with the aim of enhancing specific capacitance, with nitrogen groups being investigated by several research groups over the past decade. Many studies propose

that a combination of several factors produces an augmented specific capacitance in nitrogen-enriched carbon electrodes. The factors usually cited include an increased wettability of the material surface (which can result in an enlarged electrochemically active surface area), enhanced electron conduction through the electrode, and 'pseudocapacitance', where it is assumed that charge is transferred between the electrolyte and electrode.

However, in the last section of chapter 2 it has been demonstrated that the interpretation of electrochemical data is usually complicated by the influence of electrode porosity and the presence of oxygen functional groups that frequently accompany the addition of nitrogen groups. In light of recent studies it is clear that the surface area normalisation process by which the effect of nitrogen content is usually investigated is inappropriate, especially where there is a large disparity between the values of surface area. Also, from the review of related literature it is clear that the term 'pseudocapacitance' is often used to describe situations where the specific capacitance exceeds that normally found when using carbon materials of the same surface area, despite the absence of changes in the rate of charge acceptance with changes in potential.

In this work it has been confirmed that when using RF xerogels as a carbon precursor the average pore size can be controlled by simply altering the R/C ratio, under the provision that a constant temperature is maintained during the gelation process. It has also been shown that the co-carbonisation method can be used to produce materials with a controllable pore structure and nitrogen content.

R/C = 100 derived materials were predominantly microporous and displayed a unimodal pore size distribution, with the micropore volume decreasing with increasing mass fraction of *m*PDA added before carbonisation. The specific surface area of the materials was found to decrease from 515 to 27 m^2g^{-1} as the fraction of *m*PDA was increased from 0 to 40 wt.%. R/C = 300 and 500 derived materials were mesoporous in nature and exhibited a bimodal pore structure with micropore volumes similar to those seen in the R/C = 100 derived materials. The mesopore size distribution of the materials was found to change irregularly with increasing mass fraction of *m*PDA which rendered these materials unsuitable for further analysis.

Additionally, it was found that the amount of polymer binder required to form mechanically stable electrodes with R/C = 300 and 500 derived carbon materials resulted in relatively high values of resistance that overwhelmed the electrical response from the cell. With the benefit of hindsight, rather than adding polymer binder materials to carbon materials on a gravimetric basis in the construction of electrodes, a better practice may be to use a volumetric basis to allow for the negative influence that polymer has on electrode conductivity.

Activation of the R/C = 100 derived carbon materials for 60 mins in CO_2 was found to increase their micropore volumes and specific surface areas. The nitrogen content of these materials was shown to increase with increasing fraction of added *m*PDA, and the values obtained using combustive elemental analysis and X-ray photoelectron spectroscopy were found to concur. The materials had nitrogen contents in the region of 0.0 wt.% to 5.6 wt.% and the composition of the nitrogen groups, as determined by XPS, in each of these materials were found to be similar. From elemental analysis it was found that the materials contained a significant and variable amount of incombustible matter. In this work data was adjusted using the ash content determined through proximate analysis. However a better method would be to introduce an acid wash step to the synthesis procedure to remove any catalyst present and the uncertainty over data adjustment could be avoided if an alternative ball mill was used.

Using electrochemical impedance spectroscopy the specific capacitances of the materials were determined, and it was shown that the material with the highest specific surface area, X00CA, produced the largest specific capacitance of 128.7 Fg^{-1}. When the specific capacitances of the materials were normalised on the basis of specific surface area, the values were found to increase from 16.6 $\mu F\ cm^{-2}$ at a nitrogen content of 0.0 wt.% to 44.2 $\mu F\ cm^{-2}$ at 5.6 wt.%. Moreover, one sample (X20CA) which had a specific surface area of 420 m^2g^{-1} and contained *ca.* 3.5 wt.% nitrogen produced a specific capacitance of 114.5 Fg^{-1} which is marginally larger than the 109.2 Fg^{-1} produced using X10CA which had a slightly larger specific surface area of 430 m^2g^{-1} and contained *ca.* 2.2 wt.% nitrogen. This indicates that

the addition of nitrogen groups can be of benefit in a practical device using KOH electrolyte.

This behaviour was confirmed by the results of Galvanostatic cycling at rates up to roughly 12 A g^{-1}, and the influence of nitrogen content was more apparent at lower rates of discharge which could be taken to indicate that reactions between the nitrogen groups and electrolyte species occur. However, the cyclic Voltammetry results seem to show no evidence that pseudocapacitive reactions occur.

In this study of nitrogen-enriched carbon materials as EC electrodes, a similar trend to those previously published between the surface area normalised capacitance of the materials was found, but the mechanism by which this occurs was not clear. The complicated relationship between nitrogen content and specific surface area seen in previous reports was also encountered with these materials and is an inevitable consequence of the nitrogen-enrichment process. Ideally, materials with the same pore structure and varying chemical composition would be utilised to investigate this topic but in the absence of a suitable synthesis method, an alternative technique that can be used to control the nitrogen content while retaining a similar pore structure was proposed. Rather than the conventional method of adding a greater proportion of nitrogen precursor to control nitrogen content, it was shown that nitrogen groups can be selectively removed from a nitrogen-enriched carbon material through treatment at an elevated temperature under a hydrogen atmosphere. In addition, it was found that the fraction of pyridinic nitrogen removed during this procedure was dependent on the hydrogen concentration, which provides a method by which the composition of nitrogen groups on the carbon surface can be controlled.

Treatment at 1000°C under different atmospheres was carried out nitrogen enriched carbon materials derived from the co-carbonisation of R/C = 100 RF xerogels with 20% *m*PDA (X20CA). Physical characterisation using nitrogen adsorption showed that materials with specific surface areas between 580 m^2g^{-1} and 465 m^2g^{-1} were produced, and that the micropore volume increased with hydrogen concentration during thermal treatment. The mesopore size distribution was shown to be similar for these materials and the modal equivalent pore width was determined to be roughly 1.4 nm. Chemical characterisation of the materials showed that nitrogen

content decreases with increasing hydrogen concentration during thermal treatment. It was found that in a pure hydrogen atmosphere, the resultant material contained *ca.* 1 wt.% nitrogen, whereas the material produced in an inert atmosphere contained *ca.* 2.2 wt.% nitrogen. Moreover the composition of the nitrogen groups determined using XPS was found to vary with the type atmosphere used during thermal treatment. In a pure hydrogen atmosphere, the relative quantity of pyridinic nitrogen groups was 11.7 at.%, however when an inert atmosphere was used, the resultant material contained 27.5 at.%. of the contained nitrogen in the form of pyridinic nitrogen.

A brief analysis of SANS experiments using X20CA derived carbon materials was found to compare favourably with the results of nitrogen adsorption measurements, although a more extensive analysis (possibly using the fully penetrable polydisperse spheres model) would be required to obtain detailed pore characteristics and specific surface areas. In this work it has been proposed that contrast-matching small-angle neutron scattering can be used to investigate the degree of unaccessed (and hence electrochemically inactive) porosity in carbon electrode materials.

Results using deuterium oxide as the contrast-matching fluid were presented and it was shown that the values of differential scattering cross-section decreased by at least three orders of magnitude in the low-q range when compared with the SANS experiments. This shows that an excellent contrast-match was obtained using this fluid and that very little closed porosity was present in the materials. These results also indicate that the nitrogen concentration has little influence on the amount of unaccessed porosity and that it is unlikely that the electrochemically active surface area differs greatly from that determined using nitrogen adsorption. Greater detail regarding the filling of the smallest pores would require experiments to be run using a different instrument geometry that gives higher statistical precision for values of scattering wave vector greater than 0.2 $Å^{-1}$.

During electrochemical testing it was found that there was a greater degree of variability between cells constructed using the same carbon materials than was seen when using the co-carbonised materials. Also, it was evident that the materials exhibited a hydrophobic nature which was attributed to a large amount of

graphitisation in the structure. This was supported by the results of helium pycnometry, where the skeletal density of X20 CA H was found to be 2.19 g cm^{-3}, which approaches that of pure graphite.

By fitting the results from EIS experiments to Randles' circuit it was found that the Faradaic resistance increased in a linear fashion with increasing nitrogen content, and that this probably occurs due to the mechanisms of self-discharge present. The values of specific capacitance derived from EIS experiments show no direct trend with nitrogen content but, as with the materials derived through co-carbonisation, an enhancement of specific capacitance was observed.

A sample, X20CA Ar, which had a specific surface area of 465 m^2g^{-1} and contained *ca.* 2.2 wt.% nitrogen produced a specific capacitance of 93.1 Fg^{-1} which is larger than the 83.9 Fg^{-1} produced using X20CA H which has a more extensive specific surface area of 580 m^2g^{-1} and contained *ca.* 1 wt.% nitrogen. This supports the previous findings using co-carbonised materials where a material with a lower surface area but higher nitrogen content (X20CA) exhibited a larger specific capacitance in comparison with a similar material that possessed a greater specific surface area (X10CA).

When the data was corrected to allow for the ash content of the materials and then normalised on the basis of surface area, an obvious relationship with nitrogen content was not seen. However, fairly linear behaviour was observed when the surface area normalised capacitance was plotted against the pyridinic nitrogen content. This trend was confirmed by the results of Galvanostatic cycling at rates between 0.5 Ag^{-1} and 12 Ag^{-1}.

However, as seen in previous experiments using co-carbonised materials, and the majority of reports, the cyclic Voltammograms obtained using the materials treated at 1000°C in different atmospheres are devoid of the characteristic peaks caused by pseudocapacitive reactions. This indicates that the double-layer mechanism is responsible for the specific capacitance seen in nitrogen-enriched carbons and that the enhancement seen may be due to a comparatively greater amount of charge being displaced at pyridinic nitrogen sites.

The self-discharge behaviour of the cells initially showed no trend with nitrogen content but indicated that charge redistribution effects were responsible for the drop in potential seen. However after 1000 cycles, the self-discharge profile was found to be under diffusion control and the potential drop was found to be smallest in the material with the lowest surface area and highest nitrogen content. This may be attributed to a stronger adsorption of electrolyte ions at pyridinic nitrogen sites or simply a consequence of the reduced surface area for interaction with shuttle species.

Extended cycling to 10000 cycles revealed that the specific capacitance increased by 10 – 20% over this period and this was determined to occur due to chemical incompatibility between the polymer binder and electrolyte solution. Therefore an alternative binder is required for use with KOH electrolyte in practical devices but it was shown that this did not affect the interpretation of electrochemical results to any great extent, as the trends seen in the surface area normalised specific capacitance remain even after extended cycling.

To summarise, electrochemical capacitors are devices that have the potential to be very useful in the supply of electrical energy but are not widely used at present due to an inadequate cost/ performance ratio. As a consequence, a great amount of research has been carried out recently with the aim of understanding the effects that material properties have on the charge storage mechanisms that occur. This work has been focussed on investigating the influence that nitrogen content has on the specific capacitance of carbon electrodes when an aqueous potassium hydroxide solution is used as the electrolyte. In an appraisal of recent literature it was found that the electrochemical behaviour of nitrogen-enriched carbon materials is influenced by several factors that are difficult to decouple. This study employed a different synthesis technique, that of co-carbonisation between resorcinol-formaldehyde xerogels with *m*PDA, in an attempt to reduce the influence of errors that are introduced when data is normalised on the basis of surface area. However, the data still showed that the specific surface area of the materials had a large influence over the analysis of the electrochemical behaviour and an alternative method of nitrogen control was proposed. Treatment of nitrogen-enriched carbon

materials at 1000°C in the presence of hydrogen was found to selectively remove nitrogen groups from the materials and moreover, was found to remove a greater proportion of pyridinic nitrogen groups. In this work the technique of CM-SANS was proposed as a unique tool that can be used to investigate the degree of electrochemically inactive porosity in carbon electrode materials. The analysis of electrochemical data revealed that the presence of nitrogen in the carbon electrode materials can have a beneficial effect on specific capacitance, and that pyridinic nitrogen in particular is responsible for this effect. It was also argued that electrode reactions are not responsible for this effect but that the enhancement seen may be due to a comparatively greater amount of charge being displaced at pyridinic nitrogen sites. Further work in this area could be directed towards establishing the relationships between pyridinic nitrogen content and surface area normalised capacitance values, particularly by producing a larger range of materials with a wider range of nitrogen contents. However, from this work it became clear that the influence of increased specific surface area was significantly greater than that of nitrogen addition and can be achieved in a much more cost-effective manner through activation processes.

7 Appendices

Appendix A: Maximum Power Output [10]

The maximum power delivered from an EC can be calculated by considering an equivalent circuit consisting of a resistor, *R*, (representing the equivalent series resistance of the EC) in series with a capacitor. In this circuit, a discharge current, *I*, reduces the initial potential, V_i, across the circuit by the product of the current and resistance as indicated in Eq. A.1.

$$V = V_i - IR \qquad \textbf{Eq. A.1}$$

The power that corresponds to the discharge step in Eq. A.1 is given by the relation shown in Eq. A.2.

$$P = IV_i - I^2R \qquad \textbf{Eq. A.2}$$

Eq. A.2 is at a maximum when the derivative of power with respect to current is equal to zero, which is illustrated in Eq. A.3.

$$\frac{dP}{dI} = V_i - 2IR = 0 \qquad \textbf{Eq. A.3}$$

Therefore at the point where the maximum power is supplied from the cell the discharge current, I_{maxP}, is given by Eq. A.4.

$$I_{maxP} = \frac{V_i}{2R} \qquad \textbf{Eq. A.4}$$

The relationship in Eq. A.4 results in a potential at maximum power output equal to half that of the initial cell potential through the relation shown in Eq. A.5.

$$V_{maxP} = V_i - IR = V_i - \left(\frac{V_i}{2R}\right)R = \frac{V_i}{2} \qquad \textbf{Eq. A.5}$$

The product of the current and potential for the situation where the power is at a maximum yields the value of maximum power as shown in Eq. A.6.

$$P = V_{maxP} I_{maxP} = \left(\frac{V_i}{2}\right)\left(\frac{V_i}{2R}\right) = \frac{{V_i}^2}{4R} \qquad \textbf{Eq. A.6}$$

Appendix B: Langmuir Adsorption Model [260, 265]

From the kinetic theory of gases, the incident molecular flux $\mathbb{N}$ of a gaseous adsorptive on a surface (*i.e.* the number of molecules striking each cm^2 of surface per second) is proportional to the pressure of adsorptive as shown in Eq. B.1 where *k* is a constant and N_A is Avogadro's number. *P* and *M* represent the pressure and molecular weight of the adsorptive respectively, *R* represents the universal gas constant and *T* is the absolute temperature.

$$\mathbb{N} = kP = \frac{N_A P}{\sqrt{2\pi MRT}} \qquad \textbf{Eq. B.1}$$

For a surface completely free of adsorbate molecules, the uncovered surface fraction is defined as θ_0, and the number of collisions $\mathbb{N}_c$ is given by Eq. B.2.

$$\mathbb{N}_c = kP\theta_0 \qquad \textbf{Eq. B.2}$$

A fraction of incident adsorptive molecules, A_1, condense onto the surface of the solid and are held by the attractive surface forces until the molecule evaporates. Eq. B.3 relates this fraction to the number of molecules of gas adsorbed $\mathbb{N}_{ad}$.

$$\mathbb{N}_{ad} = \mathbb{N}_c A_1 = kP\theta_0 A_1 \qquad \textbf{Eq. B.3}$$

For a surface saturated with a monolayer of adsorbate molecules, the uncovered surface fraction θ_0 is equal to zero, and the covered surface fraction is represented by θ_1 in Eq. B.4.

$$\theta_0 + \theta_1 = 1 \qquad \textbf{Eq. B.4}$$

The molecular flux of adsorbed molecules evaporating from the surface is assumed to vary with the fraction of covered surface θ_1 in accordance with Eq. B.5 where N_m is the number of adsorbed molecules on a saturated surface per cm^2, *E* is the energy

of adsorption and ν_1 is the oscillation frequency of the adsorbed molecules normal to the adsorbent surface.

$$\mathbb{N}_{de} = N_m \theta_1 \nu_1 e^{-E/RT} \quad \textbf{Eq. B.5}$$

At equilibrium the rates of adsorption and desorption are equal *i.e.* Eq. B.3 and Eq. B.5 can be combined to yield Eq. B.6.

$$kP\theta_0 A_1 = N_m \theta_1 \nu_1 e^{-E/RT} \quad \textbf{Eq. B.6}$$

Substituting $\theta_0 = (1 - \theta_1)$ into Eq. B.6 and rearranging gives Eq. B.7.

$$\theta_1 = \frac{k\ PA_1}{N_m \nu_1 e^{-E/RT} + k\ P\ A_1} \quad \textbf{Eq. B.7}$$

κ can be defined using previously described parameters by Eq. B.8 under the assumption that the adsorbent surface is energetically uniform (*i.e. E* is a constant).

$$\kappa = \frac{k\ A_1}{N_m \nu_1 e^{-E/RT}} \quad \textbf{Eq. B.8}$$

Substituting κ into Eq. B.7 gives Eq. B.9.

$$\theta_1 = \frac{\kappa P}{1 + \kappa P} \quad \textbf{Eq. B.9}$$

When considering monolayer coverage the mass of adsorbed molecules *W* varies with the number of molecules adsorbed *N*, and can be expressed in terms of the covered surface fraction as shown in Eq. B.10.

$$\theta_1 = \frac{N}{N_m} = \frac{W}{W_m}$$ **Eq. B.10**

Substituting the relative mass fraction of adsorbate from Eq. B.10 for θ_1 in Eq. B.9 gives the Langmuir equation (Eq. B.11).

$$\frac{W}{W_m} = \frac{\kappa P}{1 + \kappa P}$$ **Eq. B.11**

Eq. B.11 can be rearranged to give Eq. B.12.

$$\frac{P}{W} = \frac{1}{\kappa W_m} + \frac{P}{W_m}$$ **Eq. B.12**

Eq. B.12 is useful in the consideration of experimental isotherms as a plot of P/W versus P produces a linear slope of gradient $1/W_m$ and an intercept of $1/\kappa W_m$, which permits the determination of the mass of adsorbate required for complete monolayer coverage.

The surface area of the adsorbent S can then be calculated as the product of the number of molecules in a saturated monolayer (using W_m determined from the Langmuir plot) and the apparent cross-sectional area of a single adsorbate molecule, σ:

$$S = N_m \sigma = \frac{W_m N_A \sigma}{M}$$ **Eq. 3.4**

Appendix C: Brunauer-Emmett-Teller (BET) Adsorption Model [257, 260]

The BET theory of multilayer adsorption is an extension of the Langmuir theory which allows for the formation of multiple layers of adsorbate. Under the assumption that the rate of adsorption on to the surface is equal to the rate of evaporation from the adsorbed layer at equilibrium, this situation can be expressed in the form seen in Eq. C.1 using the same notation from Appendix B.

$$kP\theta_0 A_1 = N_m\,\theta_1 \nu_1 e^{-E_1/RT} \qquad \textbf{Eq. C.1}$$

Eq. C.1 can be extended to apply to a number *n* of multiple layers using Eq. C.2.

$$kP\theta_{n-1} A_n = N_m\,\theta_n \nu_n e^{-E_n/RT} \qquad \textbf{Eq. C.2}$$

E is then replaced by the heat of liquefaction *L* to produce Eq. C.3 for the second and higher layers. This is under the assumption that *v*, *E* and *A* are constants, and that these layers are sufficiently far from the surface to be equivalent to the adsorbate being in the liquid state.

$$kP\theta_{n-1} A = N_m\,\theta_n \nu e^{-\frac{L}{RT}} \qquad \textbf{Eq. C.3}$$

The assumption that the heat of adsorption in the second and higher layers is equal to the latent heat is overly simplistic, as polarization forces may still affect the heat of adsorption in these higher layers.

The fractional surface coverage for the first layer, α, and subsequent layers, β, with repect the layer beneath can be defined by Eq. C.4 and Eq. C.5 respectively.

$$\alpha = \frac{\theta_1}{\theta_0} = \frac{k\,P\,A_1}{N_m\,\nu_1 e^{-E_1/RT}} \qquad \textbf{Eq. C.4}$$

$$\beta = \frac{\theta_n}{\theta_{n-1}} = \frac{k\ P\ A}{N_m\ \nu e^{-L/RT}} \qquad \textbf{Eq. C.5}$$

Therefore, for the first layer, Eq. C.6 applies.

$$\theta_1 = \alpha\ \theta_0 \qquad \textbf{Eq. C.6}$$

And for the subsequent layers Eq. C.7 is applicable.

$$\theta_n = \beta\ \theta_{n-1} = \alpha\ \beta^{n-1}\ \theta_0 \qquad \textbf{Eq. C.7}$$

At equilibrium the total number of molecules adsorbed can be considered to be the summation of the number of molecules adsorbed in each of the layers represented by Eq. C.8.

$$\begin{aligned} N &= N_m\ \theta_1 + 2\ N_m\ \theta_2 + \cdots + n\ N_m\ \theta_n \\ &= N_m(\theta_1 + 2\ \theta_2 + \cdots + n\ \theta_n) \end{aligned} \qquad \textbf{Eq. C.8}$$

Substituting for each value of fractional surface coverage, θ, in terms of θ_0 in Eq. C.8 produces Eq. C.9.

$$\begin{aligned} \frac{N}{N_m} &= \alpha\ \theta_0 + 2\ \alpha\ \beta\ \theta_0 + \cdots + n\ \alpha\ \beta^{n-1}\ \theta_0 \\ &= \alpha\ \theta_0\ (1 + 2\ \beta + \cdots + n\ \beta^{n-1}) \end{aligned} \qquad \textbf{Eq. C.9}$$

As both α and β are constants, the BET constant, C, can be defined as a constant of proportionality between α and β, as shown in Eq. C.10.

$$\alpha = C\ \beta \qquad \textbf{Eq. C.10}$$

Substituting for α in Eq. C.9 yields Eq. C.11.

$$\frac{N}{N_m} = C\,\theta_0(\beta + 2\,\beta^2 + \cdots + n\,\beta^n) = \frac{C\,\theta_0\,\beta}{(1-\beta)^2} \qquad \textbf{Eq. C.11}$$

As the total number of molecules adsorbed is the summation of the fractions of adsorbed molecules in each layer θ_0 can be expressed in the form shown in Eq. C.12 and Eq. C.13.

$$\theta_0 = 1 - (\theta_1 + \theta_2 + \cdots + \theta_n) = \left(1 - \sum_{n=1}^{\infty} \theta_n\right) \qquad \textbf{Eq. C.12}$$

$$\left(1 - \sum_{n=1}^{\infty} \theta_n\right) = \left(1 - \alpha\,\theta_0 \sum_{n=1}^{\infty} \beta^{n-1}\right) = \left(1 - C\,\theta_0 \sum_{n=1}^{\infty} \beta^n\right) = \left(1 - C\theta_0 \frac{\beta}{1-\beta}\right) \qquad \textbf{Eq. C.13}$$

θ_0 can also be expressed in terms of the BET constant, C, and β by dividing the above factor through by θ_0 and rearranging as shown in Eq. C.14, Eq. C.15 and Eq. C.16.

$$1 = \left(\frac{1}{\theta_0} - \frac{C\,\beta}{1-\beta}\right) \qquad \textbf{Eq. C.14}$$

$$1 + \frac{C\beta}{(1-\beta)} = \frac{1}{\theta_0} \qquad \textbf{Eq. C.15}$$

$$\theta_0 = \frac{1}{1 + {C\,\beta}/{(1-\beta)}} \qquad \textbf{Eq. C.16}$$

Substituting for θ_0 in Eq. C.11 allows the ratio of adsorbed molecules to that of a completed monolayer to be expressed in terms of the BET constant and β as shown in Eq. C.17.

$$\frac{N}{N_m} = \frac{C\,\beta}{(1-\beta)^2}\,\frac{1}{\left(1 + {C\,\beta}/{(1-\beta)}\right)} = \frac{C\,\beta}{(1-\beta)(1-\beta+C\,\beta)} \qquad \textbf{Eq. C.17}$$

When the equilibrium adsorbate pressure is equal to the saturation pressure of the adsorbate (*i.e.* $P/P_0 = 1$), β becomes unity and equilibrium can be represented by Eq. C.18.

$$k\,P_0\,A = N_m\,\nu\,e^{-L/RT} \qquad \textbf{Eq. C.18}$$

And from the definition of β in Eq. C.5, Eq. C.18 can be used to express β in terms of the system pressure and saturation pressure, as shown in Eq. C.19. This can then be substituted into Eq. C.17 to express the fraction of molecules adsorbed in terms of the relative pressure, as shown in Eq. C.20.

$$\beta = \frac{k\,P\,A}{N_m\,\nu e^{-L/RT}} = \frac{k\,P\,A}{k\,P_0\,A} = \frac{P}{P_0} \qquad \textbf{Eq. C.19}$$

$$\frac{N}{N_m} = \frac{C\,\left({P}/{P_0}\right)}{\left(1-\left({P}/{P_0}\right)\right)\left(1-\left({P}/{P_0}\right)+C\,\left({P}/{P_0}\right)\right)} \qquad \textbf{Eq. C.20}$$

As with the Langmuir equation, the number of molecules adsorbed is more conveniently expressed in terms of the mass adsorbed, *W*, as shown in Eq. C.21.

$$\frac{W}{W_m} = \frac{C\left(P/P_0\right)}{\left(1-\left(P/P_0\right)\right)\left(1-\left(P/P_0\right)+C\left(P/P_0\right)\right)} \qquad \textbf{Eq. C.21}$$

This can be rearranged to yield the linear form of the BET equation (Eq. C.25) through the steps shown in Eq. C.22, Eq. C.23and Eq. C.24.

$$W\left(1-\left(P/P_0\right)\right)\left(1-\left(P/P_0\right)+C\left(P/P_0\right)\right) = W_m C\left(P/P_0\right) \qquad \textbf{Eq. C.22}$$

$$\frac{1}{W\left(1-\left(P/P_0\right)\right)} = \frac{\left(1-\left(P/P_0\right)+C\left(P/P_0\right)\right)}{W_m C\left(P/P_0\right)} \qquad \textbf{Eq. C.23}$$

$$\frac{\left(P/P_0\right)}{W\left(1-\left(P/P_0\right)\right)} = \left(\frac{1}{W_m C} - \frac{\left(P/P_0\right)}{W_m C} + \frac{C\left(P/P_0\right)}{W_m C}\right) \qquad \textbf{Eq. C.24}$$

$$\frac{1}{W\left(\left(P_0/P\right)-1\right)} = \left(\frac{1}{W_m C} + \frac{(C-1)\left(P/P_0\right)}{W_m C}\right) \qquad \textbf{Eq. C.25}$$

From this equation, a plot of $1/W[(P_0/P)-1]$ versus P/P_0 (sometimes referred to as a BET plot) yields a straight line over a discrete range of relative pressures. Typically, a straight line is obtained for relative pressures in the range $0.05 \leq P/P_0 \leq 0.35$, however some adsorbents produce a linear plot at significantly lower values of relative pressure [**170**].

The slope, *s*, of the line and the intercept, *i*, are then used to solve the equations for the mass of an adsorbed monolayer and the BET constant as shown in Eq. 3.6 and Eq. 3.7 respectively.

$$W_m = \frac{1}{s + i} \qquad \textbf{Eq. 3.6}$$

$$C = \frac{s}{i} + 1 \qquad \textbf{Eq. 3.7}$$

The calculated mass of an adsorbed monolayer can then be used to obtain the total surface area using the same relationship as used with the Langmuir equation (*i.e.* Eq. 3.4).

$$S = N_m \sigma = \frac{W_m N_A \sigma}{M} \qquad \textbf{Eq. 3.4}$$

When adsorption is limited to a finite number of adsorbed layers, *n*, the mass of adsorbate can be found through Eq. C.26.

$$\frac{W}{W_m} = \frac{C}{\left(\left({}^{P_0}/_{P}\right) - 1\right)} \frac{\left(1 - (n+1)\left({}^{P}/_{P_0}\right)^{n} + n\left({}^{P}/_{P_0}\right)^{n+1}\right)}{\left(1 + (C-1)\left({}^{P}/_{P_0}\right) + C\left({}^{P}/_{P_0}\right)^{n+1}\right)} \qquad \textbf{Eq. C.26}$$

Eq. C.26 reduces to the Langmuir equation for monolayer adsorption (*i.e.* *n*=1), and to the BET equation where the number of adsorbed layers is infinite.

Appendix D: Barrett-Joyner-Halenda Method [258]

The Barrett-Joyner-Halenda (BJH) method can be used to estimate the volume and surface area in porous materials. This technique combines calculations of multilayer adsorption thickness with the Kelvin equation for capillary condensation which applies when liquid adsorbate in a pore is separated from gaseous adsorptive by a meniscus.

The BJH model assumes that adsorption occurs by both physical adsorption on the pore walls and condensation in the capillary volume, and that the pore volume and capillary volume are related to each other as they are in a cylinder. The radius of the inner capillary, r_k, in Figure 3.4 can be related to the relative pressure (P/P_0) through the Kelvin equation, (Eq. 3.10 [**268**]).

$$\ln\left(\frac{P}{P_0}\right) = \frac{-2\sigma V}{r_k RT}\cos\theta \qquad \textbf{Eq. 3.10}$$

In Eq. 3.10 σ represents the surface tension of liquid adsorbate, V the molar volume of the adsorbate, R the gas constant, T the absolute temperature, and θ the contact angle between the liquid adsorbate and solid surface. In the case of cylindrical pores and a wetting angle of zero this can be reduced to Eq. D.1.

$$\ln\left(\frac{P}{P_0}\right) = \frac{-2\sigma V}{r_k RT} \qquad \textbf{Eq. D.1}$$

Figure 7.1 [**258**] illustrates the stepwise desorption process from open ended cylindrical pores that have been filled *via* capillary condensation. It is assumed that pores of the same radius respond to pressure changes in the same manner, and that all pores are filled with adsorbate at a relative pressure of $(P/P_0)_1$.

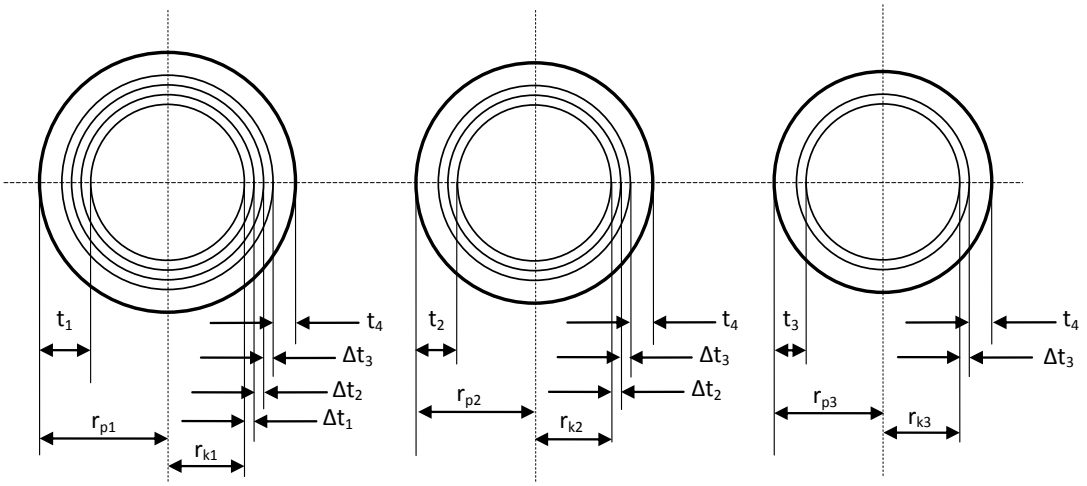

Figure 7.1: Schematic representation of the desorption process showing three different pores and the thinning of the physically adsorbed layer over the first three pressure decrements

In Figure 7.1 the pore of radius r_{p1} consists of the physically adsorbed layer of thickness t_1 and an inner capillary of radius r_{k1}. With the stepwise reduction of relative pressure to $(P/P_0)_2$ a quantifiable volume of adsorbate, ΔV_1, evaporates. This volume corresponds to a thinning of the physically adsorbed layer by Δt_1 and the evaporation of the capillary condensate. The volume of pore r_{p1} in Figure 7.1 can be expressed in the forms given in Eq. D.2 and Eq. D.3.

$$V_{p1} = V_{k1} \frac{{r_{p1}}^2}{{r_{k1}}^2} \qquad \textbf{Eq. D.2}$$

$$V_{p1} = \frac{{r_{p1}}^2}{(r_{k1} + \Delta t_1)} \Delta V_1 = R_1 \Delta V_1 \qquad \textbf{Eq. D.3}$$

Figure 7.1 also shows a narrower pore that is filled with capillary condensate at $(P/P_0)_2$ and has a radius r_{p2} (consisting of a physically adsorbed layer of thickness t_2 and a capillary of radius r_{k2}). At this relative pressure, pore r_{p2} from Figure 7.1 has an adsorbed layer of thickness (t_1-Δt_1).

Further reduction of the relative pressure to $(P/P_0)_3$ results in the desorption of a second volume of adsorbate, ΔV_2. This is equal to the volume of capillary condensate and the reduction in the physically adsorbed layer in from the pore of radius r_{p2} in Figure 7.1, as well as a second diminution of the adsorbed layer in the larger pore with an associated volume of $V_{\Delta t2}$. The volume of the pore in Figure 7.1 is then represented by Eq. D.4.

$$V_{p2} = \frac{{r_{p2}}^2}{(r_{k2} + \Delta t_2)}(\Delta V_2 - V_{\Delta t_2}) = R_2(\Delta V_2 - V_{\Delta t_2}) \qquad \textbf{Eq. D.4}$$

Representing the length of the pores in Figure 7.1 by L_1 it is possible to calculate the volume of adsorbate desorbed from the pore on reduction of the relative pressure from $(P/P_0)_2$ to $(P/P_0)_3$ using the relationship in Eq. D.5.

$$V_{\Delta t_2} = \pi L_1(r_{k1} + \Delta t_1 + \Delta t_2)^2 - \pi L_1(r_{k1} + \Delta t_1)^2 \qquad \textbf{Eq. D.5}$$

As the relative pressure decreases further this relationship becomes unwieldy and an alternative method of calculating $V_{\Delta t2}$ becomes more useful. This is shown in Eq. D.6. where Ac_1 represents the average area from which the physically adsorbed gas desorbed.

$$V_{\Delta t_2} = \Delta t_2 Ac_1 \qquad \textbf{Eq. D.6}$$

Eq. D.6 can be generalised to represent the volume reduction due to the thinning of the physically adsorbed layer as a result of any stepwise desorption step as shown in Eq. D.7, and the corresponding pore volume by Eq. D.8.

$$V_{\Delta t_n} = \Delta t_n \sum_{j=1}^{n-1} Ac_j \qquad \textbf{Eq. D.7}$$

$$V_{p_n} = R_n \Delta V_n - R_n \, \Delta t_n \sum_{j=1}^{n-1} Ac_j \qquad \textbf{Eq. D.8}$$

However, as the average area, A_c, is a function of the relative pressure, a method of relating the actual area of the pores to the average area from which desorption occurs at each step is required. Considering that A_p, the area of each pore, is a constant which is calculable from the pore volume and radius and therefore for any step in the desorption process the value of ΣA_p can be established. A relationship between ΣA_c and ΣA_p can be defined under the assumption that all capillaries emptied during a decrement in relative pressure have an average radius of $\overline{r_p}$, as indicated in Figure 7.2 [**258**].

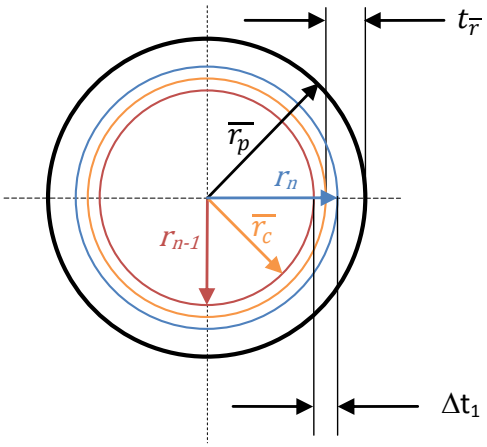

Figure 7.2: Relationship of capillary area to pore area at nth desorption step

By defining the change in thickness of the physically adsorbed layer resulting from the pressure decrement as Δt_n, the radii of the capillary before desorption is r_{n-1} and after desorption r_n. The average diameter of the capillary is $\overline{r_c}$. Since it has been assumed that the capillary is concentric with the pore , the average area of the capillary A_c during the desorption where the adsorbed layer decreases by Δt_n is related to the ratio of pore and capillary radii by the relationship shown in Eq. D.9.

$$A_c = A_p \frac{\overline{r_c}}{\overline{r_p}}$$ **Eq. D.9**

The average capillary radius, $\overline{r_c}$, during the pressure decrement is equal to the pore radius, $\overline{r_p}$, less the thickness of the adsorbed layer at the corresponding relative pressure, $t_{\overline{r}}$, shown in Eq. D.10.

$$\overline{r_c} = \overline{r_p} - t_{\overline{r}}$$ **Eq. D.10**

Replacing the ratio of capillary to pore radii with *c*, as shown in Eq. D.11 allows for the formation of Eq. D.12 which provides a basis for the calculation of pore volume distributions with respect to pore radii.

$$c = \frac{\overline{r_c}}{\overline{r_p}} = \frac{\overline{r_p} - t_{\overline{r}}}{\overline{r_p}}$$ **Eq. D.11**

$$V_{p_n} = R_n \Delta V_n - R_n \, \Delta t_n \sum_{j=1}^{n-1} c_j \, A_{pj}$$ **Eq. D.12**

Appendix E: XPS

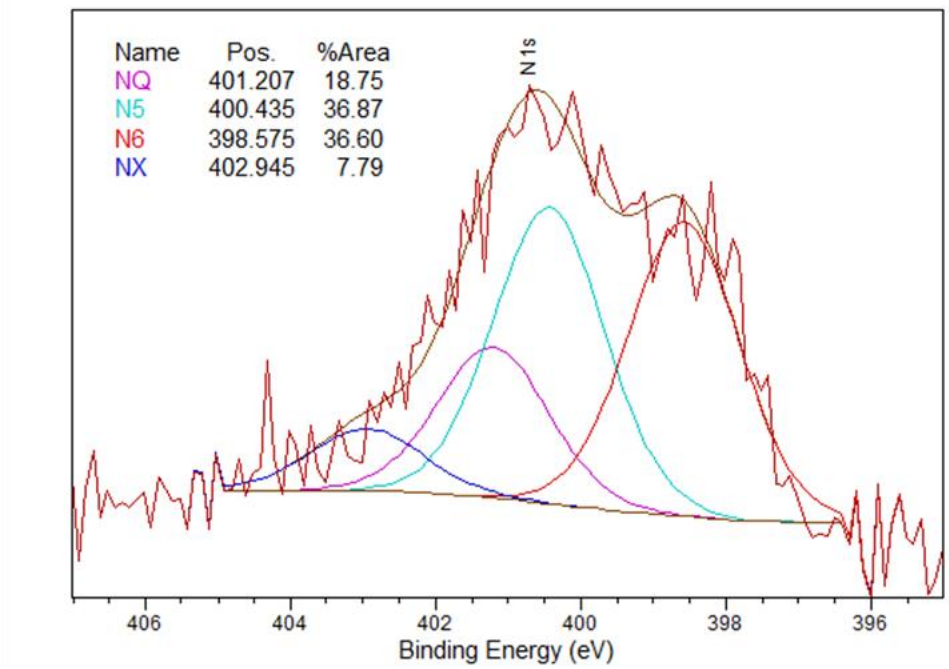

Figure 7.3: N1*s* X-ray photoelectron spectra for X10CA with deconvolution analysis

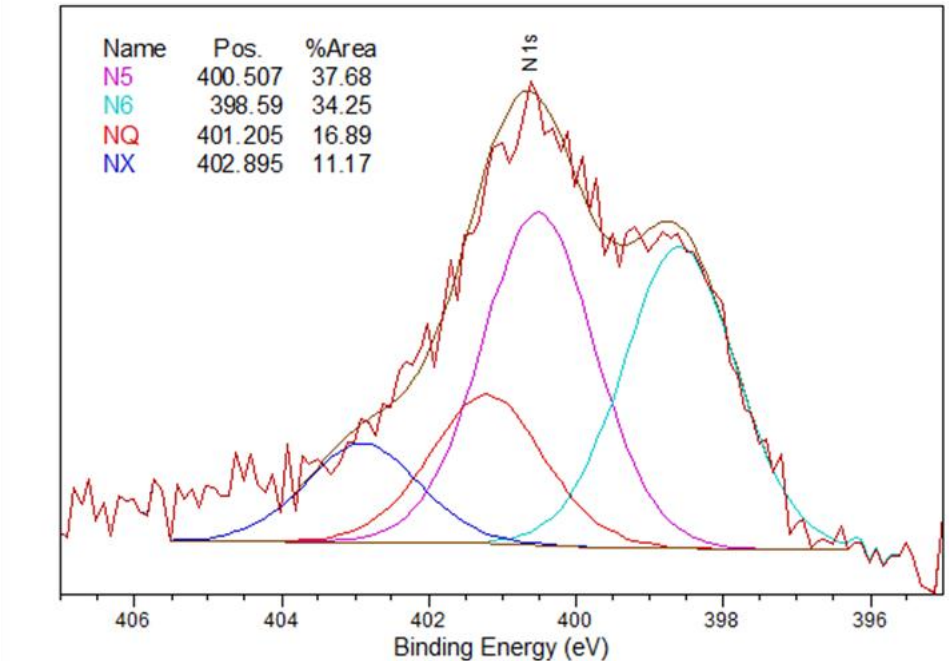

Figure 7.4: N1*s* X-ray photoelectron spectra for X20CA with deconvolution analysis

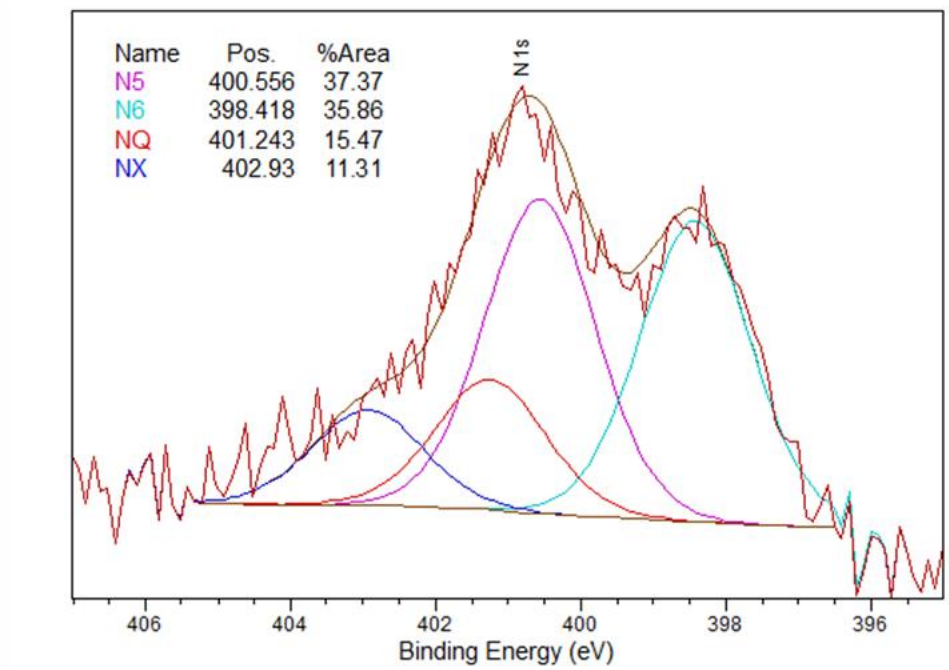

Figure 7.5: N1*s* X-ray photoelectron spectra for X30CA with deconvolution analysis

Appendix F: SANS

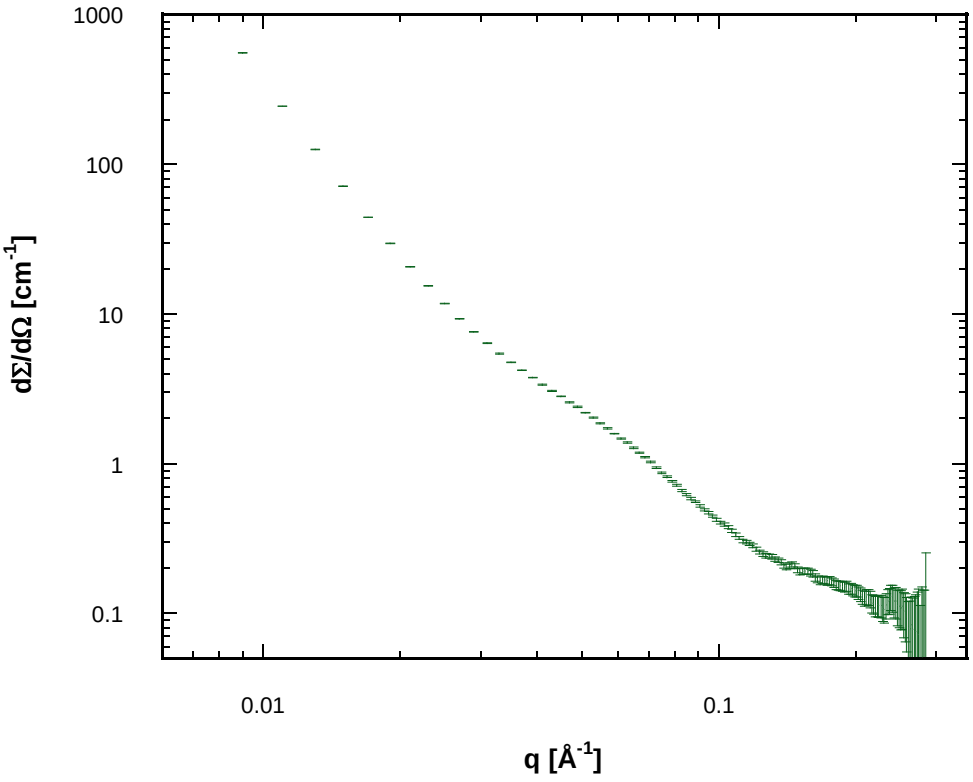

Figure 7.6: SANS for X20CA Ar (with error bars)

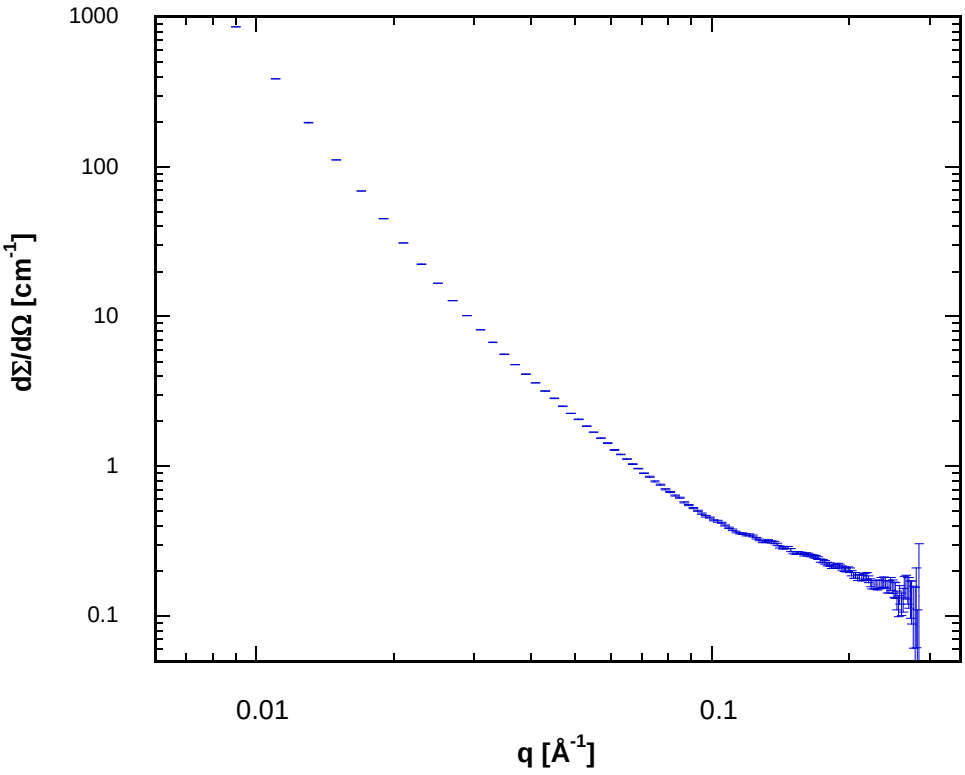

Figure 7.7: SANS for X20CA H_Ar (with error bars)

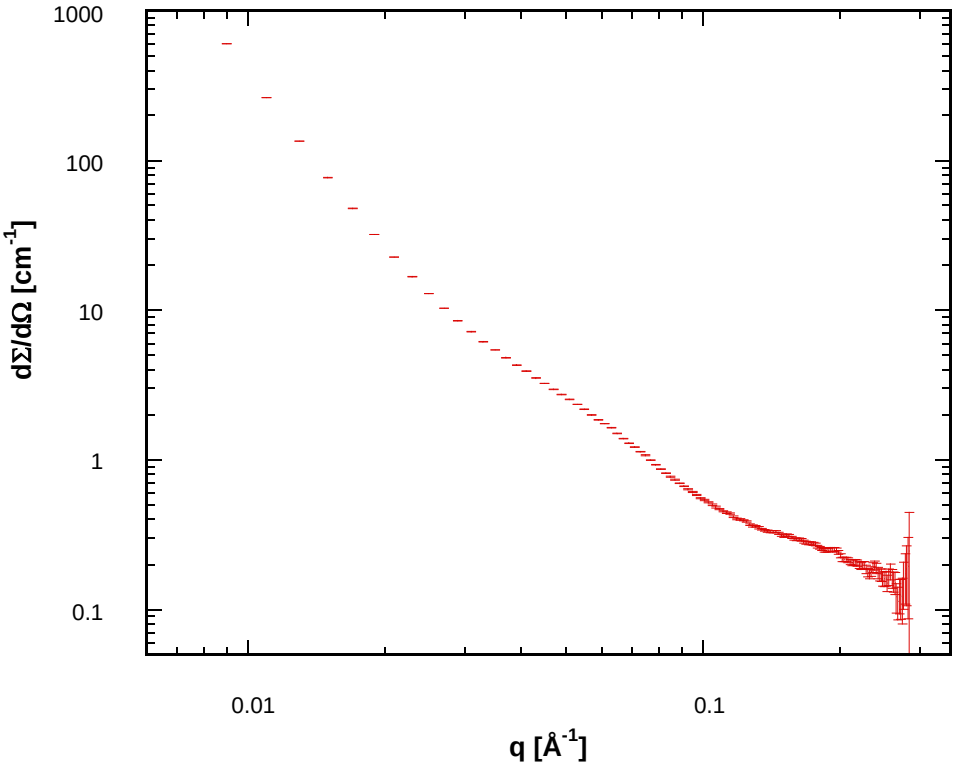

Figure 7.8: SANS for X20CA H (with error bars)

8 References

[1] Intergovernmental Panel on Climate Change, *Climate Change 2007 - The Physical Science Basis: Working Group I Contribution to the Fourth Assessment Report of the IPCC*, Cambridge University Press, 1st edn., 2007

[2] J. M. Cullen and J. M. Allwood, *Energy Policy*, 2010, **38**, 75-81

[3] International Energy Agency, *World Energy Outlook 2008*, Organisation for Economic Co-operation and Development, 2008

[4] P. J. Hall, *Energy Policy*, 2008, **36**, 4363-4367

[5] P. J. Hall and E. J. Bain, *Energy Policy*, 2008, **36**, 4352-4355

[6] http://decc.gov.uk/en/content/cms/statistics/climate_change/data/data.aspx

[7] http://www.berr.gov.uk/files/file48653.pdf

[8] http://www.statistics.gov.uk/STATBASE/ssdataset.asp?vlnk=7801

[9] C. White, R. Steeper, and A. Lutz, *Int. J. Hydrogen Energy*, 2006, **31**, 1292-1305

[10] B. E. Conway, *Electrochemical Supercapacitors: Scientific Fundamentals and Technological Applications*, Kluwer Academic/ Plenum Publishers, New York, 1999

[11] T. Christen, *J. Power Sources*, 2000, **91**, 210-216

[12] P. Simon and Y. Gogotsi, *Nat. Mater.*, 2008, **7**, 845-854

[13] S. Trasatti and P. Kurzweil, *Platinum Metals Rev.*, 1994, **38**, 46-56

[14] A. Rudge, J. Davey, I. Raistrick, S. Gottesfeld, and J. P. Ferraris, *J. Power Sources*, 1994, **47**, 89-107

[15] S. Ashley, *Mech. Eng.*, 1995, **117**, 76

[16] B. E. Conway, V. Birss, and J. Wojtowicz, *J. Power Sources*, 1997, **66**, 1-14

[17] R. Kötz and M. Carlen, *Electrochim. Acta*, 2000, **45**, 2483-2498

[18] A. Burke, *J. Power Sources*, 2000, **91**, 37-50

[19] E. Frackowiak and F. Béguin, *Carbon*, 2001, **39**, 937-950

[20] M. Winter and R. J. Brodd, *Chem. Rev.*, 2005, **105**, 1021

[21] J. R. Miller and P. Simon, *Science*, 2008, **321**, 651 -652

[22] A. G. Pandolfo and A. F. Hollenkamp, *J. Power Sources*, 2006, **157**, 11-27

[23] V. V. N. Obreja, *Physica E*, 2008, **40**, 2596-2605

[24] K. Naoi and P. Simon, *The Electrochemical Society, Interface*, Spring 2008, 34-37

[25] P. Simon and A. Burke, *The Electrochemical Society, Interface*, Spring 2008, 38-43

[26] K. Naoi and M. Morita, *The Electrochemical Society, Interface*, Spring 2008, 44-48

[27] D. Bélanger, T. Brousse, and J. W. Long, *The Electrochemical Society, Interface*, Spring 2008, 49-52

[28] J. R. Miller and A. Burke, *The Electrochemical Society, Interface*, Spring 2008, 53-57

[29] M. Jayalakshmi and K. Balasubramanian, *Int. J. Electrochem. Sci.*, 2008, **3**, 1196-1217

[30] Y. Zhang, H. Feng, X. Wu, L. Wang, A. Zhang, T. Xia, H. Dong, X. Li, and L. Zhang, *Int. J. Hydrogen Energy*, 2009, **34**, 4889-4899

[31] P. J. Hall, M. Mirzaeian, S. I. Fletcher, F. B. Sillars, A. J. R. Rennie, G. O. Shitta-Bey, G. Wilson, A. Cruden, and R. Carter, *Energy Environ. Sci.*, 2010, **3**, 1238

[32] C. D. Lokhande, D. P. Dubal, and O.-S. Joo, *Curr. Appl Phys.*, 2011, **11**, 255-270

[33] R. M. Dell and D. A. J. Rand, *Understanding Batteries*, RSC, Cambridge, UK, 2001

[34] http://www.bussmann.com/pdf/a2b036aa-1d80-4333-ab9c-4229854c96b7.pdf

[35] http://www.maxwell.com/docs/200904_CASESTUDY_SMARTSYNC.PDF

[36] http://www.popularmechanics.com/technology/gadgets/4223118

[37] http://www.maxwell.com/docs/SUPERIOR_TOOLS_CASESTUDY.PDF

[38] http://www.cap-xx.com/solutions/wireless.htm

[39] http://www.powercastco.com//PDF/Power-Out-of-Thin-Air.pdf

[40] http://www.perpetuum.com/resources/PMG17%20Product%20Information.pdf

[41] http://www.cap-xx.com/solutions/consumer.htm

[42] R. Carter and A. Cruden, *IEEE Int. Symp. on Power Electronics, Electrical Drives, Automation & Motion*, 2008, **1-3**, 727-732

[43] T. Markel, A. Brooker, T. Hendricks, V. Johnson, K. Kelly, B. Kramer, M. O'Keefe, S. Sprik, and K. Wipke, *J. Power Sources*, 2002, **110**, 255-266

[44] http://www.afstrinity.net/afstrinity-xh150-pressrelease.pdf

[45] http://world.honda.com/FuelCell/FCX/ultracapacitor/

[46] http://www.vag.de/Busses/id124/The-Ultracapbus.html#

[47] http://www.mantruckandbus.com/en/Products_and_solutions /Current_topics/Lions_City_Hybrid.jsp

[48] http://www.bombardier.com/en/transportation/products-services/propulsion---controls/product-overview/mitrac-energy-saver?docID=0901260d8000e614#

[49] http://www.technologyreview.com/energy/23754/?a=f

[50] http://www.esma-cap.com/Use/Transportation/@lang=English#N59741B

[51] H. E. Becker, US Patent 2,800,616 (to General Electric Co.), 1957

[52] D. C. Grahame, *Chem. Rev.*, 1947, **41**, 441-501

[53] S. Trasatti and G. Buzzanca, *J. Electroanal. Chem.*, 1971, **29**, App. 1-5

[54] K. West, B. Zachau-Christiansen, T. Jacobsen, and S. Skaarup, *J. Power Sources*, 1993, **43**, 127-134

[55] S. Razhoumov, US Patent 6,222,723, (to Joint Stock Company "Elton"), 2001

[56] K. Kinoshita, *Carbon: Electrochemical and Physicochemical Properties*, Wiley, 1988

[57] B. E. Conway, *J. Electrochem. Soc.*, 1991, **138**, 1539-1548

[58] Y. Kibi, T. Saito, M. Kurata, J. Tabuchi, and A. Ochi, *J. Power Sources*, 1996, **60**, 219-224

[59] H. Y. Lee and J. B. Goodenough, *J. Solid State Chem.*, 1999, **144**, 220-223

[60] H. Y. Lee and J. B. Goodenough, *J. Solid State Chem.*, 1999, **148**, 81-84

[61] H. Y. Lee, V. Manivannan, and J. B. Goodenough, *C.R. Acad. Sci., Ser. IIc: Chim.*, 1999, **2**, 565-577

[62] J. Park, *J. Power Sources*, 2002, **105**, 20-25

[63] M. S. Hong, S. H. Lee, and S. W. Kim, *Electrochem. Solid-State Lett.*, 2002, **5**, A227-A230

[64] R. N. Reddy and R. G. Reddy, *J. Power Sources*, 2006, **156**, 700-704

[65] J. Li, X. Wang, Q. Huang, S. Gamboa, and P. J. Sebastian, *J. Power Sources*, 2006, **158**, 784-788

[66] A. Chandra, A. J. Roberts, E. L. How Yee, and R. C. T. Slade, *Pure Appl. Chem.*, 2009, **81**, 1489-1498

[67] A. J. Roberts and R. C. T. Slade, *Electrochim. Acta*, 2010, **55**, 7460-7469

[68] A. J. Roberts and R. C. T. Slade, *J. Mater. Chem.*, 2010, **20**, 3221-3226

[69] S.-C. Pang, M. A. Anderson, and T. W. Chapman, *J. Electrochem. Soc.*, 2000, **147**, 444-450

[70] C.-C. Hu and T.-W. Tsou, *Electrochem. Commun.*, 2002, **4**, 105-109

[71] M. Toupin, T. Brousse, and D. Belanger, *Chem. Mater.*, 2002, **14**, 3946-3952

[72] T. Brousse and D. Belanger, *Electrochem. Solid-State Lett.*, 2003, **6**, A244-A248

[73] O. Ghodbane, J.-L. Pascal, and F. Favier, *ACS Appl. Mater. Int.*, 2009, **1**, 1130-1139

[74] http://resource.invensys.com/instrumentation/documentation/eib/ti/ti_027-072.pdf

[75] P. Kilaru, G. A. Baker, and P. Scovazzo, *J. Chem. Eng. Data*, 2007, **52**, 2306-2314

[76] K. Kim, C. Lang, R. Moulton, and P. A. Kohl, *J. Electrochem. Soc.*, 2004, **151**, A1168-A1172

[77] Y.-J. Kim, Y. Matsuzawa, S. Ozaki, K. C. Park, C. Kim, M. Endo, H. Yoshida, G. Masuda, T. Sato, and M. S. Dresselhaus, *J. Electrochem. Soc.*, 2005, **152**, A710-A715

[78] D. R. McFarlane, J. Sun, J. Golding, P. Meakin, and M. Forsyth, *Electrochim. Acta*, 2000, **45**, 1271-1278

[79] H. Matsumoto, M. Yanagida, K. Tanimoto, M. Nomura, Y. Kitagawa, and Y. Miyazaki, *Chem. Lett.*, 2000, **29**, 922-923

[80] H. Matsumoto, H. Kageyama, and Y. Miyazaki, *Chem. Lett.*, 2001, **30**, 182-183

[81] J. Sun, M. Forsyth, and D. R. MacFarlane, *J. Phys. Chem. B*, 1998, **102**, 8858-8864

[82] W. Lu, K. Henry, C. Turchi, and J. Pellegrino, *J. Electrochem. Soc.*, 2008, **155**, A361-A367

[83] http://www.merck-chemicals.co.uk/brochures/c_qAGb.s1OHEIAAAEh2AURLYY3

[84] S. I. Fletcher, F. B. Sillars, N. E. Hudson, and P. J. Hall, *J. Chem. Eng. Data*, 2010, **55**, 778-782

[85] J. M. Crosthwaite, M. J. Muldoon, J. K. Dixon, J. L. Anderson, and J. F. Brennecke, *J. Chem. Thermodyn.*, 2005, **37**, 559-568

[86] M. Galinski, A. Lewandowski, and I. Stepniak, *Electrochim. Acta*, 2006, **51**, 5567-5580

[87] K. R. Harris, L. A. Woolf, and M. Kanakubo, *J. Chem. Eng. Data*, 2005, **50**, 1777-1782

[88] D. R. MacFarlane, P. Meakin, J. Sun, N. Amini, and M. Forsyth, *J. Phys. Chem. B*, 1999, **103**, 4164-4170

[89] A. B. McEwen, H. L. Ngo, K. LeCompte, and J. L. Goldman, *J. Electrochem. Soc.*, 1999, **146**, 1687-1695

[90] M. E. Kandil, K. N. Marsh, and A. R. H. Goodwin, *J. Chem. Eng. Data*, 2007, **52**, 2382-2387

[91] A. Noda, K. Hayamizu, and M. Watanabe, *J. Phys. Chem. B*, 2001, **105**, 4603-4610

[92] H. Ohno and M. Yoshizawa, *Solid State Ionics*, 2002, **154-155**, 303-309

[93] H. Tokuda, K. Hayamizu, K. Ishii, M. A. B. H. Susan, and M. Watanabe, *J. Phys. Chem. B*, 2004, **108**, 16593-16600

[94] H. Tokuda, K. Hayamizu, K. Ishii, M. A. B. H. Susan, and M. Watanabe, *J. Phys. Chem. B*, 2005, **109**, 6103-6110

[95] H. Tokuda, K. Ishii, M. A. B. H. Susan, S. Tsuzuki, K. Hayamizu, and M. Watanabe, *J. Phys. Chem. B*, 2006, **110**, 2833-2839

[96] J. A. Widegren, E. M. Saurer, K. N. Marsh, and J. W. Magee, *J. Chem. Thermodyn.*, 2005, **37**, 569-575

[97] W. Xu and C. A. Angell, *Science*, 2003, **302**, 422-425

[98] D. Rochefort and A.-L. Pont, *Electrochem. Commun.*, 2006, **8**, 1539-1543

[99] R. Mysyk, E. Raymundo-Piñero, M. Anouti, D. Lemordant, and F. Béguin, *Electrochem. Commun.*, 2010, **12**, 414-417

[100] W. Dmowski, T. Egami, K. E. Swider-Lyons, C. T. Love, and D. R. Rolison, *J. Phys. Chem. B*, 2002, **106**, 12677-12683

[101] J. M. Fletcher, W. E. Gardner, B. F. Greenfield, M. J. Holdoway, and M. H. Rand, *J. Chem. Soc. (A)*, 1968, 653-657

[102] J. B. Goodenough, *Prog. Solid State Chem.*, 1971, **5**, 145-399

[103] W. D. Ryden, A. W. Lawson, and C. C. Sartain, *Phys. Rev. B*, 1970, **1**, 1494-1500

[104] J. P. Zheng and T. R. Jow, *J. Electrochem. Soc.*, 1995, **142**, L6-L8

[105] J. P. Zheng, P. J. Cygan, and T. R. Jow, *J. Electrochem. Soc.*, 1995, **142**, 2699-2703

[106] I.-H. Kim, J.-H. Kim, Y.-H. Lee, and K.-B. Kim, *J. Electrochem. Soc.*, 2005, **152**, A2170-A2178

[107] C.-C. Hu, W.-C. Chen, and K.-H. Chang, *J. Electrochem. Soc.*, 2004, **151**, A281-A290

[108] K.-C. Liu and M. A. Anderson, *J. Electrochem. Soc.*, 1996, **143**, 124-130

[109] V. Srinivasan and J. W. Weidner, *J. Electrochem. Soc.*, 1997, **144**, L210-L213

[110] M. Wu, J. Gao, S. Zhang, and A. Chen, *J. Power Sources*, 2006, **159**, 365-369

[111] C. Lin, J. A. Ritter, and B. N. Popov, *J. Electrochem. Soc.*, 1998, **145**, 4097-4103

[112] T.-C. Liu, W. G. Pell, and B. E. Conway, *Electrochim. Acta*, 1999, **44**, 2829-2842

[113] V. Srinivasan and J. W. Weidner, *J. Power Sources*, 2002, **108**, 15-20

[114] Y. Sato, T. Nomura, H. Tanaka, and K. Kobayakawa, *J. Electrochem. Soc.*, 1991, **138**, L37-L39

[115] S. Passerini, J. J. Ressler, D. B. Le, B. B. Owens, and W. H. Smyrl, *Electrochim. Acta*, 1999, **44**, 2209-2217

[116] T. Kudo, Y. Ikeda, T. Watanabe, M. Hibino, M. Miyayama, H. Abe, and K. Kajita, *Solid State Ionics*, 2002, **152-153**, 833-841

[117] S. Suzuki, M. Hibino, and M. Miyayama, *J. Power Sources*, 2003, **124**, 513-517

[118] W. Dong, J. Sakamoto, and B. Dunn, *J. Sol-Gel Sci. Technol.*, 2003, **26**, 641-644

[119] Z. J. Lao, K. Konstantinov, Y. Tournaire, S. H. Ng, G. X. Wang, and H. K. Liu, *J. Power Sources*, 2006, **162**, 1451-1454

[120] I.-H. Kim, J.-H. Kim, B.-W. Cho, Y.-H. Lee, and K.-B. Kim, *J. Electrochem. Soc.*, 2006, **153**, A989

[121] N.-L. Wu, S.-Y. Wang, C.-Y. Han, D.-S. Wu, and L.-R. Shiue, *J. Power Sources*, 2003, **113**, 173-178

[122] S.-Y. Wang, K.-C. Ho, S.-L. Kuo, and N.-L. Wu, *J. Electrochem. Soc.*, 2006, **153**, A75-A80

[123] X. Zhao, C. Johnston, and P. S. Grant, *J. Mater. Chem.*, 2009, **19**, 8755

[124] X. Du, C. Wang, M. Chen, Y. Jiao, and J. Wang, *J. Phys. Chem. C*, 2009, **113**, 2643-2646

[125] Y. Chabre and J. Pannetier, *Prog. Solid State Chem.*, 1995, **23**, 1-130

[126] F. Jiao, J. Bao, A. Hill, and P. Bruce, *Ang. Chem., Int. Ed.*, 2008, **47**, 9711-9716

[127] M. Toupin, T. Brousse, and D. Belanger, *Chem. Mater.*, 2004, **16**, 3184-3190

[128] E. Raymundo-Pinero, V. Khomenko, E. Frackowiak, and F. Beguin, *J. Electrochem. Soc.*, 2005, **152**, A229-A235

[129] T. Brousse, M. Toupin, R. Dugas, L. Athouel, O. Crosnier, and D. Belanger, *J. Electrochem. Soc.*, 2006, **153**, A2171-A2180

[130] T. Cottineau, M. Toupin, T. Delahaye, T. Brousse, and D. Bélanger, *Appl. Phys. A*, 2006, **82**, 599-606

[131] T. Shinomiya, V. Gupta, and N. Miura, *Electrochim. Acta*, 2006, **51**, 4412-4419

[132] C.-K. Lin, K.-H. Chuang, C.-Y. Lin, C.-Y. Tsay, and C.-Y. Chen, *Surf. Coat. Technol.*, 2007, **202**, 1272-1276

[133] I.-H. Kim, J.-H. Kim, B.-W. Cho, and K.-B. Kim, *J. Electrochem. Soc.*, 2006, **153**, A1451

[134] G. G. Amatucci, F. Badway, A. Du Pasquier, and T. Zheng, *J. Electrochem. Soc.*, 2001, **148**, A930-A939

[135] A. Du Pasquier, A. Laforgue, P. Simon, G. G. Amatucci, and J.-F. Fauvarque, *J. Electrochem. Soc.*, 2002, **149**, A302-A306

[136] A. Du Pasquier, I. Plitz, S. Menocal, and G. Amatucci, *J. Power Sources*, 2003, **115**, 171-178

[137] V. Khomenko, E. Raymundo-Piñero, and F. Béguin, *J. Power Sources*, 2008, **177**, 643-651

[138] S. R. Sivakkumar, J. Y. Nerkar, and A. G. Pandolfo, *Electrochim. Acta*, 2010, **55**, 3330-3335

[139] A. Yoshino, T. Tsubata, M. Shimoyamada, H. Satake, Y. Okano, S. Mori, and S. Yata, *J. Electrochem. Soc.*, 2004, **151**, A2180-A2182

[140] Y.-G. Wang and Y.-Y. Xia, *Electrochem. Commun.*, 2005, **7**, 1138-1142

[141] Y.-G. Wang and Y.-Y. Xia, *J. Electrochem. Soc.*, 2006, **153**, A450-A454

[142] Y.-G. Wang, J.-Y. Luo, C.-X. Wang, and Y.-Y. Xia, *J. Electrochem. Soc.*, 2006, **153**, A1425-A1431

[143] A. Burke, *Electrochim. Acta*, 2007, **53**, 1083-1091

[144] C. Arbizzani, M. Mastragostino, and L. Meneghello, *Electrochim. Acta*, 1996, **41**, 21-26

[145] E. Frackowiak, V. Khomenko, K. Jurewicz, K. Lota, and F. Béguin, *J. Power Sources*, 2006, **153**, 413-418

[146] Q. Wang, J.-ling Li, F. Gao, W.-sheng Li, K.-zhong Wu, and X.-dong Wang, *New Carbon Mater.*, 2008, **23**, 275-280

[147] E. Frackowiak, *Phys. Chem. Chem. Phys.*, 2007, **9**, 1774

[148] H. Marsh and F. Rodríguez-Reinoso, *Activated Carbon*, Elsevier, 2006

[149] D. R. Lide, Ed., *CRC Handbook Of Chemistry And Physics Version 2005*, CRC Press, 2004

[150] J.-P. Randin and E. Yeager, *J. Electrochem. Soc.*, 1971, **118**, 711

[151] A. K. Geim and K. S. Novoselov, *Nat Mater*, 2007, **6**, 183-191

[152] A. K. Geim, *Science*, 2009, **324**, 1530-1534

[153] S. Amini, J. Garay, G. Liu, A. A. Balandin, and R. Abbaschian, *J. Appl. Phys.*, 2010, **108**, 094321

[154] M. Choucair, P. Thordarson, and J. A. Stride, *Nat Nano*, 2009, **4**, 30-33

[155] M. D. Stoller, S. Park, Y. Zhu, J. An, and R. S. Ruoff, *Nano Lett.*, 2008, **8**, 3498-3502

[156] X. Zhao, H. Tian, M. Zhu, K. Tian, J. J. Wang, F. Kang, and R. A. Outlaw, *J. Power Sources*, 2009, **194**, 1208-1212

[157] X. Du, P. Guo, H. Song, and X. Chen, *Electrochim. Acta*, 2010, **55**, 4812-4819

[158] H. W. Kroto, J. R. Heath, S. C. O'Brien, R. F. Curl, and R. E. Smalley, *Nature*, 1985, **318**, 162-163

[159] S. Iijima, *Nature*, 1991, **354**, 56-58

[160] M. Monthioux and V. L. Kuznetsov, *Carbon*, 2006, **44**, 1621-1623

[161] X. Lu and Z. Chen, *Chem. Rev.*, 2005, **105**, 3643-3696

[162] Y. Show and K. Imaizumi, *Diamond Relat. Mater.*, November, **15**, 2086-2089

[163] A. Jänes, L. Permann, M. Arulepp, and E. Lust, *Electrochem. Commun.*, 2004, **6**, 313-318

[164] M. Arulepp, J. Leis, M. Lätt, F. Miller, K. Rumma, E. Lust, and A. F. Burke, *J. Power Sources*, 2006, **162**, 1460-1466

[165] J. Chmiola, G. Yushin, R. Dash, and Y. Gogotsi, *J. Power Sources*, 2006, **158**, 765-772

[166] J. Chmiola, *Science*, 2006, **313**, 1760-1763

[167] C. Largeot, C. Portet, J. Chmiola, P.-L. Taberna, Y. Gogotsi, and P. Simon, *J. Am. Chem. Soc.*, 2008, **130**, 2730-2731

[168] J. Chmiola, C. Largeot, P.-L. Taberna, P. Simon, and Y. Gogotsi, *Angew. Chem. Int. Ed.*, 2008, **47**, 3392-3395

[169] J. Rouquerol, D. Avnir, C. W. Fairbridge, D. H. Everett, J. M. Haynes, N. Pernicone, J. D. F. Ramsay, K. S. W. Sing, and K. K. Unger, *Pure Appl. Chem.*, 1994, **66**, 1739-1758

[170] K. S. W. Sing, D. H. Everett, R. A. W. Haul, L. Moscou, R. A. Pierotti, J. Rouquerol, and T. Siemieniewska, *Pure Appl. Chem.*, 1985, **57**, 603-619

[171] R. C. Bansal, J.-B. Donnet, and F. Stoeckli, *Active Carbon*, Marcel Dekker Inc, 1988

[172] T. J. Bandosz, *Activated Carbon Surfaces in Environmental Remediation*, Academic Press, 2006

[173] A. Linares-Solano, I. Martín-Gullon, C. Salinas-Martínez de Lecea, and B. Serrano-Talavera, *Fuel*, 2000, **79**, 635-643

[174] E. Wiberg, N. Wiberg, and A. F. Holleman, *Inorganic Chemistry*, Academic Press, 2001

[175] S. H. Joo, S. Jun, and R. Ryoo, *Microporous Mesoporous Mater.*, 2001, **44-45**, 153-158

[176] E. Frackowiak, G. Lota, J. Machnikowski, C. Vix-Guterl, and F. Béguin, *Electrochim. Acta*, 2006, **51**, 2209-2214

[177] M. Sevilla, S. Álvarez, T. A. Centeno, A. B. Fuertes, and F. Stoeckli, *Electrochim. Acta*, 2007, **52**, 3207-3215

[178] W. Xing, S. Z. Qiao, R. G. Ding, F. Li, G. Q. Lu, Z. F. Yan, and H. M. Cheng, *Carbon*, 2006, **44**, 216-224

[179] M. G. Sullivan, B. Schnyder, M. Bartsch, D. Alliata, C. Barbero, R. Imhof, and R. Kotz, *J. Electrochem. Soc.*, 2000, **147**, 2636-2643

[180] A. Braun, J. Kohlbrecher, M. Bärtsch, B. Schnyder, R. Kötz, O. Haas, and A. Wokaun, *Electrochim. Acta*, 2004, **49**, 1105-1112

[181] F. Beck, M. Dolata, and E. Grivei, *J. Appl. Electrochem.*, 2001, **31**, 845-853

[182] R. Richner, S. Müller, and A. Wokaun, *Carbon*, 2002, **40**, 307-314

[183] R. W. Pekala, *J. Mater. Sci.*, 1989, **24**, 3221-3227

[184] K. Barral, *J. Non-Cryst. Solids*, 1998, **225**, 46-50

[185] G. C. Ruben and R. W. Pekala, *J. Non-Cryst. Solids*, 1995, **186**, 219-231

[186] M. H. Nguyen and L. H. Dao, *J. Non-Cryst. Solids*, 1998, **225**, 51-57

[187] R. W. Pekala, C. T. Alviso, X. Lu, J. Gross, and J. Fricke, *J. Non-Cryst. Solids*, 1995, **188**, 34-40

[188] G. Biesmans, A. Mertens, L. Duffours, T. Woignier, and J. Phalippou, *J. Non-Cryst. Solids*, 1998, **225**, 64-68

[189] W.-C. Li, A.-H. Lu, and S.-C. Guo, *Carbon*, 2001, **39**, 1989-1994

[190] R. Zhang, Y. Lu, L. Zhan, X. Liang, G. Wu, and L. Ling, *Carbon*, 2003, **41**, 1660-1663

[191] S. R. Mukai, C. Tamitsuji, H. Nishihara, and H. Tamon, *Carbon*, 2005, **43**, 2628-2630

[192] J. Yamashita, T. Ojima, M. Shioya, H. Hatori, and Y. Yamada, *Carbon*, 2003, **41**, 285-294

[193] J. Lee, G. Gould, and W. Rhine, *J. Sol-Gel Sci. Technol.*, 2009, **49**, 209-220

[194] S. T. Mayer, R. W. Pekala, and J. L. Kaschmitter, *J. Electrochem. Soc.*, 1993, **140**, 446-451

[195] F. B. Sillars, PhD Thesis, University of Strathclyde, 2010

[196] F. B. Sillars, S. I. Fletcher, M. Mirzaeian, and P. J. Hall, *Energy Environ. Sci.*, 2011, **4**, 695

[197] M. Mirzaeian and P. J. Hall, *J. Mater. Sci.*, 2009, **44**, 2705-2713

[198] C. Lin and J. A. Ritter, *Carbon*, 1997, **35**, 1271-1278

[199] H. Tamon, H. Ishizaka, M. Mikami, and M. Okazaki, *Carbon*, 1997, **35**, 791-796

[200] N. Job, A. Théry, R. Pirard, J. Marien, L. Kocon, J.-N. Rouzaud, F. Béguin, and J.-P. Pirard, *Carbon*, 2005, **43**, 2481-2494

[201] T. Horikawa, J. Hayashi, and K. Muroyama, *Carbon*, 2004, **42**, 1625-1633

[202] N. Job, C. J. Gommes, R. Pirard, and J.-P. Pirard, *J. Non-Cryst. Solids*, 2008, **354**, 4698-4701

[203] M. A. Elsayed, PhD Thesis, University of Strathclyde, 2007

[204] A. Léonard, N. Job, S. Blacher, J.-P. Pirard, M. Crine, and W. Jomaa, *Carbon*, 2005, **43**, 1808-1811

[205] L. Zubizarreta, A. Arenillas, J. A. Menéndez, J. J. Pis, J.-P. Pirard, and N. Job, *J. Non-Cryst. Solids*, 2008, **354**, 4024-4026

[206] T. Yamamoto, T. Nishimura, T. Suzuki, and H. Tamon, *J. Non-Cryst. Solids*, 2001, **288**, 46-55

[207] R. W. Pekala, J. C. Farmer, C. T. Alviso, T. D. Tran, S. T. Mayer, J. M. Miller, and B. Dunn, *J. Non-Cryst. Solids*, 1998, **225**, 74-80

[208] S.-W. Hwang and S.-H. Hyun, *J. Non-Cryst. Solids*, 2004, **347**, 238-245

[209] D. Hulicova, J. Yamashita, Y. Soneda, H. Hatori, and M. Kodama, *Chem. Mater.*, 2005, **17**, 1241-1247

[210] M. Seredych, D. Hulicova-Jurcakova, G. Q. Lu, and T. J. Bandosz, *Carbon*, 2008, **46**, 1475-1488

[211] H. Shi, *Electrochim. Acta*, 1996, **41**, 1633-1639

[212] D. Qu and H. Shi, *J. Power Sources*, 1998, **74**, 99-107

[213] E. Raymundo-Piñero, K. Kierzek, J. Machnikowski, and F. Béguin, *Carbon*, 2006, **44**, 2498-2507

[214] C. O. Ania, J. Pernak, F. Stefaniak, E. Raymundo-Piñero, and F. Béguin, *Carbon*, 2006, **44**, 3126-3130

[215] P. Delahay, *Double Layer and Electrode Kinetics*, Interscience, 1965

[216] J. Huang, B. G. Sumpter, and V. Meunier, *Chem. Eur. J.*, 2008, **14**, 6614-6626

[217] A. B. Fuertes, F. Pico, and J. M. Rojo, *J. Power Sources*, 2004, **133**, 329-336

[218] V. V. Strelko and Y. D. Lavrinenko-Ometsinkaya, *J. Mol. Struct. THEOCHEM*, 1989, **188**, 193-197

[219] V. V. Strelko, V. S. Kuts, and P. A. Thrower, *Carbon*, 2000, **38**, 1499-1503

[220] V. V. Strelko, N. T. Kartel, I. N. Dukhno, V. S. Kuts, R. B. Clarkson, and B. M. Odintsov, *Surf. Sci.*, 2004, **548**, 281-290

[221] H. A. Andreas and B. E. Conway, *Electrochim. Acta*, 2006, **51**, 6510-6520

[222] M. L. Studebaker and C. W. Snow, *J. Phys. Chem.*, 1955, **59**, 973-976

[223] A. Yoshida, I. Tanahashi, and A. Nishino, *Carbon*, 1990, **28**, 611-615

[224] C.-T. Hsieh and H. Teng, *Carbon*, 2002, **40**, 667-674

[225] T. Morimoto, K. Hiratsuka, Y. Sanada, and K. Kurihara, *J. Power Sources*, 1996, **60**, 239-247

[226] K. Y. Kang, B. I. Lee, and J. S. Lee, *Carbon*, 2009, **47**, 1171-1180

[227] M.-C. Huang and H. Teng, *Carbon*, 2003, **41**, 951-957

[228] S. Sepehri, B. B. García, Q. Zhang, and G. Cao, *Carbon*, 2009, **47**, 1436-1443

[229] K. Jurewicz, K. Babel, A. Ziólkowski, H. Wachowska, and M. Kozlowski, *Fuel Process. Technol.*, 2002, **77-78**, 191-198

[230] K. Jurewicz, K. Babel, A. Ziólkowski, and H. Wachowska, *Electrochim. Acta*, 2003, **48**, 1491-1498

[231] K. Jurewicz, K. Babel, A. Ziólkowski, and H. Wachowska, *J. Phys. Chem. Solids*, 2004, **65**, 269-273

[232] K. Jurewicz, K. Babel, R. Pietrzak, S. Delpeux, and H. Wachowska, *Carbon*, 2006, **44**, 2368-2375

[233] D. Hulicova-Jurcakova, M. Kodama, S. Shiraishi, H. Hatori, Z. H. Zhu, and G. Q. Lu, *Adv. Funct. Mater.*, 2009, **19**, 1800-1809

[234] R. Pietrzak, K. Jurewicz, P. Nowicki, K. Babel, and H. Wachowska, *Fuel*, 2010, **89**, 3457-3467

[235] M. Kodama, J. Yamashita, Y. Soneda, H. Hatori, S. Nishimura, and K. Kamegawa, *Mater. Sci. Eng., B*, 2004, **108**, 156-161

[236] G. Lota, B. Grzyb, H. Machnikowska, J. Machnikowski, and E. Frackowiak, *Chem. Phys. Lett.*, 2005, **404**, 53-58

[237] F. Béguin, K. Szostak, G. Lota, and E. Frackowiak, *Adv. Mater.*, 2005, **17**, 2380-2384

[238] D. Hulicova, M. Kodama, and H. Hatori, *Chem. Mater.*, 2006, **18**, 2318-2326

[239] K. Leitner, A. Lerf, M. Winter, J. O. Besenhard, S. Villar-Rodil, F. Suárez-García, A. Martínez-Alonso, and J. M. D. Tascón, *J. Power Sources*, 2006, **153**, 419-423

[240] W. Li, D. Chen, Z. Li, Y. Shi, Y. Wan, J. Huang, J. Yang, D. Zhao, and Z. Jiang, *Electrochem. Commun.*, 2007, **9**, 569-573

[241] Y. J. Kim, Y. Abe, T. Yanagiura, K. C. Park, M. Shimizu, T. Iwazaki, S. Nakagawa, M. Endo, and M. S. Dresselhaus, *Carbon*, 2007, **45**, 2116-2125

[242] G. Lota, K. Lota, and E. Frackowiak, *Electrochem. Commun.*, 2007, **9**, 1828-1832

[243] J. Jiang, Q. Gao, K. Xia, and J. Hu, *Microporous Mesoporous Mater.*, 2009, **118**, 28-34

[244] E. J. Ra, E. Raymundo-Piñero, Y. H. Lee, and F. Béguin, *Carbon*, 2009, **47**, 2984-2992

[245] D. Hulicova-Jurcakova, M. Seredych, G. Q. Lu, and T. J. Bandosz, *Adv. Funct. Mater.*, 2009, **19**, 438-447

[246] G.-Q. Zhang and S.-T. Zhang, *J. Solid State Electrochem.*, 2009, **13**, 887-893

[247] H. Wang, Q. Gao, and J. Hu, *Microporous Mesoporous Mater.*, 2010, **131**, 89-96

[248] X. Yang, D. Wu, X. Chen, and R. Fu, *J. Phys. Chem. C*, 2010, **114**, 8581-8586

[249] F. Su, C. K. Poh, J. S. Chen, G. Xu, D. Wang, Q. Li, J. Lin, and X. W. Lou, *Energy Environ. Sci.*, 2011, **4**, 717

[250] N. Setoyama, T. Suzuki, and K. Kaneko, *Carbon*, 1998, **36**, 1459-1467

[251] S. J. Gregg and K. S. W. Sing, *Adsorption, Surface Area, and Porosity*, Academic Press, 1991

[252] N. Setoyama, K. Kaneko, and F. Rodriguez-Reinoso, *J. Phys. Chem.*, 1996, **100**, 10331-10336

[253] http://www.carbonblack.jp/en/product/list2_01.html#32

[254] J. E. B. Randles, *Discuss. Faraday Soc.*, 1947, **1**, 11

[255] J. R. Pels, F. Kapteijn, J. A. Moulijn, Q. Zhu, and K. M. Thomas, *Carbon*, 1995, **33**, 1641-1653

[256] http://www.micromeritics.com/Library/DFT-NLDFT-Density-Functional-Theory/NLDFT-DFT-Bibliography.aspx

[257] S. Brunauer, P. H. Emmett, and E. Teller, *J. Am. Chem. Soc.*, 1938, **60**, 309-319

[258] E. P. Barrett, L. G. Joyner, and P. P. Halenda, *J. Am. Chem. Soc.*, 1951, **73**, 373-380

[259] M. M. Dubinin and V. A. Astakhov, in *Molecular Sieve Zeolites-II*, ACS, 2011, vol. 102, pp. 69-85

[260] S. Lowell and J. E. Shields, *Powder Surface Area and Porosity*, Springer, 1991

[261] M. Polanyi, *Trans. Faraday Soc.*, 1932, **28**, 316

[262] M. M. Dubinin, *Chem. Rev.*, 1960, **60**, 235-241

[263] E. J. Bain, PhD Thesis, University of Strathclyde, 2006

[264] S. Brunauer, L. S. Deming, W. E. Deming, and E. Teller, *J. Am. Chem. Soc.*, 1940, **62**, 1723-1732

[265] I. Langmuir, *J. Am. Chem. Soc.*, 1918, **40**, 1361-1403

[266] G. Halsey, *J. Chem. Phys.*, 1948, **16**, 931

[267] W. D. Harkins and G. Jura, *J. Chem. Phys.*, 1943, **11**, 431

[268] W. Thomson, *Phil. Mag.*, 1871, **42**, 448

[269] J. Medek, *Fuel*, 1977, **56**, 131-133

[270] G. Horváth and K. Kawazoe, *J. Chem. Eng. Japan*, 1983, **16**, 470-475

[271] B. C. Lippens and J. H. de Boer, *Journal of Catalysis*, 1965, **4**, 319-323

[272] D. Briggs and M. P. Seah, *Practical Surface Analysis*, John Wiley & Sons Ltd, Chichester, 2nd edn., 1990, vol. Volume 1- Auger and X-ray Photoelectron Spectroscopy

[273] K. Jurewicz and K. Babeł, *Energy Fuels*, 2010, **24**, 3429-3435

[274] G. L. Squires, *Introduction to the Theory of Thermal Neutron Scattering*, Courier Dover Publications, 1996

[275] J. S. Higgins and H. Benoît, *Polymers and Neutron Scattering*, Oxford University Press, 1997

[276] R. A. Pethrick and J. V. Dawkins, *Modern Techniques for Polymer Characterisation*, Wiley, 1999

[277] J. M. Calo and P. J. Hall, *Carbon*, 2004, **42**, 1299-1304

[278] A.-J. Dianoux and G. Lander, *Neutron Data Booklet*, OCP Science, 1st edn., 2003

[279] M. D. Foster and K. F. Jensen, *Journal of Colloid and Interface Science*, 1990, **135**, 132-146

[280] E. Y. Sheu, *Phys. Rev. A*, 1992, **45**, 2428

[281] T. Freltoft, J. K. Kjems, and S. K. Sinha, *Phys. Rev. B*, 1986, **33**, 269

[282] O. Glatter and O. Kratky, *Small Angle X-ray Scattering*, Academic Press, 1982

[283] J. S. Gethner, *J. Appl. Phys.*, 1986, **59**, 1068

[284] J. M. Calo, P. J. Hall, and M. Antxustegi, *Colloids and Surfaces A: Physicochemical and Engineering Aspects*, 2001, **187-188**, 219-232

[285] Y. C. Chiew and E. D. Glandt, *Journal of Colloid and Interface Science*, 1984, **99**, 86-96

[286] M. M. Antxustegi, P. J. Hall, and J. M. Calo, *J. Coll. Interface Sci.*, 1998, **202**, 490-498

[287] P. J. Hall, S. Brown, J. Fernandez, and J. Calo, *Carbon*, 2000, **38**, 1257-1259

[288] N. Cohaut, A. Thery, J. M. Guet, J. N. Rouzaud, and L. Kocon, *Carbon*, 2007, **45**, 1185-1192

[289] P. J. Hall, M. Antxustegi, and W. Ruiz, *Fuel*, 1998, **77**, 1663-1665

[290] P. J. Hall, S. D. Brown, and J. M. Calo, *Fuel*, 2000, **79**, 1327-1332

[291] A. J. Bard and L. R. Faulkner, *Electrochemical Methods: Fundamentals and Applications*, Wiley, 2nd edn., 2000

[292] R. de Levie, *Electrochim. Acta*, 1964, **9**, 1231-1245

[293] E. Gileadi, *Electrode Kinetics for Chemists, Chemical Engineers and Materials Scientists*, John Wiley and Sons, 1993

[294] K. Kierzek, E. Frackowiak, G. Lota, G. Gryglewicz, and J. Machnikowski, *Electrochimica Acta*, 2004, **49**, 515-523

[295] J. Black and H. A. Andreas, *Electrochim. Acta*, 2009, **54**, 3568-3574

[296] D. A. Shirley, *Phys. Rev. B*, 1972, **5**, 4709

[297] http://www.isis.stfc.ac.uk/

[298] R. K. Heenan, J. Penfold, and S. M. King, *J. Appl. Crystallogr.*, 1997, **30**, 1140-1147

[299] http://www.isis.stfc.ac.uk/instruments/loq/documents/the-loq-beamline9961.jpg

[300] G. D. Wignall and F. S. Bates, *J. Appl. Crystallogr.*, 1987, **20**, 28-40

[301] A. M. White and R. C. T. Slade, *Synth. Met.*, 2003, **139**, 123-131

[302] S. I. Fletcher, F. B. Sillars, R. C. Carter, A. J. Cruden, M. Mirzaeian, N. E. Hudson, J. A. Parkinson, and P. J. Hall, *J. Power Sources*, 2010, **195**, 7484-7488

[303] S. J. Kim, S. W. Hwang, and S. H. Hyun, *J Mater Sci*, 2005, **40**, 725-731

[304] D. H. Everett and F. S. Stone, in *The Structure and Properties of Porous Materials, Colston Research Society Papers*, Butterworths, London, 1958, vol. 10